

Selected Experiments with Proteins at Solid-Liquid Interfaces

by

Jonathan Teichroeb

A thesis
presented to the University of Waterloo
in fulfillment of the
thesis requirement for the degree of
Doctor of Philosophy
in
Physics

Waterloo, Ontario, Canada, 2008

©Jonathan Teichroeb 2008

AUTHOR'S DECLARATION

I hereby declare that I am the sole author of this thesis. This is a true copy of the thesis, including any required final revisions, as accepted by my examiners.

I understand that my thesis may be made electronically available to the public.

Abstract

This thesis describes a number of novel experiments contributing to the understanding of protein adsorption from both a fundamental and applied perspective.

The first three papers involve the use of the localized surface plasmon resonance of gold nanospheres to measure protein conformational dependencies during heat and acid denaturation. Thermal denaturation of BSA is shown to proceed differently depending on the size of nanosphere to which it is conjugated. Activation energies are extracted for thermal denaturing on nanoparticles. These energies decrease with decreasing radius of curvature. Under pH perturbation in the acid region, the multiple transition states of bulk BSA are suppressed, and only one apparent transition around pH 4 is evident. Smaller spheres (diameter $< 20\text{nm}$) do not exhibit any transition. A significant finding of all three studies is that the state and stability of BSA depends strongly upon local curvature.

The last two papers investigate protein adsorption relevant to the biomaterial field. Investigation of protein adsorption to polyHEMA hydrogels is carried out using a quartz crystal microbalance. Single and mixed protein adsorption kinetics for BSA, lysozyme and lactoferrin are extracted and interpreted. Selected commercial cleaning solutions are shown to be no more effective than simple buffer solution.

Examination of commercial lenses indicates that the morphology of adsorption is material dependent and that siloxane-based hydrogels only deposit low levels of protein. A unique fibril-like morphology is identified on galyfilcon A. Protein morphology is discussed in terms of bare lens morphology, roughness, and surface composition.

Acknowledgements

I would like to acknowledge everyone who has been a part of supporting me in this degree. I would like to thank Drs. James Forrest and Lyndon Jones for their supervision and guidance throughout my degree. I want to thank my coworkers: James Benson, James Chan, Zahra Fakhraai, Dongping Qi, Patrick McVeigh, Ryan Speller, Mark Ilton, Kanwarjeet Kaur, Maria Khomenko, and Valentina Ngai. The degree was made much more fun with their help and friendship. I must thank my brother Andrew for believing in me, despite my being in science. My parents deserve an enormous amount of gratitude and appreciation for their moral and emotional support, untold hours driving me to school, checking my grammar, letting me live at home throughout my degree, and above all being my friends. And lastly I want to thank my fiancée Andrea for her endless support, love, and kindness, and for being a constant source of inspiration.

Dedication

I dedicate this thesis to my parents Woldemar and Nancy Teichroeb, and my beautiful fiancée Andrea Boadway.

Table of Contents

List of Tables.....	ix
List of Illustrations	x
List of Abbreviations.....	xii
Introduction	1
1.1 Overview	1
1.2 History	1
1.3 The Structure of Protein	3
1.4 Intra-protein Forces	8
1.5 Forces Driving Protein Conformation	10
1.6 Protein-Surface Interactions	11
Studies of Protein at Solid Interfaces	14
2.1 Studies of Fundamental Properties of Adsorption	14
2.1.1 Contributions to Adsorption.....	14
2.1.2 Protein Adsorption in Chromatography	23
2.1.3 Aggregation.....	25
2.1.4 Morphology of Adsorbed Protein.....	26
2.1.5 Protein Alignment	27
2.2 Applied Studies of Proteins at Interfaces	28
2.2.1 Blood Contacting Materials.....	28
2.2.2 Contact Lenses.....	30
2.2.2.1 Background	30
2.2.2.2 Food and Drug Administration Grouping vs. Protein Deposition.....	30
2.2.2.3 The State and Type of Protein.....	33
2.2.2.4 Kinetics.....	35
2.2.2.5 Location of Protein Adsorption.....	35
2.2.2.6 Dependence on Tear-Film Composition	37
2.2.2.7 Experimental Methods	38

2.2.2.8	Cleaning Methods.....	42
2.2.2.9	Pathogen Relationship to Protein Deposits	44
2.3	Nanoparticle-Protein Interactions.....	46
2.4	Multicomponent Systems	53
2.5	Adsorption Modeling	54
2.5.1	The Problem of Modeling Protein Adsorption.....	54
2.5.2	Colloidal Treatments	55
2.5.3	Atomistic Treatments	59
2.5.4	Intermediate, Lattice, and Miscellaneous Approaches.....	61
2.5.5	General Mean Field Approaches.....	63
Experimental Techniques		65
3.1	Measurement Techniques.....	65
3.1.1	Atomic Force Microscopy.....	65
3.1.1.1	General Background.....	65
3.1.1.2	Measuring Contact Lenses with AFM.....	67
3.1.2	Extinction Spectroscopy.....	67
3.1.3	Surface Plasmon Resonance.....	69
3.1.3.1	Dielectric Constant Models.....	70
3.1.3.2	Localized Surface Plasmon Resonance.....	72
3.1.3.3	Computer Modelling of Mie Theory.....	76
3.1.4	Quartz Crystal Microbalance.....	78
Conclusion.....		85
Appendices		
Appendix A: Mie Theory		86
Appendix B: Bulk Plasma Frequency Shift		107
Appendix C: Refractive Index/Thickness Contour Plot Generator.....		112
Appendix D: Contour Plot Search Algorithm for Inversion of Mie Calculation		116
Appendix E: Homogeneous, No-Slip, N-Layer Voigt Model of QCM		120
Bibliography		123
Summary of Papers.....		151
List of Papers Not Included in Thesis		152

Papers

Anomalous thermal denaturing of proteins adsorbed to nanoparticles.	153
Size dependent denaturing kinetics of proteins adsorbed onto nanospheres.....	161
Influence of nanoparticle size on the pH dependent structure of adsorbed proteins studied with quantitative localized surface plasmon spectroscopy	168
Quartz Crystal Microbalance Study of Protein Adsorption Kinetics on Poly(2- hydroxyethyl methacrylate).....	187
Imaging Protein Deposits on Contact Lens Materials.....	197

List of Tables

Table 1. List of major amino acids and their properties. NP—non-polar, P—polar, A—acid, B—base, N—neutral, WB—weak base..... 4

List of Illustrations

Figure 1. General form of amino acid.	3
Figure 2. Left-handed amino acid.	3
Figure 3. Polypeptide showing peptide bond, and dipole moment of bond.	5
Figure 4. Polypeptide indicating coplanar bonds (shaded region) and rotation bonds ϕ and ψ	5
Figure 5. Antiparallel beta sheet (dotted lines are hydrogen bonds).	7
Figure 6. Parallel beta sheet (dotted lines are hydrogen bonds).	7
Figure 7. 3D structure of bovine lactoferrin (ribbon model).	8
Figure 8. 3D structure of Hen Egg White Lysozyme (ribbon model).	8
Figure 9. Atomic Force Microscope on translation stage with contact lens on glass sphere.	65
Figure 10. Schematic of A.F.M. operation.	65
Figure 11. Example of convolution of tip and structure.	66
Figure 12. Contact lens on glass sphere.	67
Figure 13. Schematic of extinction experiment. I_i and I_t are incident and transmitted intensities.	67
Figure 14. Sphere of radius a , with coating thickness $(b-a)$. The subscript I denotes incident fields, while the subscripts 1, 2, and s denote fields internal to the sphere, fields in the coating, and the scattered field respectively.	69
Figure 15. Dielectric functions for bulk gold as a function of frequency. [209].	72
Figure 16. Dielectric functions for bulk gold as a function of wavelength.	74
Figure 17. Side view schematic of quartz crystal in shear mode	78
Figure 18. 5MHz AT-cut quartz crystal with gold electrodes.	79
Figure 19. Schematic of typical QCM setup.	81
Figure 20. Actual QCM setup. A) QCM liquid cell, B) electronics that operate QCM, C) water bath and liquid introduction site, D) heater for water bath, F) temperature loop, E) crystal loop.	82
Figure 21. Voigt element.	83

Figure 22. Sphere of radius a , with coating thickness $(b-a)$. The subscript I denotes incident fields, while the subscripts 1 , 2 , and s denote fields internal to the sphere, fields in the coating, and the scattered field respectively..... 86

List of Abbreviations

AFM	atomic force microscope
ALA	α -lactalbumin
ATR-FTIR	attenuated total internal reflectance - Fourier transform infrared spectroscopy
BCA	bicinchonic acid
BPTI	bovine pancreatic trypsin inhibitor
BSA	bovine serum albumin
CD	circular dichroism
DNA	deoxyribonucleic acid
DPI	dual polarization interferometry
DSC	differential scanning calorimetry
EWC	equilibrium water content
HEMA	hydroxyethyl methacrylate
HEWL	hen egg white lysozyme
HIC	hydrophobic interaction chromatography
HPA	human plasma albumin
HPLC	high performance liquid chromatography
HSA	human serum albumin
igG	immunoglobulin G
LSPR	localized surface plasmon resonance
LSZ	lysozyme
MAA	methacrylic acid

MALDI	matrix assisted laser desorption/ionization
MGB	myoglobin
NMR	nuclear magnetic resonance
NVP	N-vinyl pyrrolidone
PBS	phosphate buffer solution
PEG	poly(ethylene glycol)
PEO	poly(ethylene oxide)
PHEMA	poly(hydroxyethyl methacrylate)
pI	isoelectric point
PMMA	poly(methyl methacrylate)
POM	poly(oxymethylene)
PPO	poly(phenylene oxide)
PS	polystyrene
PTFE	poly(tetrafluoroethylene)
PVP	poly(vinyl pyrrolidone)
QCM	quartz crystal microbalance
RNase	bovine pancreas ribonuclease
RPC	reverse phase chromatography
RSA	random sequential adsorption
SAM	self assembled monolayer
SDS-PAGE	sodium dodecyl sulfate - polyacrylamide gel electrophoresis
SEM	scanning electron microscopy
SPR	surface plasmon resonance
STM	scanning tunneling microscopy
TIRF	total internal reflectance fluorescence

tPA	tissue plasminogen activator
UV-VIS	ultraviolet/visible
XPS	x-ray photoelectron spectroscopy

Introduction

1.1 Overview

The area of proteins at solid-liquid interfaces is an enormous field, both in impact and scope. Research undertaken in this area can take a number of directions. A fundamental direction usually involves attempting to elucidate the forces, and general mechanisms responsible for protein adsorption. A more applied direction on the other hand involves attempting to improve, or understand a real world system, which in many cases is very difficult to reduce to simple fundamental components. To maintain an appreciation for the breadth of the topic, this thesis has strived to include both applied and fundamental aspects.

The thesis takes the following form:

- A general introduction to proteins and the general considerations involved in their behaviour
- An overview of the current state of the field of proteins at interfaces, with special sections dedicated to its application to nanoparticles, and contact lenses
- A methods section outlining some of the techniques, equations, and programs used in the published papers
- Some concluding remarks pertaining to the papers
- Appendices containing extended Mie theory calculations and Matlab code used during modeling of experimental data for the published papers
- The original works, in a series of five papers, all of which are either published, or in press, and bound in the back of the thesis

1.2 History

Protein interaction with interfaces has been utilized for thousands of years. Anecdotally, as early as 2600B.C., Egyptians used egg whites and other materials as glue for making

furniture and paint. However, it wasn't until the mid 1800's that serious work began on investigating protein-containing materials. In 1839, a landmark paper by Gerrit Jan Mulder, entitled "On the Composition of Some Animal Substances" [1], was published. Mulder was able to measure the elemental compositions of several proteins, and showed their similarities. Throughout the 1800's various units, of what would later be called amino acids, were discovered. Finally, in 1902 at the 74th Annual Meeting of The Society of German Naturalists and Physicians, the concept of protein as a polypeptide was created. Franz Hofmeister subsequently published a paper "On the Structure and Grouping of the Protein Bodies"[2], in which he described the proper linkage, stating that amino acids could be linked by the amide bond. It wasn't until around 1945-1955, however, that Frederick Sanger began publishing papers on the sequencing of proteins (winning the Nobel Prize in 1958 for the sequence of the insulin protein). This allowed the exact sequence of amino acids to be determined.

Despite rudimentary understanding, proteins at interfaces were already being studied as early as 1905, just three years after the polypeptide theory was announced. In this remarkably innovative paper by Landsteiner and Uhliz [3], several different proteins were adsorbed onto inorganic powders such as clay and talc. Knowledge of how to precipitate and to purify protein was already present. Rudimentary measurements of the mass of adsorbed protein were made. While it appears that no conclusive results were found, they were clearly ahead of their time in attempting to relate adsorption to the physical and chemical nature of the particles, including electrostatic forces. In 1925, another landmark paper in adsorption was published, this time by David Hitchcock [4]. This paper investigated the adsorption of gelatin and egg albumin to collodion membranes. Beautiful adsorption isotherms were generated, and were fit by the Langmuir equation for adsorption. The effect of varying pH was also examined, and the maximum adsorption found to be at the isoelectric point of the protein. Salt was found to increase the total amount of protein adsorbed.

Interfacial protein behaviour is a broad topic, but one which plays an incredibly important role. Cell adhesion occurs through glycoproteins such as fibronectin, and the ability of cells to organize into well-defined structures is a result of specific protein interactions [5, 6]. This is desirable for the organization of cells into high organisms.

Bacteria, however, may also use the same mechanism to adhere onto surfaces such as biomaterials. In addition, protein aggregation at biomaterial interfaces can elicit immunological responses. Hence, an understanding of both how to promote, as well as to prevent, protein adhesion, is desired.

1.3 The Structure of Protein

Proteins are really a special case of linear polymers. The monomers in this case are amino acids, linked together by peptide bonds. The general form of an amino acid is displayed in Figure 1. It consists of an amine group, and a carboxyl group, between which a side group is attached (labeled R). The α -carbon joins the three groups. Amino acids produced by nature are almost exclusively left-handed as depicted in Figure 2. There are 20 main amino acids (Table 1.), with at least two other amino acids found in biological proteins, and many others not found in proteins. Generally amino acids are categorized by two categories, according to the hydrophilicity (or hydrophathy) of the side group, and whether the group is acidic, basic, or neutral. These properties are also listed in Table 1.

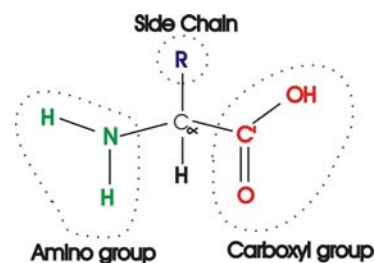


Figure 1. General form of amino acid.

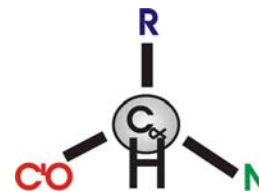


Figure 2. Left-handed amino acid.

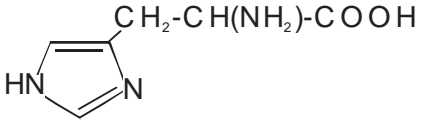
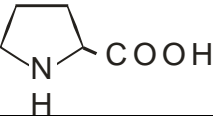
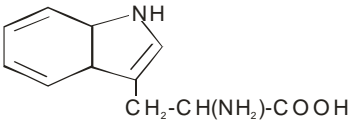
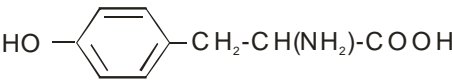
Amino acid	Short Form		Chemical formula (side chain is highlighted in red)	Polarity	Acid/Base
	Ala	A			
Alanine	Ala	A	$\text{CH}_3\text{-CH(NH}_2\text{)-COOH}$	NP	N
Arginine	Arg	R	$\text{H}_2\text{N-C(=NH)-NH-[CH}_2\text{]}_3\text{-CH(NH}_2\text{)-COOH}$	P	B
Asparagine	Asn	N	$\text{H}_2\text{N-CO-CH}_2\text{-CH(NH}_2\text{)-COOH}$	P	N
Aspartic acid	Asp	D	$\text{HOOC-CH}_2\text{-CH(NH}_2\text{)-COOH}$	P	A
Cysteine	Cys	C	$\text{HS-CH}_2\text{-CH(NH}_2\text{)-COOH}$	P	N
Glutamine	Gln	Q	$\text{H}_2\text{N-CO-[CH}_2\text{]}_2\text{-CH(NH}_2\text{)-COOH}$	P	N
Glutamic acid	Glu	E	$\text{HOOC-[CH}_2\text{]}_2\text{-CH(NH}_2\text{)-COOH}$	P	A
Glycine	Gly	G	$\text{H-CH(NH}_2\text{)-COOH}$	NP	N
Histidine	His	H		P	WB
Isoleucine	Ile	I	$\text{C}_2\text{H}_5\text{-CH(CH}_3\text{)-CH(NH}_2\text{)-COOH}$	NP	N
Leucine	Leu	L	$\text{(CH}_3\text{)}_2\text{CH-CH}_2\text{-CH(NH}_2\text{)-COOH}$	NP	N
Lysine	Lys	K	$\text{H}_2\text{N-[CH}_2\text{]}_4\text{-CH(NH}_2\text{)-COOH}$	P	B
Methionine	Met	M	$\text{CH}_3\text{-S-[CH}_2\text{]}_2\text{-CH(NH}_2\text{)-COOH}$	NP	N
Phenylalanine	Phe	F	$\text{C}_6\text{H}_5\text{-CH}_2\text{-CH(NH}_2\text{)-COOH}$	NP	N
Proline	Pro	P		NP	N
Serine	Ser	S	$\text{HO-CH}_2\text{-CH(NH}_2\text{)-COOH}$	P	N
Threonine	Thr	T	$\text{CH}_3\text{-CH(OH)-CH(NH}_2\text{)-COOH}$	P	N
Tryptophan	Trp	W		NP	N
Tyrosine	Tyr	Y		P	N
Valine	Val	V	$\text{(CH}_3\text{)}_2\text{CH-CH(NH}_2\text{)-COOH}$	NP	N

Table 1. List of major amino acids and their properties. NP—non-polar, P—polar, A—acid, B—base, N—neutral, WB—weak base.

Amino acids are linked by peptide bonds formed between the amino, and carboxyl groups, generating a water molecule, and a polypeptide (Figure 3). A dipole moment is formed in the amide group between the carbonyl group which is electronegative, and the amine group which is electropositive (Figure 3). Regular ordering in secondary structures such as α -helices causes a summing of neighbouring dipoles to produce a large overall dipole moment. The inclusion of acidic/basic amino acids in a protein leads to a net pH dependent charge, which

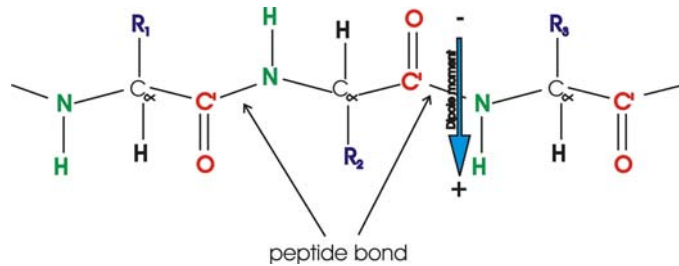


Figure 3. Polypeptide showing peptide bond, and dipole moment of bond.

goes to zero at the isoelectric point of the protein. Rotations which change the relative orientation of one residue with respect to another can occur about the bonds, as shown in Figure 4. The π bond in the carbonyl group between the C' carbon and oxygen becomes delocalized across the neighbouring nitrogen. This has the effect of preventing rotations, and making these groups coplanar as indicated by the shaded planes. Rotation can occur between the α -carbon and the nitrogen, labeled ϕ , as well as between the α -carbon and C' carbon, labeled ψ . Large residues will experience more steric hindrance, and thus have fewer acceptable ϕ/ψ angles, especially if situated next to another large R group. Glycine, for instance, whose side chain consists of a single hydrogen atom has much more freedom in position.

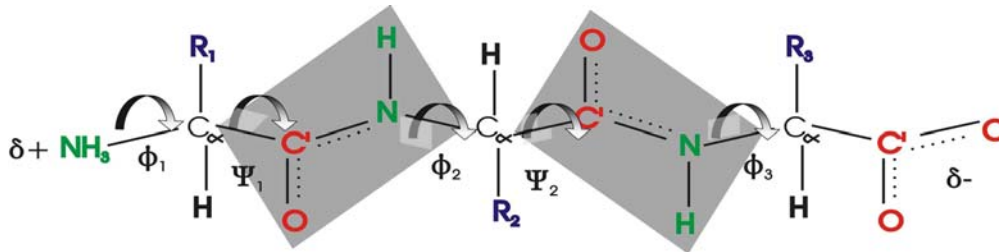


Figure 4. Polypeptide indicating coplanar bonds (shaded region) and rotation bonds ϕ and ψ .

Life has evolved a simple space-saving blueprint so that complex three dimensional functional machines can be made. DNA encodes, in its nucleic acids, the information for the linear sequence of peptides. Residues on this peptide will experience differing forces,

depending on their hydrophathy, charge, polarity, and steric constraints. It is through these forces, coupled with Brownian motion, that the peptide is able to spontaneously fold into a regular structure. The process of self-assembly is driven by the Brownian search for an energy minimum. However, a random sampling of states alone does not account for the speed at which proteins fold [7]. Intrachain forces cause a preferential folding, allowing the protein to fold on short timescales (generally ms, but can be μ s to hours). Recent studies suggest that many proteins are not in their true energy minima, or that there may be more than one minimum with similar energy levels. The protein becomes trapped in a local minimum, and under certain circumstances will revert to a different conformational minimum. This mechanism has been implicated in a number of diseases such as Alzheimer's and Bovine Spongiform Encephalopathy.

Folding can be divided into several levels of hierarchy termed primary, secondary, tertiary, and quaternary. Intermediary between secondary and tertiary are the motifs, and domains. Primary structure is simply the linear sequence of amino acids, which in turn tends to determine all other levels. The most important secondary structures are the α -helix and β -sheet. Others include the α -sheet, γ -helix, left handed α -helix, 3_{10} -helix, π -helix, 2_7 ribbon, polyproline helix, and "random" coil. The reason the α -helix, and β -sheet are so common is that they represent structures which allow unstrained hydrogen bonding to occur.

In the α -helix (see Figure 7) there are 3.6 residues per turn, and hydrogen bonds are formed every 13 atoms between the C' oxygen on a given residue, and the NH group four residues later (ie. n and $n+4$). ψ/ϕ are around 120° , and 130° (or -60° , and -50° depending on convention) [8]. This is a particularly favourable structure, as the hydrogen bonds are optimized, and the side chains are rotated as far as possible from the sterically-hindering carbonyl groups. The π -helix has hydrogen bonds between the n^{th} , and $n+5^{\text{th}}$ residues, while the 3_{10} helix and 2_7 ribbon have hydrogen bonds between the n^{th} and $n+3^{\text{rd}}$, and $n+2^{\text{nd}}$ residues [8]. This leads to strain in the hydrogen bonds making these structures less favourable. 2_7 ribbons are very rare, and force the NH and C'=O groups much too close, greatly stressing the hydrogen bonds. 3_{10} helices tend to occur at the ends of α -helices where the rules for a proper α -helix are not met as rigidly. Left handed helices are limited in the types of residues that can take part, since the side chains tend to point towards the

=C'=O group, making the residues sterically hindered. Amino acid sequence thus determines what structures will be made. Proline, and hydroxyproline, for example, can not be accommodated by a right handed α -helix, and must occur in turns, or in a left-handed helix such as those forming tropocollagen. Polyproline, and collagen helices cannot satisfy hydrogen bonding intrachain, and must form interchain bonds.

β -sheets can be parallel or anti-parallel, or can include both [8]. Examples of a β -sheets are given in Figure 5 and Figure 6. In the parallel case, the N-terminus to C-terminus direction of adjacent strands making up the sheet are the same, and are opposite in the anti-parallel case. ψ/ϕ

are around 315° and 40° .

Hydrogen bonds are formed between adjacent strands, and side chains are oriented perpendicularly above and

below the sheet. This allows β -sheets to pack with side

chains interlocking, held together by van der Waals forces. Anti-parallel and parallel sheets both satisfy all hydrogen bonds internally (with the exception of the edge strands), with slightly different patterns.

Motifs are simple combinations of α -helices and β -sheets which are used on their own, or to build up larger domains [9]. There are numerous motifs such as the helix-turn-helix, and greek key motif. The three main domain types are those built purely of α -helices, purely of β -sheets, and those that are a mix of α -helices, and β -sheets.

Tertiary structure defines the three dimensional conformation of the overall protein. The tertiary structure of hen egg white lysozyme [10] and bovine lactoferrin [11], from the Protein Databank [12], are shown in Figure 8 and Figure 7 respectively. These ribbon models indicate the arrangement of the main secondary structures in a protein. For example, in lysozyme one can see the α -helices, as well as β -sheets (opposing arrows). It is the three dimensional structure which gives the protein its function [9]. This means that proteins may have the same function despite having differing primary sequence. That is to

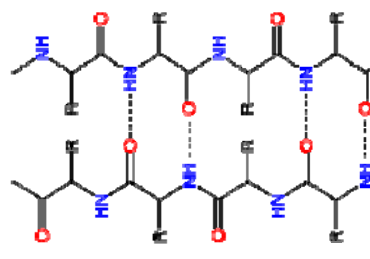


Figure 5. Antiparallel beta sheet (dotted lines are hydrogen bonds)

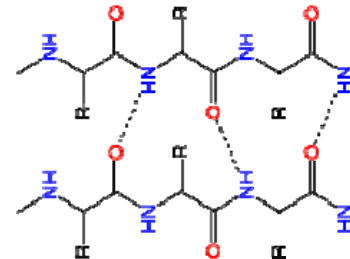


Figure 6. Parallel beta sheet (dotted lines are hydrogen bonds)

say, that for a given sequence, the function will generally be unique, but a given function does not necessitate a unique sequence. Frequently the random coil sections contain the functional groups that are used for binding other molecules. Metal ions are also often bound to proteins, adding functionality. In hemoglobin, for instance, the heme pocket formed by the protein binds a heme group with an iron atom, which in turn can bind oxygen, and carbon dioxide, transporting them throughout the body [8]. In zinc fingers a zinc molecule stabilizes an alpha-helix and two anti-parallel beta strands, allowing them to bind to DNA [9].

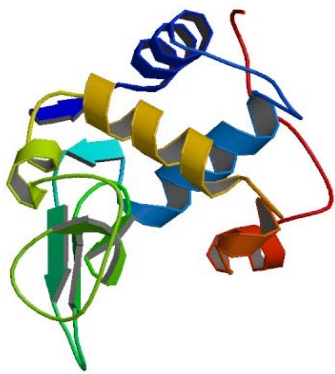


Figure 8. 3D structure of Hen Egg White Lysozyme (ribbon model)

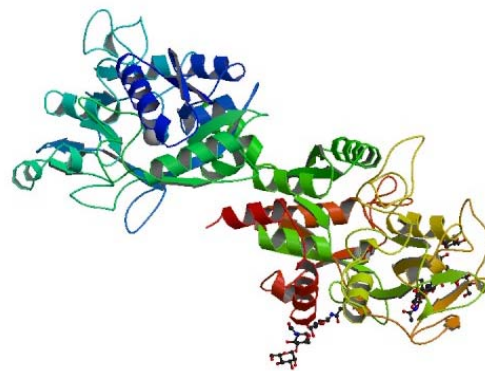


Figure 7. 3D structure of bovine lactoferrin (ribbon model)

Proteins with a single function may be built of more than one polypeptide chain. Examples of this include hemoglobin which is made of four associated subunit polypeptides. This level of organization is termed quaternary structure.

1.4 Intra-protein Forces

Most proteins carry multiple polar and non-polar groups, as well as multiple charged groups, making them amphiphilic polyelectrolyte molecules capable of refolding to suit a particular environment. Inter/intra-molecularly acting forces determine how proteins will act. These include: electrostatic interactions, Lifshitz-van der Waals interactions, hydrogen bonding, covalent bonds and thermal fluctuations [13]. These result in such effects as

intramolecular conformational entropy, hydrophobic bonding, and bond energy considerations. These forces are present in protein-protein, protein-self (residue-residue), protein-surface, and protein-solvent interactions, all of which are concerns for adsorption behaviour.

There are a number of forces that act inter/intra-molecularly to dictate protein-macromolecule, protein-substrate, and protein-solvent interactions. Most interactions between molecules arise from electromagnetic considerations. Other considerations are entropic in nature. The primary types of electric interactions are permanent ion-ion, ion-dipole, dipole-dipole interactions, and those between induced dipoles and permanent ions, permanent dipoles, and other induced dipoles [13].

Assuming the molecule is small, and undergoes Brownian motion, the following can be said of the forces: The energy between ions simply follows the simple Coulomb dependence $E \propto q_1q_2/r_{12}$ where q_i is the charge on ion i , and r_{ij} is the distance between ion i and j . Permanent ion-dipole, dipole-dipole interactions will depend on the orientation of the dipoles, which is in turn a function of $k_B T$ —the thermal energy. In the absence of Brownian motion, the static ion-dipole, and dipole-dipole energies, would vary as $1/r^2$ and $1/r^3$ respectively (and depend on the angle the dipole(s) make). However, the presence of Brownian motion causes the orientation of the permanent dipole to fluctuate randomly if the energy between it and the other ion/dipole is much less than $k_B T$. This has the effect of reducing the time averaged ion-dipole and dipole-dipole interaction energies to r^4 , and r^6 dependence [13].

Induced dipoles occur as a result of a molecule being placed in an electric field, causing a separation of charge within the molecule. This depends on the polarizability of the molecule α , so that the induced dipole moment is proportional to $\alpha \mathbf{E}$ where \mathbf{E} is the electric field. The energy for an ion-induced dipole, and a permanent dipole-induced dipole have $1/r^4$ and $1/r^6$ dependences. Induced dipole forces, better known as van der Waals forces, vary as $1/r^6$. If atoms come too close, the electron clouds will overlap. This overlap of charges causes a repulsive energy. The repulsion occurs over very short range and is usually given a repulsive $1/r^{12}$ dependence as in the Lennard-Jones potential.

One of the most important bonds is the hydrogen bond, which is very directional. A hydrogen bond is formed when one atom donates a proton to another atom. The donor group will be polar, and the acceptor group must be very electronegative due to electrons not occupied with covalent bonding. As with the van der Waals force, hydrogen bonding cannot be calculated purely from classical considerations, and requires a quantum treatment. A standardized model does not exist yet, and various functions are used to approximate the bond [13].

1.5 Forces Driving Protein Conformation

To consider what will drive adsorption, we must first look at how the previous considerations stabilize a protein. Many amino acid residues contain charged groups (eg. Asp, Glu, Lys, Arg), which generally reside on the outside of the molecule to promote contact with the surrounding buffer solution. These charge groups are weak acids and bases, and thus have buffering capacity [14, 15]. Water tends to be a good solvent for proteins, when folded with their charge/polar groups facing out. Electrolytes, on the other hand, result in an ionic double layer, which reduces electrostatic interactions. This has the effect of expanding the protein (reduces ion-pair interactions). It is generally the case that ions buried inside a protein (and often on the surface) pair with opposite charges to stabilize the conformation (at least near the isoelectric point [16]). However, internal charge pairing tends not to be a driving force for conformation since contact with external water leads to similarly favourable hydration of the ion [17]. Interior non-ionized residues will tend to favour unfolding in order to become ionized [18]. Overall, it will depend on the pH, charge distribution, and electrolyte concentration as to whether charged residues will stabilize or destabilize the protein conformation.

Lifshitz-van der Waals interactions are unclear in their role, since much of the interaction with water is replaced with interaction internal to the protein upon folding. However, due to the high packing density of protein, it is generally assumed the interactions will be supportive of folding. The same is true of hydrogen bonds between water and hydrogen bonding residues, which are then satisfied internally by residue-

residue hydrogen bonds. No major net change is generally evident, although slight differences in the bond energies due to non-ideal alignment (bending), may favour one over the other [16]. Albeit, once folding has occurred, it is then favourable to satisfy van der Waals interactions and broken hydrogen bonds as much as possible within the molecule. This leads to the general consensus that protein compaction is supported, but probably not driven by these two forces. That is not to say that charge, van der Waals, and residue-hydrogen bonding are irrelevant and cannot be major factors under certain conditions.

Folding the molecule has the unfavourable tendency to strain bonds, especially in the functional regimes [19]. Additionally, the rotational constraints induced by folding vastly reduce the conformational entropy. Along with entropy loss, the folding also results in non-equilibrium bond angles and lengths, between adjacent residues. This will always favour unfolding. Hence it is generally believed that the major driving force for protein folding is hydrophobic bonding. This effect is due solely [20] to disruption of the hydrogen bond network in water. Apolar residues cause this disruption. Attraction can occur between apolar-apolar, as well as apolar-polar entities. Apolar entities do not form hydrogen bonds with the surrounding water molecules, and as a result, water must reorder to try and satisfy them. On small scales, this causes an ordering of the water into clathrate structures to preserve the bond network. On larger scales, water is unable to order over long ranges, and cannot satisfy hydrogen-bonding requirements, causing enthalpy increases [20]. The former effect causes a decrease in entropy, while the latter, an increase in energy of the system. Both are unfavourable situations. It is therefore much more favourable for the one protein to accept a loss in entropy by folding the apolar residues to its inside, than for many water molecules to re-order, losing many times the entropy.

1.6 Protein-Surface Interactions

For a protein interacting with a surface, adsorption will occur if the Gibbs free energy ($G=H-TS$) is lowered, that is, if the entropy (S) of the system is increased, and/or the enthalpy (H) decreased. Because a protein consists of many residues, a small lowering in

free energy/residue can generate extremely high affinities for surfaces. Strong intramolecular forces holding proteins together mean they generally have low entropy. Denaturation, in the case of proteins, refers to a change in conformation from the generally accepted protein form or “native” state. This is generally thought of as unfolding causing a loss of function, but as the root of the word implies, it is really any *change in nature* of the protein. It can thus be used to denote more subtle conformational changes from the “native” state. Proteins can undergo spreading, which is a form of denaturation, to contact more surface area. Adsorption to a surface may thus provide the protein an opportunity to unfold, leading to an increase in entropy, and a major driving force to adsorb [21]. The major forces driving adsorption are charge interactions, and the hydrophobic effect, with van der Waals forces playing a role.

Hydrophobic surfaces may allow the protein to arrange its apolar residues close to the surface, leaving its polar residues exposed to solvent. Bonds broken internally are thus satisfied externally, while allowing an increase in entropy. Unlike polymers, protein spreading is much slower. Thus the rate of adsorption can exceed the spreading rate, causing the quantity of adsorbed protein to be strongly kinetically limited [22]. If either the surface, or protein, or both, are hydrophobic, water will be excluded between them. This dehydration creates a pressure from water molecules residing around, but not in-between them, driving adsorption [20]. This effect plays a large role in many adsorption processes, but because modeling water requires huge computational power, it is one of the lesser understood contributors to adsorption.

Where present, charge plays a huge role in adsorption between a charged protein and/or surface. Counter-ions, in the form of an electrical double layer, normally surround both protein, as well as charged surface. These have the effect of screening charge on both protein, and surface, leading to an increase in attraction for like charged objects, and decrease in attraction for oppositely charged objects. It is these double layers that interact as the protein and surface near each other. When the protein adsorbs, some ions may be stuck between the protein, and the surface. Generally a protein will stop adsorbing close to the protein/sorbent isoelectric point. If the charge density per area coverage of the protein does not exactly match that of the surface, an electric potential arises. Low permittivity in the dehydrated space between protein and surface means large electric fields forcing

counter-ions to fill in around the protein to lower the field energy [23]. However, because protein does not solvate ions as well as water, there is a net reduction in attraction if ions reside in between protein and surface. Hence, the maximum attraction occurs, generally at the isoelectric point of the protein-sorbent complex, where no counter-ions are needed to balance charge. Static dipole moments not only lead to attraction, but tend to orient molecules on a surface. This may be an important factor in adsorption, determining the time it takes for a protein to seek out favourable interactions.

Electrolytes also play other roles in adsorption such as protein-solvent effects. High salt concentrations generally lead to aggregation and precipitation of proteins. This occurs when an excess of salt out competes the protein for solvating water molecules. However, addition (to a point) of salt to a solution lacking electrolytes increases solubility lowering adsorption force. A small amount of salt will screen the protein charge, lower the protein electrostatic free energy, and thus decrease the protein activity coefficient, enhancing solubility. The former effect is termed salting-out, while the latter effect is termed salting-in.

Most of the above mentioned effects are on a microscopic scale. The following sections will give examples of some of the multitude of experiments, and models, which have been done in the area of proteins at interfaces. The importance of all of these effects at a microscopic level will be seen in many cases. This leads to a need to understand the microscopic heterogeneity of both protein and sorbent. Protein-protein interactions, and protein-solvent interactions, are in most cases just as important, and in some cases more important, than protein-surface interactions in determining adsorption. Protein deposition also has a strongly kinetically controlled component to it due to spreading, reorientation, and surface exclusion effects.

Studies of Protein at Solid Interfaces

There are many good reviews of proteins at interfaces: [21, 24-26]. An attempt will be made to discuss some of the major findings in this field, with particular emphasis on systems having at least some relation to our own. However, the field is so enormous that any one of the sub-topics in the following sections could be expanded into a book on its own, with many hundreds of references. As such the following is meant to act as a sampling overview of the field.

2.1 Studies of Fundamental Properties of Adsorption

2.1.1 Contributions to Adsorption

The hydrophobic effect is one of the least understood contributions to adsorption. Because it arises from hydrogen bond interactions with water, it is difficult to study, both experimentally, and theoretically. This challenge has resulted in a large number of papers, which investigate this, either as a primary, or secondary concern in protein-surface interactions. Hydrophobic surfaces, in general, denature protein more than hydrophilic surfaces, and this is a major concern for biomaterial design [27].

Wertz et al. [28] find that for albumin and fibrinogen adsorption to hydrophobic C16 self-assembled monolayers (SAMs), the initial adsorption rate is constant and is transport-limited. This is somewhat expected, since adsorption in this case would be largely due to hydrophobic effects, as opposed to being dominated by electrostatics. The final adsorbed quantity is found to be kinetically controlled, and is dominated by the rate of relaxation of the protein (as opposed to chemical potential). Relaxation, at least in this case, is shear rate independent. Wertz et al. [28] measure an approximately constant rate of $0.12 \text{ nm}^2/\text{s}$ for albumin and $0.15 \text{ nm}^2/\text{s}$ for fibrinogen (at least over about 15min), indicating lateral interaction effects. For slow relaxation, and quick adsorption, the molecules will not

have time to spread, and thus adsorb more. Quick relaxation times relative to the adsorption rate will allow the molecules to spread out, covering the free surface area quicker, and resulting in less total adsorbed protein (assuming only monolayer formation). Spreading increases the surface coverage by up to 5 times in the case of albumin, and 3 for fibrinogen. Indications are that the relaxation is due largely to interfacial denaturation, as well as reorientation of the molecule. A competitive study, with albumin deposited before fibrinogen is added, shows a decrease in fibrinogen adsorption with the amount of time albumin is on the surface by itself. This suggests that relaxation is key to preventing the fibrinogen adsorption, and that the albumin-surface affinity increases with relaxation, preventing fibrinogen from displacing it. Another study by Wertz and Santore [29] shows that spreading increases with hydrophobicity of the surface, by measuring albumin and fibrinogen on SAMs of varying hydrophobicity. Competitive studies also back this result, showing a decrease in the amount of time albumin requires to prevent fibrinogen deposition. Model calculations of this system, [30] indicate that past a certain spreading “footprint” size, a protein cannot be removed on hydrophobic surfaces, and any additional spreading will not change this. On the hydrophilic surface, however, Wertz and Santore find smaller “footprint” areas, suggesting that orientation effects are more important than denaturation. This is based on the number of equal “footprints” which correspond to the loosely bound protein energy value. Comparison to a kinetic model shows that the amount of loosely bound protein depends much more on history than on the tightly bound material. Loosely bound protein has approximately the same binding energy on both hydrophobic and hydrophilic substrates. Recently Wertz and Santore have performed similar experiments with lysozyme on hydrophobic surfaces [31]. As opposed to the albumin fibrinogen case, the total amount of lysozyme adsorbed does not exhibit flow, or bulk concentration dependence, but rather an overshoot appears during initial adsorption for high shear/concentration. The adsorption is irreversible and the kinetics strongly transport-limited. Furthermore, the change in footprint is due to a transition from end-on to side-on (it is an ellipsoidal molecule), rather than spreading. This transition is compared to a model where the end-on molecules were replaced by side-on molecules, and a second model where the end-on molecules simply roll over, without coming off the surface. The roll-over model agrees with their data, and combining this model with a reversible end-on

adsorption model, they are able to predict quantitative results for various conditions. All of Wertz and Santore's studies are performed using total internal reflectance fluorescence (TIRF) intensity measurements.

Giacomelli et al. [32], in their attenuated total reflectance-fourier transform infrared spectrometry (ATR-FTIR) study of bovine serum albumin (BSA), and immunoglobulin IgG, see little change in native secondary structure upon adsorption to a hydrophilic silica surface. They repeated the study with a hydrophobic silica surface, but due to hydrophobic displacement of surface bound water were unable to generate a proper background IR spectrum, and are thus unable to interpret their results in this case. For a hydrophobic surface with a preadsorbed small triblock copolymer (PEO-PPO-PEO) in a brush formation, they see a decrease in the amount adsorbed, possibly due to steric hindrances. However, chain length is not long enough to prevent adsorption. IgG undergoes a change in its beta sheets, with BSA exhibiting a more ordered alpha helix. If the non-saturated polymer brush surface is considered as a non-aqueous solvent (similar to ethanol), and BSA is completely surrounded by this solvent, then it may be prevented from spreading as in Wertz, and Santore's study. Unable to satisfy as many external hydrogen bonds in this new solvent, the internal bonds (in the alpha helix) may have a dominant effect.

Neutron reflection measurements point to BSA adsorbing to hydrophilic silica side on, which would maximize its contact with the surface [33]. Even on the hydrophilic surface some spreading is evident. Increases in bulk concentration prevent the molecules from spreading very much, just like a hydrophobic surface. However, unlike a hydrophobic surface, the reversibility of changes with pH suggests that BSA is much less denatured [33].

Giacomelli and Norde [34] have also looked at a BSA-silica system. In particular they used calorimetry and circular dichroism to study BSA adsorbing, and desorbing from colloidal silica particles. Adsorbed BSA is conformationally changed, and more thermostable than native BSA. This adsorption is reversible, as is the conformation change induced by the surface. Aggregation was not possible, and this may explain its reversibility. Two regions are identified during the process of denaturation, the first of which is enthalpically driven and includes only a slight conformational change, but

intermolecular association. The second region contains the major unfolding events, and is somewhat reversible, refolding some of the alpha helices. Further denaturation, however results in aggregation, which removes the reversibility.

A good way to study how various residues affect adsorption is to look at shorter chains of them, rather than trying to deconvolute their effect from massively complex proteins. For example, Read and Burkett [35] look at the adsorption of a small polypeptide which consists of a short chain of the alpha helix promoter alanine, capped on one end with a chain of anionic aspartate, and on the other end by cationic arginine. The surface under study is silica colloid, and alumina-capped silica colloid, investigated with circular dichroism and NMR. This provides both an anionic and cationic surface. The peptide end, with the opposite charge to the colloid, adsorbs due to electrostatic interactions. This causes a loss in the alpha helix structure, distinct from heat denaturation, which does not change as much. On both anionic and cationic colloids, the alpha helix loss is observed, in which the alpha helicity of aspartate is largely preserved, while the alanine and arginine lose their structure. One would not expect arginine to lose its favourable helical structure on the complementary anionic colloid. However, since arginine is not as strong an alpha helix former, it may be more favourable to increase contact with the surface, and maximize electrostatic and other interactions. This study shows the subtle differences in the residues, which lead to overall conformation change in protein-interfacial associations.

A good review of the excellent opportunity SAM's provide for studying the effects of various chemical groups in a controlled and ordered fashion is given by Mrksich et al. [36]. A particularly good study is conducted by Ostuni et al. [37], in which the effect on hydrophobic adsorption, of the density, size, and shape of hydrophobic groups in a SAM surface, is explored. One of their motivations for this more in-depth study, is that they tried to find correlation between the wetting properties of a surface, and how well that surface adsorbs protein [38]. They have discarded this idea for several reasons, including that both hydrophilic and hydrophobic surfaces will adsorb protein with intermediate surfaces being the most resistant. They now recognize that wetting is an average phenomenon, whereas adsorption is dependent on the local heterogeneity of both protein and surface. Some heterogeneity could be measured, however, if advancing and receding angles are compared [25]. Large hydrophobic groups capable of interacting with a single protein would be

desirable to de-convolute interactions. Despite lacking large groups, the data is interpreted for several proteins in terms of a hard sphere model. Density of groups seems to be the largest determining factor in denaturation. However, adsorption is seen to increase for a given density of groups with the size of the hydrophobic head-group on non-mixed SAMs. For mixed hydrophilic/hydrophobic SAMs, adsorption decreases with the size of head group. Smaller proteins act similar to the larger ones, at higher densities of hydrophobic groups. Concentration dependence of adsorbed amount is seen, as well as indications of spreading of the proteins once adsorbed. AFM/SPR studies of SAMs [39] also indicate that hydrophilic carboxylic acid-terminated SAMs adsorb more with increasing temperature. Hydrophobic methyl-terminated SAMs do not depend on temperature, and this is largely attributed to the fact that their interaction with water molecules is not changed much with temperature. The hydrophobic surfaces also adsorb more lysozyme and BSA than the hydrophilic surface, and appear to do so faster, and irreversibly. Li et al. [39] suggest that the proteins compete with water molecules for the hydrophilic carboxylic acid binding sites, lowering their affinity for adsorption. Defects in the SAM at lower temperatures, lead to more interpenetrating water, and thus less adsorption.

Using tapping mode Atomic Force Microscopy (AFM) in liquid, it has been observed that deposition of Ferritin decreases with increasing pH, with a maximum around pH 5 [40] on trimethoxysilylpropyldiethylenetriamine, and transferred stearic acid methyl ester, stearyltrimethylammonium bromide films. More absorption occurs at higher ionic strengths, and agreement with the Random Sequential Adsorption (RSA) model is seen at low ionic strengths (see section 4.2.1). This suggests that there are competing protein-protein, and protein-surface forces, which will cause a maximum in adsorption for a particular ionic strength. This maximum is indeed seen, and indicates the importance of protein-protein forces in surface interactions.

Norde and Lyklema have systematically studied human plasma albumin (HPA) and bovine pancreas ribonuclease (RNase) adsorption using polystyrene colloids with negative surface charges [23, 41-46]. Using a battery of tests, they are able to separate the contributions from various effects such as pH, temperature, surface charge, and electrolyte concentration. It is found [41] that HPA plateau values peak at the isoelectric point, and are symmetrical about the isoelectric point. The slope of the adsorption isotherm depends on

temperature, and with the exception of the isoelectric point, increasing the concentration of KNO_3 enhances adsorption, possibly due to a stabilizing/destabilizing effect on the protein conformation. Steps in HPA's adsorption isotherm point to differing modes of adsorption at high and low concentration. RNase adsorption plateaus do not vary as much with pH, temperature or with salt concentration. Both proteins, however, exhibit an unexpected characteristic, in that they adsorb when both protein, and sorbent surface are negative. In fact the plateau adsorption increases with a more negative (and thus electrostatically repulsive) surface. This is suggested to be a hydrophobic effect compensating the electrostatic penalty. HPA is thus interpreted to be a "soft" molecule with low internal coherence which can change conformation easily on surfaces, while RNase is a "hard" protein with strong internal coherence and stability, preventing it from adapting its conformation to surfaces. It is also suggested that hydrophobic effects play a larger role in the internal stabilization of HPA, and hence, also in adsorption of HPA. Unfolding of HPA may provide favourably reduced rotational constraints. It is curious, however, that electrostatically unfavourable conditions are tolerated in the dehydration layer, where very high potentials would be generated. Titration experiments [42] help to answer this. It is known that proteins contain acidic, and basic groups which have buffering capabilities which can be modeled [14, 15]. A difference in buffering capacity between the adsorbed protein, and the combination of the bulk protein and sorbent, must be due to changes in protonation of buffer groups. Both HPA, and RNase are adsorbed irreversibly with respect to pH. Upon adsorption under electrostatically repulsive conditions, some ϵ -amino groups are prevented from deprotonation, allowing them to pair with sorbent groups, and reduce net charge in the dehydration layer. Carboxyl groups are located close to polystyrene surfaces upon adsorption. Their weak hydration compared to smaller groups may make them more favourable for dehydration. It is also likely, given the aforementioned results, that other ions besides protons may help to neutralize the charge difference. Using electrophoresis, the net charge in the adsorption complex can be measured [43]. Knowing the contribution of protons from the previous titration experiments [42], it is possible to determine approximately the number of other ions taking part in adsorption. RNase mobility differences between adsorbed and bulk states are much more significant than for HPA, suggesting that RNase incorporates more ions. The overall conclusion is that at low

pH where the protein is positive, a net uptake of negative ions helps to charge-match the sorbent surface, while at high pH, a net uptake of positive ions occurs. The system can be modeled as three regions [44]. Region 1 is the dehydration layer between protein and sorbent, and contains charge from the protein, sorbent, and any trapped ions. Region 2 is the protein bulk, and hydration layer. Region 2 is uncharged, as all ions occur in pairs. The third region is the protein surface and Stern layer, containing protein bound charge. When both protein and sorbent are negatively charged, positive ions will accumulate in region 1. Microcalorimetry adds the final information needed to decipher the enthalpic contributions to adsorption [45]. Positive values of enthalpy change are found in several situations. Clearly then, the entropy gain must drive adsorption in these cases. HPA adsorbs due to hydrophobic dehydration on weakly charged polystyrene at high pH, and due to an increase in rotational freedom at lower pH. On the more strongly negative polystyrene, which is less hydrophobic, dehydration is less favourable, but allowed by more structural freedom in the protein upon adsorption and the ionic medium effect (transfer of ions to the dehydration layer). RNase, on the other hand, does not experience hydrophobic dehydration, or entropic gains from conformational freedom as the major driving force for adsorption. Finally, a much more rigorous determination of the thermodynamic contributions is derived from modeling and proper irreversible thermodynamic considerations [46]. In particular, the enthalpic gain due to structural rearrangement is determined by subtracting all other contributions to enthalpy from the total enthalpy. The other enthalpic terms are considered to be proton, and ion adsorption/release, electrostatic attraction/repulsion, and van der Waals attraction.

Using radiolabelled Na^+ , Ba^{2+} , and Mn^{2+} ions, the concept of coadsorption of ions for charge balance was tested [47]. Adsorption is larger in solutions with divalent ions than monovalent ions, and is dependent on electrostatic considerations, and not the pH, or ionic concentration. The free energy of inserting a Ba^{2+} ion into region 1 is larger than Na^+ because Ba^{2+} is larger, more polarizable, and more negative than Na^+ .

Differences are found if hydrophobic polystyrene surfaces are replaced with hydrophilic hematite surfaces for RNase, and HPA adsorption [48]. Enthalpy of HPA adsorption is positive, suggesting the entropic considerations are dominant. At small surface coverages, the protein conformation is changed the most. Near the isoelectric point,

protein-protein repulsion is minimized. Away from the isoelectric point, lateral repulsion plays an increasingly central role in determination of the plateau. RNase adsorption, on the other hand, is mostly dominated by electrostatic considerations. Under charge repulsive conditions, RNase will not adsorb. Electrostatics play a much larger role in the case of the hydrophilic substrate, even in the case of HPA. Ion coadsorption occurs in this case as well.

In the case of RNase, considerations are electrostatic, and quite simple, but the case of HPA is synergistic, requiring consideration of the interplay between a number of complex phenomena. A study, by Haynes et al., of lysozyme (LSZ) and α -lactalbumin (ALA) on polystyrene particles indicates many of these effects [49]. Protein adsorption can be enhanced by hydrophobic dehydration and decreased rotational constraints due to changes in protein conformation. It is undesirable generally to coadsorb ions, however, it is preferential in cases of electrostatic repulsion. Rigid proteins will have a hard time conforming to the surface, and expelling water in hydrophobic situations. They also experience a harder time matching charges on the sorbent, since ion-pairing cannot be satisfied. In addition, lateral repulsion between adsorbed proteins can affect plateau values. The example is given of lysozyme, which adsorbs only weakly to negative hematite. Because it cannot dehydrate the surface as strongly, the native conformation will be more stable, making ion-pairing less rigorous and preventing entropy-increasing rotational freedoms. Attributing its lack of adsorption simply to the fact that the particle is hydrophilic is thus only one effect in a host of contributions.

Another study investigating RNase, lysozyme (LSZ), myoglobin (MGB), and α -lactalbumin (ALA) [50] also found that “hard” proteins with a strong internal coherence (large native Gibbs energy of stabilization) behave differently than “soft” proteins with low Gibbs energies of stabilization. Differences in adsorption of these similarly sized proteins on polystyrene (PS), polyoxymethylene (POM), and hematite were examined. All proteins adsorb to PS, but on POM which is intermediate in hydrophobicity, both soft proteins (MGB, and ALA) adsorb, but of the hard proteins, only the strongly positive LSZ adsorbs. On hematite, the hard proteins only adsorb under electrostatically favourable conditions, while again, the soft proteins adsorb under all conditions. In almost all cases adsorption lowers the overall charge of the system, even when both protein, and surface are negative.

Thus ions must be coadsorbed with the protein to help charge matching. Overall, as in the previous cases, hard proteins adsorb onto hydrophobic substrates even under electrostatic repulsion, but only adsorb to hydrophilic substrates during electrostatic attraction. Soft proteins can undergo conformational changes, providing enough Gibbs energy lowering to even dominate hydrophilic dehydration and electrostatic repulsion, allowing adsorption under all conditions. Competitive and sequential adsorption experiments have also been performed on these proteins [51]. As an example, on PS, after RNase has adsorbed, the positively charged protein LSZ can adsorb more, even on positively charged PS. Lysozyme contains a small hydrophobic patch which may account for this. On hydrophilic substrates, however, no adsorption occurs in repulsive conditions, and the most electrostatically attractive protein wins the competition. Thus, electrostatics mostly dominate which protein will win in sequential, and competitive tests. However, MGB and ALA can undergo additional conformational changes, and ALA always out-competes all other proteins, at all sorbent surfaces. ALA's remarkable affinity for adsorption probably arises from its particularly low internal coherence. Except in the case of lysozyme which has a loosely bound part on PS, adsorption at hydrophobic surfaces is irreversible. Thus in mixtures of proteins, kinetics will determine, to a large extent, the composition of adsorbed layers on hydrophobic surfaces.

Lysozyme, ribonuclease, beta-lactoglobulin, alpha-lactoglobulin, cytochrome c, myoglobin, and hemoglobin, were adsorbed to chemically modified silica particles with differing hydrophobicities [52]. Differential scanning calorimetry (DSC) on the various combinations showed decreases in the denaturation point of all proteins except cytochrome c upon adsorption. This suggests that in all cases adsorption decreased stability of the protein. Fluorescence measurements also indicated lowered stability upon adsorption. Examining lysozyme on silica using DSC, fluorescence, and Fourier transform infrared spectroscopy (FTIR), various hydrophobicities showed that the stability decreased with increasing hydrophobicity, and the conformation was changed. Additionally, the conformational heterogeneity was greatly increased upon adsorption. This is different than the previous studies, however, in that lysozyme is generally considered to be a hard protein, undergoing very little denaturing.

Infrared spectroscopy applied to the study of the blood proteins serum albumin, prothrombin, and fibrinogen, all on silica particles, supports the idea that proteins with strong internal stability do not change conformation during adsorption [53]. However, this is a hydrophilic substrate, and for hydrophilic protein it is not expected that gross conformational changes would take place.

Normally, measurements of protein adsorption can only differentiate between adsorbed and desorbed protein totals. By labeling protein, such as BSA, with fluorescent compounds like rhodamine, it is possible to use total internal reflection fluorescence microscopy to measure the rate constants at equilibrium [54]. By photobleaching the adsorbed layer it is possible to measure recovery from exchange with unbleached molecules. In addition, by using varying laser beam widths it is possible to measure lateral diffusion at equilibrium. Results indicate that there may be multilayers bound, and that there are three rates of exchange: A very slow rate which is essentially due to the irreversibly adsorbed BSA, a medium rate which is due to a reversibly adsorbed second layer, and very rapid desorption due to very loosely bound reversible layers at the solution interface of the adsorbed layer. Reversibly bound amounts increase with increasing bulk concentration. In addition, lateral diffusion is observed to occur, presumably in the loosest bound layer. By attaching both a donor and acceptor fluorescent group, it is also possible to use total internal reflection fluorescence spectroscopy to monitor energy transfer. The energy transfer is sensitive to the distance between the donor and acceptor groups, which is dependant on BSA conformation [55]. Using this technique, BSA was found to be conformationally changed at the surface [55].

2.1.2 Protein Adsorption in Chromatography

Many chromatography methods are popular for separating and identifying proteins. Their complex interactions with the proteins make them interesting tools for studying protein fundamentals. One such technique is hydrophobic interaction chromatography (HIC), which attaches hydrophobic groups to a hydrophilic cross-linked matrix. Proteins are separated on the bases of hydrophobic/hydrophilic interactions. α -lactalbumin is a structural homologue to lysozyme, and its partial denaturation during HIC shows similar

two peaks corresponding to similar denatured domains [56]. This suggests that there is a possible conversion back and forth between two conformations within the protein. One peak represents a native type state, which is not retained on the chromatographic column. The second peak corresponds to a denatured state, which retains only partial structure. The hydrophobic core appears to be a key protection factor, and appears to retain structure. Jones et al. [56] suggest this may mean that the regions of protein most in contact with the solvent are the first to be destabilized. Non-specific hydrophobic denaturation appears to always stabilize/destabilize the same structures. The protein is able to refold upon elution from the substrate.

Bovine pancreatic trypsin inhibitor (BPTI) protein, studied on reversed-phase chromatography (RPC) and HIC, indicates that salt content plays a major role in preventing hydrophobic denaturation. What role this is, however, is not clear, and McNay et al. [57] have investigated this for RPC. They find that increasing salt content increases protein hydrogen exchange protection, and changes the kinetics of denaturation. They suggest that while the anionic charge content of the RPC surface may not destabilize a protein on its own, in conjunction with hydrophobic interactions, it may be a key factor. It is known, as well, that certain salts help to stabilize a protein's overall structure. There is also a dependence on the type of salt as to which residues are protected. Interestingly, no correlation can be found between the degree of unfolding and the degree of retention. In an earlier study by McNay et al. [58], they look at pore size influence, and discover that the largest hydrogen exchange is for a pore size that is approximately equal to the protein molecule. A pore of this size will be largely occupied by the carbon chains, which will surround the protein molecule. Such a pore will have the greatest interaction area with the protein. Unfolding of BPTI is found to occur in two steps, characterized by time constants on the order of five minutes for one, and up to two hours for the other. It is also noted that long times of contact with the RPC surface before elution resulted in more denaturation. This is consistent with a kinetically controlled unfolding process, such as that seen by Wertz and Santore [28-31]. McNay et al. [58] also observe that there is generally a preservation of the hydrophobic core much like the native state. This is consistent with the HIC observations of Jones et al. [56]. An investigation of protein on two chromatographically relevant surfaces showed that a protein which carries the same net

charge as a surface, can still bind [59]. For the one surface (butylated), salt effect on adsorbed concentration appeared to act through solubility effects (salting-in and out), while on the second surface (aminopropylated), electrostatic screening of the repulsive charge between the protein and surface seemed to dominate. Adsorption rate is contended to be a complex function, due to such factors as irreversibility, which make modeling difficult [60].

2.1.3 Aggregation

High salt concentrations increase the screening of charge, and decrease both attractive interactions, as well as repulsive interactions between proteins. This can lead to aggregation and precipitation [61]. AFM shows that lysozyme adsorbed to a hydrophilic SAM surface is randomly oriented, and distributed (based on heights), while lysozyme on a hydrophobic SAM surface is clumped together [39]. This would suggest possible hydrophobic aggregation on the hydrophobic surface. In contrast to heat denaturing free protein, interfacial denaturation and lateral interfacial aggregation of protein may occur approximately simultaneously under certain conditions [27].

Alzheimer's disease and spongiform encephalopathy are now believed to be the result of protein aggregation in the brain and nervous system, forming amyloid β -sheets. Amyloid β protein is part of larger transmembrane proteins. Under certain conditions, these proteins can be changed into β -sheets, which promote aggregation, formation of more β -sheet proteins, and formation of amyloid fibrils instigated in Alzheimer's disease. To understand the factors that lead to this, Giacomelli and Norde [62] allowed amyloid- β proteins to contact hydrophobic Teflon, and to measure the result. In solution, monomers, dimers, small regular β oligomers, as well as large aggregations of twisted β sheets co-exist. The largest degree of aggregation occurs around pH 7, which is the isoelectric point of the protein. Teflon, on the other hand, promoted α -helix formation for low coverage, and even appeared to convert some of the aggregates in α -helices. For higher concentrations, however, β -sheet formation was promoted, clearly as a result of lateral interactions.

2.1.4 Morphology of Adsorbed Protein

Most studies that use averaging techniques will agree with mean field theories, which treat the lateral dependence of protein deposition as homogenous. It would be desirable, however, to have some idea of the two dimensional structure of deposits, in addition to their overall height. AFM presents the opportunity for such an investigation. Jandt has written a good review of the uses of AFM for studying biomaterials and their interactions with biomolecules [63]. Radial distribution curves of the surface protein, measured by Johnson et al. [40], agree well with a random sequential adsorption (RSA) model of deposition (i.e. random placement). Ionic considerations indicate that this system will match an RSA jamming limit for low ionic strengths and that at intermediate strengths, equilibrium is reached. The equilibrium implies reversibility in adsorption, which is not allowed in the RSA model. Generally, short-range order is seen in the radial distribution of surface protein. However, long-range order is observed for adsorption at fluid (Langmuir-Blodgett) films, but no true crystallization is observed.

In another AFM study, submonolayer coverage of apparently irreversibly adsorbed lysozyme is observed on mica [64]. The images are able to show that for low concentration, adsorbed lysozyme diffuses on the surface with minute timescales, and forms five molecule clusters. At higher concentration, protein adsorption occurs uniformly over 2h until complete monolayer coverage is achieved, at which point a second layer is able to deposit. Conformational changes, upon adsorption to the surface, expose hydrophobic groups, and it is suggested that these hydrophobic groups drive the aggregation of the molecules at low concentrations. Additional groups are exposed that may assist in the formation of multilayers, although at a slower rate, since the adsorbed lysozyme presents a more hydrophilic surface.

Haggerty and Lenhoff [65] have used STM to look at lysozyme on graphite. They are able to observe similar long-range order, and packing of the molecules on the surface into two-dimensional arrays, for both wet and dry imaging. A ring pattern is visible, but no definitive explanation can be given. Islands in the structures suggest that the growth may be the result of a nucleation process. Surface coverage decreases with increasing salt, and decreasing protein concentration. Since the surface itself is uncharged, the effect must be

due to intermolecular effects. One would expect charge repulsion between the molecules to decrease with increasing salt, and thus support a higher surface coverage. It may be that this does not happen due to the salting-in phenomenon, where protein is actually more soluble in the solution with increasing salt, reducing adsorption affinity. Salting-in and out is also observed in other adsorption experiments [59] which also exhibit a dependence of the rate of adsorption on ionic strength. A second view proposed [65] is that due to charge anisotropy, the molecules can pack better. This anisotropy is screened at higher ionic strengths, leading to a more uniform, and thus repulsive intermolecular field.

2.1.5 Protein Alignment

Control to selectively prevent, or promote adsorption of certain proteins onto surfaces is desired for both biomaterials, and biosensors. The ability to do this is, of course, directly connected with protein interactions at interfaces. Xia et al. [66] have attempted to create two surfaces: one which will adsorb protein, and one which will not. Both surfaces are gold with SAMs. The first polymer suggested for preventing adsorption is a copolysiloxane backbone with disulfide and poly(ethylene glycol) PEG side chains. The second polymer made to adsorb protein is a terpolysiloxane molecule with disulfide, PEG and ester-terminated PEG side chains. Using surface plasmon resonance (SPR), they are able to show that the first polymer does indeed resist protein adsorption, while the second surface is able to bind IgG through its ester group as they predicted. If biosensors are to work, they must of course have a fairly specific orientation so that the pertinent functional group of an antibody will be exposed to a solution. Because proteins often contain very unique charge distributions, it may be possible to control orientation through careful tuning of electrolyte, surface charge, and pH. Chen et al. [67] find, using SPR and AFM, that between IgG1 and IgG2a, IgG1 can be oriented more strongly because of its larger dipole moment. In addition, increasing charge density in their SAM, combined with other selective forces (e.g. hydrophobic), should be able to improve orientation quite a bit. A more unique approach [68] makes use of the fact that most proteins have specific binding sites, which are used for coupling with other molecules and proteins to carry out a task, such as adhesion, catalysis of a reaction, etc. Certain bacteria bind to specific areas on fibronectin

through short peptide sequences. One such sequence was bound to streptavidin on glass coated with amine-terminated silane. Fibronectin, on this substrate, bound with its COOH end pointing away from the substrate.

Crystal formation can be mediated by certain proteins, creating bone structure, teeth [69] and other hard biological structures, such as mollusc shells [70]. For example, it is demonstrated that certain proteins catalyze the formation of gold crystals, and alter their morphology [71]. Denaturation of the proteins results in their removal, and shows that they do not bind covalently with the gold during the process. It is proposed that it is the acidic nature of the protein used that results in acid catalysis of the crystal formation. The shape of the crystals is determined largely kinetically. Some proteins may have repeating units, which will bind with specific repeats in the crystal lattice [72]. This in turn can slow the growth of certain interfaces, and leads to new morphologies. Proteins in free solution may inhibit nucleation, and when adsorbed to certain surfaces, may facilitate nucleation through a lowering of the activation energy [72]. An initial layer of protein nucleates and orients crystal growth on mollusk shells [70]. This in turn orients a second layer, causing an abrupt transition between the two types of crystals. It is found that this is not the result of a new protein, but rather one protein. The interlamellar spacing of proteins controls the spacing between layers. This shows that orientation of proteins is sensitive to microscopic heterogeneities in inorganic materials, and that the protein, in turn, can generate oriented surfaces.

2.2 Applied Studies of Proteins at Interfaces

2.2.1 Blood Contacting Materials

Blood contacting materials are perhaps the biomaterial demonstrating most acutely the need for understanding interfacial protein behaviour. It is critical that materials used for such things as heart stents, heart valves, and vasculature be well understood in the presence of protein. A failure in this case can result in thrombosis (clot formation) and death. There are many good overviews of concerns associated with blood contacting materials [73], and of methods applied to studying blood contacting biomaterials [25]. Thrombus formation is

activated by the adhesion of plasma protein (fibrinogen, and fibronectin in particular) to the biomaterial, which then promotes platelet adhesion [74, 75], and ultimately leads to clot formation.

Even early ex-vivo studies with dog's veins [75] suggested that fibrinogen/fibronectin deposition lead to thrombosis in a material dependent way. While no correlation between deposit morphology and deposition magnitude could be found, the study hinted that one could possibly find a material resistant to thrombosis. Many studies have searched for such a material. Fibronectin adsorption to hydrophilic and hydrophobic silica, studied using TIRF spectroscopy, indicates that hydrophobic substrates adsorb fibronectin faster, and have higher plateau values [76, 77]. Conformational changes were also noted on hydrophobic silica. By adding 2-methacryloyloxyethyl phosphorylcholine (MPC) to polysulfone (a common biomaterial) protein adsorption, and denaturation can be minimized [78]. Phosphorylcholine is a polar phospholipid group, which helps to mimic the phospholipid heads on a cell's surface to some extent. This technique has also been exploited with some success in contact lenses (omafilcon A in particular) [79, 80]. Attaching polyethyleneoxide (PEO) is another common technique, which exploits the steric repulsion abilities of this polymer to reduce fibrinogen adsorption [81, 82].

In addition to clot promoters such as fibrinogen, blood contains substances capable of dissolving clots. Tissue plasminogen activator or tPA can activate plasminogen into a form capable of clot dissolution. Rather than search for a surface that simply does not adsorb fibrinogen, another approach is to promote the adsorption of desirable proteins such as tPA. A substrate such as this rich in ϵ -lysine has been created, allowing large amounts of tPA to be preadsorbed [83, 84]. In contact with blood plasma the surface is capable of dissolving clots, but loses about half of its tPA after approximately thirty minutes. This is due to another common effect, that of competitive adsorption, that in this case means plasminogen displaces some of the tPA. However, radiolabelled plasminogen indicates that up to 75% of the molecules can exchange with bulk. While tPA is better in terms of dissolving clots, plasminogen will still help prevent their formation, and exchange with the bulk may be desirable, allowing the surface to regenerate itself.

2.2.2 Contact Lenses

2.2.2.1 Background

One of the more commonly studied systems of biomaterials is the eye-contact lens system. This is largely due to the ease with which it allows the investigation of a biomaterial in contact with a bodily fluid (the tear film). The problem of protein adsorption at the solid liquid interface of the contact lens is of great relevance, since deposits can create a variety of problems. As well as clouding the lens, and possibly increasing friction, protein can also illicit immune responses (giant papillary conjunctivitis) and can promote bacterial adhesion.

Early lenses were made of PMMA [85], and other polymers, which did not suit the oxygen, wettability, or nutrient transport demands of the eye. With the advent of hydrogel lenses, and more recently silicone hydrogels, these problems have been greatly minimized, leaving protein adsorption as one of the last hurdles to overcome for lenses to be used multiple times, or for extended wear times (eg. overnight).

The Food and Drug Administration (FDA) classifies contact lens materials according to the ionicity, and equilibrium water content (EWC) of the lens. There are four groups categorized according to water content and ionicity as: Group I –low water, non-ionic; Group II –high water, non-ionic; Group III –low water, ionic; and Group IV –high water ionic [86]. This simple grouping system is meant to give some indication of the chemical properties of the lenses.

2.2.2.2 Food and Drug Administration Grouping vs. Protein Deposition

Many studies have been performed to characterize, and quantify the protein and lipids according to group number. Protein can adsorb either to the surface, or into the matrix of the polymer, which will be seen to be important later. Minarik, and Rapp [86], in their in-vivo patient studies, find that lenses, ordered in terms of most total protein adsorption, are Group IV, II, III, and I. From this fact, they draw the conclusion that water content is the dominant determining factor in protein adsorption. Minno et al. [87], on the contrary, find that total protein deposition followed the group number and thus Group III absorbed more

than Group II, leading to ionicity being the dominant factor. Prager et al. [88] find that Group II adsorbs more radiolabelled lysozyme than Group III. That this would be the case seems somewhat counterintuitive, since lysozyme in general, deposits more upon hydrophobic materials [39]. Keith et al. [89] also find the same order as Minarik, and suggest that lysozyme is the major component of the deposits, with albumin only adsorbing significantly to Group I, III, and to a lesser extent Group II lenses. Minarik, however, finds that when lysozyme alone is considered, Group III lenses adsorb more than Group II. These differing points of view are characteristic of studies which do not consider the type of protein, or the chemical nature of the lens in addition to ionicity and water content.

One point studies generally agree on is that Group IV lenses deposit the most total protein [85, 86, 88, 90-101], with one study [102] finding up to 17x more protein than a Group II lens. Group I lenses deposit the least protein [91, 93, 100, 101]. Lin et al. [91] find that lysozyme is the major component causing this dramatic increase, and that on Group I lenses, almost no lysozyme is adsorbed. Other studies [93, 98, 101, 103] agree that lysozyme is the predominant component of deposits on Group IV lenses, along with PMFA, protein G [93], IgA, and IgG [104]. Tighe et al. [94] find that between two Group IV materials (etafilcon and Vifilcon), the most anionic of the two (etafilcon) shows the greatest adsorption both surface and matrix bound, with Group II showing little surface, and no matrix bound protein. The negative charge arises from additives, generally used to increase water content. The fact that lysozyme is a very basic protein (carries net positive charge up to pH 11), suggests that electrostatics are the driving force for adsorption, at least to Group IV lenses for lysozyme. Group I (including polymacon) shows the lowest amounts, and will adsorb a submonolayer coverage of protein [96]. This is likely due to the lack of charge attraction for protein such as lysozyme. Albumin, however, deposits in greater amounts on polymacon (Group I) than on etafilcon (Group IV) [105].

Garret et al. [106] have tried to correlate the proportion of MAA (methacrylic acid) or NVP (N-vinyl pyrrolidone), to adsorption of lysozyme and human serum albumin (HSA). HEMA lenses are often made with either common additive: MAA, which increases anionicity and water content, or NVP, which increases water content without charge. Not surprisingly, lysozyme deposition onto the surface, and into the matrix, increases with MAA proportion, while HSA (isoelectric point pH 5) decreases. This matches with

electrostatic expectations for positive lysozyme, and negatively charged HSA. NVP increases both lysozyme and HSA, but less significantly. A combination of NVP and MAA shows that MAA dominates the effects. Garret notes that for hydrogels with similar water content, lysozyme adsorption varies largely, but HSA does not, again indicating that electrostatics dominate, at least for lysozyme. The suggested mechanism is an increase in anionicity and pore size for MAA content, and an increase in polar content for NVP. The increased polarity allows hydrogen bonding and increased hydrophilicity, which, it is noted is somewhat counterintuitive for lysozyme, which normally prefers hydrophobic surfaces. Soltys-Robitaille et al. [107] include a cationic group I material in their study with anionic, and non-ionic materials. They find that anionic HSA adsorbs significantly to the cationic lens, while lysozyme to the anionic lens. Even within RGP lenses, which adsorb little protein, Botempo et al. [108] find a greater deposition onto higher charged siloxanyl polymers. Other studies back up the importance of electrostatics [109, 110]. This demonstrates that electrostatic charge is a dominant effect in adsorption, but the increase with NVP shows it is not the only one. Interestingly, however, there appears to be a relationship between the oxygen permeability of the RGP lenses and the surface roughness [111], a fact which may lead to increased adsorption of pathogens.

A study [112] of HSA finds that it adsorbs in the following order of decreasing adsorption vifilcon (polyvinylpyrrolidone (PVP) containing Group IV), tefilcon (Group I), etafilcon (non-PVP, MAA Group IV). This clearly shows the effect chemical makeup has, considering vifilcon is less ionic. Two Group IV materials, differing mainly in their additives, have completely different adsorption patterns for HSA. Decreasing pH increased adsorption, as the protein approached its isoelectric point. For purely electrostatic reasons, one might expect that etafilcon would thus become more favourable since charge repulsion is lowered. That this is not the case shows that PVP may be a major factor in adsorption. For tefilcon, hydrophobic dehydration may increase adsorption, or the fact that tefilcon is lathe-cut may increase surface porosity. Most lathe cut lenses are polished, however, leading to a smooth surface with small scratches. It is noted here [112] that the hydrophilicity of the bulk material does not necessarily correlate with the hydrophilicity of the surface.

One conventional lens worth mentioning, omafilcon, takes a unique approach to preventing adsorption by mimicking a cell surface to which little adsorbs. By incorporating phosphorylcholine, the surface of the hydrogel mimics the head groups of phospholipids. Investigations [79, 80] have shown that compared to Group IV etafilcon, and Group II atafilcon, and permafex lenses, omafilcon exhibits less protein deposition, and less lipid deposition than any other Groups I, II, IV lenses tested. This clearly demonstrates that chemical makeup is a significant factor in adsorption. In addition, patients find that omafilcon lenses are more comfortable to wear [80].

It is clear that the conditions of water content, and especially ionicity are important factors. For example, CSITM lenses, which had previously been found to adsorb much less protein than other lenses, were no more resistant to deposits when compared to lenses from the same group [113]. However, in another study comparing CSITM to PreferenceTM (Group I), they were found to be more protein resistant [114]. Etafilcon has twice the lysozyme uptake of vifilcon [110], both group IV materials. These, and the previously mentioned examples show that there is dependence upon chemical structure. This is consistent with some theoretical models, which have found the heterogeneity of a surface can play a large role in adsorption.

2.2.2.3 The State and Type of Protein

New lenses are being made which incorporate silicone in them to improve oxygen transfer to the non-vascularized cornea. These materials are low water content non-ionic lenses (Group I). Because the silicone makes the surfaces poorly wettable, surface treatments such as plasma oxidation, or plasma polymerization are carried out [115]. The surfaces of some of these have been characterized using XPS [116] and SEM [115]. Jones et al. [117] looked for differences between etafilcon (conventional group IV hydrogel) and balafilcon, and lotrafilcon (both silicone hydrogels). Conventional hydrogel deposition was much greater (not surprising for a Group IV material) than the silicone materials. It was significant, however, that the protein on silicone lenses had a much greater percentage of denaturation than conventional lenses (also seen in [118]), and that lipid deposition was increased (since silicone is hydrophobic). PurevisionTM (balafilcon) also exhibits a rather

unique structure, containing holes which are several hundred nanometers in size [115]. Pores of this size may help transport water and ions, but may also have a dramatic effect on protein adsorption. This brings up the question of whether it is simply the amount of protein, or the type and state of the protein, which is related to its pathogenicity.

Ultimately, the words pellicle, biofilm and deposit are frequently interchanged, along with many other words in the discussion of protein adsorption to lenses. Hart et al. [99] have tried to prevent this sort of language ambiguity. After all, a certain amount of protein may be beneficial, and furthermore, necessary to make the lens biocompatible with the eye. The pellicle, referring to the normal coating, is found by Hart to be from 0.1 to 8.6 μm thick (thicker on group IV lenses). Deposits and biofilms, on the other hand, should be reserved for potentially pathological protein. They believe that it is not the pellicle, consisting mostly of loosely associated protein, which causes problems, but the matrix and denatured “abnormal” protein. Unfortunately, most studies detect overall protein, and do not differentiate.

A significant finding on group IV lenses was a 30KDa previously unidentified protein [119], which turns out to be a lysozyme dimer [120]. It is determined [120] that this dimer appears within one hour of wear on the group IV lenses, but is not detectable in the tear film. The dimer is not present on group I, or II lenses, and is denatured, and irreversibly bound to the lenses. However, much of the lysozyme found on the group IV lenses is still biologically active, which may be of importance for bacteria adhering to the lenses [94, 109]. In contrast, lysozyme on non-ionic contact lenses is found to be predominantly inactive [109]. ATR-FTIR investigation has shown that γ -globulin protein denatures and orients itself during adsorption to PHEMA lenses and that binding affinity increases with the amount of denaturation.

Much work is concentrated on lysozyme, and albumin, which may be responsible for pathogenicity. However, other proteins may be problematic as well. Lenses from patients with Giant Papillary Conjunctivitis show increased IgM protein deposition [121], and decreased IgA deposition [122] on their lenses [121]. Lysozyme, lactoferrin, and several other immunoglobulin deposits show no difference between unaffected and affected patients [121]. It is not clear, however, whether this is the cause or result of the condition.

2.2.2.4 Kinetics

The kinetics of deposition are also frequently studied on contact lenses. Many groups find that protein adsorption occurs rapidly at first, and then slowly for some time, often reaching a plateau. This is, however, dependent on the type of protein and lens. For example, Lin et al. [91] find that protein is present after as little as one minute, and plateaus after as little as 24 hours. Lysozyme continues depositing for over a week. This illustrates the downfall of total protein assays, which do not differentiate between particles. Leahy et al. [93] also find that most studies only look at long term deposition but that significant adsorption has occurred after only one minute of wear. Ionic lenses are often found to have long term adsorption, while non-ionic lens adsorption halts after the quick initial adsorption [98]. These results agree with the work of Lin, since lysozyme has little affinity for non-ionic lenses. Because proteins are capable of changing conformation upon adsorption, kinetics are not a mere problem of particle adsorption (as in colloidal models). Indeed Garret et al. [112] see total adsorption occurring very fast and reaching a plateau, while irreversible adsorption grows slowly with no plateau in sight. This suggests that irreversible deposit growth is time-limited by the kinetics of denaturation, a postulate supported by ATR findings [112]. Of course these averaging techniques say nothing about how these deposits are forming in three dimensions. It is found, for example using AFM, that deposits build up uniformly initially, and over longer times begin to form non-uniform deposits [123]. A “foundation” layer of mucin has been found beneath protein deposits during study of one hydrogel contact lens [124]. This may be beneficial, as mucin normally coats the eye, promoting wettability.

2.2.2.5 Location of Protein Adsorption

A few studies find differences in adsorption between different areas of the lens. Using immunofluorescence in one case, and antigen-conjugated gold in the other, it is observed [93, 125] that there is more protein deposited on the front surface of the lens than the back. Possible reasons for this are the effect of blinking, differences in posterior and anterior tear

film, a thinning or drying of the tear film on the front surface [93], or additional mucus on the front [125]. Heiler et al. [126] look at the adsorption difference between an inner portion and outer (rim) portion of the lens. Using ninhydrin assay, they find Groups III and IV hydrogels deposit more on the outer portion of the lens than the inner portion, while Groups I and II show no difference. They suggest that it may be related to a difference in how the lenses are cleaned (such as rubbing them) or that the differential thickness of the lens may be responsible. They also postulate that the lens may be macroscopically inhomogeneous, however, inhomogeneity over lengths of many mm's seems unlikely.

The phenomenon of matrix bound protein is interesting in itself, and Jones et al. [95] find that while surface protein reaches a plateau after one day, total protein on Group IV lenses took longer (up to seven days), and Group II lenses did not reach a plateau. They conclude that chemical structure is a determining factor. Albumin and lactoferrin are suggested to be the contributors to the growth on Group II lenses due to their affinity for NVP (also [98]). Some studies have tried to quantify the matrix bound protein, and it has been found to be up to 33% in Group IV lenses [88]. Meadows and Paugh [97] find that in terms of surface protein quantity, Group I and IV lenses are similar, but that Group IV has a large amount of matrix bound protein. In general, there is more surface bound protein than matrix protein [98].

Lysozyme is predominantly the smallest most positively charged molecule studied, and thus is implicated as being the major component in most deposits. While it is by far the largest component of this group of proteins in the tear film, other proteins exist which are smaller, with greater positive charges. These should have even greater affinity for Group IV lenses, and the matrix. Major Basic Protein (MBP) is such a protein, which can cause vernal Keratoconjunctivitis. Using immunofluorescence, one study [96] is unable to find MBP on group I lenses, but it is contended that it may bind better to group IV lenses, which is undoubtedly true. There are also other small proteins, which are not normally studied [96].

2.2.2.6 Dependence on Tear-Film Composition

While all of this is very informative, the real tear film is a multi-component system, containing not only many proteins, but many types of lipids as well. For example, in a study by Botempo et al. [127], protein, lipid, and protein-lipid solutions are tested for the amount of protein and lipid deposited. They find that lipid presence decreases protein adsorption only to Group IV lenses, while protein decreases lipid deposition to all lenses, particularly Group II. Suggested reasons are that for Group IV lenses, once proteins adsorb, they decrease the hydrophilicity of the surface slightly, which allows lipids (especially polar lipids) to adsorb, increasing the hydrophobicity and preventing further protein adsorption. On Group II lenses the protein is able to out-compete the polar lipids for the limited polar binding sites. Thus, the overall effect is a reduction in the preferential adsorption of a lens for protein or lipid. Botempo et al. [108] repeated this study on rigid gas permeable lenses which incorporate silicone and contain no water. They find that lipid deposition is greater than protein deposition when considered individually. When combined, however, protein deposition increases by four times, while lipid deposition is reduced on siloxanyl alkyl acrylate lenses. Silicone being hydrophobic, would naturally attract more lipid. Polar lipids will leave their hydrophilic head pointing away from the material. This makes the effective surface much more hydrophilic, allowing protein to deposit. The depositing protein, and polar lipid headgroups in turn, make an unfavourable surface for hydrophobic lipid parts to adsorb. Thus, the finding is consistent with their previous study, showing a reduction in preferential adsorption. A three-step adsorption process is therefore suggested for lipid-protein solutions.

Ultimately patients would like to be able to wear contact lenses at night, but this has not been possible to achieve safely. One reason for this is that during eye closure there is less oxygen transport, but it is also known that the closed eye tear film differs from the open eye tear film. It has been found [128] that the loosely adsorbed protein mimics the open, or closed eye tear film composition. Closed eye tear film contains less lysozyme, and more of other proteins such as IgG, SigA, C3. The rate of adsorption is also found to be lower in closed eye rather than open eye. It is postulated, that because reflex tear flow is reduced by 90%, and lysozyme is reduced, bacterial growth may be favoured.

A problem with in-vivo studies is the patient-to-patient variation in tear film composition. Most studies have found this to have little effect on adsorption (eg. [93]). This suggests that adsorbed quantities of protein reach a maximum well below the tear film quantity. A study on tefilcon (Group I), and vifilcon (Group IV) [129] finds that lysozyme deposition on Group IV lenses exhibits subject dependence, but not on Group I. On low-water non-ionic lenses, there are few binding sites, and little total protein adsorbed, allowing only those proteins with the highest affinity to adsorb. Group IV lenses, on the other hand, have an abundance of both polar, and apolar binding sites, allowing the proteins in highest concentration to initially bind, to be replaced later by higher affinity ones. This allows subject dependence, where protein concentrations will vary (Group IV dependence also found in [130]). Jones et al. [95], however find no dependence on variations of tear film protein for Group II, and IV lenses, as opposed to lipids. In-vitro studies by Prager et al. [88] find that different combinations of proteins yield different depositions, indicating that competition for binding sites may be non-negligible. Sack et al. [131] study only non-ionic lenses, and find that low water content lenses exhibit arbitrary selectivity, which can not be related to chemical makeup. This suggests patient dependence. High water content lenses, on the other hand, adsorb predominantly lysozyme.

2.2.2.7 Experimental Methods

Various methods have been used to study contact lens deposition. Since many methods focus on total protein adsorption, the data may not be as informative as once thought. The type and state of protein most likely have far more profound an effect upon the pathogenicity of a deposit.

Optical microscopy has been frequently used to try and classify deposits. For example, Kurashige [132] makes the assumption that visible protein equates to the total amount of protein. Not only has this been shown to be quite unreliable [87, 133], but also does not allude to the state of protein. Minno et al. [87] have tried to find a correlation between visible deposition and quantitative methods. Normally a scale, such as the Rudko method, is used, which categorizes deposits according to their ability to be seen under various conditions (naked eye, 7x magnification etc). They compare their results to a

commonly used colorimetric quantitative method called the Ninhydrin assay. Not surprisingly, it is found that visible deposits increase with wear time, though heavier deposits are not correlated to increasing wear. They conclude that probably the state of the protein is more important than simply the amount. Protein is not normally visible, and thus visible protein deposits may represent denatured protein which scatters more.

Scanning Electron Microscopy (SEM) has frequently been applied, but like optical microscopy is not easy to correlate to amounts of protein. The only measurement that can generally be made is the area of coverage after the lens is coated with gold, and this area does not include matrix bound protein, or homogenous layers of protein, and takes no account of the volume of deposits [113]. In addition, extensive preparation is required before imaging can begin. This often leaves deposits which can't be distinguished from protein deposits [93, 134]. Thus, while SEM is important in characterizing the deposits, it cannot be correlated quantitatively with assay, or spectrophotometry methods. Because of this, many studies use optical microscopy and/or SEM only as a support to other more quantitative methods [87, 92, 93, 113, 133, 135].

Atomic Force Microscopy (AFM), when applicable, is probably a better method than SEM, or optical microscopy, due to its ability to carry out measurements in environmentally relevant situations such as buffer liquids, and its ability to measure volume [136]. Unlike area, volume can be related, at least somewhat, to the quantity of protein deposited. For single proteins, it is found that there is a direct correlation between protein volume and molecular weight [137]. Baguet et al. [136] used AFM in conjunction with sodium dodecyl sulfate - polyacrylamide gel electrophoresis (SDS-PAGE) to quantify proteins. They found both uniform deposits, which appeared initially, and larger discrete "granules" which appeared after longer times. Baguet also attempted to find the thickness of deposits by scratching a hole in them, but because it was not possible to find the surface the usefulness of this method is questionable. It would have been difficult to tell if the bottom of the deposit had been reached, or if they were scratching through the lens surface itself.

One of the most informative methods, especially for in-vivo studies is gel electrophoresis [105, 117, 120, 127, 129, 136], which is able to distinguish between

different types of proteins. It is not always possible to distinguish the exact protein, but at the very least, groups with proteins of similar mass/charge can be distinguished. Lin et al. [91] were able to distinguish that the continually increasing component on Group IV lenses is lysozyme, and that other proteins are more or less maximally adsorbed within 1 minute. Leahy et al. [93] distinguished deposition anywhere from one minute to eight hours.

Coomassie blue staining gels, in conjunction with absorbance measurements, has also been found to be an acceptable but tricky method, exhibiting linearity in the 14-100 μg range [138]. Goldenberg and Beekman [139] find Coomassie blue R sensitive to 2 $\mu\text{g}/\text{cm}^2$ lysozyme. A problem of many dyes is that they adsorb themselves onto, and into the hydrogel material, creating massive non-protein-specific staining. As a result, a de-staining procedure must take place in order to remove non-protein bound stain. Unfortunately, de-staining is not easy, and possibly unachievable with many other dyes [139]. While Coomassie blue may not be the most sensitive method available, it has been shown to agree with the Ninhydrin method [130].

When using assay methods such as Lowry, Biuret, and BCA (bicinchonic acid), it is important to calibrate the data according to the protein being studied [87]. This is an important point, since the molecules that are used to bind to the proteins and “color” them, do not bind equally across different types of proteins. It is also likely that the state of protein may affect binding, leading to erroneous conclusions. Ninhydrin assay is used quite commonly [87, 126, 133, 140]. It, along with other assay methods, and gel electrophoresis, is subject to the efficiency with which the protein can be removed from the lens itself, and to an assumption that the protein is largely unchanged by the methods used to extract it. Trifluoroacetic acid (TFA) and acetonitrile are one method suggested by Keith et al. [89] to remove protein. They use HPLC, BCA, and SDS-PAGE to measure the extracted protein, concluding it is near 100% efficient. Hydrolysis of the proteins is found to be a better method than SDS extraction [100], which may remove as little as 25% of the bound protein. Polymer hydrolysis accounted for little of the measured values. An additional concern is adsorption to the container the protein is in, which has been seen to be up to 2/3 of the removed protein [141]. The previously mentioned factors mean that these assay methods have detection limits, which make them useful only for large quantities, and thus longer adsorption times. Dark field, phase contrast, and polarization optical microscopy,

along with Coomassie blue, and oil red O staining are such methods [93]. Most assay methods such as BCA and Lowry can detect as low as 5 μ g of protein, which is acceptable in most circumstances.

Confocal Microscopy [97, 106] in conjunction with fluorescence labeling, allows some measure of both surface and matrix bound protein. However, the protein content can only be measured with depth resolution of about 1 μ m.

X-ray Photoelectron Spectroscopy (XPS) [96, 142] can be used to quantify protein through nitrogen content, for polymer substrates that have little or no nitrogen. Ichijima et al. [142] applied this method to siloxanylpropylmethacrylate lenses, calculating relative protein adsorption through nitrogen content, to test the efficiency of cleaning solutions. XPS is also useful in characterizing the surface of the biomaterial itself. Attenuated total reflection fourier transform infrared spectroscopy (ATR-FTIR) could also be applied to characterize both protein content, and biomaterial composition, albeit very thin films are required [143]. Additionally, electron induced vibrational spectroscopy may find similar usefulness in the study of biomaterials [144]. It does not damage the sample, while allowing measurement of hydrogen content (unavailable in XPS), and the ability to discriminate aliphatic and aromatic molecules.

Other common techniques include UltraViolet Spectroscopy [95, 98, 102, 107, 145], chromatography techniques [89, 114, 127, 141], and fluorescence techniques (either direct, or through labeling) [93-95, 97, 98, 104, 106, 146]. These normally yield good quantitative results, and some techniques, such as UV/fluorescence are quite easy to apply, often without having to remove the protein from the lens. Ellipsometry has also been attempted for the measurement of the thickness of protein films on hydrogels, with possible resolution of 30-40 \AA [147]. MALDI [96, 107] is a relatively new technique capable of measuring submonolayer adsorption, and small protein <15KDa. Unlike XPS, it is capable of detecting different types of proteins. An interesting technique is suggested by Rebeix et al. [123], for estimating which surfactant cleaners will be efficient at removing protein. Maron's method forms the basis for their estimates. This consists of measuring the delay in the appearance of the critical micellar concentration between a liquid surfactant solution, and the same solution containing a lens. The longer the delay, the more the

affinity is for the lens. Comparing the affinity to quantitative protein measurements using BCA colorimetric assay shows good correlation.

2.2.2.8 Cleaning Methods

Since protein cannot be prevented from depositing at this time, many contact lens companies have adopted various cleaning regimens meant to prolong lens life. Some of the methods include disinfection with chemicals such as hydrogen peroxide, surfactant cleaning, enzyme cleaners, and rubbing the lens while in solutions. The effectiveness of many of these methods is unclear, and consequently studies have tried to look at their efficiency. Two popular enzyme cleaners are papain, which removes only protein, and pancreatin, which can also remove lipase, and amylase. By examining lenses with optical microscopy Kurashige et al. [132] found that papain was better at removing protein. They found that cleaning efficiency also depended on the type of deposit. Light deposits could be removed after several cleanings, but heavy deposits could not, suggesting that the protein must be in a different state, giving it a higher affinity for the surface. Hence they stress that regular cleanings are better than one long occasional cleaning. Myers et al. [90], however, found that papain enzymatic cleaners did reduce visible protein (which is what Kurashige [132] looked at), but that the overall protein is not significantly reduced. This poses a problem, since as they suggest, the enzyme may remove the top unperturbed proteins, but leave behind the denatured and matrix bound protein. If this is indeed the case, the cleaner may be of no use, since it is the denatured protein that is most often implied to be problematic. There have also been indications that while papain removes some protein, that papain irreversibly adsorbs onto the surface [148]. Studies of three commercial cleaners [133] using optical microscopy and ninhydrin assay, found no significant difference between their cleaning efficiency, except on a Group II lens. The Group II lens indicated that Sensitive Eyes™ produced by Bausch and Lomb was more effective than Coopervisions Miraflo™. In addition, neither alcohol nor nylon particles appeared to have any significant advantage. A study of six commercial cleaning systems on the four FDA categories of lenses using high resolution gel electrophoresis, and protein assay, indicated that only 1/3 to 1/2 of protein is removed [149]. Lysozyme is the only

protein measured to be removed. Lactoferrin, albumin, and glycoprotein, are unable to be removed, which might be because these are fairly hydrophilic proteins. It is apparent that even the effective cleaners are not able to remove all the protein [86, 133]. In fact, Senchyna et al. [118] found an increase in lysozyme adsorption to etafilcon (group IV) after polyaminopropyl biguanide (PHMB) based regimen (ReNu Multiplus™) cleaning, however PolyQuad (PQ) based solution (Opti-Free Express™) resulted in less denatured protein.

Different methods are used in cleaning solutions. Complete Comfort Plus™, for example, uses high ionic strength to disrupt the ionic bonding of lysozyme and other proteins, and to prevent re-deposition. ReNu™, on the other hand, strips calcium ions that stabilize lysozyme bonding. Simmons et al. [150] find that while Complete Comfort Plus™ removes the most protein, neither Complete™ nor ReNu Multiplus™ are able to remove all protein. They also believe that Complete™ removes more “less available” protein, which refers to matrix, or irreversibly bound protein. They base this on the fact that there is approximately the same surface protein left after cleaning, however, Complete™ removes more protein, which may have come from the matrix. Liu et al. [145] also find Complete™ to be more effective by up to two times in-vitro, and even more in-vivo. One of their suggestions is that ReNu™ is more basic than Complete™, which would lower the cationic charge on lysozyme, and thus its affinity for contact lenses.

An alternative to using chemicals to try and remove already deposited protein is to use chemicals to alter the proteins so that they do not want to deposit, or are reversibly adsorbed. Bendazac lysine, a non-steroidal anti-inflammatory drug (NSAID), is supposedly capable of preventing lysozyme denaturation, which has been implicated in irreversible adsorption. Missiroli et al. [135] state that there are indications that denaturation probably depends on the polymer used, rather than just equilibrium water content (EWC). Lysozyme adsorption is reduced to a quarter its original value in the presence of bendazac lysine, and is more easily removed. The reduction in deposition is also backed by several other studies [151, 152].

It has been noticed in several clinics that a hazing of contact lenses occasionally occurs, which reduces visibility, and Sack et al. have studied this phenomenon [103].

Originally, because all patients experiencing the hazing had used hydrogen peroxide disinfection, a connection had been drawn. A detailed study of the lenses indicated that this was occurring only on Group IV lenses, and that lysozyme was the culprit protein. It was found that rather than hydrogen peroxide, stannate anion which is added to stabilize cleaning solutions, bound to the lysozyme, presumably causing it to denature, become opaque, and increased its affinity for the lens. Because lysozyme is so cationic, it allows itself to bind to the anionic Group IV hydrogel (due to MAA), and bind extra anionic species as well. Clearly, the components in some cleaning solutions are actually making the protein problem worse.

Much more work must be done in the area of cleaners to elucidate their efficiency at removing protein, as well as to determine optimum cleaning times, and the type and state of protein they remove. Care must be taken to ensure that cleaning solutions are not making matters worse. For enzymatic cleaners, one would expect, in general, that the longer the cleaning time the better, and this is seen in at least one study [153]. Increased cleaning times (under 1 minute) with surfactants has also been shown to improve the amount of protein removed [154]. Interestingly, beyond some point (30 to 72 hours), it appears that the removed protein may begin to redeposit [145]. An interesting approach to predicting the efficiency of a cleaner [123] is presented in the experimental methods section.

2.2.2.9 Pathogen Relationship to Protein Deposits

The pathogenicity of a lens is not only related to its protein content alone, but to unicellular organism deposition which is affected by the protein deposits. Foreign organisms such as bacteria, fungi, yeast, and amoeba are all present under normal conditions, but can create severe problems if an imbalance in the eye allows them to propagate. The complete removal of one species, for example bacteria, may not be a good thing, as this may allow yeast, or fungi, to be favoured.

Acanthamoeba are responsible for Acanthamoeba keratitis infection. Simmons et al. [92] have studied whether or not this may be related to the amount of protein deposition on the four FDA lens groups. Interestingly, they find that the active form of amoeba

(trophozoite) adsorbs more to all worn (protein covered) lenses except Perfilcon (group IV material). Cyst adsorption, however, is increased, but on etafilcon (group IV) mostly. A correlation between extent of deposit and *Acanthamoeba* adsorption is unable to be drawn.

Similarly, bacterial infection and irritation may be promoted by adhesion to contact lenses. This has been examined in a number of studies [105, 152, 155-157]. Lysozyme is an antibacterial protein and its adsorption to group IV lenses may turn out to be beneficial. Thakur et al. [155], however, find that lysozyme greatly increases bacterial adhesion, but that it inhibits elastase activity, which may decrease the pathogenicity. Another study [157] finds that neither lysozyme nor lactoferrin inhibited growth of bacteria on soft contact lenses.

Increasing bacterial adsorption correlates with increasing albumin concentrations. Many bacteria, such as *P. Aeruginosa* adhere to the deposits themselves. Interestingly, it is noted that for Polymacon, the rate of bacterial adsorption decreases with increasing adsorbed albumin concentration, while the reverse is true for etafilcon. This may indicate differences in the conformation of the protein in the deposits [105]. This is all well and good for single bacterial species, but special polysaccharides and oligosaccharides on proteins carry out bacterial adhesion [101]. As we have seen, protein deposition is type dependent on both lens and protein, and we should thus expect some dependence in protein adhesion. This is, in fact, what has been observed [157].

It has been documented [156] that 15-day Acuvue™ lenses show more protein deposition than 1-day lenses. This is not very surprising even given their daily cleaning regime, having seen in the previous section that most cleaning solutions are ineffective. What is notable in this particular study is that bacterial adhesion was worse on 1-day lenses than 15-day. The indication is that the cleaning solutions are residing in or on the lenses and altering the tear film, which may in turn generate resistance in bacteria. Another possibility not mentioned, is that the cleaning has altered the protein in some way as to prevent bacterial adhesion.

Bendazac lysine, previously discussed for its ability to prevent protein denaturation, has also been found to help prevent bacterial adhesion. Pre-treating the lens with bendazac

lysine before wearing it, provides additional protection. This again indicates, that the state of protein is important, as previously mentioned [152].

2.3 Nanoparticle-Protein Interactions

Colloidal nanoparticles can be made quite easily today in a variety of shapes. These small particles present unique ways to study protein adsorption. At present, nanoparticles can be made with various surface-to-volume ratios, and out of a host of materials. Recently nanoparticles have been investigated as candidates for use in selective cell destruction, imaging, and transporting drugs through the body [158-162]. This inevitably requires coating the nanoparticles to prevent immune recognition. Understanding their behaviour on surfaces, that in many cases have similar length scales as the adsorbed protein, is an essential problem. There have been some concerns as to the unique properties these particles possess, and whether or not they may present potentially harmful effects to humans [163-165].

Fibrinogen adsorbed to silica particles appears to form aggregates [53], which would likely promote the formation of a clot if injected into the blood stream. As another example, the fibrillation of β 2m protein has been found to increase its rate dramatically in the presence of N-isopropylacrylamide/N-tert-butylacrylamide (NIPAM/BAM) copolymer, cerium oxide, gold, quantum dot, and carbon nanotube nanoparticles [166]. These particles had a range of sizes, materials, and different affinities for water. While fibril formation was increased, the fibrils were not elongated faster, and thus it seems it is a nucleation phenomenon. It is possible that the enhancement is simply due to the fact that proteins associated with the surface are packed denser than in the bulk, and thus a nucleation event is more likely, or that the surface actually aids in folding to a fibrillar state. Fibrillar states such as amyloids are implicated in a number of diseases such as “mad cow” and Alzheimer’s disease [166]. However, a point is raised that the parameters were not within the biologically relevant window (pH 2.5, 37°C), and increased fibrillar formation may not be directly associated with proteins on the particle surface. Instead the surface may act as a more conventional catalyst [167]. It has been seen in other studies that proteins which have

been reversibly associated with nanoparticles may still sustain conformational changes upon desorption [168-170].

There are a number of studies investigating fundamental properties of adsorption to colloidal particles. Modified polystyrene nanoparticle surfaces with different acidic and basic groups have been studied with 2-D electrophoresis and bicinchoninic acid (BCA) assay [171-173]. In general, after classifying the surfaces, and proteins according to acidity/basicity, basic groups on latex (giving positive charge at pH 7) adsorbed proteins with $pI < 5$ (and thus negative charge at pH 7) the most, and vice versa for acidic latex groups [171]. Changes in the charge groups on the sphere generally only affected the total amount of protein, and not the ratios of different types of protein [171, 172]. Fibrinogen exhibits particularly high affinity for adsorption [172]. Increases in adsorption of plasma proteins are also generally correlated with an increase in hydrophobicity [173]. However, the actual chemistry of groups used plays a strong role. For example, methylstyrene has relatively the same hydrophobicity as tert-butylstyrene, but adsorbs much more protein.

Lysozyme and bovine serum albumin (BSA) both decrease in α -helix content after adsorption to silica particles [170]. By varying the protein:particle ratio, different amounts of protein adsorb to the silica. The α -helix content decreases more at low levels of adsorbed protein, especially for lysozyme, which exhibits some charge dependence. BSA still shows strong conformational changes even at plateau adsorption, and does not recover all its helicity when desorbed from the silica surface [170]. Magnetic relaxation studies of methaemoproteins adsorbed to latex particles also indicate conformational alterations [174]. The haem pocket is more open than its bulk form in the case of myoglobin, and more closed than its bulk form in haemoglobins case.

Since protein will only congregate at an interface in relatively small numbers compared to bulk, calorimetric measurements are difficult to perform. Nanoparticles create a high surface to volume ratio, leading to a number of calorimetric studies exploiting this fact [175-177]. Larsericsdotter et al. [175] find that for low salt concentration, protein lysozyme, ribonuclease A (RNase) adsorbs strongly onto silica with up to 25% reduction in the denaturation enthalpy, and a decrease in the denaturation midpoint – T_m of up to 6°. This study does not use maximal adsorption values, as they want to decrease protein-

protein interactions on the surface. Decreased enthalpy can be attributed to the high electrostatic attraction to the surface. No change in enthalpy is seen for higher ion concentrations, indicating less denaturation upon adsorption. A decrease in T_m is still present though, and suggests that the stability of the protein is reduced. An increase in width upon adsorption is seen for all the proteins. The increase in width is attributed to a greater range of conformations of adsorbed proteins, and disappears at high ionic strength.

Addition of calcium ions, which are known to stabilize proteins, decreases the width of the denaturing transition due to less distribution in conformation. Haynes et al. [176] have seen similar effects on negatively charged polystyrene colloid using titration microcalorimetry. The maximum amount of protein adsorbed (plateau value) for lysozyme and α -lactalbumin occurs at the isoelectric point of the protein-sorbent complex. This is somewhat expected, as this state represents an almost perfect match of charge density between the sphere and protein. This is consistent with an electrostatically driven adsorption process. Carboxyl groups lie close to the surface and a significant degree of denaturation is inferred from differences in titration between free and adsorbed states [176, 177]. Dehydration force, denaturation, and charge regulation are identified as the main contributors to adsorption.

In another study by Haynes et al. [177], entropic effects, such as hydrophobic dehydration, are identified as favourable occurrences for adsorption. An increase in rotational entropy may also be an entropic contributor. Haynes notes [177] that electrostatic and other energetic effects are also important. On the other hand, hydrophobic dehydration allows bonding in otherwise electrostatically repulsive situations as shown in an extensive series of experiments with RNase and HPA on polystyrene particles [23, 41-46] (discussed in Contributions to Adsorption). These experiments exploit titration, electrophoresis, and radiolabelling measurements to show that re-protonation of charged groups, and ion coadsorption also play important roles in charge matching of the protein and sorbent surface [23, 41-47]. On hydrophilic hematite particles, hard proteins such as RNase will only adsorb if electrostatically favourable, while soft proteins can adsorb purely from entropic considerations, even under charge repulsion [48]. The “synergistic” contributions from the entropic and enthalpic terms are studied and discussed in a study of lysozyme and α -lactalbumin on polystyrene particles [49]. Other studies show that

competitive and sequential adsorption onto colloidal particles is determined mostly by electrostatics, so long as the proteins have moderately similar internal stability [50, 51]. However, the competition will always be won by proteins with very low internal stability. Irreversibility on hydrophobic substrates means the adsorbed layer is kinetically determined. It has also been shown, using silica particles, that of seven proteins studied, all had their internal stability decreased upon adsorption [52].

A bit different approach is presented by Kandori et al. [178], who use colloidal calcium hydroxyapatite rods to show that there is an adsorption dependence on mean particle length. This indicates that there is a dependence on the ratio of C (calcium ions, positive charge), or P (not charged) sites which changes with the changing crystal dimensions. BSA apparently binds more strongly to C sites, whereas lysozyme does not. Electrostatically this makes sense, as lysozyme is positively charged and would require hydrophobic interactions to make adsorption favourable.

HSA adsorbed onto TiO₂ (titanium dioxide) nanoparticles reaches a steady state of coverage within a few minutes, even under electrostatically unfavourable conditions [179]. This suggests conformational change plays an important role. By calculating the area each HSA molecule occupies in its adsorbed state vs. bulk, it is possible to deduce a number of details [179]. In particular, it appears that HSA adsorbs with a minimum at the isoelectric point (max. proteins/unit area), and that it is only weakly dependent on electrolyte concentration. At the isoelectric point, interprotein charge repulsion is minimized, allowing proteins to pack closely together. Independence on electrolyte concentration means HSA must act as a soft, deformable protein. Monitoring pH changes after addition of protein determines whether the act of adsorption elicits, or consumes H⁺ ions, allowing possible bonding mechanisms to be suggested. Below pH 6, ion-ion interactions, ligand reaction, and possibly hydrogen bonding involving carboxylate groups are responsible for adsorption, while between pH 6 and 7, a mix of amine and carboxylic groups are involved in ion-dipole, and ion-ion bonds. Above pH 7, hydrogen bonding due to amine groups is dominant. All of this information can be inferred with a UV spectrometer, centrifuge, and electrophoresis device, demonstrating the usefulness of a nanoparticle approach to general understanding of adsorption.

Bonding to nanoparticles, like other surfaces, can be reversible. HSA binds reversibly to TiO₂, however, exchange with bulk leaves the protein in an altered state [168]. Human carbonic anhydrase I reaches a dynamic equilibrium between adsorbed and bulk protein. This equilibrium, however, shifts to longer residence times on the silica as time progresses, indicating that the protein denatures in a progressive state, never quite regaining its structure previous to adsorption [169]. On flat hydrophobic substrates, proteins are reversible at low spreading, and irreversible after they have had a chance to spread more [30]. Thus, while often true, conformational change does not necessitate irreversible adsorption.

Metallic nanoparticles such as gold and silver exhibit a localized surface plasmon resonance (LSPR) that is size, shape, and material dependent (see section 3.1.3 Surface Plasmon Resonance). The shift in resonance depends strongly on the boundary conditions, in particular the surrounding indices of refraction, and can be used as a measure of the protein state [166] [180]. The LSPR of yeast iso-1-cytochrome c conjugated to gold nanoparticles, measured as a function of pH, could in principle determine conformational changes [180]. Unfortunately, in this case, the extremely large magnitude of the shift indicates it is simply particle aggregation occurring. During aggregation, coupling of modes between near, and joined particles leads to new and longer modes, which often continue to shift with time. This shifts the SPR peak to much longer wavelengths than are seen for thin coating (ie. protein conformational) changes, and broadens the peak. Cycling the pH has the effect of cycling the maximum absorbance (SPR peak). It returns to a slightly shifted position each time, however, suggesting that the protein undergoes irreversible denaturation, and that renaturation is prevented by protein aggregation, and thus, particle aggregation [180]. The results agree very well with planar SPR results, suggesting that this is a valuable method.

The aggregation in the above study [180] indicates one of the major problems, in that nanoparticles must be either charge stabilized, or sterically stabilized. Charge stabilized nanoparticles will aggregate if high levels of electrolytes are present, screening their mutual repulsion. Polymers can sterically stabilize nanoparticles, but proteins can undergo conformational changes, rendering their steric repulsion null. Hence, while a

valuable tool, some caution is needed in interpretation of results, as there are extra complicating factors that arise with nanoparticle studies.

The following study indicates the sometimes difficult nature of interpreting results. Shang et al. [181] perform a study which involves looking at pH effects on BSA conjugated to 15nm Au nanoparticles. Their method is unusual, in that they do not conjugate the protein to the Au before changing pH, or placing in buffer. Thus, even at pH 2.7, aggregation takes place, presumably due to charge screening, forcing them to concentrate on higher pH's. Comparing the plasmon resonances of their conjugates reveals the peak wavelength of those at pH 3.8 are much more red shifted than those at either pH 7.0, or pH 9.0. This could suggest that more BSA packed onto the Au, especially since it is overall positively charged at pH 3.8 (and closer to isoelectric than at pH 7, or 9), leading to favourable attraction with the negative Au.

An increasing blue shift in fluorescence may well demonstrate that a surface Trp residue is placed in a more hydrophobic environment, but does not necessitate a change in conformation as suggested by Shang et al. It can be accommodated by an orientation or packing change. If, on average, at positive charge, BSA orients itself away from the sphere and other BSA to face Trp, one would also expect in this electrostatic interpretation, for the strength order of the blue shift to be $\text{pH } 3.8 < \text{pH } 7 < \text{pH } 9$. A similar interpretation may be applied to their red edge excitation study.

Circular dichroism (CD) studies performed by Shang et al. [181] are analyzed by calculating helicity from a single point on the CD curve vs. Au particle concentration. This greatly increases error, and it is not clear that CD fitting done in other studies of protein on nanoparticles is valid, since basis proteins (and thus secondary structures) are generally taken in their native, unperturbed state, and not associated with curved, field enhancing surfaces. The amount of error as quoted by Shang et al. precludes any conclusions about the slope of the CD helicity vs. concentration graph. However, in terms of absolute helicity, the pH 3.8 spheres are the most denatured for **all** concentrations used in the study. Further FTIR studies by Shang et al. indicate at best a decrease in unordered structures at pH 3.8 and 9.0 as compared to 7.0. The net results of Shang et al.'s multi-technique study

is that it can be interpreted in two opposing ways: BSA is more stable on 15nm Au at lower pH (as suggested by Shang et al.), or BSA is more stable on 15nm Au at higher pH.

Not all nanoparticles are simple metallic crystallites, but can be more complex entities such as micelles, or liposomes. Understanding interaction with this type of biological particle is just as important as inorganic nanoparticles. Modified negatively charged liposomes adsorb more fibrinogen than neutral liposomes [182]. Adding PEG to the liposomes decreases adsorption to negatively charged liposomes, but does not affect adsorption to neutral ones. Neutral liposomes adsorb such small quantities of protein that any decrease probably can't be detected. For PEG quantities high enough to form a polymer brush on the liposome, adsorption on negative liposomes is reduced to that on neutral ones. This suggests that polymer brushes are indeed a good way to prevent adsorption, and that they can completely counteract the effects of charge, presumably through steric hindrances.

Apart from these studies, the availability of a range of sizes of nanoparticles also presents a chance to study the effect of physical constraints such as curvature. For example, adsorbed cytochrome c (cyt c) behaves differently on Au colloid of different sizes (2-4nm Au, and 16nm Au) [183]. Using a variety of techniques (UV-Vis spectroscopy, CD, FTIR), it was shown that conformational changes involve mainly conversion to β -sheets on 16nm Au, but involve some transition to α -helices on 2-4nm Au. Bonding is mainly electrostatic on 16nm Au, but hydrophobic bonding dominates on 2-4nm Au on which cyt c forms a more compact, more active, protein [183].

Another study used CD, NMR, and analytical centrifugation, and a range of silica nanoparticles (6, 9, and 15nm). 15nm silica exhibits up to 6 times the effect on the secondary structure of human carbonic anhydrase I (HCAI) that 6nm particles do. This is mostly a curvature effect, as only 20% could be attributed to differences in zeta potential between sphere sizes. Small spheres (high curvature) may require too extensive a perturbation in protein structure to favourably denature the protein. Curiously though, CD suggests that the tertiary structure is similar between all three sizes of spheres, but the secondary is different. This may indicate an error in interpretation, or insensitivity in the

near-UV region, since the secondary structure is normally a defining force of tertiary structure.

Lysozyme adsorbed to silica colloids from 4-100nm, shows size dependence as well [184]. Lysozyme retains its most unperturbed conformation on small spheres, including more activity, and loses some of this on larger spheres. Multilayer adsorption is inferred on 100nm spheres. More α -helix content is lost on larger spheres, and it is suggested that at least some of this may be due to a larger electrostatic potential.

Perhaps the most clear demonstration of the complicated nature of nanoparticle phenomena is a study that adsorbs BSA and fibrinogen adsorbed to a range of silica particles from 15-165nm [185]. Higher curvature (smaller particles) tends to denature fibrinogen more, while BSA denatures more on lower curvature particles under the same conditions [185]. This highlights the fact that curvature effects are not clear cut, and probably cannot be easily generalized. They will depend on the ratio of protein:particle size, and on the internal coherence, and thus nature of the protein adsorbing. Other effects are more general. For example in this same study both proteins denature more on hydrophobic particles, as compared to hydrophilic particles [185].

2.4 Multicomponent Systems

Most studies look at only one component of adsorption at a time, due to the difficulty in separating effects. For more complicated systems, in which several proteins are present, it is difficult to distinguish adsorbed amounts of each protein. One approach [186], allowing for measurement of a mixture of several proteins, corroborates data from Electron Spectroscopy Chemical Analysis (ESCA) and Time-of-Flight Secondary Ion Mass Spectrometry (ToF-SIMS) with radiolabeled protein. Radiolabeled protein allows one to distinguish each quantity of protein adsorbed in a mixture, by labeling one at a time. Using ESCA, the orientation of Fgn protein can be determined to be end-on [186]. ToF-SIMS can give information about the surface layer. It is stated [186] that the most biologically relevant layer is the surface layer, which may not be correct, as this layer is often the most native, and loosely bound. Because it is loosely bound, the top layer may be exchanged

with other proteins, allowing the bottom layer to interact. Unfortunately, for ToF-SIMS, the films must be dried. There are indications that drying alters the films, and may denature the proteins in some cases. To get around this, Xia et al. [187] soak protein films in a solution of the disaccharide Trehalose, which can prevent high temperature and drying denaturation in proteins. The Trehalose used in their study is able to protect the activity of the proteins, allowing them to still bind their antigens.

2.5 Adsorption Modeling

2.5.1 The Problem of Modeling Protein Adsorption

A discussion of protein at interfaces is not complete without mentioning some theoretical work in the field. Ultimately, one would like to possess the ability to predict the affinity and state of an arbitrary protein, during interaction with an arbitrary surface. This would allow the determination of biocompatibility without expensive and time consuming experimental and clinical trials. Unfortunately, at this time, our capability does not even extend so far as to predict the folding of a residue sequence into a protein. There are several reasons for our current failure, including the following:

- 1) Different residues in a protein may carry various charges, polar moments, as well as varying degrees of hydrophobicity. This variation between residues leads to heterogeneity in the protein molecule on length scales of a residue. If the surface is heterogeneous on similar length scales, which is almost always the case, then effects at this scale are generally non-negligible. Thus, for general solutions, detail on an atomic length scale, or at least a residue length scale must be included.
- 2) Many proteins are macromolecules, made up of hundreds, and possibly thousands, of residues. Each amino acid is made up of tens of atoms. This amounts to possibly tens of thousands of atoms, whose interactions with every

other atom must be accounted for. An atomistic treatment thus requires enormous computational power that is prohibitive.

- 3) Biologically relevant environments are aqueous, and must include water molecules. Water molecules account for the hydrophobic/hydrophilic residue effects, as well as solvation effects. These effects may extend several hydration layers deep, and require many water molecules to be present for each residue in a model. In addition, dissolved ions must be included to properly account for solvation and charge screening effects. This compounds the problem of computation, in principal requiring water-water, water-ion, water-residue, and ion-residue interactions to be calculated for all possible pairs.
- 4) Proteins are flexible, and capable of large conformational changes. This destroys any hope of reducing the degrees of freedom by calculating interactions internal to the protein only once. In turn, the large conformational changes may lead to irreversible adsorption. Irreversible effects are hard to account for thermodynamically, due to lack of dynamic equilibrium [188].
- 5) Many biologically relevant surfaces being studied today are complex polymeric materials themselves, possessing many of the same modeling difficulties as proteins.

The situation is far from hopeless, however, and many theoretical modeling attempts are being made, often in conjunction with complementary experiments. All approaches to date include varying degrees of approximation, but most still yield interesting, albeit mostly qualitative results.

2.5.2 Colloidal Treatments

One of the simplest ways to model protein is through colloidal approximations. These models ignore several of the complicating factors such as heterogeneity, hydrophobic effects, and complex flexibility. Colloidal methods treat the protein generally as if it were a rigid, solid object, possessing the main properties of the protein. Normally this means that net charge is the main quantity preserved. If conformational changes are included, it is

normally through the foreknowledge of what the final, and any intermediate states will be, and is not predicted based on the model itself. Since the protein contains no heterogeneity, the surface is treated as homogenous and uniform.

To model ion chromatography, one model [189] considers both the protein and surface as flat planar surfaces of homogenous charge densities, which interact purely through electrostatic forces. As the planes come closer together, the influence of the charge on the surface plane causes a change in the charge on the protein plane. This mimics the effect of the phenomenon known as charge regulation in a protein, in which its charge distribution is rearranged in the presence of an electric field. Calculations with this model show that this additional factor should be considered, since it generates a higher affinity for the surface than would be seen with purely static charge. This helps to explain protein retention in ion-exchange chromatography. The model is extremely rudimentary, but highlights some important features of the underlying physics that should be considered in protein adsorption.

The most common colloidal approaches are variations of the Random Sequential Adsorption, or RSA model. An extensive review of colloidal adsorption including the RSA, and several other models is presented by Adamczyk et al. [190]. The simplest form of RSA model works as follows:

- Spherical particles are placed at random positions on a surface at a constant rate.
- Particles that land on top of another particle's projected area are rejected.
- Otherwise, the particle is irreversibly bound, with no lateral diffusion.

The "jamming" coverage is defined as the point at which no more particles can be placed, without covering an already adsorbed particle. The model is good for low shear rates, and low to moderate surface coverages. The beauty of this model is its simplicity, and the fact that it can easily be extended, or combined with other models to enhance it. Solvent effects are generally not taken into account in colloidal models, since there are no residues with which hydrogen bonding patterns can be promoted or disrupted. Electrolyte effects are normally handled with a Debye parameter. RSA does not account for reversible adsorption of proteins with weaker affinities [188].

An easy extension to the RSA model is to have the adsorption probability governed by the Boltzmann distribution, as opposed to a 100% adsorption probability to unoccupied surface. This allows the inclusion of an interaction energy with the local environment [190]. Another extension made by Adamczyk et al. [191] allows spheroidal particles of non-unity axis ratio (not perfect spheres). Additionally, random surface orientations are allowed, with the blocking area being the projected area of the spheroid onto the surface. It is suggested [191] that most globular proteins form prolate spheres, which adsorb irreversibly. To simplify matters, Adamczyk models both non-interacting and interacting hard spheroids according to the Effective Hard Particle Model (EHP). The EHP model replaces interacting spheres of a given size by hard, non-interacting spheres of a larger size, corresponding to the effective radius of interaction. They find that electrostatic interactions between the spheroids tend to decrease the jamming value, but increase the short-range order, orienting more spheroids perpendicular to the surface. In another paper using spheroids, Adamczyk et al. [192] find again that electrostatic interactions decrease adsorption.

Since conformational changes often play such a big role in adsorption, it is desirable to have a model that includes this. Conformational changes tend to increase the affinity with which a protein is bound. Van Tassel et al. [193] propose a model, similar to the RSA model. Discs are randomly placed onto a surface at a given rate. If they overlap they are rejected, otherwise the disc sticks. Particles on the surface have the additional attribute that they will attempt to spread at a given rate, mimicking a conformational change. If the spreading causes overlap, the particle does not change. Van Tassel et al. [193] are able to solve this system by relating it to an equivalent RSA model. The model contains one type of disc with an effective diameter accounting for both spread, and unspread discs. They are able to correlate this data with fibronectin adsorption to silica-titania quite nicely. Several parameters are again needed to fit the data, some of which may be difficult to obtain, and depend on the given protein, surface and conditions. A further improvement of this model is made by Brusatori et al. [194], which allows the discs to also desorb. Because RSA analogies will not permit this, they attempt to apply Scaled Particle Theory to the problem (SPT). This amounts to calculating the thermodynamic effects from the work required to create a region on the surface without any particles. It provides only

an approximate solution. The approach assumes thermodynamic equilibrium on the surface between adsorbates, which presumes quick lateral diffusion relative to adsorption and spreading rates.

Adamczyk's extensions still do not contain true particle surface interactions. The particles continue to be placed directly onto the surface with some probability, and while they can interact between adsorbates, they cannot diffuse on the surface. Additionally, there are still no interactions between free and adsorbed protein. For these reasons, Oberholzer et al. [195] use Brownian dynamics to drive the adsorption, considering both electrostatic, and van der Waals interactions. Desorption is allowed if the thermal force is great enough. The surface is homogeneous and uniformly charged. To mimic an infinite reservoir of protein at constant chemical potential, Monte Carlo method is used on the grand canonical ensemble. The Monte Carlo method is run periodically as particles are removed from the bulk solution onto the surface. Two cases are considered, one in which there is unrestricted diffusion on the surface, and another where diffusion is not allowed. Applying this model, Oberholzer et al. [195] find that for lysozyme, in the high salt region, the adsorbed amount depends on the protein concentration, while in the low salt region it is independent of protein concentration. At low salt concentrations, protein-protein interactions limit adsorption, and thus even at low protein concentrations, there is enough protein to achieve equilibrium coverage. As salt is added in the low salt regime, total adsorption increases. In contrast, in the high salt regime, an increasing electrolyte composition decreases coverage. The reason for this is interplay between the decreases in protein-protein repulsion in the low salt regime, and a decrease in protein-surface attraction in the high salt regime. The former effect will increase adsorption, and the latter decrease it. They suggest that a specific salt concentration for maximum adsorption exists. That this is not seen in experiment is recognized as a possible consequence of idealizations within the model.

Oberholzer and Lenhoff [188] present a colloidal model, which adds interactions between particles that have adsorbed. Surface concentrations in this model are assumed to be directly proportional to the concentration of the bulk solution, which is rarely true for irreversibly adsorbable proteins [191]. Their attempt is to model reversible conditions, and so this assumption may be more easily made. Electrostatic and van der Waals interactions

are considered in the development of the isothermic adsorption, for adsorbate-adsorbate, and adsorbate-surface, but not protein-protein. They [188] assume that adsorbate-adsorbate interactions can be decoupled from protein-surface interactions, which is not generally true. Many proteins “spread” to increase surface contact, which results in a greater affinity, and this cannot occur if neighbouring molecules are too close. In addition, several parameters are introduced, being the equilibrium constant, a constant related to the strength of adsorbate-adsorbate interactions and the Debye parameter. At some point, if there are too many parameters, as in some models, one must practically perform the experiment to be able to predict the outcome.

2.5.3 Atomistic Treatments

Atomic level computer simulations would, of course, be the ideal for modeling, since the interaction potentials would be the only approximations, if any. Today, however, atomic level treatments are not computationally feasible. As a result, proteins are often still treated as rigid, and energies of attraction are calculated as the protein molecule is rotated sequentially through various angles and heights. This is better than rigid colloidal methods, but still does not represent the true situation. Water is often given a continuum treatment, as are electrolytes, in order to reduce the number of interactions. Simulations that do allow flexibility in the protein are extremely hard to model, and consequently, they typically simulate nanosecond timescales.

Hen egg white lysozyme (HEWL) modeled atomistically, but as a rigid object yielded some interesting results [196]. Electrostatic and van der Waals interactions are used in a dielectric (screened) medium to account for water, and a 2D lattice of charges as the substrate. Ravichandran et al. start the protein in a random orientation above the surface, and using Brownian dynamics, track its adsorption. Lysozyme, being a positively charged molecule, would not be expected to adsorb to a positively charged homogeneous surface if just net charge is considered. However, they find that it does indeed adsorb, and that increasing ionic strength increases the amount of successful trajectories due to charge screening. They propose that the heterogeneity of charge distribution on proteins must play

an important role in adsorption, as opposed to just net charge, and even a single residue may be responsible for adsorption.

In another rigid atomistic model, Noinville et al. [197] calculate HEWL, and alpha-lactalbumin(ALC) interactions with poly(vinylimidazole) for multiple orientations, and for multiple heights above the surface. Electrostatic, and van der Waals effects are included, and solvent effects are included as a varying dielectric permittivity (but no dipole interactions). As in the previous study [196], they find dependence on the heterogeneous distribution of charge. This system models ion-exchange chromatography, and their results agree with predictions.

A slightly more realistic model is presented by Asthagiri et al. [198]. The protein is treated almost atomistically, by accurately modeling almost its exact shape, and location of charges. They do not consider van der Waals interactions however, and consider the protein rigid. Their surfaces are modeled in three ways. First, they use a homogenous distribution of charge opposite to that of the protein. Second, they use a heterogeneous mixture of positive and negative charges, which yield a net positive charge. Third, they include 3D topography of the surface in addition to charge. They find that the homogeneous model is the least accurate and the 3D topography model is the most accurate. A heterogeneous model is best, because a protein can align its heterogeneous charge distribution in a favourable way with the surface. Residues, which may have been able to interact favourably with the substrate, are often sterically hindered from approaching the substrate. In the 3D topography, some steric hindrances can be overcome through orientation. It is suggested, that one reason colloidal and other simple methods are successful, is that they contain fitting parameters, which can be adjusted, and that they generally consider very straightforward phenomena. Asthagiri [198] suggests that the test of a model should be whether or not it describes the more exotic occurrences, one of which is the adsorption of a protein of net charge that matches the surface.

In order to allow conformational changes, one method used by Raffaini et al. [199] to reduce calculations, models different domains separately. Albumin deposition onto graphite presents such an enormous task, Raffaini et al. opt to model two of the subdomains in albumin, with the assumption that all charge groups are neutral. They

minimize the structure, first with either an effective dielectric medium, or explicit water, above the substrate. Molecular dynamic simulations are then performed either with an effective dielectric to simulate water, or for much shorter times with explicit water. The longer runs in dielectric lasted for a maximum of 1ns. Runs which had occurred in dielectric were then re-run in explicit water to see if they would change further; however, this was not the case. The short runs in explicit water show little conformation change, while the runs in dielectric show large changes. Interestingly, the “final” conformations of the domains are monolayers on the surface, which create high affinity for the surface. They propose two stages of adsorption, one during which the molecule approaches the surface, losing little secondary structure, and a second stage during which the molecule changes orientation, and completely unfolds. This is the same spreading effect discussed previously in colloidal type models, and may not occur fully if other albumin molecules are present. A second layer depositing onto the first should not show as much rearrangement, since the first layer makes the surface more hydrophilic.

2.5.4 Intermediate, Lattice, and Miscellaneous Approaches

A number of approaches lie somewhere in between the full rigor of an atomistic treatment, and the simplicity of a colloidal treatment. In principle, these may offer the best, most constructive method of modeling adsorption, since they include some heterogeneity, but are still tractable numerically. Generally, either whole domains, or residues are modeled as being a single entity (often spheres), possessing the main properties of interaction of that domain or residue. This is not an implausible approximation since residues are generally not highly mobile away from the surface. Conformational changes are generally ignored, limiting the applications of this approach.

An approximate domain model is presented by Sheng et al. [200], in which IgG is replaced with 12 spheres representing its domains. In this model, net charge has a stronger effect, since many residues are lumped into each sphere. However, because the overall shape will not be spherical, orientation effects can still occur. Orientation is dominated in the electrostatic regime by dipole interactions, which can cause the molecule to adsorb

vertically. In the van der Waals regime, however, the molecule prefers to lie flat, so as to bring all of its domains into contact with the surface.

Since the area of protein folding is related to adsorption modeling, it is not surprising that many of the methods used for adsorption are adopted from the folding field. One method that shows promise is the residue or united-residue method [201]. In this method, interactions between all residues and surfaces are calculated atomistically. These values are then fed into a model of a protein, which can now consider just several hundred residues, rather than several thousand atoms. This is very desirable because individual residues are small enough that exact solvent and other effects can be included. With this in mind, many studies are devoted to calculating interaction energies for various residues, most commonly with self-assembled monolayer surfaces (SAM's) [201-204]. Unfortunately, some of these models still only consider one hydration shell around a residue [202]. Residue-residue interactions could also be calculated. There is still an underlying assumption that residues are static entities, which are not affected chemically by the presence of other residues. However, this assumption is probably not a huge approximation, and the advantages of this approach outweigh its disadvantages. At the very least, knowledge of how the various forces drive residue adsorption, is gained. For example, it is confirmed computationally that hydrophobic residues bond favourably to hydrophobic surfaces, mostly through entropic effects. Adsorption to neutral hydrophilic surfaces is unfavourable and energetically driven, while adsorption to charged hydrophilic surfaces is energetically driven and either slightly favourable, or unfavourable [201, 203]. Zhou et al. [204] apply a residue model, in which each residue is replaced with a sphere having the equivalent properties at the alpha-carbon. They model IgG1 and IgG2a, finding that there is orientational preference at high charge density/low ionic strength due to electrostatic interactions. For low charge density/high ionic strength, there is less preference for orientation. IgG2a exhibits less orientation due to a smaller dipole moment. This agrees with the 12 sphere model of Sheng [200], and presents a much more accurate approach.

Most simplification is directed at the number of objects present (residues, atoms, water molecules), and mean properties of these. An alternate method is to discretize space, so that we reduce the positional freedom. This approach is used in lattice models, of which

the HP (hydrophilic-polar) model is the most famous for folding problems. In this model, residues are replaced by a chain of connected hydrophilic or hydrophobic units (or any two generally opposing properties A and B). Continuum space is replaced by a three dimensional lattice of points that are either occupied or unoccupied. There can be given three energy-of-contact values (although usually just two), which correspond to H-H, P-P, or H-P occupying neighbouring lattice sites. Castells et al. [205] use A-B types, with an energy bonus for A-A or B-B sites, over A-B sites. Two surfaces are investigated. One in which both A and B interact equally with the surface, and another in which A interacts more strongly than B. The “protein” is 27 units long, and is chosen with contact energies that result in a unique “native” conformation of lowest energy. Minimization of the energy of native, and adsorbed states are carried out by Monte Carlo method. They find the chain unfolds into a low-internal-contact/100%-surface-contact chain, and then refolds into a new conformation. On the A-affinity surface, the refolding brings many of the units off the surface, and is a secondary maximum, showing a possible activation process. As temperature is raised, the equal affinity case decreases surface contact, and the A-affinity case increases surface contact.

2.5.5 General Mean Field Approaches

Once a protein has been modeled atomistically, or semi-atomistically, some parameters - such as its net interaction potential as a function of height and orientation - will be known. At this point it is desirable to be able to predict the behaviour of a large ensemble of proteins (either of the same, or different types). Unfortunately, purely thermodynamic approaches are limited in their applications, as the entire adsorption system is rarely in equilibrium. However, if some part of it, such as the protein reservoir, is in approximate equilibrium, then thermodynamics may be used for this portion of the model.

A generalized thermodynamic molecular approach is presented by Fang et al. [206]. The sudden appearance of a surface in a protein solution induces a non-uniform chemical potential. To obtain the kinetics of the system, the free energy is used to calculate the new chemical potential function, which in turn is used to drive a diffusion equation. Fang’s approach is very general, allowing as many configurational changes as desired. They are

able to derive a general expression for the equilibrium total deposit in terms of the potential of mean force, which is a function of the internal energy of conformation, protein-surface interactions, and the intermolecular repulsion and attraction. Lateral diffusion, and dynamics are assumed to be instantaneous because this is a mean field approach. Using values from atomistic calculations, they investigate two simplified systems. In one, there is a binary mixture of two spherical proteins which have a single conformation. In the second, there is a single type of protein, but it can undergo a change from sphere to “disc” on adsorption. For this model, however, many parameters are required, (eg. rate of conformation change, surface-protein and intermolecular interactions etc). These parameters must either be measured experimentally, or by numeric simulations. In addition, solvent rearrangement is assumed instantaneous, and the diffusion constant of the protein is the same for all conformations. Both systems yield informative results. The binary mixture exhibits the experimentally observed Vroman effect under certain conditions, in which smaller proteins adsorb first, to be replaced later by larger ones.

One method proposed to prevent deposition of protein is to graft a polymer to a substrate. The idea is that the polymer will provide steric hindrances to prevent protein adsorption. Polymers can prevent adsorption through two effects: an entropic penalty as the polymer is confined to a smaller volume, and another possible penalty due to the exchange of polymer-water hydrogen bonds with less favourable polymer-protein hydrogen bonds. This effect has been modeled with some success by Satulovsky et al. [207]. They include two effects, the attraction of the protein to a surface, and its repulsion by grafted polymers. The free energy is calculated with all intramolecular and protein-surface interactions treated “exactly”, while intermolecular contributions are treated as a mean-field. By “exactly”, they mean that they have taken their protein-surface interaction potential (as a function of z only) from atomistic calculations for lysozyme approaching a hydrophobic substrate. The assumption is made that the polymers can rearrange much faster than the protein. They find two opposing effects. In a kinetically dominated regime, the most protein-resistant polymer is one that is long, densely packed, and not attracted to the substrate, causing large conformational penalties for protein adsorption. This is desirable for short-term prevention. For long term prevention in a thermodynamic regime, highly packed polymers with strong surface attractions are desired.

Experimental Techniques

3.1 Measurement Techniques

3.1.1 Atomic Force Microscopy

3.1.1.1 General Background

Atomic Force Microscopy (AFM) is a subtype of Scanning Probe Microscopy (SPM) that tracks surface topography using a sharp tip that interacts with surface forces. The main forces exerted on the AFM tip are the van der Waals forces, Pauli repulsion and electrostatic forces. Normally electrostatic charges on the sample are minimized, and the tip is kept in the attractive regime, making van der Waals the main forces of interest. A picture of the Explorer AFM head is given in Figure 9 and a schematic diagram of a generic AFM is given in Figure 10. Typically a laser diode is focused onto the back of a cantilever coated with a reflective material. The laser then reflects back onto a four quadrant photodiode.

Piezoelectric crystals (either x, and y crystals or a tube scanner) are then used to move either the tip, or the surface, relative to each other.

The AFM can be operated in two modes: constant height mode in which the deflection of the tip is measured as the tip is scanned without adjusting height, or as is more commonly the case, constant deflection mode in which the tip height is adjusted to maintain a constant surface force. Maintaining a constant surface force does not maintain a perfectly constant height



Figure 9. Atomic Force Microscope on translation stage with contact lens on glass sphere.

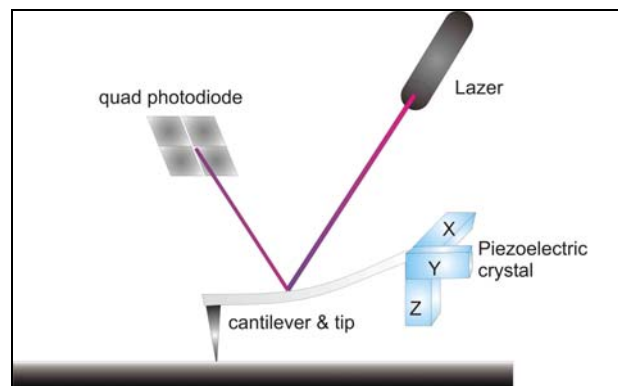


Figure 10. Schematic of A.F.M. operation.

above a sample, as different materials will present differing surface forces. However, for most purposes, it is acceptable to ignore these differences and take adjustments in the tip height to be representative of changes in the height of the surface. Another method of maintaining a constant height above the surface is by oscillating the tip at resonant frequency. The resonant frequency, being subject to varying surface force gradients, will change according to the height above the sample. A PID (proportional, integral, differential) circuit is typically used, which adjusts the piezo voltage according to the error signal from the resonant frequency at some small distance above the sample. This mode is often desirable since it avoids contact, and thus degradation of the surface in question. In practice, however, a purely non-contacting mode is often not achieved, and the tip will intermittently come into contact, or “tap” the sample. Hence this method is often referred to as tapping mode.

By rastering the tip across the sample and recording the piezo extension in a grid of points, a topographic representation of the surface is generated. The resolution of this image can be far below the wavelength of light, with sub-nanometer precision possible in the z direction. The lateral resolution is limited by the physical size of the tip, of which typical dimensions are a length of $10\mu\text{m}$, and tip radius of $<20\text{nm}$. The resulting image is thus a convolution of both the true topographical surface, and the shape of the tip as depicted in Figure 11. Deconvolution to regenerate the true surface image is possible only in a few circumstances. Simply keeping the effect of tip shape in mind during interpretation is usually sufficient for most applications.

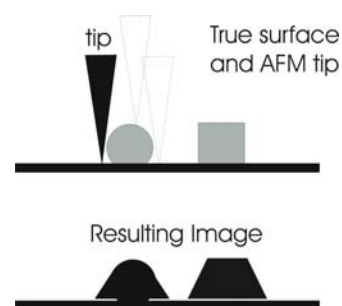


Figure 11. Example of convolution of tip and structure.

3.1.1.2 Measuring Contact Lenses with AFM

Any sample to be measured should be approximately level, so that the tip does not need to adjust more than the maximum piezo extension on the scale of the image. Often samples are very small, or flattened to accommodate imaging. In the case of contact lenses, however, it was felt that too much handling of the soft lens material could damage its surface. To hold the lens, a glass sphere close to the radius of the cornea was attached to a substrate and placed on the AFM translation stage. The contact lens could then be placed directly onto the lens holder (Figure 12), rinsed and allowed to dry.



Figure 12. Contact lens on glass sphere.

3.1.2 Extinction Spectroscopy

Papers I through III were carried out using visible light extinction measurements. These are performed as shown in Figure 13. White unpolarized light is collimated through the sample cell, and refocused into a spectrometer. To measure extinction, our beam should be suitably narrow, however, for small particles, with less forward scattering, it is not as critical. For our experiments, extinction is plotted vs. wavelength, and the value, and wavelength of the peak extinction is extracted. The method through which this is accomplished is described in more detail in papers I-III. Q_{ext} of a single particle can be calculated from the overall extinction of a solution of spheres in a cuvette.

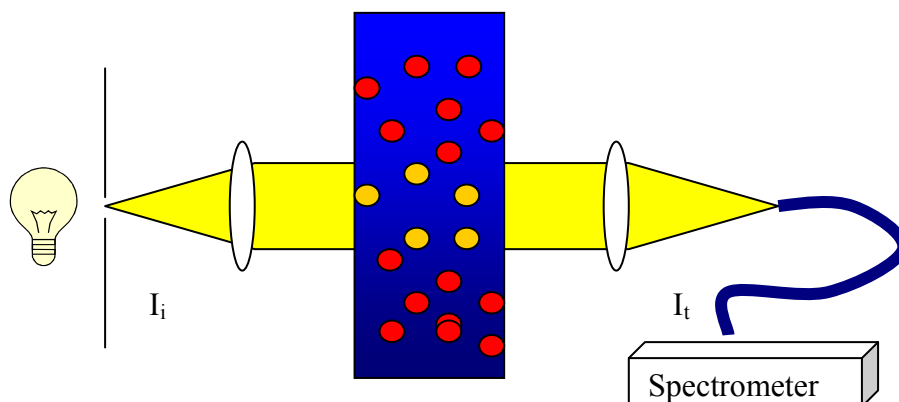


Figure 13. Schematic of extinction experiment. I_i and I_t are incident and transmitted intensities.

Since Beer-Lambert law is obeyed

$I_t = I_i e^{-\alpha_{ext} h}$ where I_t and I_i are transmitted and incident light,
 α_{ext} is the attenuation coefficient, and h is the thickness of sample

$$\alpha_{ext} = -\frac{\log\left(\frac{I_t}{I_i}\right)}{h}$$

If there is a concentration C of particles contributing to the extinction

$$C_{ext} = \frac{\alpha_{ext}}{C}$$

The definition of extinction efficiency for a sphere of radius a is:

$$Q_{ext} = \frac{C_{ext}}{\pi a^2}$$

So the result is:

$$Q_{ext} = -\frac{\log\left(\frac{I_t}{I_i}\right) \alpha_{ext}}{Ch\pi a^2}$$

The following section will develop the theoretical value of Q_{ext} for coated and uncoated spheres, following the method of Bohren and Huffman.

3.1.3 Surface Plasmon Resonance

The fairly extensive derivations of Mie theory results that are used in this section and in bound papers I-III are included in Appendix A: Mie Theory. The derivations follow that of Bohren and Huffman [208] of a homogenous sphere made of a linear isotropic material and are exact. Definitions of variables are found in the appendix. If we assume that the sphere is much smaller than the wavelength, in otherwords if $|m|x \ll 1$, we may gain some more intuitive understanding. Let

$x=ka=2\pi Na/\lambda$, and $m=k_i/k=N_i/N$, where k and N are the wavevector and refractive index of the respective region denoted by the subscript.

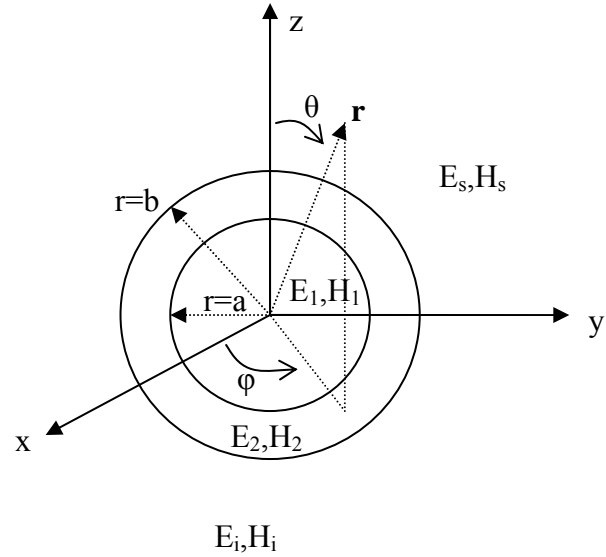


Figure 14. Sphere of radius a , with coating thickness $(b-a)$. The subscript I denotes incident fields, while the subscripts 1, 2, and s denote fields internal to the sphere, fields in the coating, and the scattered field respectively.

Expanding the extinction, scattering, and absorption efficiencies to order x^4 :

$$Q_{ext} \approx 4x \operatorname{Im} \left\{ \left(\frac{m^2 - 1}{m^2 + 2} \right) \left[1 + \frac{x^2}{15} \left(\frac{m^2 - 1}{m^2 + 2} \right) \left(\frac{m^4 + 27m^2 + 38}{2m^2 + 3} \right) \right] \right\} + \frac{8}{3} x^4 \operatorname{Re} \left\{ \left(\frac{m^2 - 1}{m^2 + 2} \right)^2 \right\}$$

$$Q_{sca} \approx \frac{8}{3} x^4 \left| \frac{m^2 - 1}{m^2 + 2} \right|^2$$

$$Q_{abs} = Q_{ext} - Q_{sca} \approx 4x \operatorname{Im} \left\{ \frac{m^2 - 1}{m^2 + 2} \right\} \left[1 - \frac{4x^3}{3} \operatorname{Im} \left\{ \left(\frac{m^2 - 1}{m^2 + 2} \right)^2 \right\} \right] \quad \text{for } |m|x \ll 1$$

Spheres much smaller than the wavelength will satisfy:

$$Q_{abs} \approx 4x \operatorname{Im} \left\{ \frac{m^2 - 1}{m^2 + 2} \right\}$$

Which gives the fact that

$$Q_{abs} \propto \frac{1}{\lambda}$$

$$Q_{sca} \propto \frac{1}{\lambda^4}$$

These facts explain a number of phenomena of gold particles. Under transmitted light, small gold colloids in a bottle appear red due to strong absorption of small wavelengths. Viewing backscattered light, large (approaching 100nm) gold colloids will appear gold in color due to the dominance of scattering of yellow gold wavelengths. However, in viewing small colloids (<50nm) the backscattered light will tend to still look extremely reddish. This is due to the fact that the absorbance only goes down as the 1st power of the radius for a given wavelength, while scattering decreases as the 4th power of the radius. Absorbance is then dominant by several orders of magnitude for very small spheres. Since we usually have some stray light due to reflections absorbance will strongly dominate with a red color for gold, mixed with a small amount of greenish backscattered light. However, for large gold colloid (for which the relations no longer hold proper) scattering dominates with a yellow-gold color.

3.1.3.1 Dielectric Constant Models

Relationships between the various optical constants are given by the following set of equations. n and k are the real and imaginary parts of the index of refraction, and ϵ' and ϵ'' are the real and imaginary parts of the dielectric function.

$$\epsilon' = \frac{\epsilon'}{\epsilon_0} = n^2 - k^2$$

$$\epsilon'' = \frac{\epsilon''}{\epsilon_0} = 2nk$$

Or conversely:

$$n = \sqrt{\frac{\sqrt{\epsilon'^2 + \epsilon''^2} + \epsilon'}{2}}$$

$$k = \sqrt{\frac{\sqrt{\epsilon'^2 + \epsilon''^2} - \epsilon'}{2}}$$

Approximating the charge oscillations as simple harmonic oscillations we have the Lorentz model for bound charges:

$$\begin{aligned}\varepsilon &= 1 + \chi = 1 + \sum_j \frac{\omega_{pj}^2}{\omega_j^2 - \omega^2 - i\gamma_j\omega} \\ \varepsilon' &= 1 + \chi' = 1 + \sum_j \frac{\omega_{pj}^2(\omega_j^2 - \omega^2)}{(\omega_j^2 - \omega^2)^2 + \gamma_j^2\omega^2} \quad \text{where } \omega_{pj} = \frac{N_{cj}e_j^2}{m_j\varepsilon_0} \text{ and } \gamma_j \text{ is the damping constant} \\ \varepsilon'' &= \chi'' = \sum_j \frac{\omega_{pj}^2\gamma_j\omega}{(\omega_j^2 - \omega^2)^2 + \gamma_j^2\omega^2}\end{aligned}$$

Where N_{cj} , e_j and m_j the density, magnitude and mass of the j th type of charge oscillator. ω_{pj} is the plasmon resonance of the j th oscillator type. A plasmon resonance is the collectively quantized oscillations of charge in the system. This generally involves quantized lattice charge, or free electron charge depending on the material. For a metal containing free electrons, $\omega_j = \omega_e = 0$ since there is no effective “physical” restorative force as in ion oscillators. The restorative force comes from a displacement of the overall free electrons to one side of the fixed charges, which leads to a dipole moment, and thus a restoring force:

$$\begin{aligned}\varepsilon &= 1 + \chi = 1 - \frac{\omega_p^2}{\omega^2 + i\gamma\omega} \\ \varepsilon' &= 1 + \chi' = 1 - \frac{\omega_p^2}{\omega^2 + \gamma^2} \\ \varepsilon'' &= \chi'' = \frac{\omega_p^2\gamma}{\omega(\omega^2 + \gamma^2)}\end{aligned}$$

This is the Drude model for free electron metals. ω_p in this case refers to the plasmon resonance of free electrons. In this case it arises from the free electrons being perturbed by the incident field. This perturbation sets up a dipole opposing the motion, and acts as a loose restoring force. The damping constant is due to electron collisions, and scattering by phonons. The plasmon resonance is a longitudinal mode in which ε goes to zero in the absence of damping.

The combined result is then:

$$\varepsilon = 1 + \chi = 1 - \frac{\omega_{pe}^2}{\omega^2 + i\gamma_e\omega} + \sum_j \frac{\omega_{pj}^2}{\omega_j^2 - \omega^2 - i\gamma_j\omega}$$

Where the first term is due to free electrons, and the second term includes lattice vibrations. Since the superposition principle holds we have obviously separated our dielectric function into $\varepsilon = \varepsilon_{free} + \varepsilon_{bound}$. This is useful, because for an experimentally measured dielectric function we find that we need to correct for a number of effects in the free electron term (for example for finite size effects). We can easily subtract the free electron part with standard parameters from the experimental data, and add it back in with the corrected constants. The dielectric functions for bulk gold are given in Figure 15.

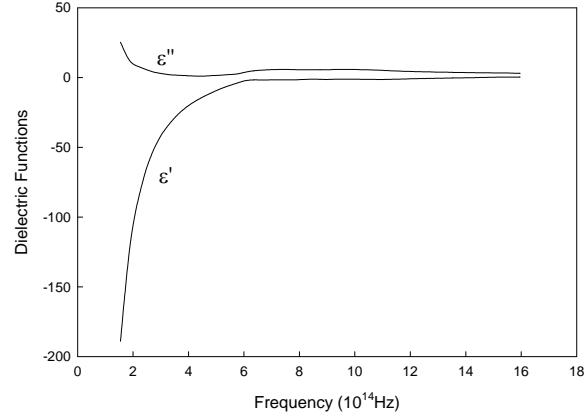


Figure 15. Dielectric functions for bulk gold as a function of frequency. [209]

3.1.3.2 Localized Surface Plasmon Resonance

In Appendix A we solve for a_n and b_n . These are the coefficients of the various electromagnetic modes. If the denominator of a_n or b_n go to zero the corresponding modes will become infinite. That is they will enter a plasmon resonance. In the case of a real system, the coefficient will not go to zero, but will approach it with varying rigor.

For the uncoated sphere this means:

for a_n

$$\mu m^2 [x h_n^{(1)}(x)]' j_n(mx) - \mu_1 h_n^{(1)}(x) [m x j_n(mx)]' = 0$$

for b_n

$$\mu_1 [x h_n^{(1)}(x)]' j_n(mx) - \mu h_n^{(1)}(x) [m x j_n(mx)]' = 0$$

Where μ , j , and $h^{(1)}$ are the magnetic permeability, Bessel function of the first kind, and hankel function of the first kind respectively, corresponding to the region denoted by the subscript.

So that the zero condition is:

For c_n, b_n :

$$\frac{[xh_n^{(1)}(x)]'}{h_n^{(1)}(x)} = \frac{\mu[mxj_n(mx)]'}{\mu_1 j_n(mx)}$$

For a_n, d_n :

$$\frac{[xh_n^{(1)}(x)]'}{h_n^{(1)}(x)} = \frac{\mu_1[mxj_n(mx)]'}{\mu m^2 j_n(mx)}$$

For the coated sphere this means:

for a_n

$$\xi_n(y)[\psi_n'(m_2 y) - A_n \chi_n'(m_2 y)] - m_2 \xi_n'(y)[\psi_n(m_2 y) - A_n \chi_n(m_2 y)] = 0$$

for b_n

$$m_2 \xi_n(y)[\psi_n'(m_2 y) - B_n \chi_n'(m_2 y)] - \xi_n'(y)[\psi_n(m_2 y) - B_n \chi_n(m_2 y)] = 0$$

where

$$A_n = \frac{m_2 \psi_n(m_2 x) \psi_n'(m_1 x) - m_1 \psi_n'(m_2 x) \psi_n(m_1 x)}{m_2 \chi_n(m_2 x) \psi_n'(m_1 x) - m_1 \chi_n'(m_2 x) \psi_n(m_1 x)}$$

$$B_n = \frac{m_2 \psi_n(m_1 x) \psi_n'(m_2 x) - m_1 \psi_n'(m_1 x) \psi_n(m_2 x)}{m_2 \chi_n'(m_2 x) \psi_n(m_1 x) - m_1 \chi_n(m_2 x) \psi_n'(m_1 x)}$$

$$\xi_n(\rho) = \rho h_n^{(1)}(\rho)$$

and $\psi_n(\rho) = \rho j_n(\rho)$

$$\chi_n = i\xi_n - i\psi_n$$

Consider the uncoated sphere. Inside the sphere we have j_n , which to first order is proportional to ρ^n , so $N_{e1n-r} \propto \rho^{n-1}$ where $\rho=kr$. This means that in general, to the most dominant term in N , the radial component will be constant for $n=1$ (electrostatic approximation), and grow increasingly quickly towards the surface ($r=a$). Hence, for the infinite sum, the mode will predominantly localize at the surface of the particle, and is thus termed a localized surface plasmon resonance.

To gain more physical intuition it is useful to examine the limit of an infinitesimal sphere existing in a medium that is free space.

$$Q_{sca} \approx \frac{8}{3} x^4 \left| \frac{m^2 - 1}{m^2 + 2} \right|^2$$

$$Q_{abs} \approx 4x \operatorname{Im} \left\{ \frac{m^2 - 1}{m^2 + 2} \right\}$$

These both blow up for the condition:

$$m^2 + 2 = 0$$

$$\rightarrow m^2 = \left(\frac{\epsilon_1}{\epsilon_m} \right)^2 = -2$$

for free space:

$$\left(\frac{N_1}{N_0} \right)^2 = \frac{n^2 + k^2 + i2nk}{1} = -2$$

$$n^2 + k^2 = -2 \text{ and } 2nk = -2$$

$$\rightarrow n = 0 \text{ and } k = \sqrt{2},$$

$$\text{or more generally } \epsilon' = -2\epsilon_m, \epsilon'' = 0$$

Where ϵ_m denotes the dielectric function of the medium.

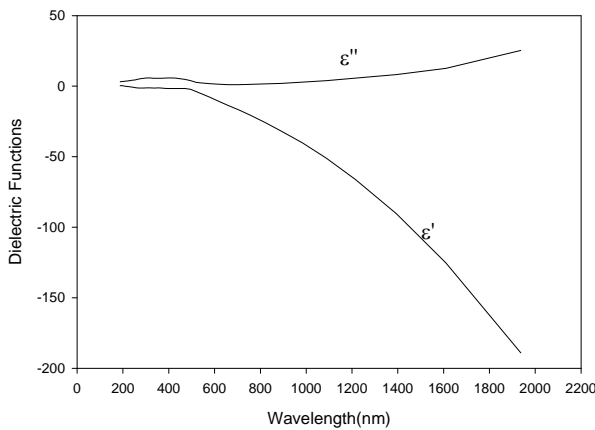


Figure 16. Dielectric functions for bulk gold as a function of wavelength.

with $\epsilon' = -3.6$, and $\epsilon'' \sim 0$. Examining the zoomed in region of the gold curve in Figure 15 it

As an aside, no solution can be found for b_n becoming large in the limiting case. This resonance condition defines the Fröhlich mode, and requires the refractive index to be purely imaginary. This is not satisfied in any real material, but is approached in certain regions. Consider for example gold nanoparticles in water. Water has a refractive index of approximately 1.33, giving an ϵ' of about 1.78. So we need to find a region

is clear that ϵ' is negative for a large range of values, which means we will be able to satisfy the conditions to various degrees of rigidity. $\epsilon' = -3.6$ somewhere around 500-520nm. 20nm gold spheres have a resonance peak somewhere around a wavelength of 522nm. The accuracy of this result is especially impressive given that we have used the infinitely small sphere which is equivalent to the electrostatics approximation in which the field is uniform throughout the sphere.

For the coated sphere the Fröhlich mode is given by:

$$\epsilon_1 = -2\epsilon_2 \left[\frac{\epsilon_2(1-f) + (2+f)}{\epsilon_2(2f+1) + 2(1-f)} \right], \text{ where } f = \frac{a^3}{b^3}$$

Adding more terms will improve these approximations, and the general equations must be calculated to find the precise position, and magnitude of the maximum.

One last note must be made about very small metallic particles. Electrons normally have a mean free path which is dictated by the material and conditions. The distance

between collisions is approximately given by: $d = \frac{\sigma m v_f}{n e^2}$ in bulk where σ is the

conductivity, m the mass, v_f the Fermi velocity, e the charge, and n the free electron

density. The damping constant in Drude theory is $\gamma = \frac{1}{\tau}$, where τ is the lifetime before

scattering from a phonon or defect. If scattering from different causes is assumed to be

independent then $\gamma = \gamma_{bulk} + \gamma_{size_effect}$. The distance between collisions with the boundary of a sphere is given by $L = 4a/3$ [210], where a is the radius of the sphere (the constant may

vary). This means $\gamma = \gamma_{bulk} + \frac{3v_f}{4a}$.

A decrease in the mean free path increases the imaginary portion of the dielectric constant, which weakens the ability to meet the condition that the imaginary portion is zero, and consequently lowers the peak height, and broadens the resonance.

3.1.3.3 Computer Modelling of Mie Theory

The computer modeling of coated and uncoated spheres was carried out using a Matlab routine by C. Mätzler [211], which were called through a custom Matlab routines to generate the peak height and position of resonance. Routines used to perform these calculations are given in Appendix B, Appendix C, and Appendix D. The Mätzler [211] routine provides an output of the extinction amplitude given the following parameters: incident wavelength, complex indices of nanosphere, coating, and surrounding medium, as well as the thickness of coating and size of nanosphere. We thus provide the complex indices of gold and water, as well as the size of gold from standard data for programs B, C, and D.

In all cases, before the Mätzler routine is called, the dielectric function is split into free and bound parts ($\varepsilon = \varepsilon_{free} + \varepsilon_{bound}$) using the Drude model to represent the contribution of free electrons. The free electron damping constant is then corrected for finite size effects ($\gamma = \gamma_{bulk} + \frac{3v_f}{4a}$). The corrected free electron dielectric contribution is now added back to the bound contribution. This is discussed in sections 3.1.3.2 and 3.1.3.3. Finite size effects, however, tend to red-shift the resonance away from that using bulk values. We found that, experimentally for small gold nanospheres (5-15nm), there was a blue shifting of the resonance, not predicted by the theory. The origin of this effect was not known. To correct for it, once the damping frequency had been adjusted, the bulk plasma frequency was also shifted in the free electron contribution to agree with the experimentally obtained peaks. Appendix B accomplishes this shift in w_p through the following steps:

- 1) The experimental wavelength is provided to the program.
- 2) A guess value for w_p can be provided to speed up the process.
- 3) The Mätzler routine is called upon in a loop to generate the extinction amplitudes for a range of wavelengths (between 490 and 580 in our case of gold) for an uncoated sphere of desired size. The wavelength of the maximum extinction (corresponding to the plasmon peak) can then be determined.
- 4) If this peak wavelength does not match the experimental peak within the provided bounds of accuracy, the plasma frequency w_p is shifted accordingly. The program

returns to step 3 generating a new plasmon peak until it matches suitably with the experimental value.

- 5) The correction to w_p is recorded for use in further programs.

Appendix C generates contour plots. This is accomplished through the following process:

- 1) Experimental parameters (indices, size of particle, and w_p shift from Appendix B program) are provided to the program.
- 2) The Mätzler routine is called upon in a loop to generate the extinction amplitudes for a range of wavelengths (between 490 and 580 in our case of gold) for the sphere size desired. The wavelength of the maximum extinction (corresponding to the plasmon peak) can then be determined.
- 3) The routine then uses a nested loop to output the extinction peak and wavelength for a range of indices and thicknesses of coating (indices are forced to be real in this case).

The net effect is the production of contours of extinction peak wavelength and amplitude. These are produced to allow the inversion of the general Mie solution.

Appendix D interpolates the contour grid to allow better resolution, and returns the index of refraction and thickness when given a peak extinction amplitude and wavelength. To accomplish this, the contour data from Appendix C is input into the program.

Overall, the program in Appendix B is called upon to generate the w_p shift, which is then fed into the program in Appendix C. The result of Appendix C is then fed into Appendix D in order to invert the information and extract the index of refraction and thickness given a particular extinction peak amplitude and wavelength.

One problem is that while Mie theory is generally quite accurate in predicting the peak wavelength, it is not as accurate at predicting the peak amplitude. It seems sensible to

simply find a scaling factor that will cause the experimental bare sphere peak amplitude to match the theoretical one, and then use this scaling factor to shift all coated spheres. This procedure generated unrealistically high values for the refractive index in a number of cases. The cause of this must be related to the fact that the scaling factor for a coated sphere is not necessarily the same as an uncoated sphere. This presents a problem, as we have no a priori value for the theoretical protein coated sphere. To circumvent this problem we have made the assumption that the index of refraction upon conjugation at pH 7 is 1.57. This is taken from ellipsometry data done by Hans Arwin [212] of bovine serum albumin on $\text{Hg}_{0.71}\text{Cd}_{0.29}\text{Te}$ for wavelengths between about 546nm and 632nm. To use this assumption, the programs in Appendices B, and C are used as usual. However, the value of extinction is determined which will reproduce the experimental peak wavelength (corresponding to the initially conjugated protein on Au nanospheres at pH 7), as well as an index of 1.57. The factor needed to scale the experimental extinction to the value just determined is then used to scale all extinctions for that particular sphere size. This assumption may seem very limiting; however, a choice of a different scaling value (within reason) will not drastically change the shape of the denaturing path (in index/thickness).

3.1.4 Quartz Crystal Microbalance

The quartz crystal microbalance (QCM) is a type of bulk acoustic wave sensor or BAW. The basis of its operation is that a resonating piezoelectric crystal has a resonant frequency which depends strongly on its thickness, and density. Even a minute change in mass effects a change in resonance frequency. Because modern electronics are capable of measuring very small changes in frequency, we can measure very small changes in mass.

Gold or another metal is deposited on the faces of the crystal. The active area of the crystal is defined approximately by the overlap between metallic films, between which the electric field will be generated.

Figure 17 illustrates characteristic operation of a crystal in shear mode. Figure 18 is an image of a typical AT-

cut crystal with gold electrodes. A voltage applied between the two electrodes creates a

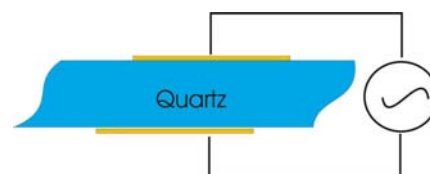


Figure 17. Side view schematic of quartz crystal in shear mode

stress in the non-centro-symmetric crystal, which is responded to by generating shear strain. An oscillating voltage will result in oscillating shear strain. At a particular frequency the crystal will oscillate in resonance.

This resonance can depend quite strongly on temperature. Consequently, the piezoelectric materials of choice are specific cuts of quartz. SC and AT cut crystals both vibrate in a thickness shear mode, and both exhibit greatly reduced temperature dependence. In particular, AT-cut α -quartz is most commonly used due to cheaper manufacturing costs, and its temperature dependence having an inflection point near room temperature. The resonant frequency is also dependent on any mechanical stress on the crystal due to mounting, or pressures applied during injection of a sample. Careful preparation allows these effects to be considered negligible. The amplitude of the strain falls off approximately exponentially at the edges of the overlap of the top and bottom electrode. This allows the crystal to be mounted by its edges without damping the oscillations. The amplitude of shear displacement is typically of the order of a nanometer or less.

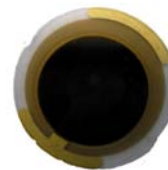


Figure 18. 5MHz AT-cut quartz crystal with gold electrodes

The Q-Sense QCM is a commercial device, and comes as a liquid cell for housing the crystal, and a “black-box” with all electronics to run the system. However, the basic components involved in the operation of a generalized QCM are illustrated in Figure 19. The steps of operation are generally as follows:

- 1) The computer will ask the oscilloscope to sweep the quartz crystal through a range of frequencies about the factory labeled fundamental frequency (eg. 4.95MHz +/- 200KHz). At each frequency after the sinusoidal signal is sent, the signal relay is opened to stop the excitation, and the crystal response is then measured by the oscilloscope. This process allows the exact maximum where resonance f_r occurs to be identified.

- 2) The signal generator is then adjusted to frequency f_r and the crystal is driven at resonance for a brief moment before the relay is opened, and the crystal allowed to oscillate “freely”. Because the decay of the signal is several orders of magnitude slower than the frequency itself, it is not efficient, or feasible to collect data at a rate fast enough to generate smooth peaks for the entire decay curve. Consequently the signal of the

undriven crystal is mixed with the inverted reference signal $f_r + \Delta$ where Δ is normally of the order of KHz. The peaks in the signal now represent the beat frequency $f_r - (f_r + \Delta) = -\Delta$ which is KHz and proportionally decays in a reasonable time. The mixed frequency is read by the oscilloscope, converted to a digital signal and sent to the computer. The computer can then fit the signal with a damped harmonic oscillator equation $A(t) = A_0 e^{-\pi(-\Delta)Dt} \sin(2\pi(-\Delta)t + \delta)$ where D is the dissipation value extracted and $D = (\text{Energy dissipated}) / (2\pi \text{Energy stored})$. The resonance frequency is found to be $-\Delta + \Delta + f_r = f_r$.

3) If the resonance conditions have changed slightly in the process of reading, the crystal will be driven at f_r but will oscillate at $f_r + \sigma$ once the relay is opened. When the signal is mixed, the frequency that enters the oscilloscope will be $(f_r + \sigma) - (f_r + \Delta) = (\sigma - \Delta)$, and the new fitted equation will read $A(t) = A_0 e^{-\pi(\sigma - \Delta)Dt} \sin(2\pi(\sigma - \Delta)t + \delta)$ such that the new D can be determined and the new resonance frequency is now determined to be $(\sigma - \Delta) + (f_r + \Delta) = \sigma + f_r = f_r'$. The resonance frequency is now set so that the new $f_r = f_r'$, and the process is repeated, tracking the D , and f_r values throughout the experiment.

4) If it is desired that other harmonics should be tracked, then these are done in series. In other words $f_1, f_3, f_5 \dots$ are measured one after another, followed by f_1 and the process is repeated.

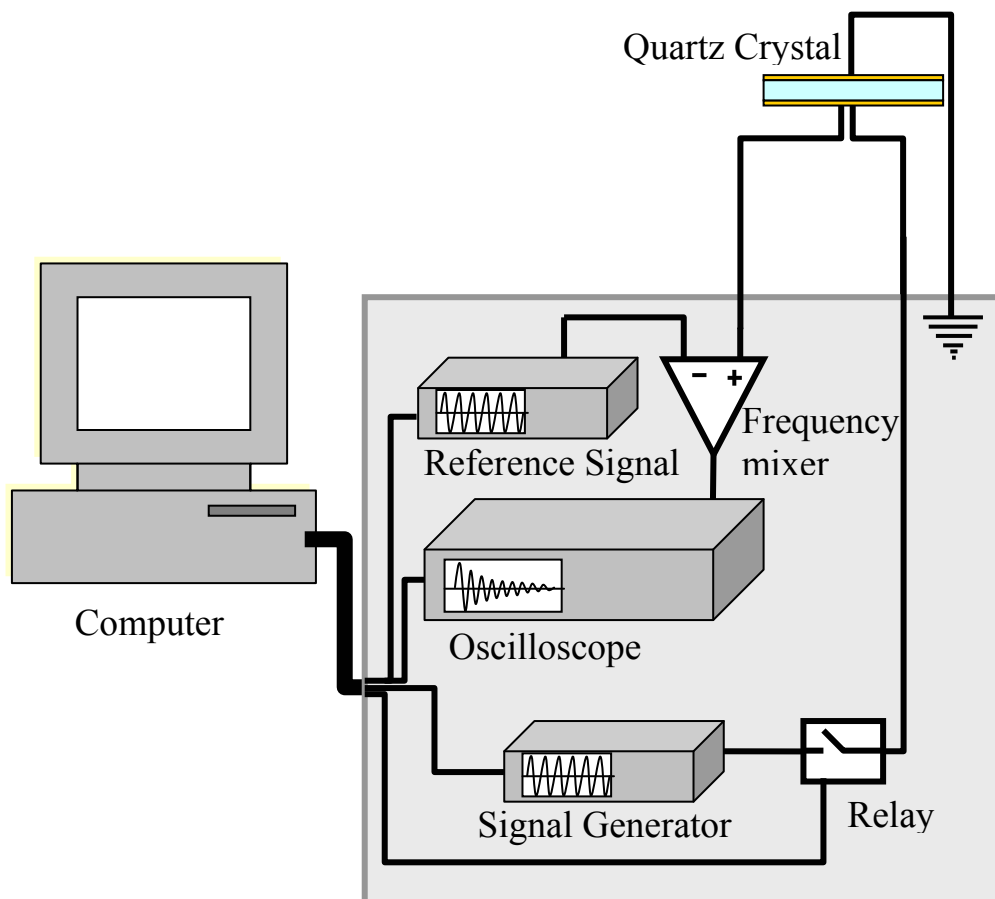


Figure 19. Schematic of typical QCM setup.

A photograph of the Q-Sense QCM used in the experiment is given in Figure 20. In a typical experiment buffer is warmed in a syringe case immersed in water in C, sitting atop the heater D. This will prevent temperature effects from altering the resonant frequency of the crystal, and prevent any degassing and bubble formation of the liquid. The temperature of the water bath is generally held 3-4 degrees warmer than the QCM cell. This is to account for temperature loss in traveling through the tubes to the heating loop in the QCM. After the buffer has equilibrated to the correct temperature, it is allowed to flow into the heating loop in the QCM cell until it runs out tube F. Flow is purely gravitational, and the lab-jack in Figure 20 is adjusted so as to minimize the flow rate. Even with the warmed buffer, a small temperature deviation will be present, and the solution is allowed to equilibrate further in the temperature loop to remove this. The buffer is then allowed to flow into the crystal chamber and out of tube E. Flow rate, and volume are kept to a minimum to prevent any pressure changes on the crystal. Once the system has equilibrated

and been measured, the old solution is pipetted out of the syringe case and the new solution added. The above steps are then repeated until the solution flows out of tube E again.

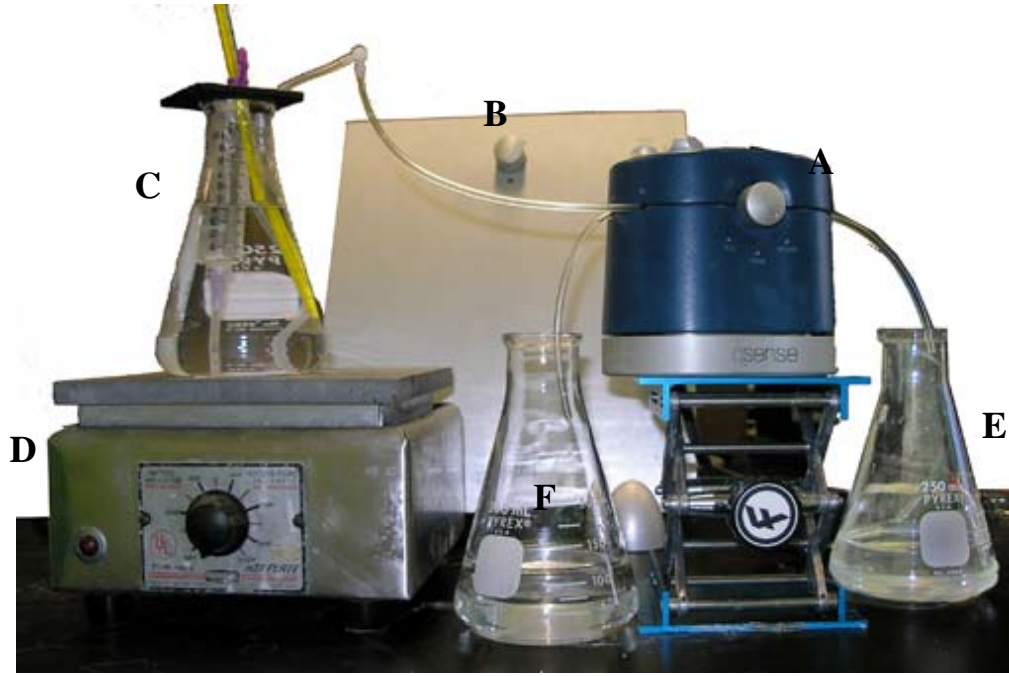


Figure 20. Actual QCM setup. A) QCM liquid cell, B) electronics that operate QCM, C) water bath and liquid introduction site, D) heater for water bath, F) temperature loop, E) crystal loop.

The frequency of the bare crystal is given approximately as

$$f_0 = \frac{nv_0}{2h_0} = \frac{n}{2h_0} \sqrt{\frac{\mu_0}{\rho_0}} = \frac{n}{2} \sqrt{\frac{\mu_0}{h_0 M_0}}$$

where n is the overtone number, h the thickness, M the areal mass, v the velocity of sound, μ the elastic modulus, and ρ the density, all of quartz.

In 1959 G. Sauerbrey [213] showed that the decrease in frequency was linearly

proportional to the mass, giving the Sauerbrey equation: $\Delta f = -\frac{2f_0^2}{A\sqrt{\rho_q\mu_q}} \Delta m$ where f_0 is

the resonant frequency, A the active area, ρ_q the density of quartz, and μ_q the shear modulus of quartz.

The amplitude of displacement of an AT-crystal with thickness T , and parallel plates of radius R , is $A(r, y) = A_0 \sin\left(\frac{\pi y}{T}\right) \cos^2\left(\frac{\pi r}{2R}\right)$ for a crystal that has antinodes at both surfaces (y being measured from the center of the crystal so that a surface is at $y=T/2$).

This result depends on the exact wiring. For a crystal with one face grounded as is commonly the case, the grounded face will be a node, and the open face an antinode, giving rise to odd overtones (1, 3, 5...) being allowed.

This equation had wide success, and is still frequently used today. It was limited generally to gaseous atmospheres, and rigid thin films. Operation in fluid, it was thought, would dissipate all of the energy of the crystal, and quench the oscillations. However, two decades later, in 1980, Nomura et al. showed that this was not the case and extended function of the QCM to viscous environs such as fluids [214]. This opened the door to new applications, such as protein deposition. Operation in fluids violated the assumptions of the Sauerbrey equation, and required more sophisticated methods of modeling [215, 216]. Voinova et al. [215] have approached the problem with continuum mechanics. Viscoelastic layers are modeled as Voigt elements in series.

By measuring the dissipation as well as the frequency, measurements of viscoelastic properties can be made in addition to simple thickness. In general $\sigma_{ik}=G^*\varepsilon_{ik}$ where σ is the generalized stress tensor and ε is the generalized strain tensor, with $G^*(\omega)$ the complex frequency dependent shear modulus. The QCM with homogenous layers on top can be represented mechanically as a series of Voigt elements. A Voigt element (Figure 21) involves a spring and dashpot connected in parallel, for which the stress is proportional to the sum of a viscous term and an elastic term

$$\sigma_{xy} = \mu \frac{\partial u_x}{\partial y} + \eta \frac{\partial \partial(u_x)}{\partial y \partial t}. \text{ The crystal and subsequent layers must}$$

obey Cauchy's equations of motion $\frac{\partial \sigma_{xy}}{\partial y} = \rho \frac{\partial^2 u_x}{\partial t^2}$. If, in

addition, we assume that the motion is time harmonic, ie. $u_x(y,t) = A(y)e^{i\omega t}$, then putting these results together we have:

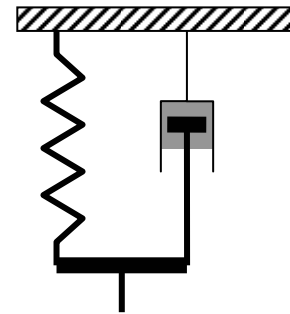


Figure 21. Voigt element.

$$\frac{\partial}{\partial y} \left(\mu \frac{\partial A(y)e^{i\omega t}}{\partial y} + \eta \frac{\partial \partial A(y)e^{i\omega t}}{\partial y \partial t} \right) = \rho \frac{\partial^2 A(y)e^{i\omega t}}{\partial t^2}$$

$$\mu \frac{\partial^2 A(y)e^{i\omega t}}{\partial y^2} + i\omega\eta \frac{\partial^2 A(y)e^{i\omega t}}{\partial y^2} = \rho i^2 \omega^2 A(y)e^{i\omega t}$$

$$(\mu + i\omega\eta) \frac{\partial^2 u_x}{\partial y^2} = -\rho\omega^2 u_x$$

$$\mu^* \frac{\partial^2 u_x}{\partial y^2} = -\rho\omega^2 u_x$$

where $\mu^*(\omega) = \mu + i\omega\eta$ is the effective complex shear modulus for a Voigt element [217].

This is a wave equation which has the auxillary equation $\xi = \sqrt{-\frac{\rho\omega^2}{\mu^*}}$. The full solution is

then $u_x(y, t) = (Ae^{\xi y} + Be^{-\xi y})e^{i\omega t}$, in which A and B are constants. All we require now for a particular solution is to apply the boundary conditions to this equation.

A derivation of the solution form for n-layers is given in Paper IV. The solution uses no slip boundaries in which the stress, displacement (and thus velocity) across the boundary must be continuous. The Matlab code used to perform the calculation of ΔF and ΔD for n-layers in Paper IV is given in Appendix E: Homogeneous, No-Slip, N-Layer Voigt Model of QCM.

Conclusion

A complete understanding of the behaviour of proteins at interfaces cannot be gained through directed focus upon one aspect of the field. This thesis has strived to make advancements through experiment; both in fundamental aspects such as curvature dependence of protein stability, as well as applied aspects such as contact lens applications. However, it has also made a significant contribution to the advancement of nanoparticles as new tools for investigation of interfacial protein. Ultimately protein adsorption is an exceedingly complex phenomenon. Varying microscopic surface chemistries may lead to very different adsorption behaviour for a single type of protein. The unique morphologies on Galyfilcon A in paper V clearly demonstrate this. Alternately, protein may adsorb to the same surface in vastly different ways, depending on the type of protein. In paper IV, such behaviour ranges from concentration-independent monolayers, to complex, concentration-dependent multilayer formation. Finally, even for similar surface chemistries, the same protein may be drastically affected by the radius of curvature of the surface, as in papers I-III. The search for new ways to investigate protein behaviour led us to utilize new methods of measurement. In papers I-III, we exploited the LSPR of Au nanospheres to measure conformational changes during both thermal and pH perturbations, and in paper V we used nanosphere-protein conjugates to visualize adsorption.

Appendix A: Mie Theory

The following derivation follows that of Bohren and Huffman [208] of a homogenous sphere made of a linear isotropic material.

Because we are dealing with a sphere the solution will be easiest if we use spherical coordinates centered at the center of the sphere. We would like to rewrite the planar waves incident on the sphere in terms of spherical coordinates. While this is somewhat difficult, it makes the overall solution to the scattering and absorbance of a sphere quite easy. We start with a brief derivation following that of Bohren and Huffman for expanding a plane wave in spherical coordinates:

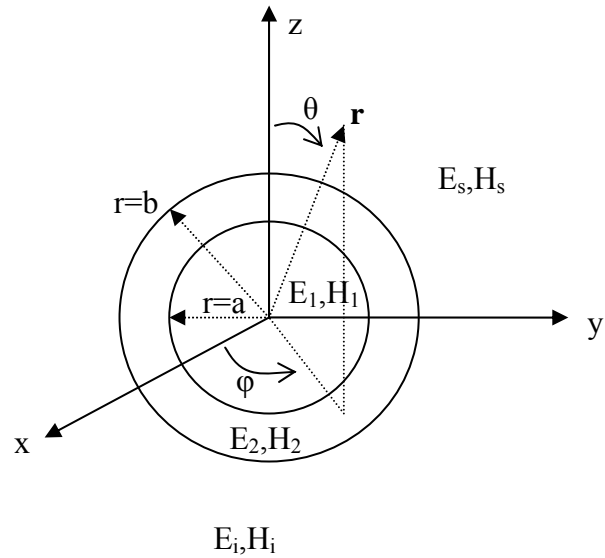


Figure 22. Sphere of radius a , with coating thickness $(b-a)$. The subscript i denotes incident fields, while the subscripts $1, 2,$ and s denote fields internal to the sphere, fields in the coating, and the scattered field respectively.

The full vector wave equation must satisfy:

$$\nabla^2 \vec{E} + k^2 \vec{E} = 0 \text{ and } \nabla^2 \vec{H} + k^2 \vec{H} = 0 \text{ with } k^2 = \omega^2 \epsilon \mu \quad \nabla \cdot \vec{E} = 0 \text{ and } \nabla \cdot \vec{H} = 0$$

(of course we only need to find one of E or H , and we have the other according to Maxwell's equations $\nabla \times \vec{E} = i\omega\mu\vec{H}$ and $\nabla \times \vec{H} = -i\omega\epsilon\vec{E}$)

These assume that the field is time harmonic, ie. $\vec{E}_{full} = \vec{E}e^{i\omega t}$, which is no real sacrifice, since we can always build up any field we want by summing an infinite series of harmonic fields.

To reduce the problem to a scalar solution Bohren and Huffman now use the vector valued functions \mathbf{M} , and \mathbf{N} which are defined below, and will satisfy the wave equation, while ultimately making calculations easier.

$\vec{M} = \nabla \times (\vec{c} \psi)$ and $\vec{N} = \frac{\nabla \times \vec{M}}{k}$, where \vec{c} is a constant vector, and ψ will be a scalar wave

function. We can show that these will satisfy the vector wave equation if the scalar wave equation is satisfied.

$\nabla \cdot \vec{M} = \nabla \cdot (\nabla \times (\vec{c} \psi)) = 0$ since the divergence of the curl of a vector is always zero.

Similarly, since \mathbf{N} involves a curl, its divergence will also be zero.

For any vector, the identity $\nabla \times (\nabla \times \vec{A}) = \nabla(\nabla \cdot \vec{A}) - \nabla^2 \vec{A}$ holds true. If we apply this to \mathbf{M} and \mathbf{N} we produce two new wave equations.

$$\text{L.S.} \quad \nabla \times (\nabla \times \vec{M}) = \nabla(\nabla \cdot \vec{M}) - \nabla^2 \vec{M} = -\nabla^2 \vec{M}$$

$$\text{R.S.} \quad \nabla \times (\nabla \times (\nabla \times (\vec{c} \psi))) = (\nabla(\nabla \cdot \nabla \times \vec{c} \psi) - \nabla^2 \nabla \times \vec{c} \psi)$$

$$\nabla^2 \vec{M} + k^2 \vec{M} = (-\nabla(\nabla \cdot \nabla \times \vec{c} \psi) + \nabla^2 \nabla \times \vec{c} \psi) + k^2 \nabla \times \vec{c} \psi$$

$$\text{But } \nabla(\nabla \cdot \nabla \times \vec{c} \psi) = 0$$

$$\begin{aligned} \text{So} &= \nabla \times (\nabla^2 \vec{c} \psi + k^2 \vec{c} \psi) \\ &= \nabla \times (\vec{c} (\nabla^2 \psi + k^2 \psi)) \end{aligned}$$

$$\text{L.S.} \quad \nabla \times (\nabla \times \vec{N}) = \nabla(\nabla \cdot \vec{N}) - \nabla^2 \vec{N} = -\nabla^2 \vec{N}$$

$$\text{R.S.} \quad \nabla \times \left(\frac{\nabla \times \vec{M}}{k} \right) = \nabla \left(\nabla \cdot \frac{\vec{M}}{k} \right) - \nabla^2 \frac{\vec{M}}{k} = -\nabla^2 \frac{\vec{M}}{k}$$

$$\begin{aligned} \nabla^2 \vec{N} + k^2 \vec{N} &= \nabla \times \nabla^2 \frac{\vec{M}}{k} + k^2 \nabla \times \frac{\vec{M}}{k} \\ &= \frac{1}{k} \nabla \times (\nabla^2 \vec{M} + k^2 \vec{M}) \end{aligned}$$

Clearly, from the equation in M, since \mathbf{c} is not in general the zero vector, if we satisfy the scalar wave equation $\nabla^2\psi + k^2\psi = 0$ then the vector equations are zero, and satisfy the wave vector equation.

The Laplacian in spherical coordinates is given by:

$$\frac{1}{r^2} \frac{\partial}{\partial r} r^2 \frac{\partial}{\partial r} + \frac{1}{r^2 \sin \theta} \frac{\partial}{\partial \theta} \sin \theta \frac{\partial}{\partial \theta} + \frac{1}{r^2 \sin^2 \theta} \frac{\partial^2}{\partial \phi^2}$$

Hence the scalar wave equation $\nabla^2\psi + k^2\psi = 0$ in spherical coordinates becomes:

$$\frac{1}{r^2} \frac{\partial}{\partial r} (r^2 \frac{\partial \psi}{\partial r}) + \frac{1}{r^2 \sin \theta} \frac{\partial}{\partial \theta} (\sin \theta \frac{\partial \psi}{\partial \theta}) + \frac{1}{r^2 \sin^2 \theta} \frac{\partial^2 \psi}{\partial \phi^2} + k^2 \psi = 0$$

This equation is separable if we assume solutions of the form $\psi(r, \theta, \phi) = R(r)\Theta(\theta)\Phi(\phi)$.

Substituting this assumption into the above equation yields the separated equations:

$$2 \quad \frac{d^2\Phi}{d\phi^2} + m^2\Phi = 0$$

$$3 \quad \frac{1}{\sin \theta} \frac{d}{d\theta} (\sin \theta \frac{d\Theta}{d\theta}) + \left[n(n+1) - \frac{m^2}{\sin^2 \theta} \right] \Theta = 0$$

$$4 \quad \frac{d}{dr} (r^2 \frac{dR}{dr}) + [k^2 r^2 - n(n+1)] R = 0$$

We can now write solutions for the separated equations.

For equation 2 which is a simple second order linear D.E. having solutions:

$\Phi = Ae^{\pm im\phi}$, however, for a real electromagnetic field we require real solutions, and thus choose: $\Phi_e = \cos m\phi$ and $\Phi_o = \sin m\phi$ to be our linearly independent solutions, where e and o are even and odd m. The choice of A as 1 is arbitrary, but does not limit us, as the amplitude of the wave can be added in later.

ψ is required to be single valued in ϕ , which insists that m is an integer of zero. Equation 3 has the solution of the associated Legendre functions of the first kind $P_n^m(\cos \theta)$, and $n=m, m+1$ etc.

The final equation 4, has the solution of spherical Bessel functions when $\rho=kr$, and

$Z = R\sqrt{\rho}$ such that:

$$j_n(\rho) = \sqrt{\frac{\pi}{2\rho}} J_{n+\frac{1}{2}}(\rho) \text{ and } y_n(\rho) = \sqrt{\frac{\pi}{2\rho}} Y_{n+\frac{1}{2}}(\rho) \text{ are solutions, as are any linear}$$

combination z_n forming two independent solutions, where J_n and Y_n are ordinary Bessel functions.

Hence, the solutions to 1 are:

$$\psi_{emn} = \cos m\phi P_n^m(\cos \theta) z_n(kr)$$

$$\psi_{omn} = \sin m\phi P_n^m(\cos \theta) z_n(kr)$$

The combined general solution is given by:

$$\psi(r, \theta, \phi) = \sum_{m=0}^{\infty} \sum_{n=m}^{\infty} (A_{mn} \cos m\phi + B_{mn} \sin m\phi) P_n^m(\cos \theta) z_n(kr)$$

where z_n is a Bessel function of the first, second or third kind, and A_m , and B_m can be determined once a particular arrangement is decided on.

Then in terms of M , and N :

$$\begin{aligned} \vec{M} &= \nabla \times (\vec{r} \psi) \\ &= \sum_{m=0}^{\infty} \sum_{n=m}^{\infty} \left[(-A_{mn} \sin m\phi + B_{mn} \cos m\phi) \frac{m}{\sin \theta} P_n^m(\cos \theta) z_n(\rho) \right] \vec{e}_\theta \\ &+ \left[(-A_{mn} \cos m\phi - B_{mn} \sin m\phi) \frac{dP_n^m(\cos \theta)}{d\theta} z_n(\rho) \right] \vec{e}_\phi \end{aligned}$$

$$\begin{aligned}
\bar{\mathbf{N}} &= \frac{\nabla \times \bar{\mathbf{M}}}{k} \\
&= \sum_{m=0}^{\infty} \sum_{n=m}^{\infty} \left[(A_{mn} \cos m\phi + B_{mn} \sin m\phi) \frac{z_n(\rho)}{\rho} n(n+1) P_n^m(\cos \theta) \right] \bar{\mathbf{e}}_r \\
&\quad + \left[(A_{mn} \cos m\phi + B_{mn} \sin m\phi) \frac{dP_n^m(\cos \theta)}{d\theta} \frac{1}{\rho} \frac{d}{d\rho} (\rho z_n(\rho)) \right] \bar{\mathbf{e}}_{\theta} \\
&\quad + \left[(B_{mn} \cos m\phi - A_{mn} \sin m\phi) m \frac{P_n^m(\cos \theta)}{\sin \theta} \frac{1}{\rho} \frac{d}{d\rho} (\rho z_n(\rho)) \right] \bar{\mathbf{e}}_{\phi}
\end{aligned}$$

Where we have used the fact that in spherical coordinates the curl of a vector \mathbf{F} is:

$$\nabla \times \bar{\mathbf{F}} = \frac{1}{r \sin \theta} \left[\frac{\partial}{\partial \theta} (\sin \theta \bar{F}_{\phi}) - \frac{\partial \bar{F}_{\theta}}{\partial \phi} \right] \bar{\mathbf{e}}_r + \frac{1}{r} \left[\frac{1}{\sin \theta} \frac{\partial \bar{F}_r}{\partial \phi} - \frac{\partial}{\partial r} (r \bar{F}_{\phi}) \right] \bar{\mathbf{e}}_{\theta} + \frac{1}{r} \left[\frac{\partial}{\partial r} (r \bar{F}_{\theta}) - \frac{\partial \bar{F}_r}{\partial \theta} \right] \bar{\mathbf{e}}_{\phi}$$

The above equations can also be split into M_{odd} , M_{even} , and N_{odd} , N_{even} where odd M/N involve the A coefficient, and even M/N involve the B coefficient.

However, so far we have generated general solutions. We would like to have plane waves incident on the sphere. We can generate a plane wave solution in terms of an expansion in a series of $\bar{\mathbf{M}}$, and $\bar{\mathbf{N}}$, since any linear combination of the two will also be solution of the vector wave equation in spherical coordinates.

Taking an x polarized wave in Cartesian coordinates: $\bar{\mathbf{E}} = E_0 e^{ikr \cos \theta} \bar{\mathbf{e}}_x$, where

$\bar{\mathbf{e}}_x = \sin \theta \cos \phi \bar{\mathbf{e}}_r + \cos \theta \cos \phi \bar{\mathbf{e}}_{\theta} - \sin \phi \bar{\mathbf{e}}_{\phi}$ in spherical coordinates.

$$\text{Setting } \bar{\mathbf{E}} = \sum_{m=0}^{\infty} \sum_{n=m}^{\infty} B_{omn} \bar{\mathbf{M}}_{omn} + B_{emn} \bar{\mathbf{M}}_{emn} + A_{omn} \bar{\mathbf{N}}_{omn} + A_{emn} \bar{\mathbf{N}}_{emn}$$

To find coefficients A and B we will use orthogonality of the vector spherical harmonics.

Clearly $\langle \bar{\mathbf{M}}_{ijk} | \bar{\mathbf{M}}_{ijk} \rangle$ are not orthogonal, however:

$$\langle \bar{\mathbf{M}}_{omn} | \bar{\mathbf{N}}_{omn} \rangle = \langle \bar{\mathbf{M}}_{emn} | \bar{\mathbf{N}}_{emn} \rangle = \langle \bar{\mathbf{M}}_{omn} | \bar{\mathbf{M}}_{emn} \rangle = \langle \bar{\mathbf{N}}_{omn} | \bar{\mathbf{N}}_{emn} \rangle = 0 \text{ because these all involve}$$

$$\int_0^{2\pi} \cos m\phi \sin m\phi d\phi = 0 \text{ in the inner product.}$$

Of course $\int_0^{2\pi} \sin m\phi \sin m'\phi d\phi = \int_0^{2\pi} \cos m\phi \cos m'\phi d\phi = 0$ for $m \neq m'$ so for the rest of the inner products we only need consider differences in n for the last orthogonality relationships.

Consider

$$\begin{aligned} \langle \bar{M}_{omn} | \bar{N}_{emn'} \rangle &= \int_0^\infty \int_0^{2\pi} \int_0^\pi \\ &0 \cdot \left(\cos m\phi \frac{z_n(\rho)}{\rho} n'(n'+1) P_{n'}^m(\cos\theta) \right) \\ &+ \left(\cos m\phi \frac{m}{\sin\theta} P_n^m(\cos\theta) z_n(\rho) \right) \cdot \left(\cos m\phi \frac{dP_{n'}^m(\cos\theta)}{d\theta} \frac{1}{\rho} \frac{d}{d\rho} (\rho z_{n'}(\rho)) \right) \\ &+ \left(-\sin m\phi \frac{dP_n^m(\cos\theta)}{d\theta} z_n(\rho) \right) \cdot \left(-m \sin m\phi \frac{P_{n'}^m(\cos\theta)}{\sin\theta} \frac{1}{\rho} \frac{d}{d\rho} (\rho z_{n'}(\rho)) \right) k\rho^2 \sin\theta d\theta d\phi d\rho \end{aligned}$$

The portion dependent on θ is:

$$\begin{aligned} &\int_0^\pi P_n^m(\cos\theta) \frac{dP_{n'}^m(\cos\theta)}{d\theta} + \frac{dP_n^m(\cos\theta)}{d\theta} P_{n'}^m(\cos\theta) d\theta \\ &= \int_0^\pi \frac{d}{d\theta} P_{n'}^m(\cos\theta) \cdot P_n^m(\cos\theta) d\theta \\ &= P_{n'}^m(\cos\theta) \cdot P_n^m(\cos\theta) \Big|_0^\pi = 0 \end{aligned}$$

and if m is zero, then the theta terms disappear in M , and the phi terms in N , so that the inner-product is zero. So $\langle \bar{M}_{omn} | \bar{N}_{emn'} \rangle = \langle \bar{M}_{emn} | \bar{N}_{omn'} \rangle = 0$

The last relations $\langle \bar{M}_{emn} | \bar{M}_{emn'} \rangle, \langle \bar{M}_{omn} | \bar{M}_{omn'} \rangle, \langle \bar{N}_{emn} | \bar{N}_{emn'} \rangle, \langle \bar{N}_{omn} | \bar{N}_{omn'} \rangle$ are zero, which follows because they all involve the integral:

$$\int_0^\pi \frac{dP_n^m(\cos\theta)}{d\theta} \frac{dP_{n'}^m(\cos\theta)}{d\theta} + m^2 \frac{P_n^m(\cos\theta) P_{n'}^m(\cos\theta)}{\sin^2\theta} d\theta$$

But from the differential equation which generated the associated Legendre functions

$$(1) \frac{1}{\sin \theta} \frac{d}{d\theta} \left(\sin \theta \frac{dP_n^m}{d\theta} \right) + \left[n(n+1) - \frac{m^2}{\sin^2 \theta} \right] P_n^m = 0$$

$$(2) \frac{1}{\sin \theta} \frac{d}{d\theta} \left(\sin \theta \frac{dP_{n'}^m}{d\theta} \right) + \left[n'(n'+1) - \frac{m^2}{\sin^2 \theta} \right] P_{n'}^m = 0$$

$$P_n^m \cdot (1) + P_{n'}^m \cdot (2)$$

$$\left(\left[n(n+1) - \frac{m^2}{\sin^2 \theta} \right] + \left[n'(n'+1) - \frac{m^2}{\sin^2 \theta} \right] \right) P_n^m P_{n'}^m + \frac{P_n^m}{\sin \theta} \frac{d}{d\theta} \left(\sin \theta \frac{dP_n^m}{d\theta} \right) + \frac{P_{n'}^m}{\sin \theta} \frac{d}{d\theta} \left(\sin \theta \frac{dP_{n'}^m}{d\theta} \right) = 0$$

Arranging terms and adding $2 \frac{dP_n^m}{d\theta} \cdot \frac{dP_{n'}^m}{d\theta}$ to both sides while multiplying through by $\sin \theta$:

$$2 \sin \theta \left(\frac{dP_n^m}{d\theta} \cdot \frac{dP_{n'}^m}{d\theta} + \frac{m^2 P_n^m P_{n'}^m}{\sin^2 \theta} \right) = [n(n+1) + n'(n'+1)] P_n^m P_{n'}^m \sin \theta$$

$$+ \left(P_{n'}^m \frac{d}{d\theta} \left(\sin \theta \frac{dP_n^m}{d\theta} \right) + \sin \theta \frac{dP_n^m}{d\theta} \cdot \frac{dP_{n'}^m}{d\theta} \right) + \left(P_n^m \frac{d}{d\theta} \left(\sin \theta \frac{dP_{n'}^m}{d\theta} \right) + \sin \theta \frac{dP_{n'}^m}{d\theta} \cdot \frac{dP_n^m}{d\theta} \right)$$

The last two terms in brackets can be recognized as the chain rule, allowing the equation to be written:

$$2 \sin \theta \left(\frac{dP_n^m}{d\theta} \cdot \frac{dP_{n'}^m}{d\theta} + \frac{m^2 P_n^m P_{n'}^m}{\sin^2 \theta} \right) = [n(n+1) + n'(n'+1)] P_n^m P_{n'}^m \sin \theta$$

$$+ \frac{d}{d\theta} \left(\sin \theta P_n^m \frac{dP_{n'}^m}{d\theta} + \sin \theta P_{n'}^m \frac{dP_n^m}{d\theta} \right)$$

So now the integral becomes

$$= \frac{1}{2} \int_0^\pi [n(n+1) + n'(n'+1)] P_n^m P_{n'}^m \sin \theta + \frac{d}{d\theta} \left(\sin \theta P_n^m \frac{dP_{n'}^m}{d\theta} + \sin \theta P_{n'}^m \frac{dP_n^m}{d\theta} \right) d\theta$$

$$= \frac{1}{2} [n(n+1) + n'(n'+1)] \int_0^\pi P_n^m P_{n'}^m \sin \theta d\theta$$

$$+ \int_0^\pi \frac{d}{d\theta} \left(\sin \theta P_n^m \frac{dP_{n'}^m}{d\theta} + \sin \theta P_{n'}^m \frac{dP_n^m}{d\theta} \right) d\theta$$

$$= 0 + \left(\sin \theta P_n^m \frac{dP_{n'}^m}{d\theta} + \sin \theta P_{n'}^m \frac{dP_n^m}{d\theta} \right)_0^\pi$$

$$= 0$$

So all vector spherical harmonics are orthogonal to each other.

To find the coefficients to the plane wave electric field written in spherical harmonics we can use the orthogonality of the harmonics and take the inner product with one harmonic at a time:

$$\begin{aligned} \langle \vec{E} | \vec{M}_{om'n'} \rangle &= \sum_{m=0}^{\infty} \sum_{n=m}^{\infty} B_{omn} \langle \vec{M}_{omn} | \vec{M}_{om'n'} \rangle + B_{emn} \langle \vec{M}_{emn} | \vec{M}_{om'n'} \rangle + A_{omn} \langle \vec{N}_{omn} | \vec{M}_{om'n'} \rangle + A_{emn} \langle \vec{N}_{emn} | \vec{M}_{om'n'} \rangle \\ &= \sum_{m=0}^{\infty} \sum_{n=m}^{\infty} B_{omn} \langle \vec{M}_{omn} | \vec{M}_{om'n'} \rangle \\ &= B_{om'n'} \langle \vec{M}_{om'n'} | \vec{M}_{om'n'} \rangle \end{aligned}$$

since it will be zero if $m \neq m'$ or $n \neq n'$. So to find B_{omn} (and all other coefficients follow similarly using orthogonality we have:

$$\begin{aligned} B_{em'n'} &= \frac{\langle \vec{E} | \vec{M}_{em'n'} \rangle}{\langle \vec{M}_{em'n'} | \vec{M}_{em'n'} \rangle} \\ &= \frac{\int_0^{\infty} \int_0^{2\pi} \int_0^{\pi} [\vec{E}_0 e^{ikr \cos \theta}] \cdot \left[\begin{array}{l} \sin \theta \cos \phi \cdot 0 \\ + (\cos \theta \cos \phi) \cdot \left(\sin m \phi \frac{-m}{\sin \theta} P_n^m(\cos \theta) z_n(\rho) \right) \\ + (-\sin \phi) \cdot \left(-\cos m \phi \frac{dP_n^m(\cos \theta)}{d\theta} z_n(\rho) \right) \end{array} \right] k \rho^2 \sin \theta d\theta d\phi d\rho}{\langle \vec{M}_{em'n'} | \vec{M}_{em'n'} \rangle} \\ &= \frac{\int_0^{\infty} \int_0^{2\pi} \int_0^{\pi} [(\cos \phi) \cdot (\sin m \phi) + (\sin \phi) \cdot (\cos m \phi)] d\phi \int_0^{\pi} k \rho^2 \sin \theta d\theta d\rho}{\langle \vec{M}_{em'n'} | \vec{M}_{em'n'} \rangle} \\ &= 0 \end{aligned}$$

$$A_{om'n'} = \frac{\langle \vec{E} | \vec{N}_{om'n'} \rangle}{\langle \vec{N}_{om'n'} | \vec{N}_{om'n'} \rangle} \text{ is zero due to the } \phi \text{ terms similarly to } B_{em'n'}.$$

Also, we can note that for any m not equal to 1 there will be different orders in ϕ , and thus result in zero. So m is restricted to being 1.

After much algebra, Bohren and Huffman have the final results:

$$A_{em'n'} = \frac{\langle \bar{E} | \bar{N}_{em'n'} \rangle}{\langle \bar{N}_{em'n'} | \bar{N}_{em'n'} \rangle}$$

$$= -iE_0 i^n \frac{2n+1}{n(n+1)}$$

$$B_{om'n'} = \frac{\langle \bar{E} | \bar{M}_{om'n'} \rangle}{\langle \bar{M}_{om'n'} | \bar{M}_{om'n'} \rangle}$$

$$= i^n E_0 \frac{2n+1}{n(n+1)}$$

So that we have the final results for the plane wave in terms of the vector spherical

harmonics: $\bar{E} = E_0 \sum_{n=1}^m i^n \frac{2n+1}{n(n+1)} (\bar{M}_{oln}^{(1)} - i\bar{N}_{eln}^{(1)})$, where the superscript 1 denotes Bessel

functions of the first kind ie. $j_n(\rho)$, which remains finite at the origin unlike the other Bessel functions, and allows our wave to pass through the origin.

$$\bar{H} = \frac{\nabla \times \bar{E}}{i\omega\mu}$$

$$= \frac{1}{i\omega\mu} E_0 \sum_{n=1}^m i^n \frac{2n+1}{n(n+1)} \nabla \times (\bar{M}_{oln}^{(1)} - i\bar{N}_{eln}^{(1)})$$

$$= \frac{1}{i\omega\mu} E_0 \sum_{n=1}^m i^n \frac{2n+1}{n(n+1)} (\nabla \times \bar{M}_{oln}^{(1)} - i\nabla \times \bar{N}_{eln}^{(1)})$$

Using the fact that $\nabla \times \bar{N} = k\bar{M}$ and $\nabla \times \bar{M} = k\bar{N}$ we have the result

$$\bar{H} = \frac{1}{i\omega\mu} E_0 \sum_{n=1}^m i^n \frac{2n+1}{n(n+1)} (\nabla \times \bar{M}_{oln}^{(1)} - i\nabla \times \bar{N}_{eln}^{(1)})$$

$$= \frac{(-1)k}{\omega\mu} E_0 \sum_{n=1}^m i^n \frac{2n+1}{n(n+1)} (i\bar{N}_{oln}^{(1)} + \bar{M}_{eln}^{(1)})$$

Now consider a sphere resting at the origin, which has a radius a . We have two regions – the region inside the sphere, and the region outside the sphere. This generates three types of waves – namely those incident on the sphere, labeled i , those scattered by the sphere labeled s , and those internal to the sphere labeled 1 . The boundary conditions of this system are the requirement that the tangential component of electric and H field must be

continuous at the boundary. Also we know that the field inside the sphere must remain finite, and therefore only involve Bessel functions of the first kind. As well, in the sphere, the wavenumber and permeability are labeled k_1 , and μ_1 . Outside the sphere the scattered field does not pass through the origin, and thus Bessel functions of both the first, and second kind are allowable. However, Bohren and Huffman make the choice to use of

Hankel functions $h_v^{(1)}(\rho) = j_n(\rho) + iy_n(\rho)$, $h_v^{(2)}(\rho) = j_n(\rho) - iy_n(\rho)$, where the superscript denotes Hankel functions

of the first and second kind. It turns out that since these functions describe the wave outside of the sphere where we can have no reflections, we only need one of the two. This is because Hankel functions can be approximated at large distances as

$$h_n^{(1)}(kr) \sim \frac{(-i)^n e^{ikr}}{ikr} \quad \text{for } kr \gg n^2$$

$$h_n^{(2)}(kr) \sim -\frac{(i)^n e^{-ikr}}{ikr}$$

If we are very far from the sphere then Hankel functions of the first kind represent a wave traveling radially outward, and the second kind represent a wave traveling radially inward. Clearly we can only be traveling outwards at that point, and so functions of the first kind are what we want.

So we have the equations:

$$\begin{aligned} \bar{H} &= \frac{\nabla \times \bar{E}}{i\omega\mu} \\ \bar{E}_i &= \sum_{n=1}^{\infty} E_n (\bar{M}_{o1n}^{(1)} - i\bar{N}_{e1n}^{(1)}) & \bar{H}_i &= -\frac{k_1}{\omega\mu_1} \sum_{n=1}^{\infty} E_n (\bar{M}_{e1n}^{(1)} - i\bar{N}_{o1n}^{(1)}) \\ \bar{E}_1 &= \sum_{n=1}^{\infty} E_n (c_n \bar{M}_{o1n}^{(1)} - id_n \bar{N}_{e1n}^{(1)}) & \bar{H}_1 &= -\frac{k_1}{\omega\mu_1} \sum_{n=1}^{\infty} E_n (d_n \bar{M}_{e1n}^{(1)} + ic_n \bar{N}_{o1n}^{(1)}) \\ \bar{E}_s &= \sum_{n=1}^{\infty} E_n (-b_n \bar{M}_{o1n}^{(3)} + ia_n \bar{N}_{e1n}^{(3)}) & \bar{H}_s &= \frac{k_1}{\omega\mu_1} \sum_{n=1}^{\infty} E_n (a_n \bar{M}_{e1n}^{(3)} + ib_n \bar{N}_{o1n}^{(3)}) \end{aligned}$$

And we have boundary conditions:

$$\begin{aligned} \text{Ie. } & (\bar{E}_i + \bar{E}_s - \bar{E}_1) \times \bar{e}_r = 0 \\ & (\bar{H}_i + \bar{H}_s - \bar{H}_1) \times \bar{e}_r = 0 \end{aligned}$$

Which means we have four equations:

$$\begin{aligned} E_{i\theta} + E_{s\theta} - E_{1\theta} &= 0 \\ H_{i\theta} + H_{s\theta} - H_{1\theta} &= 0 \\ E_{i\phi} + E_{s\phi} - E_{1\phi} &= 0 \\ H_{i\phi} + H_{s\phi} - H_{1\phi} &= 0 \end{aligned}$$

We can now solve these for coefficients a_n , b_n , c_n , and d_n .

$$\begin{aligned} \sum_{n=1}^{\infty} E_n (c_n \bar{M}_{o1n}^{(1)} - id_n \bar{N}_{e1n}^{(1)}) \cdot \bar{e}_\theta &= \sum_{n=1}^{\infty} E_n (\bar{M}_{o1n}^{(1)} - i\bar{N}_{e1n}^{(1)}) \cdot \bar{e}_\theta + \sum_{n=1}^{\infty} E_n (-b_n \bar{M}_{o1n}^{(3)} + ia_n \bar{N}_{e1n}^{(3)}) \cdot \bar{e}_\theta \\ \sum_{n=1}^{\infty} E_n (c_n \bar{M}_{o1n}^{(1)} - id_n \bar{N}_{e1n}^{(1)}) \cdot \bar{e}_\phi &= \sum_{n=1}^{\infty} E_n (\bar{M}_{o1n}^{(1)} - i\bar{N}_{e1n}^{(1)}) \cdot \bar{e}_\phi + \sum_{n=1}^{\infty} E_n (-b_n \bar{M}_{o1n}^{(3)} + ia_n \bar{N}_{e1n}^{(3)}) \cdot \bar{e}_\phi \\ -\frac{k_1}{\omega\mu_1} \sum_{n=1}^{\infty} E_n (d_n \bar{M}_{e1n}^{(1)} + ic_n \bar{N}_{o1n}^{(1)}) \cdot \bar{e}_\theta &= -\frac{k}{\omega\mu} \sum_{n=1}^{\infty} E_n (\bar{M}_{e1n}^{(1)} - i\bar{N}_{o1n}^{(1)}) \cdot \bar{e}_\theta + \frac{k}{\omega\mu} \sum_{n=1}^{\infty} E_n (a_n \bar{M}_{e1n}^{(3)} + ib_n \bar{N}_{o1n}^{(3)}) \cdot \bar{e}_\theta \\ -\frac{k_1}{\omega\mu_1} \sum_{n=1}^{\infty} E_n (d_n \bar{M}_{e1n}^{(1)} + ic_n \bar{N}_{o1n}^{(1)}) \cdot \bar{e}_\phi &= -\frac{k}{\omega\mu} \sum_{n=1}^{\infty} E_n (\bar{M}_{e1n}^{(1)} - i\bar{N}_{o1n}^{(1)}) \cdot \bar{e}_\phi + \frac{k}{\omega\mu} \sum_{n=1}^{\infty} E_n (a_n \bar{M}_{e1n}^{(3)} + ib_n \bar{N}_{o1n}^{(3)}) \cdot \bar{e}_\phi \\ \sum_{n=1}^{\infty} E_n (c_n \cos \phi \frac{1}{\sin \theta} P_n^1(\cos \theta) j_n(\rho_1) - id_n \cos \phi \frac{dP_n^1(\cos \theta)}{d\theta} \frac{1}{\rho_1} \frac{d}{d\rho_1} (\rho_1 j_n(\rho_1))) & \\ = \sum_{n=1}^{\infty} E_n (\cos \phi \frac{1}{\sin \theta} P_n^1(\cos \theta) j_n(\rho) - i \cos \phi \frac{dP_n^1(\cos \theta)}{d\theta} \frac{1}{\rho} \frac{d}{d\rho} (\rho j_n(\rho))) & \\ + \sum_{n=1}^{\infty} E_n (-b_n \cos \phi \frac{1}{\sin \theta} P_n^1(\cos \theta) h_n^{(1)}(\rho) + ia_n \cos \phi \frac{dP_n^1(\cos \theta)}{d\theta} \frac{1}{\rho} \frac{d}{d\rho} (\rho h_n^{(1)}(\rho))) & \\ \sum_{n=1}^{\infty} E_n (c_n (-1) \sin \phi \frac{dP_n^1(\cos \theta)}{d\theta} j_n(\rho_1) + id_n \sin \phi \frac{P_n^1(\cos \theta)}{\sin \theta} \frac{1}{\rho_1} \frac{d}{d\rho_1} (\rho_1 j_n(\rho_1))) & \\ = \sum_{n=1}^{\infty} E_n ((-1) \sin \phi \frac{dP_n^1(\cos \theta)}{d\theta} j_n(\rho) + i \sin \phi \frac{P_n^1(\cos \theta)}{\sin \theta} \frac{1}{\rho} \frac{d}{d\rho} (\rho j_n(\rho))) & \\ + \sum_{n=1}^{\infty} E_n (-b_n (-1) \sin \phi \frac{dP_n^1(\cos \theta)}{d\theta} h_n^{(1)}(\rho) - ia_n \sin \phi \frac{P_n^1(\cos \theta)}{\sin \theta} \frac{1}{\rho} \frac{d}{d\rho} (\rho h_n^{(1)}(\rho))) & \end{aligned}$$

$$\begin{aligned}
& -\frac{k_1}{\omega\mu_1} \sum_{n=1}^{\infty} E_n (d_n (-1) \sin \phi \frac{1}{\sin \theta} P_n^1(\cos \theta) j_n(\rho_1) + i c_n \sin \phi \frac{dP_n^1(\cos \theta)}{d\theta} \frac{1}{\rho_1} \frac{d}{d\rho_1} (\rho_1 j_n(\rho_1))) \\
& = -\frac{k}{\omega\mu} \sum_{n=1}^{\infty} E_n ((-1) \sin \phi \frac{1}{\sin \theta} P_n^1(\cos \theta) j_n(\rho) - i \sin \phi \frac{dP_n^1(\cos \theta)}{d\theta} \frac{1}{\rho} \frac{d}{d\rho} (\rho j_n(\rho))) \\
& + \frac{k}{\omega\mu} \sum_{n=1}^{\infty} E_n (a_n (-1) \sin \phi \frac{1}{\sin \theta} P_n^1(\cos \theta) h_n^{(1)}(\rho) + i b_n \sin \phi \frac{dP_n^1(\cos \theta)}{d\theta} \frac{1}{\rho} \frac{d}{d\rho} (\rho h_n^{(1)}(\rho))) \\
\\
& -\frac{k_1}{\omega\mu_1} \sum_{n=1}^{\infty} E_n (d_n (-1) \cos \phi \frac{dP_n^1(\cos \theta)}{d\theta} j_n(\rho_1) + i c_n \cos \phi \frac{P_n^1(\cos \theta)}{\sin \theta} \frac{1}{\rho_1} \frac{d}{d\rho_1} (\rho_1 j_n(\rho_1))) \\
& = -\frac{k}{\omega\mu} \sum_{n=1}^{\infty} E_n ((-1) \cos \phi \frac{dP_n^1(\cos \theta)}{d\theta} j_n(\rho) - i \cos \phi \frac{P_n^1(\cos \theta)}{\sin \theta} \frac{1}{\rho} \frac{d}{d\rho} (\rho j_n(\rho))) \\
& + \frac{k}{\omega\mu} \sum_{n=1}^{\infty} E_n (a_n (-1) \cos \phi \frac{dP_n^1(\cos \theta)}{d\theta} h_n^{(1)}(\rho) + i b_n \cos \phi \frac{P_n^1(\cos \theta)}{\sin \theta} \frac{1}{\rho} \frac{d}{d\rho} (\rho h_n^{(1)}(\rho)))
\end{aligned}$$

These reduce to:

$$\begin{aligned}
0 & = \sum_{n=1}^{\infty} E_n (-b_n \frac{1}{\sin \theta} P_n^1(\cos \theta) h_n^{(1)}(\rho) + i a_n \frac{dP_n^m(\cos \theta)}{d\theta} \frac{1}{\rho} \frac{d}{d\rho} (\rho h_n^{(1)}(\rho))) \\
& - E_n (c_n \frac{1}{\sin \theta} P_n^1(\cos \theta) j_n(\rho_1) - i d_n \frac{dP_n^1(\cos \theta)}{d\theta} \frac{1}{\rho_1} \frac{d}{d\rho_1} (\rho_1 j_n(\rho_1))) \\
& + E_n (\frac{1}{\sin \theta} P_n^1(\cos \theta) j_n(\rho) - i \frac{dP_n^1(\cos \theta)}{d\theta} \frac{1}{\rho} \frac{d}{d\rho} (\rho j_n(\rho))) \\
\\
& = \sum_{n=1}^{\infty} E_n ((-1) \frac{dP_n^1(\cos \theta)}{d\theta} j_n(\rho) + i \frac{P_n^1(\cos \theta)}{\sin \theta} \frac{1}{\rho} \frac{d}{d\rho} (\rho j_n(\rho))) \\
& + E_n (-b_n (-1) \frac{dP_n^1(\cos \theta)}{d\theta} h_n^{(1)}(\rho) - i a_n \frac{P_n^1(\cos \theta)}{\sin \theta} \frac{1}{\rho} \frac{d}{d\rho} (\rho h_n^{(1)}(\rho))) \\
& - E_n (c_n (-1) \frac{dP_n^1(\cos \theta)}{d\theta} j_n(\rho_1) + i d_n \frac{P_n^1(\cos \theta)}{\sin \theta} \frac{1}{\rho_1} \frac{d}{d\rho_1} (\rho_1 j_n(\rho_1)))
\end{aligned}$$

$$\begin{aligned}
0 &= -\sum_{n=1}^{\infty} E_n \frac{k}{\omega\mu} \left(-\frac{1}{\sin\theta} P_n^1(\cos\theta) j_n(\rho) - i \frac{dP_n^1(\cos\theta)}{d\theta} \frac{1}{\rho} \frac{d}{d\rho} (\rho j_n(\rho)) \right) \\
&\quad - E_n \frac{k}{\omega\mu} \left(-a_n \frac{1}{\sin\theta} P_n^1(\cos\theta) h_n^{(1)}(\rho) + i b_n \frac{dP_n^1(\cos\theta)}{d\theta} \frac{1}{\rho} \frac{d}{d\rho} (\rho h_n^{(1)}(\rho)) \right) \\
&\quad - E_n \frac{k_1}{\omega\mu_1} \left(-d_n \frac{1}{\sin\theta} P_n^1(\cos\theta) j_n(\rho) + i c_n \frac{dP_n^1(\cos\theta)}{d\theta} \frac{1}{\rho} \frac{d}{d\rho} (\rho j_n(\rho)) \right) \\
\\
0 &= -\sum_{n=1}^{\infty} \frac{k}{\omega\mu} E_n \left(-\frac{dP_n^1(\cos\theta)}{d\theta} j_n(\rho) - i \frac{P_n^1(\cos\theta)}{\sin\theta} \frac{1}{\rho} \frac{d}{d\rho} (\rho j_n(\rho)) \right) \\
&\quad - E_n \frac{k}{\omega\mu} \left(-a_n \frac{dP_n^1(\cos\theta)}{d\theta} h_n^{(1)}(\rho) + i b_n \frac{P_n^1(\cos\theta)}{\sin\theta} \frac{1}{\rho} \frac{d}{d\rho} (\rho h_n^{(1)}(\rho)) \right) \\
&\quad - E_n \frac{k_1}{\omega\mu_1} \left(-d_n \frac{dP_n^1(\cos\theta)}{d\theta} j_n(\rho) + i c_n \frac{P_n^1(\cos\theta)}{\sin\theta} \frac{1}{\rho} \frac{d}{d\rho} (\rho j_n(\rho)) \right)
\end{aligned}$$

Now clearly we have two sums here, one of which is real, and the other imaginary. These sums must then satisfy condition of going to zero separately. For the electric part we have then:

real

$$\begin{aligned}
0 &= \sum_{n=1}^{\infty} -E_n b_n \frac{1}{\sin\theta} P_n^1(\cos\theta) h_n^{(1)}(\rho) - E_n c_n \frac{1}{\sin\theta} P_n^1(\cos\theta) j_n(\rho_1) + E_n \frac{1}{\sin\theta} P_n^1(\cos\theta) j_n(\rho) \\
0 &= \sum_{n=1}^{\infty} -E_n \frac{dP_n^1(\cos\theta)}{d\theta} j_n(\rho) + E_n b_n \frac{dP_n^1(\cos\theta)}{d\theta} h_n^{(1)}(\rho) + E_n c_n \frac{dP_n^1(\cos\theta)}{d\theta} j_n(\rho_1)
\end{aligned}$$

imaginary

$$\begin{aligned}
0 &= \sum_{n=1}^{\infty} i a_n \frac{dP_n^m(\cos\theta)}{d\theta} \frac{1}{\rho} \frac{d}{d\rho} (\rho h_n^{(1)}(\rho)) - i d_n \frac{dP_n^1(\cos\theta)}{d\theta} \frac{1}{\rho_1} \frac{d}{d\rho_1} (\rho_1 j_n(\rho_1)) - i \frac{dP_n^1(\cos\theta)}{d\theta} \frac{1}{\rho} \frac{d}{d\rho} (\rho j_n(\rho)) \\
0 &= \sum_{n=1}^{\infty} i \frac{P_n^1(\cos\theta)}{\sin\theta} \frac{1}{\rho} \frac{d}{d\rho} (\rho j_n(\rho)) - i a_n \frac{P_n^1(\cos\theta)}{\sin\theta} \frac{1}{\rho} \frac{d}{d\rho} (\rho h_n^{(1)}(\rho)) + i d_n \frac{P_n^1(\cos\theta)}{\sin\theta} \frac{1}{\rho_1} \frac{d}{d\rho_1} (\rho_1 j_n(\rho_1))
\end{aligned}$$

This allows us to cancel all dependence on theta except for the associated Legendre polynomials $P_n^1(\cos\theta)$.

real

$$0 = \sum_{n=1}^{\infty} -E_n b_n P_n^1(\cos \theta) h_n^{(1)}(\rho) - E_n c_n P_n^1(\cos \theta) j_n(\rho_1) + E_n P_n^1(\cos \theta) j_n(\rho)$$

$$0 = \sum_{n=1}^{\infty} -E_n \frac{dP_n^1(\cos \theta)}{d\theta} j_n(\rho) + E_n b_n \frac{dP_n^1(\cos \theta)}{d\theta} h_n^{(1)}(\rho) + E_n c_n \frac{dP_n^1(\cos \theta)}{d\theta} j_n(\rho_1)$$

imaginary

$$0 = \sum_{n=1}^{\infty} a_n \frac{dP_n^m(\cos \theta)}{d\theta} \frac{1}{\rho} \frac{d}{d\rho} (\rho h_n^{(1)}(\rho)) - d_n \frac{dP_n^1(\cos \theta)}{d\theta} \frac{1}{\rho_1} \frac{d}{d\rho_1} (\rho_1 j_n(\rho_1)) - \frac{dP_n^1(\cos \theta)}{d\theta} \frac{1}{\rho} \frac{d}{d\rho} (\rho j_n(\rho))$$

$$0 = \sum_{n=1}^{\infty} P_n^1(\cos \theta) \frac{1}{\rho} \frac{d}{d\rho} (\rho j_n(\rho)) - a_n P_n^1(\cos \theta) \frac{1}{\rho} \frac{d}{d\rho} (\rho h_n^{(1)}(\rho)) + d_n P_n^1(\cos \theta) \frac{1}{\rho_1} \frac{d}{d\rho_1} (\rho_1 j_n(\rho_1))$$

We know all that the associated Legendre polynomials form an orthogonal set, which means that these sums must satisfy the null condition term-wise, and we can just divide out the terms involving theta.

real

$$0 = -b_n h_n^{(1)}(\rho) - c_n j_n(\rho_1) + j_n(\rho)$$

$$0 = -j_n(\rho) + b_n h_n^{(1)}(\rho) + c_n j_n(\rho_1)$$

imaginary

$$0 = a_n \frac{1}{\rho} \frac{d}{d\rho} (\rho h_n^{(1)}(\rho)) - d_n \frac{1}{\rho_1} \frac{d}{d\rho_1} (\rho_1 j_n(\rho_1)) - \frac{1}{\rho} \frac{d}{d\rho} (\rho j_n(\rho))$$

$$0 = \frac{1}{\rho} \frac{d}{d\rho} (\rho j_n(\rho)) - a_n \frac{1}{\rho} \frac{d}{d\rho} (\rho h_n^{(1)}(\rho)) + d_n \frac{1}{\rho_1} \frac{d}{d\rho_1} (\rho_1 j_n(\rho_1))$$

Of course this is only two unique solutions. The other two come from the H-field, and are found in the same manner. This gives us four linear independent equations in four variables.

$$b_n h_n^{(1)}(x) + c_n j_n(mx) = j_n(x)$$

$$\mu m j_n(mx) d_n + \mu_1 h_n^{(1)}(x) a_n = \mu_1 j_n(x)$$

where $x = ka = 2\pi Na/\lambda$, and $m = k_1/k = N_1/N$

$$\mu [m x j_n(mx)]' c_n + \mu_1 [x h_n^{(1)}(x)]' b_n = \mu_1 [x j_n(x)]'$$

$$[m x j_n(mx)]' d_n + m [x h_n^{(1)}(x)]' a_n = m [x j_n(x)]'$$

These can be easily solved:

$$b_n = \frac{j_n(x) - c_n j_n(mx)}{h_n^{(1)}(x)}$$

Sub into second equation:

$$\mu[mxj_n(mx)]' c_n + \mu_1[xh_n^{(1)}(x)]' b_n = \mu_1[xj_n(x)]'$$

$$\mu[mxj_n(mx)]' c_n + \mu_1[xh_n^{(1)}(x)]' \frac{j_n(x) - c_n j_n(mx)}{h_n^{(1)}(x)} = \mu_1[xj_n(x)]'$$

Solve for C_n :

$$c_n = \frac{\mu_1 h_n^{(1)}(x)[xj_n(x)]' - \mu_1[xh_n^{(1)}(x)]' j_n(x)}{\mu h_n^{(1)}(x)[mxj_n(mx)]' - \mu_1[xh_n^{(1)}(x)]' j_n(mx)}$$

The other coefficients are solved similarly, giving the full set of coefficients:

Inside the particle

$$c_n = \frac{\mu_1 h_n^{(1)}(x)[xj_n(x)]' - \mu_1[xh_n^{(1)}(x)]' j_n(x)}{\mu h_n^{(1)}(x)[mxj_n(mx)]' - \mu_1[xh_n^{(1)}(x)]' j_n(mx)}$$

$$d_n = \frac{\mu_1 m h_n^{(1)}(x)[xj_n(x)]' - \mu_1[xh_n^{(1)}(x)]' m j_n(x)}{\mu_1 h_n^{(1)}(x)[mxj_n(mx)]' - \mu m^2[xh_n^{(1)}(x)]' j_n(mx)}$$

Scattered field coefficients

$$a_n = \frac{\mu m^2 j_n(mx)[xj_n(x)]' - \mu_1 j_n(x)[mxj_n(mx)]'}{\mu m^2[xh_n^{(1)}(x)]' j_n(mx) - \mu_1 h_n^{(1)}(x)[mxj_n(mx)]'}$$

$$b_n = \frac{\mu_1 j_n(mx)[xj_n(x)]' - \mu j_n(x)[mxj_n(mx)]'}{\mu_1[xh_n^{(1)}(x)]' j_n(mx) - \mu h_n^{(1)}(x)[mxj_n(mx)]'}$$

Now, if the denominators in the coefficients go towards zero, the corresponding mode will become extremely large. This condition would be satisfied if:

For c_n, b_n :

$$\frac{[xh_n^{(1)}(x)]'}{h_n^{(1)}(x)} = \frac{\mu[mxj_n(mx)]'}{\mu_1 j_n(mx)}$$

For a_n, d_n :

$$\frac{[xh_n^{(1)}(x)]'}{h_n^{(1)}(x)} = \frac{\mu_1[mxj_n(mx)]'}{\mu m^2 j_n(mx)}$$

We can generate full scattering cross sections from the scattered and incident fields. The absorption cross section is given by the net rate at which electromagnetic energy crosses the surface of a virtual sphere that just surrounds our particle divided by the incident intensity. I.e. W_a/I_i . The time averaged Poynting vector $\bar{S} = \frac{1}{2} \text{Re}\{\bar{E} \times \bar{H}^*\}$ gives the flux of energy at any point. This can be broken into three parts:

$$\begin{aligned}\bar{S} &= \frac{1}{2} \text{Re}\{(\bar{E}_i + \bar{E}_s) \times (\bar{H}_i^* + \bar{H}_s^*)\} \\ \bar{S} &= \frac{1}{2} \text{Re}\{\bar{E}_i \times \bar{H}_i^*\} + \frac{1}{2} \text{Re}\{\bar{E}_s \times \bar{H}_s^*\} + \frac{1}{2} \text{Re}\{\bar{E}_i \times \bar{H}_s^* + \bar{E}_s \times \bar{H}_i^*\} \\ &= \bar{S}_i + \bar{S}_s + \bar{S}_{ext}\end{aligned}$$

Where i is the incident field, s the scattered, and ext denotes the interaction terms between the two (hence the mixed cross product). Radial flux does not penetrate the imaginary sphere, and thus would not contribute to the scattering flux. Thus, the total energy crossing the sphere is given by: $W_a = -\int_A \bar{S} \cdot \bar{e}_r dA = W_{ext} - W_s = -\int_A \bar{S}_{ext} \cdot \bar{e}_r dA - \int_A \bar{S}_s \cdot \bar{e}_r dA$.

And the extinction cross section is given by: $C_{ext} = \frac{W_{ext}}{I_i}$.

For our case of spherical coordinates, the calculation of C_s and C_{ext} are found in the following manner:

$$\begin{aligned}W_{ext} &= \frac{1}{2} \text{Re}\left\{\int_0^{2\pi} \int_0^\pi (E_{i\phi} H_{s\theta}^* - E_{i\theta} H_{s\phi}^* - E_{s\theta} H_{i\phi}^* + E_{s\phi} H_{i\theta}^*) a^2 \sin\theta d\theta d\phi\right\} \\ W_s &= \frac{1}{2} \text{Re}\left\{\int_0^{2\pi} \int_0^\pi (E_{s\theta} H_{s\phi}^* - E_{s\phi} H_{s\theta}^*) a^2 \sin\theta d\theta d\phi\right\}\end{aligned}$$

where we take the imaginary sphere to be the size of the particle $r=a$.

Incident field

$$E_{i\theta} = \frac{\cos \phi}{\rho} \sum_{n=1}^{\infty} E_n (\psi_n \pi_n - i\psi_n' \tau_n)$$

$$E_{i\phi} = \frac{\sin \phi}{\rho} \sum_{n=1}^{\infty} E_n (i\psi_n' \pi_n - \psi_n \tau_n)$$

$$H_{i\theta}^* = \frac{k}{\omega\mu} \tan \phi E_{i\theta}^* = \frac{k}{\omega\mu} \tan \phi \frac{\cos \phi}{\rho} \sum_{n=1}^{\infty} E_n (\psi_n \pi_n + i\psi_n' \tau_n)$$

$$H_{i\phi}^* = \frac{-k}{\omega\mu} \cot \phi E_{i\phi}^* = \frac{k}{\omega\mu} \frac{\sin \phi}{\rho} \sum_{n=1}^{\infty} E_n (i\psi_n' \pi_n + \psi_n \tau_n)$$

Scattered field

$$E_{s\theta} = \frac{\cos \phi}{\rho} \sum_{n=1}^{\infty} E_n (ia_n \xi_n' \tau_n - b_n \xi_n \pi_n)$$

$$E_{s\phi} = \frac{\sin \phi}{\rho} \sum_{n=1}^{\infty} E_n (b_n \xi_n \tau_n - ia_n \xi_n' \pi_n)$$

$$H_{s\theta}^* = \frac{-k}{\omega\mu} \frac{\sin \phi}{\rho} \sum_{n=1}^{\infty} E_n^* (ib_n^* \xi_n^* \tau_n + a_n^* \xi_n^* \pi_n)$$

$$H_{s\phi}^* = \frac{-k}{\omega\mu} \frac{\cos \phi}{\rho} \sum_{n=1}^{\infty} E_n^* (ib_n^* \xi_n^* \pi_n + a_n^* \xi_n^* \tau_n)$$

where we have used the notation substitutions of Bohren and Huffman in which:

$$\xi_n(\rho) = \rho h_n^{(1)}(\rho)$$

$$\psi_n(\rho) = \rho j_n(\rho)$$

$$\tau_n = \frac{dP_n^1}{d\theta}$$

$$\pi_n = \frac{P_n^1}{\sin \theta}$$

The solution to W_s can be found in the following manner:

$$\begin{aligned}
W_s &= \frac{1}{2} \operatorname{Re} \left\{ \int_0^{2\pi} \int_0^\pi \left(\frac{\cos \phi}{\rho} \right)^2 \left(\sum_{n=1}^{\infty} E_n (i a_n \xi'_n \tau_n - b_n \xi_n \pi_n) \right) \left(\frac{-k}{\omega \mu} \sum_{t=1}^{\infty} E_t^* (i b_t^* \xi_t^* \pi_t + a_t^* \xi_t^* \tau_t) \right) \right. \\
&\quad \left. - \left(\frac{\sin \phi}{\rho} \right)^2 \left(\sum_{n=1}^{\infty} E_n (b_n \xi_n \tau_n - i a_n \xi'_n \pi_n) \right) \left(\frac{-k}{\omega \mu} \sum_{t=1}^{\infty} E_t^* (i b_t^* \xi_t^* \tau_t + a_t^* \xi_t^* \pi_t) \right) \right\} a^2 \sin \theta d\theta d\phi \\
&= \frac{1}{2} \operatorname{Re} \left\{ \int_0^{2\pi} \int_0^\pi \left(\frac{\cos \phi}{\rho} \right)^2 \frac{k}{\omega \mu} \left(\sum_{t=1}^{\infty} \sum_{n=1}^{\infty} E_n E_t^* (b_n \xi_n \pi_n - i a_n \xi'_n \tau_n) (i b_t^* \xi_t^* \pi_t + a_t^* \xi_t^* \tau_t) \right) \right. \\
&\quad \left. + \frac{k}{\omega \mu} \left(\frac{\sin \phi}{\rho} \right)^2 \left(\sum_{t=1}^{\infty} \sum_{n=1}^{\infty} E_n E_t^* (b_n \xi_n \tau_n - i a_n \xi'_n \pi_n) (i b_t^* \xi_t^* \tau_t + a_t^* \xi_t^* \pi_t) \right) \right\} a^2 \sin \theta d\theta d\phi
\end{aligned}$$

Switching the integration and summation so that we integrate termwise and throwing out imaginary terms

$$\begin{aligned}
&= \frac{1}{2} \operatorname{Re} \left\{ \sum_{t=1}^{\infty} \sum_{n=1}^{\infty} \left(\frac{k}{\omega \mu} E_n E_t^* \int_0^{2\pi} \int_0^\pi \left(\frac{\cos \phi}{\rho} \right)^2 (i b_n b_t^* \xi_n \xi_t^* \pi_n \pi_t + b_n a_t^* \xi_n \xi_t^* \pi_n \tau_t + a_n b_t^* \xi_n \xi_t^* \tau_n \pi_t - i a_n a_t^* \xi_n \xi_t^* \tau_n \tau_t) a^2 \sin \theta d\theta d\phi \right. \right. \\
&\quad \left. \left. + \frac{k}{\omega \mu} E_n E_t^* \int_0^{2\pi} \int_0^\pi \left(\frac{\sin \phi}{\rho} \right)^2 (i b_n b_t^* \xi_n \xi_t^* \tau_n \tau_t + b_n a_t^* \xi_n \xi_t^* \tau_n \pi_t + a_n b_t^* \xi_n \xi_t^* \pi_n \tau_t - i a_n a_t^* \xi_n \xi_t^* \pi_n \pi_t) a^2 \sin \theta d\theta d\phi \right) \right\}
\end{aligned}$$

We can evaluate the ϕ part, and $\rho=ka$, and the remaining terms are repeats so that:

$$= \frac{\pi}{2k\omega\mu} \sum_{t=1}^{\infty} \sum_{n=1}^{\infty} (E_n E_t^* \operatorname{Re} \left\{ \int_0^\pi (i b_n b_t^* \xi_n \xi_t^* (\pi_n \pi_t + \tau_n \tau_t) - i a_n a_t^* \xi_n \xi_t^* (\pi_n \pi_t + \tau_n \tau_t) + 2b_n a_t^* \xi_n \xi_t^* \tau_n \pi_t + 2a_n b_t^* \xi_n \xi_t^* \pi_n \tau_t) \sin \theta d\theta \right\})$$

Using the following identities (which arise from the Legendre polynomials):

$$\begin{aligned}
\int_0^\pi (\tau_n + \pi_n)(\tau_t + \pi_t) \sin \theta d\theta &= \int_0^\pi (\tau_n \tau_t + \pi_t \tau_n + \tau_t \pi_n + \pi_n \pi_t) \sin \theta d\theta = \delta_{nm} \frac{2n^2(n+1)^2}{2n+1} \\
\int_0^\pi (\pi_n \tau_t + \tau_n \pi_t) \sin \theta d\theta &= 0
\end{aligned}$$

So continuing the result:

$$= \frac{\pi}{2k\omega\mu} \sum_{n=1}^{\infty} \frac{E_0^2 (2n+1)^2}{n^2(n+1)^2} \operatorname{Re} \left\{ (i b_n b_n^* \xi_n \xi_n^* \frac{2n^2(n+1)^2}{2n+1} - i a_n a_n^* \xi_n \xi_n^* \frac{2n^2(n+1)^2}{2n+1}) \right\}$$

$$= \frac{\pi}{k\omega\mu} \sum_{n=1}^{\infty} E_0^2 (2n+1) \operatorname{Re} \{ (ib_n b_n^* \xi_n \xi_n^* - ia_n a_n^* \xi_n' \xi_n'^*) \}$$

We can use the following result:

$$\xi_n = \rho h_n^{(1)} = \psi_n - i\chi_n$$

$$\xi_n^* = \psi_n + i\chi_n$$

$$\operatorname{Re} \{ i\xi_n \xi_n'^* \} = \operatorname{Re} \{ i\psi_n \psi_n' - \psi_n \chi_n' + \psi_n' \chi_n + i\chi_n \chi_n' \} = \psi_n' \chi_n - \psi_n \chi_n' = 1$$

$$\operatorname{Re} \{ i\xi_n' \xi_n^* \} = \operatorname{Re} \{ i\psi_n \psi_n' + \psi_n \chi_n' - \psi_n' \chi_n + i\chi_n \chi_n' \} = \psi_n \chi_n' - \psi_n' \chi_n = -1$$

$$W_s = \frac{\pi E_0^2}{k\omega\mu} \sum_{n=1}^{\infty} (2n+1) (|b_n|^2 + |a_n|^2)$$

W_{ext} follows similarly so that:

$$\begin{aligned} C_s &= \frac{W_s}{I_i} = \left(\frac{2\omega\mu}{kE_0^2} \right) \frac{\pi E_0^2}{k\omega\mu} \sum_{n=1}^{\infty} (2n+1) (|b_n|^2 + |a_n|^2) \\ &= \frac{2\pi}{k^2} \sum_{n=1}^{\infty} (2n+1) (|b_n|^2 + |a_n|^2) \end{aligned}$$

$$C_{\text{ext}} = \frac{W_{\text{ext}}}{I_i} = \frac{2\pi}{k^2} \sum_{n=1}^{\infty} (2n+1) \operatorname{Re} \{ a_n + b_n \}$$

$$\begin{aligned} C_s &= \frac{W_s}{I_i} = \left(\frac{2\omega\mu}{kE_0^2} \right) \frac{\pi E_0^2}{k\omega\mu} \sum_{n=1}^{\infty} (2n+1) (|b_n|^2 + |a_n|^2) \\ &= \frac{2\pi}{k^2} \sum_{n=1}^{\infty} (2n+1) (|b_n|^2 + |a_n|^2) \end{aligned}$$

$$C_{\text{ext}} = \frac{W_{\text{ext}}}{I_i} = \frac{2\pi}{k^2} \sum_{n=1}^{\infty} (2n+1) \operatorname{Re} \{ a_n + b_n \}$$

The extinction and scattering efficiencies are then given by:

$$Q_{\text{ext}} = \frac{C_{\text{ext}}}{\pi a^2}$$

$$Q_s = \frac{C_s}{\pi a^2}$$

Coated Sphere

Considering now the case of a coated sphere, much of the previous results can be altered. Since region 2 does not include the origin Bessel functions of both the first and second kind are permitted. The form of the equations follows similarly to the previous functions.

$$\bar{E}_2 = \sum_{n=1}^{\infty} E_n [f_n \bar{M}_{o1n}^{(1)} - i g_n \bar{N}_{e1n}^{(1)} + v_n \bar{M}_{o1n}^{(2)} - i w_n \bar{N}_{e1n}^{(2)}]$$

$$\bar{H}_2 = -\frac{k_2}{\omega \mu_2} \sum_{n=1}^{\infty} E_n [g_n \bar{M}_{e1n}^{(1)} + i f_n \bar{N}_{o1n}^{(1)} + w_n \bar{M}_{e1n}^{(2)} + i v_n \bar{N}_{o1n}^{(2)}]$$

Boundary conditions are given by:

For $r=a$

$$(E_2 - E_1) \times \bar{e}_r = 0$$

$$(H_2 - H_1) \times \bar{e}_r = 0$$

For $r=b$

$$(E_s + E_i - E_2) \times \bar{e}_r = 0$$

$$(H_s + H_i - H_2) \times \bar{e}_r = 0$$

Giving linear coefficient equations from Bohren and Huffman (where again $x=ka$, and $y=kb$):

$$f_n m_1 \psi_n(m_2 x) - v_n m_1 \chi_n(m_2 x) - c_n m_2 \psi_n(m_1 x) = 0$$

$$w_n m_1 \chi_n'(m_2 x) - g_n m_1 \psi_n'(m_2 x) + d_n m_2 \psi_n'(m_1 x) = 0$$

$$v_n \mu_1 \chi_n'(m_2 x) - f_n \mu_1 \psi_n'(m_2 x) + c_n \mu_2 \psi_n'(m_1 x) = 0$$

$$g_n \mu_1 \psi_n(m_2 x) - w_n \mu_1 \chi_n(m_2 x) - d_n \mu_2 \psi_n(m_1 x) = 0$$

$$m_2 \psi_n'(y) - a_n m_2 \xi_n'(y) - g_n \psi_n'(m_2 y) + w_n \chi_n'(m_2 y) = 0$$

$$m_2 b_n \xi_n(y) - m_2 \psi_n(y) + f_n \psi_n(m_2 y) - v_n \chi_n(m_2 y) = 0$$

$$\mu_2 \psi_n(y) - a_n \mu_2 \xi_n(y) - g_n \mu \psi_n(m_2 y) + w_n \mu \chi_n(m_2 y) = 0$$

$$b_n \mu_2 \xi_n'(y) - \mu_2 \psi_n'(y) + f_n \mu \psi_n'(m_2 y) - v_n \mu \chi_n'(m_2 y) = 0$$

The solution to this system of equations, for the scattering coefficients a_n , and b_n (we don't care about the field in the coating), for non-magnetic situations in which $\mu=\mu_1=\mu_2$, are given by:

$$a_n = \frac{\psi_n(y)[\psi_n'(m_2 y) - A_n \chi_n'(m_2 y)] - m_2 \psi_n'(y)[\psi_n(m_2 y) - A_n \chi_n(m_2 y)]}{\xi_n(y)[\psi_n'(m_2 y) - A_n \chi_n'(m_2 y)] - m_2 \xi_n'(y)[\psi_n(m_2 y) - A_n \chi_n(m_2 y)]}$$

$$b_n = \frac{m_2 \psi_n(y)[\psi_n'(m_2 y) - B_n \chi_n'(m_2 y)] - \psi_n'(y)[\psi_n(m_2 y) - B_n \chi_n(m_2 y)]}{m_2 \xi_n(y)[\psi_n'(m_2 y) - B_n \chi_n'(m_2 y)] - \xi_n'(y)[\psi_n(m_2 y) - B_n \chi_n(m_2 y)]}$$

where

$$A_n = \frac{m_2 \psi_n(m_2 x) \psi_n'(m_1 x) - m_1 \psi_n'(m_2 x) \psi_n(m_1 x)}{m_2 \chi_n(m_2 x) \psi_n'(m_1 x) - m_1 \chi_n'(m_2 x) \psi_n(m_1 x)}$$

$$B_n = \frac{m_2 \psi_n(m_1 x) \psi_n'(m_2 x) - m_1 \psi_n'(m_1 x) \psi_n(m_2 x)}{m_2 \chi_n'(m_2 x) \psi_n(m_1 x) - m_1 \chi_n(m_2 x) \psi_n'(m_1 x)}$$

Q_{ext} is found in the same way as the uncoated sphere, substituting our new E and H fields. This is the final result, that we know all fields everywhere and can calculate our Q_{ext} for any given wavelength for the coated sphere.

Appendix B: Bulk Plasma Frequency Shift

Used to find the values of w_p that will reproduce the bare wavelengths at an index of refraction of 1.33 and coating thickness of 0. Requires Matlab routine by C. Mätzler [211] Miecoated routine to be present

```
%-----Initial Setup-----  
-----  
  
clear all  
  
fid=fopen('Wp_Shift_Factor.txt','wt');  
  
  
divlambd=.05e-9;           %spacing of wavelengths  
  
Startwavelength=490*10^-9;   %Starting wavelength  
  
Stopwavelength=580*10^-9;   %Ending wavelength  
  
numpoints=round((Stopwavelength-Startwavelength)/divlambd);   %Number  
of points that will be calculated between start and stop wavelength  
  
  
ExpPeakValue=[522.3917];  
%Experimental peak wavelength of bare sphere  
  
sizes=[20];                %Sizes  
(diameter) corresponding to peak to calculate  
  
FlagValue=0;  
  
wpsizes=1*(10^16)*[0.005]; %Matrix  
of guess corrections to bulk plasmon resonance  
  
  
while(FlagValue==0)
```

```

%-----Create an array with wavelengths and corresponding
wavevectors-----

for count=1:1:numpoints

    wavelength(count)=Startwavelength + (count-1)*divlambdai;

end

Nwat=1.33;
%Surrounding medium (water)

k0=2*pi*Nwat./wavelength;
%Wavevector in Ambient material

%-----Start of Main Program-----
-----

%*****Gold Nanoparticle
Constants*****
*****

innercore=1;

a=0.5*sizes(innercore)*10^-9;           %Inner radius

gbulk=1.64*10^14;                       %Size independent
damping constant 1.64*10^14

vf=14.1*10^14;                          %Fermi velocity
1.41*10^14

gamma=gbulk + 1*vf/(a*10^9);            %Size dependent damping
constant with finite size effects included

wp=1.3*10^16;                            %Bulk plasma frequency
1.3*10^(16)

wpnew=1.3*10^16 + wpsizes(innercore);   %New Bulk plasma
frequency (0.135,0.5)

%*****
*****

```

```

%-----Fitted Index of Refraction for Bulk Gold-----
-----
eprime=31.4199 - 0.0679*wavelength*10^9;

e2prime=-416.5513 + 703616.2145./((wavelength*10^9)) -
396337158.8805./((wavelength*10^9).^2) +
74793091592.0138./((wavelength*10^9).^3);

%-----Adjust Damping for Size Dependence, and Wp Correction-----
-----

for count=1:length(wavelength)

    w(count)=2*pi*3e8/(wavelength(count));

    eprime(count)=eprime(count) - ( 1-wp^2/(w(count)^2+gbulk^2) ) + ( 1-
wpnew^2/(w(count)^2+gamma^2) );

    e2prime(count)=e2prime(count) - (
gbulk*wp^2/(w(count)*(w(count)^2+gbulk^2)) ) +
(gamma*wpnew^2/(w(count)*(w(count)^2+gamma^2)) );

end

%-----Setup Index of Refraction Arrays-----
-----

for j=1:numpoints

    n(j)=(0.5*((eprime(j)^2 + e2prime(j)^2)^(0.5) + eprime(j)))^(0.5);

    k(j)=(0.5*((eprime(j)^2 + e2prime(j)^2)^(0.5) - eprime(j)))^(0.5);

end

m1=(n+i*k)./Nwat;           %Index of refraction of sphere
relative to water array

x=k0*a;                     %Wavenumber of sphere

```

```

%-----Vary coating thickness and index of
refraction-----
Ncoating=1.33;      %Sphere coating
b=a;              %Outer radius
y=k0*b;           %Wavenumber of coating
m2=(Ncoating + 0*k)./Nwat;      %Index of refraction of coating
relative to water array

%-----Calculate Extinction Efficiency-----
-----
for j=1:numpoints
    Data=Miecoated(m1(j),m2(j),x(j),y(j),1);
    Extinction(j)=Data(1);
end

%-----Find wavelength of maximum-----
-----

[maxvalue,maxindex]=max(Extinction);
Peak_wavelengths=wavelength(maxindex)*10^9;

%-----Adjust Wp by Some Small Amount to
Fix Peak Position-----
DifferenceValue=Peak_wavelengths-ExpPeakValue

if (DifferenceValue>0.025)
    wpsizes=wpsizes + 1*(10^16)*[0.00015];    %Matrix of corrections to
bulk plasmon resonance
elseif (DifferenceValue < -0.025)
    wpsizes=wpsizes - 1*(10^16)*[0.00015];    %Matrix of corrections to
bulk plasmon resonance

```



```
else
    FlagValue=1; %The value is within the tolerance so exit
end

end %end of while loop (Wp has been found for particular value

% -----Output Results-----
-----

fprintf(fid, '%6.6f %6.6f %6.6f %6.6f \n', a*2*10^9, Peak_wavelengths,
max(Extinction), wpsizes(innercore)/(10^16));

fclose(fid);
```

Appendix C: Refractive Index/Thickness Contour Plot Generator

This program is the main routine which uses the Matlab routine by C. Mätzler [211] Micoated to generate a contour plot data of the extinction peak value, and position for a graph of index of refraction vs. coating thickness (nm).

```
%-----Initial Setup-----  
-----  
  
clear all  
  
fid=fopen('Contour_Data_For_Patricks_20nm_Wp_Vf_Shifted.txt','wt');  
  
divlambda=.05e-9;           %spacing of wavelengths  
Startwavelength=510*10^-9;  %Starting wavelength  
Stopwavelength=560*10^-9;  %Ending wavelength  
  
numpoints=round((Stopwavelength-Startwavelength)/divlambda); %Number  
of points that will be calculated between start and stop wavelength  
  
%-----Create an array with wavelengths and corresponding  
wavevectors-----  
  
for count=1:1:numpoints  
    wavelength(count)=Startwavelength + (count-1)*divlambda;  
end  
  
sizes=[20];                %Matrix of sizes to  
calculate  
  
wpsizes=1*(10^16)*[0.007550]; %Matrix of  
corrections to bulk plasmon resonance
```

```

Nwat=1.33; %Surrounding medium
(water)

k0=2*pi*Nwat./wavelength; %Wavevector in
Ambient material

for innercore=1:length(sizes)

%-----Start of Main Program-----
-----

%Gold Constants

a=0.5*sizes(innercore)*10^-9 %Inner radius

gbulk=1.64*10^14; %Size independent
damping constant 1.64*10^14

vf=14.1*10^14; %Fermi velocity
1.41*10^14

gamma=gbulk + 1*vf/(a*10^9); %Size dependent damping
constant

wp=1.3*10^16; %Bulk plasma frequency
1.3*10^(16)

wpnew=1.3*10^16 + wpsizes(innercore) %New Bulk plasma
frequency (0.135,0.5)

%-----Gold Index of Refraction-----
-----

eprime=31.4199 - 0.0679*wavelength*10^9;

e2prime=-416.5513 + 703616.2145./((wavelength*10^9)) -
396337158.8805./((wavelength*10^9).^2) +
74793091592.0138./((wavelength*10^9).^3);

```

```

%-----Adjust for size dependence-----
-----
for count=1:length(wavelength)

    w(count)=2*pi*3e8/(wavelength(count));

    eprime(count)=eprime(count) - ( 1-wp^2/(w(count)^2+gbulk^2) ) + (
    1-wpnew^2/(w(count)^2+gamma^2) );

    e2prime(count)=e2prime(count) - (
    gbulk*wp^2/(w(count)*(w(count)^2+gbulk^2)) ) +
    (gamma*wpnew^2/(w(count)*(w(count)^2+gamma^2)) );

end

%-----Interpolate Points and setup index of refraction arrays-----
-----
for j=1:numpoints

    n(j)=(0.5*((eprime(j)^2 + e2prime(j)^2)^(0.5) + eprime(j)))^(0.5);
    k(j)=(0.5*((eprime(j)^2 + e2prime(j)^2)^(0.5) - eprime(j)))^(0.5);

end

m1=(n+i*k)./Nwat;                %Index of refraction of sphere
relative to water array

x=k0*a;                          %Wavenumber of sphere

%-----Vary coating thickness and index of
refraction-----*
for outercoat=0:200
for indexcoat=0:50

Ncoating=1.30 + indexcoat*0.01;    %Sphere coating
b=a + .05*outercoat*(10^-9);      %Outer radius
y=k0*b;                            %Wavenumber of coating

```

```

m2=(Ncoating*ones(1,length(wavelength)) +
i*0*ones(1,length(wavelength))./Nwat;           %Index of refraction of
coating relative to water array

%-----Calculate Extinction Efficiency-----
-----

for j=1:numpoints
    Data=Miecoated(m1(j),m2(j),x(j),y(j),1);
    Extinction(j)=Data(1);
end

% -----The results-----
----

%Find wavelength of maximum
[maxvalue,maxindex]=max(Extinction);
%Find corresponding value of maximum
Peak_wavelengths=wavelength(maxindex)*10^9;
%Output the results
fprintf(fid, '%6.3f %6.3f %6.3f %6.3f %6.5f \n', a*2*10^9, (b-a)*10^9,
Ncoating, Peak_wavelengths, maxvalue);

end

end

end

fclose(fid);

```

Appendix D: Contour Plot Search Algorithm for Inversion of Mie Calculation

The following program searches through the generated contour plot for the best approximation to the experimentally measured peak wavelength and value, returning the associated index of refraction, and thickness.

```
clear all

fid=fopen('Output1.txt','wt');    %File in which to output results.

%*****Start of
Data*****
*****

%5nm

Peak(1,:)=[...values of peak extinction from contour generation
program...];

Extinction(1,:)=[...values of extinction wavelength from contour
generation program...];

ExpPeak(1,:)=[522.1437  521.9367  522.0878  521.5365  521.8626
              521.1002  521.5224  521.8450  521.8343];

ExpExt(1,:)=[0.1185  0.1170  0.1181  0.1217  0.1201
             0.1191  0.1200  0.1223  0.1163];

Length=length(Thickness(1,:));

%*****
****

count2=1;
```

```
%Distribution from contour generation program used to produce the arrays
Peak and Extinction

Thickness2=0:0.05:10;    %Values of thickness used to produce peak and
extinction values

Index2=1.3:0.01:1.8;    %Values of index of refraction used to produce
peak and extinction values

outercoat=201    %Number of coating thickness values
indexcoat=51    %Number of index of refraction values

for count=0:(outercoat-1)
    Peak2(count+1,:)=Peak(count2, (1 + indexcoat*count):(indexcoat +
indexcoat*count));

    Extinction2(count+1,:)=Extinction(count2, (1 +
indexcoat*count):(indexcoat + indexcoat*count));
end

%The following represent the grid spacing we'd like to have
Division1=1800;
Division2=1000;

%New coating thickness distribution
for count=1:Division1
    Thicknew(count)=0 + count*0.005;
end

%New index of refraction distribution
for count=1:Division2
    Indexnew(count)=1.4 + count*0.0005;
```

```
end

%Produce the actual Grid
[x,y]=meshgrid(Indexnew,Thicknew);
InterPeaks= interp2(Index2, Thickness2, Peak2, x, y, 'linear');
InterExtinction= interp2(Index2, Thickness2, Extinction2, x, y,
'linear');

clear Peak2;
clear Extinction2;
clear Thickness2;

%Reshape the arrays so they can be used by dsearch and for outputting
to file
TheorData= cat(2,reshape(InterPeaks,Division1*Division2,1),
reshape(InterExtinction, Division1*Division2,1));
clear InterPeaks;
clear InterExtinction;
clear IndexofRefraction;

IndexofRefraction=reshape(x,Division1*Division2,1);
CoatingThickness=reshape(y,Division1*Division2,1);

clear x;
clear y;

%Setup an array to be used by dsearchn with experimental data
```



```
for count=1:length(ExpExt(count2,:))
    ExpData(count,2)=ExpExt(count2,count);
    ExpData(count,1)=ExpPeak(count2,count);
end

%Perform a search for the first point, and adjust the initial extinction,
until the index of refraction of the first point is a specific value (eg.
1.57)

clear k;
k = dsearchn(TheorData,ExpData);

%Output the scaling factor for the data so that the first point will
produce an N value of __ (eg. 1.57)
fprintf(fid, '%6.6f \n', count2);

fprintf(fid, '%6.6f \n', count2);
for count=1:length(ExpExt(count2,:))
    fprintf(fid, '%6.6f %6.6f %6.6f %6.6f \n', TheorData(k(count),1),
TheorData(k(count),2), IndexofRefraction(k(count)),
CoatingThickness(k(count)) );
end
```

Appendix E: Homogeneous, No-Slip, N-Layer Voigt Model of QCM

The following program is used to calculate the frequency and dissipation for any number of overtones caused by depositing any number of layers for a QCM crystal. This is based on the solution of Voinova et al. [215].

```
clear all

fid=fopen('ProteinOnPHEMA.txt','wt');

%*****
%*****

%User Defined Layer Parameters. Each layer is a separate column. Any
number of layers can be added

mu=          [1.208*10^9,    2.5531e+006,    1*10^9,    0];
eta=         [0,           0.4497,         0,           0.0007];
rho=         [1050,        1098.7,        1330,        1000];
h=           [95*10^(-9),   379.95*10^(-9),  90*10^(-9),  5000*10^(-
9)];

%User Defined Bare Crystal Parameters

%Voinova Paper values

rho0=2648;

f0= 4.96*10^6;

fr=3*f0;

h0=3340/(2*f0);
```

```

%*****
%*****
%Perform calculation for fundamental frequency and first two overtones.
for freqcount=1:2:5
fr=freqcount*f0;

%Calculated parameters
NLayers=length(mu);

w=2*pi*fr;

for count=2:NLayers
    H(count-1)=h(count);
end

for count=1:NLayers
    zeta(count)=( -(rho(count)*(w^2))/(mu(count) + i*w*eta(count)) )^0.5;
    K(count)=(eta(count) - i*mu(count)/w);
end

A(NLayers)=1;
for count=(NLayers-1):-1:1
    A(count)=(K(count)*zeta(count)*(1 +
A(count+1)*exp(2*zeta(count+1)*H(count))) - K(count+1)*zeta(count+1)*(1 -
A(count+1)*exp(2*zeta(count+1)*H(count)))) / (K(count)*zeta(count)*(1 +
A(count+1)*exp(2*zeta(count+1)*H(count))) + K(count+1)*zeta(count+1)*(1 -
A(count+1)*exp(2*zeta(count+1)*H(count))));
end

```

```
BetaFunction=K(1)*zeta(1)* (1 - A(1)*exp(2*zeta(1)*h(1))) / (1 +
A(1)*exp(2*zeta(1)*h(1)) );

DeltaFrequency(freqcount)=sensitivity(freqcount)*imag(BetaFunction/(2*pi*
rho0*h0))-shiftF(freqcount);

DeltaDissipation(freqcount)=-real(BetaFunction/(pi*fr*rho0*h0))-
shiftD(freqcount);

end

fprintf(fid, '%6.2f %6.6f %6.6f %6.6f %6.6f %6.6f %6.6f \n', h(3)*10^9,
DeltaFrequency(1), DeltaDissipation(1)*10^6, DeltaFrequency(3),
DeltaDissipation(3)*10^6, DeltaFrequency(5), DeltaDissipation(5)*10^6);
```

Bibliography

1. Mulder, G.J., *Über die Zusammensetzung Einiger Thierischen Substanzen*. Journal für Praktische Chemie, 1839. **16**: p. 129.
2. Hofmeister, F., *Über Bau und Gruppierung der Eiweisskörper*. Ergebnisse der Physiologie, 1902. **1**: p. 759.
3. Landsteiner, K. and R. Uhliz, *Über die Adsorption von Eiweisskörpern*. Zentralblatt für Bakteriologie, Parasitenkunde, Infektionskrankheiten und Hygiene. 1. Abt Medizinisch-hygienische Bakteriologie, Virusforschung und tierische Parasitologie., 1905. **40**: p. 265-276.
4. Hitchcock, D., *Protein Films on Collodion Membranes*. Journal of General Physiology., 1925. **8**: p. 61-74.
5. Akiyama, S.K. and S.E. LaFlamme, *Bioadhesion and Cell Behaviour*. Colloids and Surfaces B: Biointerfaces., 1994. **2**: p. 241-250.
6. Horbett, T.A., *The Role of Adsorbed Proteins in Animal Cell Adhesion*. Colloids and Surfaces B: Biointerfaces., 1994. **2**: p. 225-240.
7. Levinthal, C., *Are There Pathways for Protein Folding?* Extrait du Journal de Chimie Physique, 1968. **65**(1): p. 44.
8. Dickerson, R.E. and I. Geis, *The Structure and Action of Proteins*. 1969, New York: Harper & Row.

9. Branden, C. and J. Tooze, *Introduction to Protein Structure*. second ed. 1999, New York, NY: Garland Publishing Inc.
10. Vaney, M.C., S. Maignan, M. Ries-Kautt, and A. Ducruix, *High-Resolution Structure (1.33 Å) of a HEW Lysozyme Tetragonal Crystal Grown in the APCF Apparatus. Data and Structural Comparison with a Crystal Grown under Microgravity from SpaceHab-01 Mission*. Acta Crystallographica Section D, 1996. **52**(3): p. 505-517.
11. Moore, S.A., B.F. Anderson, C.R. Groom, M. Haridas, and E.N. Baker, *Three-dimensional structure of diferric bovine lactoferrin at 2.8 Å resolution*. Journal of Molecular Biology, 1997. **274**(2): p. 222-236.
12. Berman, H.M., J. Westbrook, Z. Feng, G. Gilliland, T.N. Bhat, H. Weissig, I.N. Shindyalov, and P.E. Bourne, *The Protein Data Bank*. Nucleic Acids Research, 2000. **28**: p. 235-242.
13. Daune, M., *Molecular Biophysics: Structures in Motion*. 1999, New York: Oxford University Press Inc.
14. Tanford, C. and J.G. Kirkwood, *Theory of Protein Titration Curves. I. General Equations for Impenetrable Spheres*. Journal of the American Chemical Society, 1957. **79**(20): p. 5333-5339.
15. Tanford, C., *Theory of Protein Titration Curves. II. Calculations for Simple Models at Low Ionic Strength*. Journal of the American Chemical Society, 1957. **79**(20): p. 5340-5347.

16. Norde, W., *Driving Forces for Protein Adsorption at Solid Surfaces*, in *Biopolymers at Interfaces, Surfactant Science Series*, M. Malmsten, Editor. 2003, Marcel Dekker, Inc.: Stockholm, Sweden. p. 21-44
17. Barlow, D.J. and J.M. Thornton, *Ion-pairs in proteins*. *Journal of Molecular Biology*, 1983. **168**(4): p. 867-885.
18. Yutani, K., K. Ogasahara, K. Aoki, T. Kakuno, and Y. Sugino, *Effect of amino acid residues on conformational stability in eight mutant proteins variously substituted at a unique position of the tryptophan synthase alpha-subunit*. *J. Biol. Chem*, 1984. **259**(22): p. 14076-14081.
19. Herzberg, O. and J. Moult, *Analysis of the steric strain in the polypeptide backbone of protein molecules*. *Proteins*, 1991. **11**(3): p. 223-229.
20. van Oss, C.J., *Hydrophobicity of Biosurfaces—Origin, Quantitative determination and Interaction Energies*. *Colloids and Surfaces B: Biointerfaces.*, 1995. **5**: p. 91-110.
21. Norde, W., *Adsorption of proteins from solution at the solid-liquid interface*. *Advances in Colloid and Interface Science*, 1986. **25**: p. 267-340.
22. van der Veen, M., M.C. Stuart, and W. Norde, *Spreading of proteins and its effect on adsorption and desorption kinetics*. *Colloids and Surfaces B: Biointerfaces*, 2007. **54**(2): p. 136-142.
23. Norde, W., *Ion Participation in Protein Adsorption at Solid Surfaces*. *Colloids and Surfaces.*, 1984. **10**: p. 21-31.

24. Gray, J.J., *The interaction of proteins with solid surfaces*. Current Opinion in Structural Biology, 2004. **14**(1): p. 110-115.
25. Werner, C. and H. Jacobasch, *Biomaterials-Surface Characterization of Polymers for Medical Devices*. International Journal of Artificial Organs., 1999. **22,3**: p. 160-176.
26. Haynes, C.A. and W. Norde, *Globular proteins at solid/liquid interfaces*. Colloids and Surfaces B: Biointerfaces, 1994. **2**(6): p. 517-566.
27. Hopkinson, R. and R. Jones, *Unfolding and Intermolecular Association in Globular Proteins Adsorbed at Interfaces*. Langmuir., 1999. **15**: p. 5102-5110.
28. Wertz, C.F. and M.M. Santore, *Adsorption and Relaxation Kinetics of Albumin and Fibrinogen on Hydrophobic Surfaces: Single-Species and Competitive Behaviour*. Langmuir., 1999. **15**: p. 8884-8894.
29. Wertz, C.R. and M.M. Santore, *Effect of Surface Hydrophobicity on Adsorption and Relaxation Kinetics of Albumin and Fibrinogen: Single-Species and Competitive Behaviour*. Langmuir., 2001. **17**: p. 3006-3016.
30. Wertz, C.R. and M.M. Santore, *Fibrinogen Adsorption on Hydrophilic and Hydrophobic Surfaces: Geometrical and Energetic Aspects of Interfacial Relaxations*. Langmuir., 2002. **18**: p. 706-715.
31. Wertz, C.R. and M.M. Santore, *Adsorption and Reorientation Kinetics of Lysozyme on Hydrophobic Surfaces*. Langmuir., 2002. **18**: p. 1190-1199.
32. Giacomelli, C.E., M. Bremer, and W. Norde, *ATR-FTIR Study of IgG Adsorbed on Different Silica Surfaces*. J. Colloid and Interface Sci., 1999. **220**: p. 13-23.

33. Su, T.J., J.R. Lu, R.K. Thomas, Z.F. Cui, and J. Penfold, *The Conformational Structure of Bovine Serum Albumin Layers Adsorbed at the Silica-Water Interface*. J. Phys. Chem. B, 1998. **102**(41): p. 8100-8108.
34. Giacomelli, C.E. and W. Norde, *The Adsorption-Desorption Cycle Reversibility of the BSA-Silica System*. J. Colloid and Interface Sci., 2001. **233**: p. 234-240.
35. Read, M.J. and S.L. Burkett, *Asymmetric α -Helicity Loss Within a Peptide Adsorbed onto Charged Colloidal Substrates*. J. Colloid and Interface Sci., 2003. **261**: p. 255-263.
36. Mrksich, M. and G.M. Whitesides, *Using Self-Assembled Monolayers to Understand the Interactions of Man-made Surfaces with Proteins and Cells*. Annual Review of Biophysics and Biomolecular Structure, 1996. **25**(1): p. 55-78.
37. Ostuni, E., B.A. Grzybowski, M. Mrksich, C.S. Roberts, and G.M. Whitesides, *Adsorption of Proteins to Hydrophobic Sites on Mixed Self-Assembled Monolayers*. Langmuir, 2003. **19**: p. 1861-1872.
38. Sigal, G.B., M. Mrksich, and G.M. Whitesides, *Effect of Surface Wettability on the Adsorption of Proteins and Detergents*. Journal of the American Chemical Society, 1998. **120**(14): p. 3464-3473.
39. Li, L., S. Chen, and S. Jiang, *Protein Adsorption on Alkanethiolate Self-Assembled Monolayers: Nanoscale Surface Structural and Chemical Effects*. Langmuir., 2003. **19**: p. 2974-2982.
40. Johnson, C.A., Y. Yuan, and A.M. Lenhoff, *Adsorbed Layers of Ferritin at Solid and Fluid Interfaces Studied by Atomic Force Microscopy*. J. Colloid and Interface Sci., 2000. **223**: p. 261-272.

41. Norde, W. and J. Lyklema, *The adsorption of human plasma albumin and bovine pancreas ribonuclease at negatively charged polystyrene surfaces: I. Adsorption isotherms. Effects of charge, ionic strength, and temperature.* Journal of Colloid and Interface Science, 1978. **66**(2): p. 257-265.
42. Norde, W. and J. Lyklema, *The adsorption of human plasma albumin and bovine pancreas ribonuclease at negatively charged polystyrene surfaces : II. Hydrogen ion titrations.* Journal of Colloid and Interface Science, 1978. **66**(2): p. 266-276.
43. Norde, W. and J. Lyklema, *The adsorption of human plasma albumin and bovine pancreas ribonuclease at negatively charged polystyrene surfaces : III. Electrophoresis.* Journal of Colloid and Interface Science, 1978. **66**(2): p. 277-284.
44. Norde, W. and J. Lyklema, *The adsorption of human plasma albumin and bovine pancreas ribonuclease at negatively charged polystyrene surfaces : IV. The charge distribution in the adsorbed state.* Journal of Colloid and Interface Science, 1978. **66**(2): p. 285-294.
45. Norde, W. and J. Lyklema, *The adsorption of human plasma albumin and bovine pancreas ribonuclease at negatively charged polystyrene surfaces : V. Microcalorimetry.* Journal of Colloid and Interface Science, 1978. **66**(2): p. 295-302.
46. Norde, W. and J. Lyklema, *Thermodynamics of Protein Adsorption: Theory with Special Reference to the Adsorption of Human Plasma Albumin and Bovine Pancreas Ribonuclease at Polystyrene Surfaces.* Journal of Colloid and Interface Science, 1979. **71**: p. 350-366.
47. Van Dulm, P., W. Norde, and J. Lyklema, *Ion participation in protein adsorption at solid surfaces.* Journal of Colloid and Interface Science, 1981. **82**(1): p. 77-82.

48. Koutsoukos, P.G., W. Norde, and J. Lyklema, *Protein adsorption on hematite ([alpha]-Fe₂O₃) surfaces*. Journal of Colloid and Interface Science, 1983. **95**(2): p. 385-397.
49. Haynes, C.A., E. Sliwinsky, and W. Norde, *Structural and Electrostatic Properties of Globular Proteins at a Polystyrene-Water Interface*. Journal of Colloid and Interface Science, 1994. **164**(2): p. 394-409.
50. Arai, T. and W. Norde, *The behavior of some model proteins at solid-liquid interfaces 1. Adsorption from single protein solutions*. Colloids and Surfaces, 1990. **51**: p. 1-15.
51. Arai, T. and W. Norde, *The behavior of some model proteins at solid-liquid interfaces 2. Sequential and competitive adsorption*. Colloids and Surfaces, 1990. **51**: p. 17-28.
52. Steadman, B.L., K.C. Thompson, C.R. Middaugh, K. Matsuno, S. Vrona, E.Q. Lawson, and R.V. Lewis, *The effects of surface adsorption on the thermal stability of proteins*. Biotechnology and Bioengineering, 1992. **40**(1): p. 8-15.
53. Morrissey, B.W. and R.R. Stromberg, *The conformation of adsorbed blood proteins by infrared bound fraction measurements*. Journal of Colloid and Interface Science, 1974. **46**(1): p. 152-164.
54. Burghardt, T.P. and D. Axelrod, *Total internal reflection/fluorescence photobleaching recovery study of serum albumin adsorption dynamics*. Biophys. J., 1981. **33**(3): p. 455-467.

55. Burghardt, T.P. and D. Axelrod, *Total internal reflection fluorescence study of energy transfer in surface-adsorbed and dissolved bovine serum albumin*. *Biochemistry*, 1983. **22**(4): p. 979-985.
56. Jones, T.T. and E.J. Fernandez, *alpha-Lactalbumin Tertiary Structure Changes on Hydrophobic Interaction Chromatography Surfaces*. *J. Colloid and Interface Sci.*, 2003. **259**: p. 27-35.
57. McNay, J., J. O'Connell, and E. Fernandez, *Protein Unfolding During Reversed-Phase Chromatography: II Role of Salt Type and Ionic Strength*. *Biotechnology and Bioengineering.*, 2001. **76,3**: p. 234-232.
58. McNay, J. and E. Fernandez, *Protein Unfolding During Reversed-Phase Chromatography: I Effect of Surface Properties and Duration of Adsorption*. *Biotechnology and Bioengineering.*, 2001. **76,3**: p. 225-232.
59. Shibata, C. and A. Lenhoff, *TIRF [total internal reflectance fluorescence] of Salt and Surface Effects on Protein Adsorption*. *J. Colloid and Interface Sci.*, 1992. **148-149**: p. 469-484.
60. Shibata, C. and A. Lenhoff, *TIRF of Salt and Surface Effects on Protein Adsorption II Kinetics*. *J. Colloid and Interface Sci.*, 1992. **148-149**: p. 485-507.
61. Curtis, R., J. Pruasnitz, and H. Blanch, *Protein-Protein and Protein-Salt Interactions in Aqueous Protein Solution Containing Concentrated Electrolytes*. *Biotechnology and Bioengineering.*, 1998. **57,1**: p. 11-21.
62. Giacomelli, C. and W. Norde, *Influence of Hydrophobic Teflon Particles on the Structure of Amyloid ?-Peptide*. *Biomacromolecules.*, 2003. **4**: p. 1719-1726.

63. Jandt, K., *Atomic Force Microscopy of Biomaterials Surfaces and Interfaces*. Surface Science., 2001. **491**: p. 303-332.
64. Kim, D., H. Blanch, and C. Radke, *Direct Imaging of Lysozyme Adsorption onto Mica by Atomic Force Microscopy*. Langmuir., 2002. **18**: p. 5841-5850.
65. Haggerty, L. and A. Lenhoff, *Analysis of Ordered Arrays of Adsorbed Lysozyme by Scanning Tunneling Microscopy*. Biophysical Journal, 1993. **64,1-4**: p. 886-895.
66. Xia, N., D.G. Castner, Y. Hu, and D.W. Grainger, *Functionalized Poly(ethylene glycol)-Grafted Polysiloxane Monolayers for Control of Protein Building*. Langmuir., 2002. **18**: p. 3255-3262.
67. Chen, S., L. Liu, J. Zhou, and S. Jiang, *Controlling Antibody Orientation on Charged Self-Assembled Monolayers*. Langmuir, 2003. **19**: p. 2859-2864.
68. Klueh, U., T. Seery, D.G. Castner, J.D. Bryers, and D.L. Kreutzer, *Binding and Orientation of Fibronectin to Silanated Glass Surfaces Using Immobilized Bacterial Adhesin-Related Peptides*. Biomaterials., 2003. **24**: p. 3877-3884.
69. Paine, M.L., W. Luo, D.-H. Zhu, P. Bringas-JR, and M.L. Snead, *Functional Domains for Amelogenin Revealed by Compound Genetic Defects*. J. Bone and Mineral Res., 2003. **18**: p. 466-472.
70. Belcher, A.M., X.H. Wu, R.J. Christensen, P.K. Hansma, G.D. Stucky, and D.E. Morse, *Control of Crystal Phase Switching and Orientation by Soluble Mollusc-Shell Proteins*. Nature., 1996. **381**: p. 56-58.
71. Brown, S., M. Sarikaya, and E. Johnson, *A genetic analysis of crystal growth*. Journal of Molecular Biology, 2000. **299**(3): p. 725-735.

72. Addadi, L., S. Weiner, and M. Geva, *On How Proteins Interact with Crystals and their Effects on Crystal Formation*. Zeitschrift fur Kardiologie., 2001. **90,3**: p. 92-98.
73. Courtney, J.M., N.M.K. Lamba, S. Sundaram, and C.D. Forbes, *Biomaterials for blood-contacting applications*. Biomaterials, 1994. **15**(10): p. 737-744.
74. Packham, M.A., *The Behaviour of Platelets at Foreign Surfaces*. Proc. Soc. Exp. Biol. Med., 1988. **189**: p. 261-274.
75. Barber, T.A., T. Mathis, J.V. Ihlenfeld, S.L. Cooper, and D.F. Mosher, *Short-Term Interactions of Blood with Polymeric Vascular Graft Materials: Protein Adsorption, Thrombus Formation, and Leukocyte Deposition*. Scanning Electron Microscopy., 1978. **11**: p. 431-440.
76. Iwamoto, G.K., L.C. Winterton, R.S. Stoker, R.A. Van Wagenen, J.D. Andrade, and D.F. Mosher, *Fibronectin adsorption detected by interfacial fluorescence*. Journal of Colloid and Interface Science, 1985. **106**(2): p. 459-464.
77. Andrade, J.D., V.L. Hlady, and R.A.V. Wagenen, *Effects of plasma protein adsorption on protein conformation and activity*. Pure and applied chemistry 1984. **56**: p. 1345.
78. Ishihara, K., K. Fukumoto, Y. Iwasaki, and N. Nakabayashi, *Modification of polysulfone with phospholipid polymer for improvement of the blood compatibility. Part 2. Protein adsorption and platelet adhesion*. Biomaterials, 1999. **20**(17): p. 1553-1559.
79. Young, G., R. Bowers, B. Hall, and M. Port, *Clinical Comparison of Omafilcon A with Four Control Materials*. Clao J., 1997. **23**(4): p. 249-258.

80. Young, G., R. Bowers, B. Hall, and M. Port, *Six Month Clinical Evaluation of a Biomimetic Hydrogel Contact Lens*. Clao J., 1997. **23**(4): p. 226-236.
81. Amiji, M. and K. Park, *Prevention of protein adsorption and platelet adhesion on surfaces by PEO/PPO/PEO triblock copolymers*. Biomaterials, 1992. **13**(10): p. 682-692.
82. Kenausis, G.L., J. Voros, D.L. Elbert, N. Huang, R. Hofer, L. Ruiz-Taylor, M. Textor, J.A. Hubbell, and N.D. Spencer, *Poly(L-lysine)-g-Poly(ethylene glycol) Layers on Metal Oxide Surfaces: Attachment Mechanism and Effects of Polymer Architecture on Resistance to Protein Adsorption*. J. Phys. Chem. B, 2000. **104**(14): p. 3298-3309.
83. McClung, W.G., D.L. Clapper, A.B. Anderson, D.E. Babcock, and J.L. Brash, *Interactions of Fibrinolytic System Proteins with Lysine-Containing Surfaces*. J. Biomed. Mater. Res., 2003. **66A**: p. 795-801.
84. McClung, W.G., D.L. Clapper, S.P. Hu, and J.L. Brash, *Adsorption of plasminogen from human plasma to lysine-containing surfaces*. Journal of Biomedical Materials Research Part A, 2000. **49**(3): p. 409-414.
85. Brennan, N. and Coles, *Deposits and Symptomatology with Soft Contact Lens Wear*. Iclc., 2000. **27**: p. 75-100.
86. Minarik, L. and J. Rapp, *Protein Deposits on Individual Hydrophilic Contact Lenses: Effects of Water and Ionicity*. CLAO Journal., 1989. **15-16**: p. 185-188.
87. Minno, G.E., L. Eckel, S. Groemminger, B. Minno, and T. Wrzosek, *Quantitative-Analysis of Protein Deposits on Hydrophilic Soft Contact-Lenses I Comparison to*

- Visual Methods of Analysis 2 Deposit Variation Among FDA Lens Material Groups*. Optometry and Vision Science., 1991. **68,7-12**: p. 865-872.
88. Prager, M. and R. Quintana, *Radiochemical Studies on Contact Lens Soiling I Lens Uptake of ¹⁴C-Lysozyme from Simple and Complex Artificial Tear Solutions*. Journal of Biomedical Materials Research., 1997. **36**: p. 119-124.
89. Keith, D., B. Hong, and M. Christensen, *A Novel Procedure for the Extraction of Protein Deposits from Soft Hydrophilic Contact Lenses for Analysis*. Current Eye Research., 1997. **16,1-6**: p. 503-510.
90. Myers, R.I., D.W. Larsen, M. Tsao, C. Castellano, L.D. Becherer, F. Fontana, N.R. Ghormley, and G. Meier, *Quantity of Protein Deposited on Hydrogel Contact Lenses and its Relation to Visible Protein Deposits*. Optometry and Vision Science., 1991. **68,1-6**: p. 776-782.
91. Lin, S.T., R.B. Mandell, C.D. Leahy, and J.O. Newell, *Protein Accumulation on Disposable Extended Wear Lenses*. Clao J., 1991. **17-18**: p. 44-50.
92. Simmons, P.A., A. Tomlinson, R. Connor, J. Hay, and D.V. Seal, *Effect of Patient Wear and Extent of Protein Deposition on Adsorption of Acanthamoeba to Five Types of Hydrogel Contact Lenses*. Optometry and Vision Science., 1996. **73**: p. 362-368.
93. Leahy, C., R. Mandell, and S. Lin, *Initial In Vivo Tear Protein Deposition on Individual Hydrogel Contact Lenses*. Optometry and Vision Science., 1990. **67,7**: p. 504-511.

94. Tighe, B.J., L. Jones, K. Evans, and V. Franklin, *Patient-Dependent and Material-Dependent Factors in Contact Lens Deposition Processes*. *Advances in Experimental Medicine and Biology*., 1998. **438**: p. 745-751.
95. Jones, L., A. Mann, K. Evans, V. Franklin, and B. Tighe, *An in Vivo Comparison of the Kinetics of Protein and Lipid Deposition on Group II and Group IV Frequent-Replacement Contact Lenses*. *Optometry and Vision Science*., 2000. **77,10**: p. 503-510.
96. McArthur, S.L., K.M. McLean, H.A.W.S. John, and H.J. Griesser, *XPS and Surface-MALDI-MS Characterisation of Worn HEMA-Based Contact Lenses*. *Biomaterials*., 2001. **22**: p. 3295-3304.
97. Meadows, D. and J. Paugh, *Use of Confocal Microscopy to Determine Matrix and Surface Deposition Profiles in Hydrogel Contact Lenses*. *Clao J.*, 1994. **20,4**: p. 237-241.
98. Maissa, C., V. Franklin, M. Guillon, and B. Tighe, *Influence of Contact Lens Material Surface Characteristics and Replacement Frequency on Protein and Lipid Deposition*. *Optometry and Vision Science*., 1998. **75**: p. 697-705.
99. Hart, D.E., M.P. Plociniak, and G.W. Grimes, *Defining the Physiologically Normal Coating and Pathological Deposit: An Analysis of Sulfur-Containing Moieties and Pellicle Thickness on Hydrogel Contact Lenses*. *Clao J.*, 1998. **24,2**: p. 85-101.
100. Yan, G., G. Nyquist, K.D. Caldwell, R. Payor, and E.C. McCraw, *Quantitation of Total Protein Deposits on Contact Lenses by Means of Amino Acid Analysis*. *Investigative Ophthalmology and Visual Science*., 1993. **34**: p. 1804-1813.

101. Tripathi, P. and R. Tripathi, *Analysis of Glycoprotein Deposits on Disposable Soft Contact-Lenses*. Investigative Ophthalmology and Visual Science., 1992. **33**: p. 121-125.
102. Jones, L., K. Evans, R. Sariri, V. Franklin, and B. Tighe, *Lipid and Protein Deposition on N-Vinyl Pyrrolidone-Containing Group II and Group IV Frequent Replacement Contact Lenses*. Clao J., 1997. **23,2**: p. 122-126.
103. Sack, R.A., H. Harvey, and I. Nunes, *Disinfection Associated Spoilage of High Water Content Ionic Matrix Hydrogels*. Clao J., 1989. **15,2**: p. 138-145.
104. Gudmundsson, O.G., D.F. Woodward, S.A. Fowler, and M.R. Allansmith, *Identification of Proteins in Contact Lens Surface Deposits by Immunofluorescence Microscopy*. Archives of Ophthalmology., 1985. **103**: p. 196-197.
105. Taylor, R.L., M.D.P. Willcox, T.J. Williams, and J. Verran, *Modulation of Bacterial Adhesion to Hydrogel Contact Lenses by Albumin*. Optometry and Vision Science., 1998. **75**: p. 23-29.
106. Garrett, Q., B. Laycock, and R.W. Garrett, *Hydrogel Lens Monomer Constituents Modulate Protein Sorption*. Investigative Ophthalmology and Visual Science., 2000. **41,7**: p. 1687-1695.
107. Soltys-Robitaille, C.E., D.M. Ammon, and P.L. Valint, *The Relationship Between Contact Lens Surface Charge and In-Vitro Protein Deposition Levels*. Biomaterials., 2001. **22**: p. 3257-3260.
108. Botempo, A. and J. Rapp, *Protein-Lipid Interaction on the Surface of a Rigid Gas-Permeable Contact Lens in Vitro*. Current Eye Research, 1997. **16**: p. 1258-1262.

109. Sack, R.A., B. Jones, A. Antignani, R. Libow, and H. Harvey, *Specificity and Biological Activity of the Protein Deposited on the Hydrogel Surface*. Investigative Ophthalmology and Visual Science., 1987. **28**: p. 842-849.
110. Monfils, J., H. Tasker, L. Townley, R. Payor, and S. Dunkirk, *Laboratory Simulation of Protein Deposition of Vifilcon and Etafilcon Soft Contact Lens Materials*. Investigative Ophthalmology and Visual Science., 1992. **33**: p. 1292.
111. Merindano, M.D., M. Canals, C. Saona, and J. Costa, *Rigid Gas Permeable Contact Lenses Surface Roughness Examined by Interferential Shifting Phase and Scanning Electron Microscopies*. Ophthal. Physiol. Opt., 1998. **18,1**: p. 75-82.
112. Garret, Q. and B. Milthorpe, *Human Serum Albumin Adsorption on Hydrogel Contact Lenses in Vitro*. Investigative Ophthalmology and Visual Science., 1996. **37,13**: p. 2594-2602.
113. Tomlinson, A. and P. Simmons, *Surface Deposits on Low Water Content Hydrogel Contact Lenses: Comparison of SEM and Protein Assay Techniques*. Iclc., 1991. **18**: p. 88-94.
114. Llabres, C. and D. Antunez, *Evaluating Protein Deposits on Preference and CSI Lenses*. Contact Lens Spectrum., 1994. **9**: p. 23-29.
115. Lopez-Aleman, A., *Porous Structure of Purevision versus Focus Night&Day and Conventional Hydrogel Contact Lenses*. J. Biomed. Mater. Res., 2002. **63**: p. 319-325.
116. Karlgard, C.C.S., D.K. Sarkar, L.W. Jones, C. Moresoli, and K.T. Leung, *Drying Methods for XPS Analysis of Purevision, Focus Night&Day and Conventional Hydrogel Contact Lenses*. Applied Surface Science., 2004. **230**: p. 106-114.

117. Jones, L., M. Senchyna, M.-A. Glasier, J. Schickler, I. Forbes, D. Louie, and C. May, *Lysozyme and Lipid Deposition on Silicone Hydrogel Contact Lens Materials*. *Eye and Contact Lens.*, 2003. **29**: p. S75-S79.
118. Senchyna, M., L. Jones, D. Louie, C. May, I. Forbes, and M.-A. Glasier, *Quantitative and Conformational Characterization of Lysozyme Deposited on Balafilcon and Etafilcon Contact Lens Materials*. *Current Eye Research.*, 2004. **28,1**: p. 25-35.
119. Cheng, K., J. Kok, C.v. Mil, and A. Kijlstra, *Selective Binding of a 30-Kilodalton Protein to Disposable Hydrophilic Contact Lenses*. *Investigative Ophthalmology and Visual Science.*, 1990. **31**: p. 2244-2247.
120. Scott, G. and M. Mowrey-McKee, *Dimerization of Tear Lysozyme on Hydrophilic Contact Lens Polymers*. *Curr Eye Res*, 1996. **15**: p. 461-466.
121. Richard, N. and et al *Evaluation of Tear Protein Deposits on Contact Lenses from Patients With and Without Giant Papillary Conjunctivitis*. *Clao J.*, 1992. **18,3**: p. 143-147.
122. Suttorp-Schulten, M.S.A., L. Luyendijk, J.H.C. Kok, and A. Kijlstra, *HPLC Analysis of Tear Proteins in Giant Papillary Conjunctivitis*. *Documenta Ophthalmologica: Advances in Ophthalmology.*, 1989. **72**: p. 235-240.
123. Rebeix, V., F. Sommer, B. Marchin, D. Baude, and T.M. Duc, *Artificial Tear Adsorption on Soft Contact Lenses: Methods to Test Surfactant Efficacy*. *Biomaterials.*, 2000. **21**: p. 1197-1205.

124. Klein, A., *Detection of Mucin Deposits on Hydrogel Contact Lenses: Evaluation of Staining Procedures and Clinical Significance*. Optometry and Vision Science., 1989. **66,1**: p. 56-60.
125. Versura, P., M.C. Maltarello, R. Caramazza, and R. Laschi, *Immunocytochemical Analysis of Contact Lens Surface Deposits in Transmission Electron Microscopy*. Current Eye Research., 1988. **7,3**: p. 277-286.
126. Heiler, D.J., S. Gambacorta-Hoffman, S.F. Groemminger, and M.S. Jonasse, *The Concentric Distribution of Protein on Patient-Worn Hydrogel Lenses*. Clao J., 1991. **17,4**: p. 249-251.
127. Botempo, A. and J. Rapp, *Protein-Lipid Interaction on the Surface of a Hydrophilic Contact Lens in Vitro*. Current Eye Research., 1997. **16**: p. 776-781.
128. Sack, R.A., S. Sathe, L.A. Hackworth, M.D.P. Willcox, B.A. Holden, and C.A. Morris, *The Effect of Eye Closure on Protein and Complement Deposition on Group IV Hydrogel Contact Lenses: Relationship to Tear Flow Dynamics*. Current Eye Research., 1996. **15**: p. 1092-1100.
129. Botempo, R. Andrew, and J. Rapp, *Contact Lenses-Protein and Lipid Deposition onto Hydrophilic Contact Lenses In Vivo*. Clao J., 2001. **27,2**: p. 75-80.
130. Michaud, L. and C. Giasson, *Comparing the Extent of Protein Build-Up on Several Disposable Lenses by Two Spectrophotometric Methods*. Contact Lens and Anterior Eye., 1998. **21,4**: p. 104-108.
131. Sack, R. and I. Nunes, *Protein Deposition on Non-Ionic SCLs*. Optometry and Vision Science., 1989. **66**: p. 91.

132. Kurashige, L.T., J.E. Kataoha, T. Edrington, and J.G. Vehige, *Protein Deposition on Hydrogel Contact Lenses: A Comparison Study of Enzymatic Cleaners*. Iclc., 1987. **14,4**: p. 150-158.
133. Reindel, W., V. Ploscowe, G. Minno, J. Burke, C. Castellano, D. Hood, M. Piccolo, C. Snyder, S. Steel, and S. Welcker, *Comparison Study of Hydrophilic Contact Lens Surfactant Cleaners: A Clinical Evaluation of Residual Deposits*. ICLC, 1989. **16,7&8**: p. 232-236.
134. Deg, J. and P. Binder, *Electron Microscope Features of Never-Worn Soft Contact Lenses: Deposits or Artifacts?* Current Eye Research., 1986. **5**: p. 27-36.
135. Missiroli, A., F. Ricci, A. Pocobelli, C. Cedrone, and L. Cerulli, *Use of Bendazac Lysine to Limit Deposition on Soft Contact Lenses in Vitro*. Clao J., 1991. **17**: p. 126-128.
136. Bagueta, J., F. Sommer, V. Claudon-Eyla, and T.M. Duc, *Characterization of Lacrymal Component Accumulation on Worn Soft Contact Lens Surfaces by Atomic Force Microscopy*. Biomaterials., 1995. **16**: p. 3-9.
137. Schneider, S.W., J. Lärmer, R.M. Henderson, and H. Oberleithner, *Molecular Weights of Individual Proteins Correlate with Molecular Volumes Measured by Atomic Force Microscopy*. Eur. J. Physiol., 1998. **435**: p. 362-367.
138. Tan, A., B.K. Milthorpe, and J.W. Huff, *A Technique for Quantitation of Protein Deposits on Rigid Gas Permeable Contact Lenses*. Clao J., 1997. **23**: p. 177-184.
139. Goldenberg, M. and A. Beekman, *Detection of Protein Deposition on Contact Lens Type Polymeric Hydrogels by Coomassie Blue R Staining*. Biomaterials., 1991. **12**: p. 267-274.

140. Ceruli, L. and a. te, *Two Methods of Examining Protein Deposits on Hydrophilic Contact Lenses*. Clao J., 1992. **18**: p. 101-104.
141. Keith, E.O., M. Boltz, R. Gadh, R. Ghorsriz, D. Mangatt, and L.E. Janoff, *Regular Papers-Adhesion of Tear Proteins to Contact Lenses and Vials First Published on the Internet*. Biotechnology and Applied Biochemistry., 2001. **34,1**: p. 5-12.
142. Ichijima, H., T. Kawai, K. Yamamoto, and H.D. Cavanagh, *Contact Lenses-Determination of Protein Deposits on RGP Lenses by X-Ray Photoelectron Spectroscopy*. Clao J., 2000. **26**: p. 18-20.
143. Barbucci, R., M. Casolaro, and A. Magnani, *Characterization of biomaterial surfaces: ATR-FTIR, potentiometric and calorimetric analysis*. Clinical Materials, 1992. **11**(1-4): p. 37-51.
144. Pireaux, J.J., *Surface study of biomaterials by electron induced vibrational spectroscopy*. J Clinical Materials, 1992. **11**: p. 53-60.
145. Yi, L. and P. Xie, *Quantitative Assay of Protein Deposits on Hydrophilic Contact Lenses Treated with ReNu and COMPLETE Solution*. Iclc., 1999. **26**: p. 15-19.
146. Trocme, S.D., G.M. Kephart, W.M. Bourne, L.J. Maguire, and G.J. Gleich, *Eosinophil Granule Major Basic Protein in Contact Lenses of Patients with Giant Papillary Conjunctivitis*. Clao J., 1990. **16**: p. 219-222.
147. Miller, D. and N. Peppas, *The Use of Ellipsometry to Study Adsorption on Hydrogels*. Biomaterials., 1985. **6**: p. 33-40.

148. Castillo, E., J. Koenig, and J. Anderson, *Characterization of Protein Adsorption on Soft Contact Lenses IV Comparison of in Vivo Spoilage with the in Vitro Adsorption of Tear Proteins*. *Biomaterials.*, 1986. **7**: p. 89-96.
149. Jung, J. and J. Rapp, *The efficacy of Hydrophilic Contact Lens Cleaning System in Removing Protein Deposits*. *Clao J.*, 1993. **19**: p. 47-49.
150. Simmons, P.A., W.H. Ridder, T.B. Edrington, S. Ho, and K.-C. Lau, *Passive Protein Removal by Two Multipurpose Lens Solutions: Comparison of Effects on In Vitro Deposited and Patient-Worn Hydrogel Contact Lenses*. *Iclc.*, 1999. **26**: p. 33-38.
151. Evans, T., B. Levy, and J. Szabocsik, *Clinical Study of Bendazac Lysine for In Vivo Contact Lens Cleaning*. *Optometry and Vision Science.*, 1993. **70**: p. 210-215.
152. Arciola, C.R., L. Montanaro, R. Caramazza, V. Sassoli, and D. Cavedagna, *Inhibition of Bacterial Adherence to a High-Water-Content Polymer by a Water-Soluble, Nonsteroidal, Anti-Inflammatory Drug*. *Journal of Biomedical Materials Research.*, 1997. **36**: p. 119-124.
153. Hu, J., F. Jara, J. Thakrar, and K. Shih, *Quantitative Cleaning Efficacy Evaluation Methods with Protein and Lipid Lens Soiling Models*. *Clao J.*, 1995. **21**: p. 154-156.
154. Simmons, P.A., C.M. Sun, B.A. Yamamoto, and T.B. Edrington, *Comparison of Surfactant Cleaning Times on Protein Deposit Removal from Hydrogel Lenses*. *Iclc.*, 1995. **22**: p. 16-22.
155. Thakur, A., A. Chauhan, and M. Willcox, *Lens and Cornea- Effect of Lysozyme on Adhesion and Toxin Release by Staphylococcus Aureus*. *Australian and New Zealand Journal of Ophthalmology.*, 1999. **27,3**: p. 224-227.

156. Alongi, S., M. Rolando, A. Macri, A. Colonna, G. Balestra, R. Rizzetto, and G. Calabria, *Bacterial Load and Protein Deposits on 15-Day Versus 1-Day Disposable Hydrophilic Contact Lenses*. *Cornea.*, 1998. **17**: p. 146-151.
157. Williams, T., M. Willcox, and R. Schneider, *The Effect of Protein Deposits on Bacterial Adhesion to Contact Lenses*. *Investigative Ophthalmology and Visual Science.*, 1996. **37,3**: p. s871.
158. Huang, X., I.H. El-Sayed, W. Qian, and M.A. El-Sayed, *Cancer cell imaging and photothermal therapy in the near-infrared region by using gold nanorods*. *J Am Chem Soc*, 2006. **128**(6): p. 2115-20.
159. Lapotko, D.O., E. Lukianova, and A.A. Oraevsky, *Selective laser nano-thermolysis of human leukemia cells with microbubbles generated around clusters of gold nanoparticles*. *Lasers Surg Med*, 2006. **38**(6): p. 631-42.
160. Hilger, I., R. Hergt, and W.A. Kaiser, *Use of magnetic nanoparticle heating in the treatment of breast cancer*. *IEE Proc Nanobiotechnol*, 2005. **152**(1): p. 33-39.
161. Zharov, V.P., K.E. Mercer, E.N. Galitovskaya, and M.S. Smeltzer, *Photothermal nanotherapeutics and nanodiagnostics for selective killing of bacteria targeted with gold nanoparticles*. *Biophys J*, 2006. **90**(2): p. 619-627.
162. Liu, W.T., *Nanoparticles and their biological and environmental applications*. *J Biosci Bioeng*, 2006. **102**(1): p. 1-7.
163. Warheit, D.B., *Nanoparticles: Health impacts?* *Materials Today*, 2004. **7**(2): p. 32-35.

164. Tsuji, J.S., A.D. Maynard, P.C. Howard, J.T. James, C.-w. Lam, D.B. Warheit, and A.B. Santamaria, *Research Strategies for Safety Evaluation of Nanomaterials, Part IV: Risk Assessment of Nanoparticles*. Toxicological Sciences, 2006. **89**(1): p. 42-50.
165. Handy, R.D. and B.J. Shaw, *Toxic effects of nanoparticles and nanomaterials: Implications for public health, risk assessment and the public perception of nanotechnology*. Health, Risk & Society, 2007. **9**(2): p. 125 - 144.
166. Linse, S., C. Cabaleiro-Lago, W.-F. Xue, I. Lynch, S. Lindman, E. Thulin, S.E. Radford, and K.A. Dawson, *Nucleation of protein fibrillation by nanoparticles*. PNAS, 2007. **104**(21): p. 8691-8696.
167. Colvin, V.L. and K.M. Kulinowski, *Nanoparticles as catalysts for protein fibrillation*. Proceedings of the National Academy of Sciences of the United States of America, 2007. **104**(21): p. 8679-8680.
168. Oliva, F.Y., *Facultad Ciencias Químicas*. 2001, Universidad Nacional de Córdoba: Córdoba, Argentina.
169. Lundqvist, M., I. Sethson, and B.H. Jonsson, *Protein Adsorption onto Silica Nanoparticles: Conformational Changes Depend on the Particles' Curvature and the Protein Stability*. Langmuir, 2004. **20**(24): p. 10639-10647.
170. Norde, W. and J.P. Favier, *Structure of adsorbed and desorbed proteins*. Colloids and Surfaces, 1992. **64**(1): p. 87-93.
171. Gessner, A., A. Lieske, B.-R. Paulke, and R.H. Müller, *Functional Groups on Polystyrene Model Nanoparticles: Influence on Protein Adsorption*. J. Biomedical Materials Research Part A., 2003. **65A**,**3**: p. 319-326.

172. Gessner, A., A. Lieske, B.R. Paulke, and R.H. Muller, *Influence of surface charge density on protein adsorption on polymeric nanoparticles: analysis by two-dimensional electrophoresis*. European Journal of Pharmaceutics and Biopharmaceutics, 2002. **54**(2): p. 165-170.
173. Gessner, A., R. Waicz, A. Lieske, B.R. Paulke, K. Mader, and R.H. Muller, *Nanoparticles with decreasing surface hydrophobicities: influence on plasma protein adsorption*. International Journal of Pharmaceutics, 2000. **196**(2): p. 245-249.
174. Benko, B., S. Vuk-Pavlovic, G. Dezelic, and S. Maricic, *A Proton Magnetic Relaxation Study of Methaemoproteins Bound to Monodisperse Polystyrene Latex Particles*. Journal of colloid and interface science 1975. **52**(3): p. 444-451.
175. Larsericsdotter, H., S. Oscarsson, and J. Buijs, *Thermodynamic Analysis of Proteins Adsorbed on Silica Particles: Electrostatic Effects*. J. Colloid and Interface Sci., 2001. **237**: p. 98-103.
176. Haynes, C.A., E. Sliwinsky, and W. Norde, *Structural and Electrostatic Properties of Globular Proteins at a Polystyrene-Water Interface*. J. Colloid and Interface Sci., 1994. **164**: p. 394-409.
177. Haynes, C. and W. Norde, *Structures and Stabilities of Adsorbed Proteins*. J. Colloid and Interface Sci., 1995. **169**: p. 313-328.
178. Kandori, K., A. Fudo, and T. Ishikawa, *Study on the Particle Texture Dependence of Protein Adsorption by Using Synthetic Micrometer-Sized Calcium Hydroxyapatite Particles*. Colloids and Surfaces B: Biointerfaces., 2002. **24**: p. 145-153.

179. Oliva, F.Y., L.B. Avalle, O.R. Camara, and C.P. De Pauli, *Adsorption of human serum albumin (HSA) onto colloidal TiO₂ particles, Part I*. Journal of Colloid and Interface Science, 2003. **261**(2): p. 299-311.
180. Chah, S., M.R. Hammond, and R.N. Zare, *Gold Nanoparticles as a Colorimetric Sensor for Protein Conformational Changes*. Chemistry & Biology, 2005. **12**(3): p. 323-328.
181. Shang, L., Y. Wang, J. Jiang, and S. Dong, *pH-Dependent Protein Conformational Changes in Albumin: Gold Nanoparticle Bioconjugates: A Spectroscopic Study*. Langmuir, 2007. **23**(5): p. 2714-2721.
182. Price, M., R. Cornelius, and J. Brash, *Protein Adsorption to Polyethylene Glycol Modified Liposomes from Fibrinogen Solution and from Plasma*. Biochimica et Biophysica Acta., 2001. **1512**: p. 191-205.
183. Jiang, X., J. Jiang, Y. Jin, E. Wang, and S. Dong, *Effect of Colloidal Gold Size on the Conformational Changes of Adsorbed Cytochrome c: Probing by Circular Dichroism, UV-Visible, and Infrared Spectroscopy*. Biomacromolecules, 2005. **6**(1): p. 46-53.
184. Vertegel, A.A., R.W. Siegel, and J.S. Dordick, *Silica Nanoparticle Size Influences the Structure and Enzymatic Activity of Adsorbed Lysozyme*. Langmuir, 2004. **20**(16): p. 6800-6807.
185. Roach, P., D. Farrar, and C.C. Perry, *Surface Tailoring for Controlled Protein Adsorption: Effect of Topography at the Nanometer Scale and Chemistry*. Journal of the American Chemical Society, 2006. **128**(12): p. 3939-3945.

186. Wagner, M., T. Horbett, and D. Castner, *Characterization of the Structure of Binary and Ternary Adsorbed Protein Films Using Electron Spectroscopy for Chemical Analysis, Time-of-Flight Secondary Ion Mass Spectrometry, and Radiolabeling*. Langmuir., 2003. **19**: p. 1708-1715.
187. Xia, N., C.J. May, S.L. McArthur, and D.G. Castner, *Time-of-Flight Secondary Ion Mass Spectrometry Analysis of Conformational Changes in Adsorbed Protein Films*. Langmuir., 2002. **18**: p. 4090-4097.
188. Oberholzer, M.R. and A.M. Lenhoff, *Protein Adsorption Isotherms Through Colloidal Energetics*. Langmuir, 1999. **15**: p. 3905-3914.
189. Stahlberg, J. and B. Jönsson, *Influence of Charge Regulation in Electrostatic Interaction Chromatography of Proteins*. Anal. Chem., 1996. **68**: p. 1536-1544.
190. Adamczyk, Z., B. Siwek, M. Zembala, and P. Werodski, *Kinetics of Localized Adsorption of Colloid Particles*. Adv. Colloid Interface Sci., 1994. **48**: p. 151-280.
191. Adamczyk, Z. and P.M.E. Weronski, *Particle Adsorption Under Irreversible Conditions: Kinetics and Jamming Coverage*. Colloids and Surfaces A, 2002. **208**: p. 29-40.
192. Adamczyk, Z. and P. Weronski, *Unoriented Adsorption of Interacting Spheroidal Particles*. J. Colloid Interface Sci., 1997. **189**: p. 348-360.
193. Tassel, P.R.V., L. Guemouri, J.J. Ramsden, G. Tarjus, P. Viot, and J. Talbot, *A Particle-Level Model of Irreversible Protein Adsorption with a Postadsorption Transition*. Journal of Colloid and Interface Science, 1998. **207**: p. 317-323.

194. Brusatori, M.A. and P.R. Van Tassel, *A Kinetic Model of Protein Adsorption/Surface-Induced Transition Kinetics Evaluated by the Scaled Particle Theory*. J. Colloid Interface Sci., 1999. **219**: p. 333-338.
195. Oberholzer, M.R., N.J. Wagner, and A.M. Lenhoff, *Grand Canonical Brownian Dynamics Simulation of Colloidal Adsorption*. J. Chem. Phys., 1997. **107**: p. 9158-9167.
196. Ravichandran, S., J.D. Madura, and J. Talbot, *A Brownian Dynamics Study of the Initial Stages of Hen Egg-White Lysozyme Adsorption at a Solid Interface*. J. Phys. Chem. B, 2001. **105**: p. 3610-3613.
197. Noinville, V., C. Vidal-Madjar, and B. Seville, *Modeling of Protein Adsorption on Polymer Surfaces Computation of Adsorption Potential*. J. Phys. Chem, 1995. **99**: p. 1516-1522.
198. Asthagiri, D. and A.M. Lenhoff, *Influence of Structural Details in Modeling Electrostatically Driven Protein Adsorption*. Langmuir, 1997. **13**: p. 6761-6768.
199. Raffaini, G. and F. Ganazzoli, *Simulation Study of the Interaction of Some Albumin Subdomains with a Flat Graphite Surface*. Langmuir, 2003. **19**: p. 3403-3412.
200. Sheng, Y.-J., H.-K. Tsao, J. Zhou, and S. Jiang, *Orientation of a Y-Shaped Biomolecule Adsorbed on a charged surface*. Phys. Rev. E, 2002. **66**: p. 011911.
201. Latour, R.A. and L.L. Hench, *A Theoretical Analysis of the Thermodynamic Contributions for the Adsorption of Individual Protein Residues on Functionalized Surfaces*. Biomaterials, 2002. **23**: p. 4633-4648.

202. Basalyga, D.M. and R.A. Latour, *Theoretical Analysis of Adsorption Thermodynamics for Charged Peptide Residues on SAM Surfaces of Varying Functionality*. Journal of Biomedical Materials Research Part A, 2003. **64A**: p. 120-130.
203. Latour, R.A. and C.J. Rini, *Theoretical Analysis of Adsorption Thermodynamics for Hydrophobic Peptide Residues on SAM Surfaces of Varying Functionality*. Journal of Biomedical Materials Research, 2002. **60**: p. 565-577.
204. Zhou, J., S. Chen, and S. Jiang, *Orientation of Adsorbed Antibodies on Charged Surfaces by Computer Simulation Based on a United-Residue Model*. Langmuir, 2003. **19**: p. 3472-3478.
205. Castells, V., S. Yang, and P.R. Van Tassel, *Surface-Induced Conformational Changes in Lattice Model Proteins by Monte Carlo Simulation*. Phys. Rev. E, 2002. **65**: p. 031912.
206. Fang, F. and I. Szleifer, *Kinetics and Thermodynamics of Protein Adsorption: A Generalized Molecular Theoretical Approach*. Biophysical Journal, 2001. **80**: p. 2568-2589.
207. Satulovsky, J., M.A. Carignano, and I. Szleifer, *Kinetic and Thermodynamic Control of Protein Adsorption*. Proc. Natl. Acad. Sci. U.S.A., 2000. **97**: p. 9037-9041.
208. Bohren, C.F. and D.R. Huffman, *Absorption and Scattering of Light by Small Particles*. 1983, Weinheim, Germany: John Wiley & Sons, Inc.
209. Johnson, P.B. and R.W. Christy, *Optical Constants of the Noble Metals*. Physical Review B, 1972. **6**(12): p. 4370.

210. Kreibig, U., *Electronic properties of small silver particles: the optical constants and their temperature dependence*. Journal of Physics F: Metal Physics, 1974. **4**: p. 999-1014.
211. Mätzler, C., *MATLAB Functions for Mie Scattering and Absorption*, in *IAP Research Report No. 2002-08*. 2002, Institute of Applied Physics: University of Bern, Switzerland.
212. Arwin, H., *Optical Properties of Thin Layers of Bovine Serum Albumin, γ -Globulin, and Hemoglobin*. Applied Spectroscopy, 1986. **40**: p. 313.
213. Sauerbrey, G., *Verwendung von Schwingquarzen zur Wägung dünner Schichten und zur Mikrowägung*. Zeitschrift Für Physik, 1959. **155**: p. 206-222.
214. Nomura, T. and O. Hattori, *Determination of micromolar concentrations of cyanide in solution with a piezoelectric detector*. Anal Chim Acta, 1980. **115**: p. 323–326.
215. Voinova, M.V., M. Rodahl, M. Jonson, and B. Kasemo, *Viscoelastic Acoustic Response of Layered Polymer Films at Fluid-Solid Interfaces: Continuum Mechanics Approach*. Physica Scripta, 1999. **59**: p. 391-396.
216. Rodahl, M. and B. Kasemo, *On the measurement of thin liquid overlayers with the quartz-crystal microbalance*. International Conference on Solid-State Sensors and Actuators, and Eurosensors IX, Proceedings, 1995. **2**: p. 743-746.
217. Reed, C.E., K.K. Kanazawa, and J.H. Kaufman, *Physical description of a viscoelastically loaded AT-cut quartz resonator*. J. Appl. Phys., 1990. **68**(5): p. 1993-2001.

Summary of Papers

Papers I, II, and III involve the application of gold nanospheres to examining protein conformational dependencies during heat and acid denaturation. Thin planar gold films have been used for some time to extract the optical thickness and refractive index from the angle and amplitude shift of their plasmon resonance in the presence of protein. Small gold particles exhibit localized surface plasmon resonance which depends strongly on the local index of refraction surrounding the sphere. We use analogous techniques to planar SPR to extract index of refraction and thickness of bovine serum albumin (BSA) protein conjugated to various sizes of gold nanospheres. By monitoring amplitude and wavelength shifts in the peak plasmon resonance as we subject the samples to denaturing conditions, we can infer what may be happening to the protein from Mie theory (page 69).

The first paper involves heat denaturation over a ramp cycle, looking at curvature dependence of the cycle. The second paper investigates isothermal heating, and derives curvature dependent activation energies. Lastly, the curvature dependence of pH denaturation is examined in the third paper.

Papers IV, and V examine protein deposition in the applied situation of biomaterials, in particular contact lenses. Paper IV examines adsorption of hen egg white lysozyme, BSA, bovine lactoferrin and combinations of these onto crosslinked polyHEMA hydrogels deposited onto a quartz crystal microbalance. Lastly, Paper V examines deposition onto commercial contact lenses using atomic force microscopy and protein conjugated nanospheres. The conjugated nanospheres provide a labeling for the protein, allowing lateral resolution of protein deposition that would otherwise be obscured by the morphology of the lens. Structures resembling fibril-type protein are found on one lens type.

List of Papers Not Included in Thesis

1. Sharp, J.S., Forrest, J.A., Fakhraai, Z., Khomenk, M., Teichroeb, J.H., and Dalnoki-Veress, K. (2007) Reply to comment on “The properties of free polymer surfaces and their effect upon the glass transition temperature of thin polystyrene films” by S.A. Hutcheson and G.B. McKenna. *Eur. Phys. J. E.* 22:287–291
2. Ngai, V., Medley, J.B., Jones, L., Forrest, J. and Teichroeb, J. (2004) Friction of Contact Lenses: Silicone Hydrogel versus Conventional Hydrogel. *Tribology Series* 43, Elsevier.
3. Sharp, J.S., Teichroeb, J.H., and Forrest, J.A. (2004) The properties of free polymer surfaces and their influence on the glass transition temperature of thin polystyrene films. *Eur. Phys. J. E.* 15:473- 487
4. Teichroeb, J.H., and Forrest, J.A. (2003) Direct imaging of nanoparticle embedding to probe viscoelasticity of polymer surfaces. *Phys. Rev. Lett.* 91: 016104
5. Teichroeb, J.H., and Forrest, J.A. (2002) Direct Imaging of Nanoparticle Embedding Into PS Films. *MRS Proceedings.* 734:B3.2

Paper I

Anomalous thermal denaturing of proteins adsorbed to nanoparticles.¹

Protein adsorption is greatly affected by the surface onto which it deposits. One aspect of the surface that is generally overlooked is the effect of curvature upon adsorption. In particular, if the size of the roughness approaches the dimensions of the molecule, what effect will this have upon adsorption? Even more peculiar may be to ask how the behaviour of a protein will differ on a surface that is smaller than the protein dimensions. The ease with which a range of nanoparticle sizes can be made makes them ideal candidates for examining curvature effects. Additionally, due to their strong localized surface plasmon resonance, they can be used as a measurement tool with extreme sensitivity to their local surroundings. This translates into excellent resolution for monitoring layer changes. This paper seeks to demonstrate the effect of Au nanosphere curvature upon the thermal stability, and denaturing path (in index/thickness space) of bovine serum albumin. It also shows the usefulness of Au nanospheres as measurement tools. Extremely useful information can be extracted from even basic modeling of the system.

¹Reproduced with kind permission of Springer Science+Business Media [EPJ E vol 21, (2006) p 19-24.]

Dear Sir,

In answer to your request, we are pleased to inform you that we grant the permission to reproduce in your PhD thesis:

Article "Anomalous thermal denaturing of proteins adsorbed to nanoparticles, from EPJ E vol 21, (2006) p 19-24.

We thank you by advance to cite the primary published source in your new publication. (title, year, issue).

Yours sincerely,
C. GRIFFON
Copyright Dept
Phone: +33 (0)1 69 18 75 75
Fax: +33 (0)1 69 28 84 91
E-mail: griffon@edpsciences.org

Dear Mr. Teichroeb,

Thank you for your e-mail.

With reference to your request (copy herewith) to re-use material on which Springer controls the copyright, our permission is granted free of charge, on the following condition:

* full credit (journal title, volume, year of publication, page, chapter/article title, name(s) of author(s), figure number(s), original copyright notice) is given to the publication in which the material was originally published by adding: With kind permission of Springer Science+Business Media.

With best regards,

—

Alice Essenpreis
Springer
Rights and Permissions

—

Tiergartenstrasse 17 | 69121 Heidelberg GERMANY
FAX: +49 6221 487 8223
permissions.Heidelberg@springer.com
WWW.springer.com/rights

Anomalous thermal denaturing of proteins adsorbed to nanoparticles

J.H. Teichroeb, J.A. Forrest^a, V. Ngai, and L.W. Jones

Department of Physics, Department of Optometry, and Guelph-Waterloo Physics Institute, University of Waterloo, 200 University Ave. W., Waterloo, Ontario, N2L 3G1, Canada

Received 2 May 2006 /

Published online: 16 October 2006 – © EDP Sciences / Società Italiana di Fisica / Springer-Verlag 2006

Abstract. We have used localized surface plasmon resonance (LSPR) to monitor the structural changes that accompany thermal denaturing of bovine serum albumin (BSA) adsorbed onto gold nanospheres of size 5 nm–60 nm. The effect of the protein on the LSPR was monitored by visible extinction spectroscopy. The position of the resonance is affected by the conformation of the adsorbed protein layer, and as such can be used as a very sensitive probe of thermal denaturing that is specific to the adsorbed protein. The results are compared to detailed calculations and show that full calculations can lead to significant increases in knowledge where gold nanospheres are used as biosensors. Thermal denaturing on spheres with diameter > 20 nm show strong similarity to bulk calorimetric studies of BSA in solution. BSA adsorbed on nanospheres with $d \leq 15$ nm shows a qualitative difference in behavior, suggesting a sensitivity of denaturing characteristics on local surface curvature. This may have important implications for other protein-nanoparticle interactions.

PACS. 78.67.Bf Nanocrystals and nanoparticles – 87.80.-y Biological techniques and instrumentation; biomedical engineering – 87.83.+a Biomedical applications of nanotechnology

The use of nanoparticles in technology is becoming increasingly common. Continuation of this trend will necessarily increase the exposure of biological systems to nanoparticles. As a result, it is imperative to develop a detailed understanding of how biological entities, and at the most basic level, proteins, may interact with nanoscale particles. An important aspect of this problem is the presence of the interface, and this has been studied in detail [1–3]. A much less well-understood, but perhaps equally important, aspect is the curvature of the interface—an effect that is much more important for nanoparticles. Understanding this effect is also important for understanding real biological systems than can also have curvature on similar nanometer length scales. In addition to the high relevance of such systems for developing an understanding of the general problem of proteins at interfaces, there is a strong practical impetus to characterize such systems. The adsorption and possible subsequent structural change of a protein on a solid surface is of crucial and fundamental importance to the entire field of biomaterials. The interaction of biomacromolecules with surfaces is the underpinning science for many forms of biosensors, in particular those using nanoparticles.

In this article we describe an experiment and analysis that allows gold-nanosphere biosensing to be as quantitative as ellipsometric studies. We believe that our analysis technique approaches the limit of precision that can be attained with nanoparticle biosensing. We use this technique to make the first detailed study of the dependence of thermal denaturing of adsorbed protein (in this case BSA) on the local curvature of the substrate. We show that the thermal denaturing of proteins can proceed in a qualitatively different way on nanoparticles as compared to bulk solution.

There are many aspects of surface proximity that could affect protein adsorption and stability. Aspects such as charge and surface chemistry have been studied [4, 5] in detail. One aspect that has not been discussed in detail is the dependence on the local surface curvature. Native protein structures are characterized by a specific tertiary structure and surfaces with radii of curvature comparable to the protein size may have constraints to molecular adsorption and packing. This may also affect the stability of different configurations and hence the stability of the native conformation against external factors such as heat and/or solution properties. Larsericsdotter *et al.* [6] used differential scanning calorimetry (DSC) to measure the thermal denaturing of lysozyme adsorbed to silica nanoparticles. They found a broadening of the heat capacity peak as well as a

^a e-mail: jforrest@uwaterloo.ca

shift to lower temperatures indicating a decreased stability against temperature change. While motivating the need for further studies, a disadvantage of calorimetric based techniques is the need to exclude bulk protein from the experiment as all protein is sensed in such studies. Localized surface plasmon resonance is a technique that combines high sensitivity to changes in the adsorbed protein layer while not being affected by the protein in bulk solution.

The principle of the experiment is simple. Protein molecules are adsorbed onto gold nanoparticles. This is a technique that has been used for almost 50 years in immunological studies [7]. The protein is probed through its effect on the localized surface plasmon resonance of the gold spheres, which in turn is measured by optical extinction measurements. The position of the extinction peak of the nanoparticles is affected by interaction with protein or by aggregation. Qualitative analogues of this are used extensively as biosensors [8–11], a prime example being the Carter-Wallace home pregnancy test. The specific and crucial differences of the current study are twofold: First, we are not simply measuring the adsorption of the protein (though we observe this as well), but instead we are looking at the much finer effects caused by the protein undergoing structural changes upon thermal denaturing. Second, we do not rely on a qualitative analysis of the data, as is usually employed in biosensing studies, but do the full Mie scattering calculation for coated spheres to determine the full extinction spectrum. The protein-sphere system can be approximated as a coated isotropic sphere, and can be solved exactly using Mie theory [12]. The extinction displays a distinct maximum due to the Frölich resonance and the position and magnitude of this maximum is affected by the environment of the nanospheres. For bare spheres, this is the refractive index of the medium the nanospheres are in, and for the coated system it is the optical properties (density and thickness) of the coating as well as those of the medium. A notable advantage of this technique over many others used to probe properties of surface-adsorbed protein is the fact that *only* protein molecules on the nanospheres are observed. All of the protein in the bulk solution is left undetected by the experiment. Other experiments with this advantage usually require tagging some of the molecules (with radioactive nuclei or fluorescent dye for instance). Our studies show that gold nanospheres as biosensors can be used to observe structural changes of proteins, and that full calculations can lead to an enhanced ability to make quantitative conclusions.

Gold nanoparticles (sphere diameters 5 nm–60 nm) were purchased from Ted Pella Inc with concentrations ranging from 5×10^{13} /ml (for the 5 nm diameter spheres) to 2.6×10^{10} /ml (for the 60 nm diameter spheres). Phosphate buffer solution (PBS) is made twice concentrated as compared to that normally used to mimic physiological conditions. Bovine serum albumin (Sigma min 99% purity) is dissolved in the “double strength” phosphate buffer to a concentration of 0.2% b.w. In addition, a second solution is made by dissolving BSA in MilliQ water (rated at 18 M Ω resistance) to a concentration of 1 mg/mL. These solutions are gently mixed on a Vortex Genie II and then

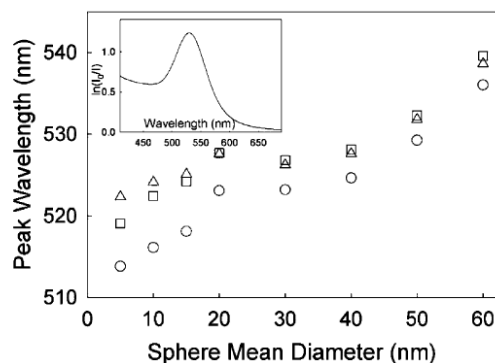


Fig. 1. Position of peak extinction for bare nanospheres (circles) as well as BSA-coated spheres in deionised water (triangles) and phosphate buffer at pH 7 (squares). The inset shows a typical extinction spectrum.

left to sit for several hours to ensure all protein has been dissolved. 1200 μ L of a given size of Ted Pella Au colloid are measured out into a polystyrene cuvette and 300 μ L of the 1 mg/mL BSA in MilliQ water are added immediately. The cuvette is mixed by turning end over end for 10 minutes, and left to conjugate for 1 hour at room temperature. After 1 hour 1500 μ L of 0.2% BSA in double-strength PBS are added, and the cuvette is again mixed end over end for 10 minutes. The solution is then left for at least 1 hour at room temperature to make sure equilibrium is reached. Samples are then stored in the refrigerator for a maximum of 2 days before use. Earlier experiments involved a centrifugation/resuspension step to remove free protein, but this was found to have no effect on the final results even over 5–6 orders of magnitude change in the free-protein concentration. The final solution of coated nanoparticles is in a phosphate buffer with a pH of 7 that mimics physiological conditions. This is essentially the same conjugation procedure described for immunological studies [7]. Extinction measurements were done in a heated cuvette. The light source was a tungsten filament lamp, and the spectrometer was an Ocean Optics USB2000. Extinction spectra were taken in the range 400 nm to 900 nm. Sphere sizes larger than 60 nm were not used as they were subject to sedimentation during the course of the experiment which would exclude a quantitative comparison to the extinction values. To find the peak of a spectrum, a numerical derivative of the data was fitted with a linear function and the zero crossing was determined to a typical accuracy of 0.05 nm. Figure 1 shows the peak position as a function of sphere size for both bare and protein-conjugated spheres (for both buffer and deionised water) for all sizes employed in the experiment. The blue shifting of the peak for small sphere sizes is not predicted by theory and cannot be accounted for by finite-size effects of plasmon damping as such effects can only result in a red shift of the peak [13]. This blue shift has been observed by others and is postulated to be

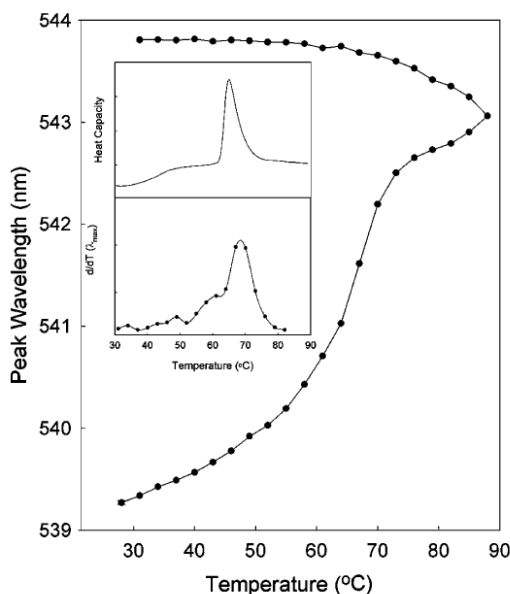


Fig. 2. Temperature dependence of the position of the maximum extinction as a function of temperature for a complete heating-cooling cycle for BSA-coated gold nanospheres. The top graph in the inset is a DSC trace for a 30 mg/ml solution and the bottom plot is the temperature derivative of the data in the main plot. The sphere size for this data is 60 nm.

a result of changes in the bulk plasmon frequency in the nanospheres [14]. Since detailed calculations require the refractive index, we split the refractive index into a part due to bound electrons, and one due to free electrons, use a Drude model to describe the free-electron part, and then modify the bulk plasmon frequency ω_p to get agreement with the measured peak positions for the bare spheres in Figure 1. It is these modified ω_p values that are used in the calculations for the protein-conjugated nanospheres.

For temperature-dependent studies an extinction spectrum was taken every ~ 2 K degrees with a time of ~ 15 – 20 minutes between spectra (due to time of heating and acquisition). The procedure was automated to control the temperature controller and spectrometer. Figure 2 shows the peak position of BSA on 60 nm nanospheres as a function of temperature. In order to make comparisons with more conventional techniques, we also used DSC to measure the thermal denaturing of BSA. This is shown in the top graph in the inset of Figure 2. The DSC is well studied [15] and has been interpreted. The small shoulder near 45–55 °C is a reversible process, and the peak at 65 °C is an irreversible thermal denaturing. Since the DSC curve shows the heat capacity that accompanies changes in the structure, and the LSPR is related to the structure of the protein layer, the temperature derivative of the LSPR maximum should correlate well with the DSC. The inset shows both of these and there is obviously a

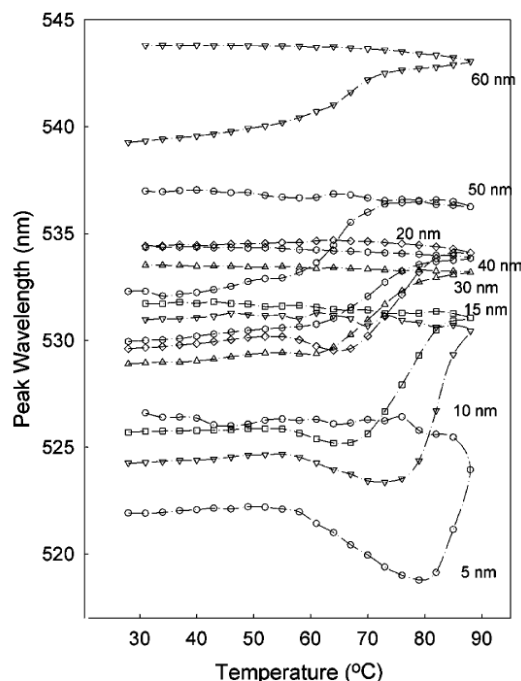


Fig. 3. Heating-cooling curves for BSA-coated gold nanospheres of sizes from 5 nm diameter to 60 nm diameter.

close agreement between the two. This is especially impressive when one notes that the concentration in the DSC measurements is typically about 10^6 times larger than the concentration of proteins on the spheres. After heating to 90 °C, cooling back down to room temperature results in very little change. This is consistent with bulk studies in that the protein has denatured and the structure does not change on subsequent cooling. By comparing the data in Figure 2, we can map the DSC curve [15] which is well understood to the shifts on the LSPR peak of the protein-coated nanospheres.

Figure 3 shows the temperature dependence of the LSPR peak of protein-coated nanospheres for sphere diameters from 5 nm to 60 nm. What is immediately obvious from the figure is the qualitative difference between the behavior observed for protein on large spheres, and that observed for protein on the small spheres. For example, if we compare the temperature dependence of the LSPR peak for the 50 nm sphere with BSA and the 5 nm sphere BSA we see that at a temperature $T \simeq 60$ °C the peak for the 50 nm sphere starts to become red shifted, while that of the 5 nm sphere becomes blue shifted. The magnitude of the effect is also large and for the 5 nm sphere, the total blue shift is approximately the same as the entire red shift for the larger spheres. There are other key differences as well. The temperature dependence for the largest spheres is essentially finished by 80 °C, while for the 5 nm sphere, 80 °C is the temperature at which the peak of the LSPR

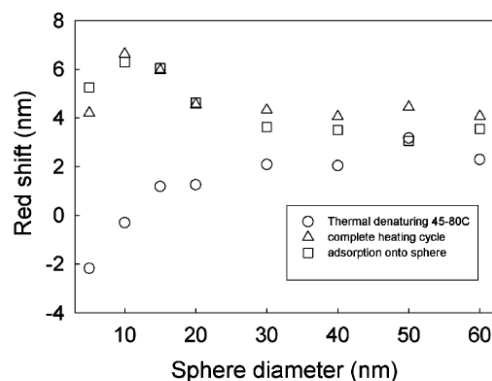


Fig. 4. Red shift observed at various stages in experiment. Squares show the red shift upon protein adsorption to the nanosphere in phosphate buffer solution, the circles show the red shift (relative to room temperature) as the sample is heated from 45 °C to 80 °C, and the triangles show the difference between room temperature measurements before and after a complete heating cycle.

starts to red shift. This continues to 90 °C. In contrast, temperature ramps of bare spheres show only reversible shifts with a magnitude < 1 nm. Figure 4 provides a quantification of some of these observations. This figure shows the shift of extinction maximum upon adsorption, the red shift upon heating the system from 45 °C to 80 °C, and the difference between the initial spectrum and the spectrum at the same temperature after a complete thermal cycle to 90 °C. The plot shows that even though the *small-sphere* behavior is qualitatively different from the *large-sphere* behaviors, the change from one type of behavior to the other is continuous (though quite rapid). It also shows that the changes start to be observed for spheres in the range 20–30 nm. While this might be associated to a relation between protein structure and the sphere curvature, it is also in the region where deviations are observed from ω_p . We note, though, that the deviations from the bulk ω_p are very small ($\sim 0.2\%$) and are unlikely to dominate the observed behavior. For this reason, we believe the effects shown in Figures 3 and 4 support the idea that the structural transitions of an adsorbed protein upon denaturing can be affected by the local curvature.

In order to relate the observed behavior to physical properties, it is necessary to make some simplifying assumptions. In particular, we treat the protein as a uniform isotropic coating and use Mie theory. This is a reasonable assumption that allows us to do a detailed calculation of the extinction coefficient that can be compared with the experimental results. The calculations are done using MatLab routines [16] based on original routines in reference [12]. We calculate the entire extinction spectrum and find the wavelength of the maximum extinction, λ_0 as well as the maximum extinction value, ϵ_0 . For each sphere size, we do the calculations for a range in layer thickness and refractive index. This procedure allows us to gener-

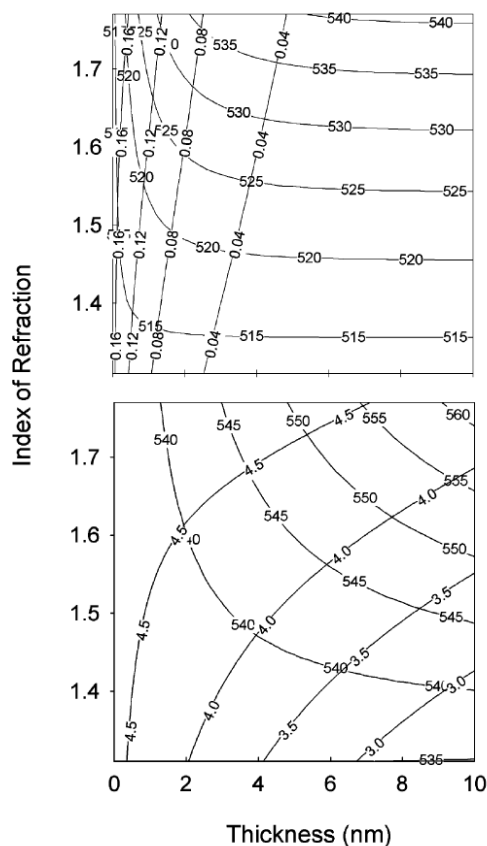


Fig. 5. Contour plots showing the result of Mie scattering calculations for a uniformly coated sphere as a function of layer thickness and refractive index. The top graph shows the position of the peak extinction and the extinction values for 5 nm coated spheres, and the bottom graph shows these same quantities for the 60 nm coated spheres. The lower graph shows the maximum extinction value as a function of coating thickness and refractive index.

ate a contour plot, such as that shown in Figure 5 for the two extreme sizes, that can be used to compare to experimental data. For this comparison we make a curve in layer thickness-refractive index space (h, n) representing the temperature dependence of the protein layer, and generate a theoretical heating curve. It is important to note that if we used only the peak position, there would be many pairs of h, n that can have a peak at λ_0 , but by measuring the extinction as well, in principle, we are able to uniquely determine an h, n for any measured λ_0, ϵ_0 . It has been noted previously that calculated extinction values do not agree exactly with measured values [12]. This means that there is a multiplicative factor between the experimental and calculated extinction values. The freedom in this scaling factor leads to too much variation in the calculated changes in thickness and refractive index. One

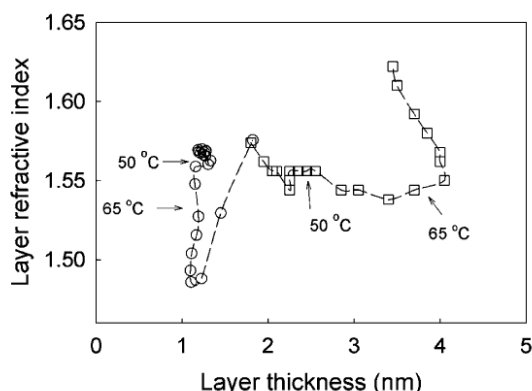


Fig. 6. Average layer thickness and refractive index for BSA on 5 nm (circles) and 60 nm (squares) gold nanospheres.

possible way to remove this difficulty is by introducing a single reasonable physical constraint. We proceed by calculating the scaling factor that gives rise to a refractive index of 1.57 upon initial adsorption. This is consistent with other measurements of refractive index of BSA films [17], and gives rise to an initial film thickness that is quantitatively similar to the thicknesses of 2.4 nm found in ellipsometric studies of adsorbed BSA layers on HgCdTe [17]. This self-consistency supports our use of the initial physical constraint.

Figure 6 shows the h, n trajectories that correspond to the experimentally determined heating curves for the 5 nm and the 60 nm spheres. One point to note from the onset is the high sensitivity of our technique and analysis. Ellipsometric techniques boast sub nm resolution and 0.01 resolution in refractive index for films on a flat surface. We are able to get the same precision on uniformly curved surfaces with instrumentation that is a small fraction of the cost. The values obtained for the thickness of the layer (both here and in Ref. [17]) are less than the 4 nm typically quoted for the smallest physical dimension of BSA. Of course the 4 nm is representative of the tertiary structure, and the fact that an adsorbed layer has a thickness less than 4 nm already indicates that at least some of the tertiary structure is lost on adsorption. However, the fact that thermal denaturing is still observed and closely resembles DSC measurements of bulk BSA, coupled with the knowledge that such denaturing indicates transformation of alpha helix indicates that the secondary structure of the protein is to a large part unchanged even when it is adsorbed to the gold nanospheres. The remaining physical necessity is that the layer thickness should be large enough to contain at least one protein molecule. We estimate this by calculating the volume of BSA in the native tertiary structure to be $\sim 4 \text{ nm} \times 4 \text{ nm} \times 14 \text{ nm} = 224 \text{ nm}^3$, and compare this to the volume of the layer $V_L = \frac{4}{3}\pi((D/2+h)^3 - (D/2)^3)$. For the 5 nm sphere with 1.25 nm coating, we get a $V_T \sim 150 \text{ nm}^3$. This is close to the volume of a single molecule, and given the fact that the tertiary structure is used to calculate

the molecular volume, coupled with the fact that space filling at the tertiary level will necessarily be less efficient than for the secondary structure (which seems to be left mostly intact upon adsorption), this is encouraging agreement. For the 60 nm sphere, the same calculation leads to ~ 100 BSA molecules adsorbed to the sphere.

Figure 6 shows that the qualitative differences noted in Figure 4 can be correlated to quantitative differences in the thermal stability of the BSA. In particular, within the context of the coated-sphere model, the 60 nm coated sphere shows evidence for two stages in the denaturing: A thickening of the coating at near constant refractive index at temperatures up to 65 °C, and increase of refractive index and concurrent decrease in thickness of the coating layer for temperatures greater than 65 °C. The existence of such a two-step process is very similar to the thermal stability of bulk BSA as measured using DSC and shown in Figure 2. For the 5 nm protein-coated sphere, while there does seem to be a two-step process it had distinct differences to that of the large sphere system. In the first case, the lower-temperature process is a decrease in refractive index with essentially constant thickness. This is followed by a very sharp rise in both refractive index and thickness, but at a temperature much higher than that separating the two processes in the large-sphere system. The temperatures $T = 50 \text{ }^\circ\text{C}$ and $65 \text{ }^\circ\text{C}$ are marked by arrows for each case. These differences provide support to our suggestions that structural changes in proteins adsorbed to a surface can be affected by local surface curvature. We note that while we had to employ an initial physical constraint ($n = 1.57$), changes in this constraint do not change the important result that different pathways for thermal denaturing exist for the small-sphere and large-sphere systems. We can speculate as to what physical processes could lead to the behavior shown in Figure 6. We propose that the change in n at near constant h is due to a loss of some of the alpha helix to disordered chain segments, and the subsequent increase again in refractive index at higher temperature is the formation of beta sheets. The idea that differing secondary structures have different refractive index follows from the fact that the macroscopic refractive index is the sum of the molecular dipole moments and will be sensitive to the spatial arrangement. This same idea is used extensively in circular-dichroism studies of protein denaturing. In contrast, the larger-sphere system shows a thickening at constant n in the range 50–65 °C. This thickening is most likely a simple increase in the amount of adsorbed protein (the fact that the thickness is *less* than 4 nm suggests the protein tertiary structure is at least partially lost in this stage). The subsequent increase in n at $T > 65 \text{ }^\circ\text{C}$ (which seems similar to DSC of bulk protein) may be conversion of alpha helix to beta sheet. FTIR experiments of these systems may be able to further quantify the actual changes in secondary structure. These differences in the way the denaturing proceeds on smaller nanospheres may provide access to other denatured states not accessible in normal denaturing conditions. An interesting result of this is that the denaturing of proteins adsorbed on nanoparticles could potentially lead to new

occurrence of protein misfolding diseases. A detailed study of intermediate and final states of proteins adsorbed on nanospheres will be necessary to determine this.

In summary, we have shown that the extinction spectra of protein-conjugated gold nanospheres can be used as a sensitive probe of structural changes in the protein. We show that it is possible to get information that is very similar to that obtained by DSC, even in cases where the concentration of adsorbed protein is 10^6 times smaller than that used in bulk DSC. This is also done without the need to remove bulk protein as required in micro DSC. By comparing the observed changes in the extinction spectra with calculations based on light scattering from a coated sphere under a reasonable physical constraint, we can correlate the observed changes to changes in the optical properties of the protein coating. The techniques discussed in this paper put nanoparticle biosensing on equal footing with techniques like ellipsometry and planar SPR, and can be used in many quantitative applications of biosensing. Using this technique and analysis, we observe a remarkable size dependence of the thermal stability of BSA adsorbed on nanospheres. There are qualitative differences in the way the protein denatures when adsorbed to nanospheres as opposed to that in bulk solution or on large spheres.

References

1. W. Norde, *Adv. Colloid Interface Sci.* **25**, 267 (1986).
2. J.J. Gray, *Curr. Opin. Struct. Biol.* **14**, 110 (2004).
3. V. Castells *et al.*, *Phys. Rev. E* **65**, 031912 (2002).
4. S. Adams, A.M. Higgins, R.A.L. Jones, *Langmuir* **18**, 4854 (2002).
5. R.J. Green, I. Hopkinson, R.A.L. Jones, *Langmuir* **15**, 5102 (1999).
6. H. Larsericsdotter *et al.*, *J. Colloid Interface Sci.* **237**, 98 (2001).
7. M.A. Hayat (Editor), *Colloidal Gold: Principles, Methods, and Applications* (Academic Press, 1989).
8. E. Hunter, J.H. Fendler, *Adv. Mater.* **16**, 1685 (2004).
9. A.J. Haes *et al.*, *J. Fluoresc.* **14**, 355 (2004).
10. N. Nath, A. Chilkoti, *J. Fluoresc.* **14**, 377 (2004).
11. C.A. Mirkin *et al.*, *Nature* **382**, 607 (1996).
12. C.F. Bohren, D.R. Huffman, *Absorption and Scattering of Light by Small Particles* (John Wiley, 1983).
13. L.B. Scaffardi *et al.*, *Nanotechnology* **16**, 158 (2005).
14. J. Lermé *et al.*, *Eur. Phys. J. D.* **4**, 95 (1998).
15. R. Wetsel *et al.*, *Eur. J. Biochem.* **104**, 469 (1980).
16. Christian Mätzler, Research Report No. 2002-08 (Institute of Applied Physics, University of Bern, Switzerland).
17. H. Arwin, *Appl. Spectrosc.* **40**, 313 (1986).

Paper II

Size dependent denaturing kinetics of proteins adsorbed onto nanospheres.²

In paper I, the curvature dependence of the denaturing path in index/thickness space was extracted for BSA on Au nanospheres. This path was a convolution of time and temperature data. Hence, paper II looks at isothermal denaturing in order to isolate the time dependence. It was apparent in paper I that certain assumptions had to be made in order to extract the desired index/thickness data. In paper II, we find a measure of the denaturing rate and extract activation energies from an Arrhenius plot without having to resort to the previous model. These energies are extracted for a series of nanosphere sizes, once again displaying dependence of denaturing on curvature.

²Reproduced with kind permission of Springer Science+Business Media, The European Physical Journal E - Soft Matter, J. H. Teichroeb, J. A. Forrest and L. W. Jones, Size-dependent denaturing kinetics of bovine serum albumin adsorbed onto gold nanospheres, 2008

License Number	1994830580456
License date	Jul 23, 2008
Licensed content publisher	Springer
Licensed content publication	The European Physical Journal E - Soft Matter
Licensed content title	Size-dependent denaturing kinetics of bovine serum albumin adsorbed onto gold nanospheres
Licensed content author	J. H. Teichroeb
Licensed content date	Jul 18, 2008
Volume number	
Issue number	
Pages	1 - 5
Type of Use	Thesis / Dissertation
Details of use	Print
Portion of the article	Full text
Title of your thesis / dissertation	Selected Experiments with Proteins at Solid-Liquid Interfaces
Expected completion date	Sep 2008
Total	0.00 USD

Size-dependent denaturing kinetics of bovine serum albumin adsorbed onto gold nanospheres

J.H. Teichroeb, J.A. Forrest^a, and L.W. Jones

Department of Physics and Astronomy, Department of Optometry, and Guelph-Waterloo Physics Institute, University of Waterloo, 200 University Ave. W., Waterloo, Ontario, N2L 3G1, Canada

Received 23 November 2007 and Received in final form 25 April 2008

Published online: 8 July 2008 – © EDP Sciences / Società Italiana di Fisica / Springer-Verlag 2008

Abstract. We have used localized surface plasmon resonance (LSPR) to monitor the kinetics of thermal denaturing of bovine serum albumin (BSA) adsorbed onto gold nanospheres of size 5 nm–100 nm. The effect of the protein on the LSPR was monitored by visible extinction spectroscopy. The wavelength of the peak extinction (resonance) is affected by the conformation of the adsorbed protein layer, and as such can be used as a very sensitive probe of thermal denaturing that is specific to the adsorbed (as opposed to free) protein. The time dependence of the denaturing is measured in the temperature range 60 °C–70 °C, and the lifetimes are used to calculate an activation barrier for thermal denaturing. The results show that thermally activated denaturing of proteins adsorbed onto nanoparticles has a nanoparticle-size-dependent activation barrier, and this barrier increases for decreasing particle size. This may have important implications for other protein-nanoparticle interactions.

PACS. 87.64.-t Spectroscopic and microscopic techniques in biophysics and medical physics – 78.67.Bf Nanocrystals and nanoparticles – 87.15.lm Folding dynamics – 87.15.hp Conformational changes

Nanoparticle-based technologies are finding increasing usage in applications ranging from textiles and cosmetic products to cancer detection and therapy. As a result it is imperative to develop a detailed understanding of how biological entities, and at the most basic level, proteins, may interact with nanoscale particles over a range of nanoparticle types and sizes. An important aspect of this problem is the presence of the interface, and this has been studied in detail [1–3]. Effects such as surface charge and hydrophobicity can lead to significant effects on protein structure near any solid interface. Since the size of proteins is on the nm scale, we might expect to see deviations in protein-nanoparticle interactions as the nanoparticle size becomes comparable to any characteristic length scale of the protein [4–11]. In addition for flat substrates with nanoscale roughness, the effect of surface topography on protein-surface interactions has not been studied in detail. The use of spheres is a model system with constant curvature to mimic nanoscale roughness on surfaces. The effect of the adsorbed protein coating on the nanoplasmon extinction spectrum of colloidal gold (an area of study that might be termed bionanoplasmonics) is reasonably well established [12–14]. We have recently shown that detailed analysis of the optical extinction spectrum for protein-coated gold nanospheres, combined with

a quantitative mathematical model, leads to an ability to describe the protein coating with a sensitivity similar to that of ellipsometry, or planar surface plasmon resonance techniques [14]. Using this technique, we reported evidence for significant differences in the temperature dependence of the physical properties of the adsorbed protein layer between BSA adsorbed on large nanospheres ($\gtrsim 20$ nm) and that on small nanospheres [14]. The irreversibility of the observed processes as well as the coincidence in temperature with denaturing in bulk BSA suggested it can be correlated with thermal denaturing. This description, while very compelling, rested on an assumption concerning the initial refractive index of the protein layer on the nanoparticle, and on the validity of the protein conjugated nanosphere being modeled by a homogeneously coated sphere. One solution to this problem is to study a process that allows one to study the thermal denaturing process without having to make assumptions about the details of the protein coating on the gold nanospheres. This, in turn, would allow a model-independent analysis of the spectroscopic data. Since it is easy to determine what the effect of denaturing is on the optical extinction spectrum of protein-coated spheres in solution (without having to model the effect), we can use such data to track the isothermal kinetics of the denaturing process. For a thermally activated process, the rate constant will have a particular temperature dependence. By determining the

^a e-mail: jforrest@uwaterloo.ca

rate of isothermal denaturing at a number of different temperatures, one can find the thermal activation barrier for the denaturing process without making any assumptions about the properties of the adsorbed protein layer. This activation barrier is determined by the actual molecular rearrangements that occur during the denaturing process. In this paper we measure the time dependence of the denaturing of bovine serum albumin that has been adsorbed onto gold nanospheres of size 5 nm–100 nm.

The experimental procedure for making the protein-coated spheres, as well as the measurement of the optical extinction have been described in detail elsewhere [14, 15]. We used essentially fatty acid, and globulin-free bovine serum albumin (BSA) with minimum purity 99% from Sigma-Aldrich (Canada). Phosphate buffer solution (PBS) was made to a pH of 7.45 according to the recipe: 0.110M NaCl, 0.0190M Na_2HPO_4 , 0.00460M NaH_2PO_4 . Nanosphere sizes of 5 nm, 10 nm, 15 nm, 20 nm, 30 nm, 40 nm, 50 nm, 60 nm and 100 nm were obtained from Ted Pella and used in the present studies. Optical extinction measurements were made using an Ocean Optics USB2000 miniature spectrometer with a tungsten filament lamp as the light source. Calorimetric studies on bulk BSA solution indicate that changes mainly occur in the temperature range 60 °C–70 °C, and so this temperature range, with 2° increments, was chosen for the isothermal optical extinction measurements. For each measurement temperature the sample was heated from room temperature to the desired 5° increments, pausing every 5° for 2 minutes to prevent any temperature overshoot and then held at the desired value for the duration of the experiment. The measured temperature was stable to within ± 0.3 degrees. Each spectrum was acquired with an integration time of 8 ms and 3000 averages. There was a 10 minute wait between the completion of one spectrum acquisition and the beginning of the next. Extinction spectra were calculated as $\epsilon(\lambda) = \log I_0(\lambda)/I(\lambda)$. The resulting extinction spectra were smoothed using a local smoothing technique with second-degree polynomial regression and Gaussian density weighting of points with a sampling proportion of 0.1. The wavelength of maximum extinction, λ_{max} , was found by determining the wavelength where the numerical derivative of the smoothed spectrum vanished. This procedure allows us to determine the value of λ_{max} to within 0.2 nm. A representative spectrum is shown in Figure 1 for BSA coated on 30 nm gold nanospheres. The calculations developed in our previous work [14] can be used to determine the protein surface coating on the nanospheres. Figure 2 shows the calculated surface coverages obtained for nanosphere sizes from 5 to 40 nm. This is compared to the maximum surface coverage of 3.7×10^{12} molecules/cm² found in reference [16]. As in that case, a molecular size of (5.5 nm \times 5.5 nm \times 9 nm) means that end-on adsorption would lead to a coverage of 3.3×10^{12} molecules/cm² and side-on adsorption would lead to a coverage of 2×10^{12} molecules/cm². The fact that the coverage on the 5 nm nanospheres is so low (1.3×10^{12} molecules/cm²) likely means that the BSA has lost its tertiary structure when adsorbed on the 5 nm spheres.

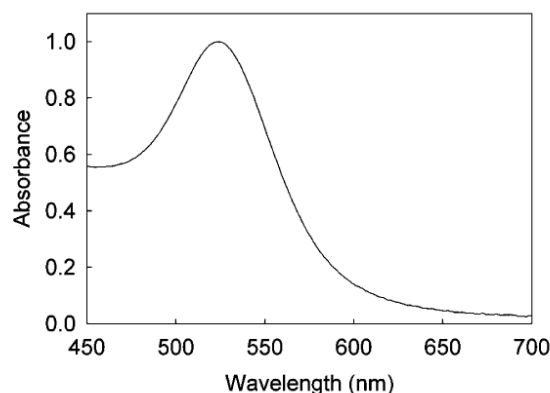


Fig. 1. Optical extinction spectrum of BSA-coated 30 nm gold nanospheres.

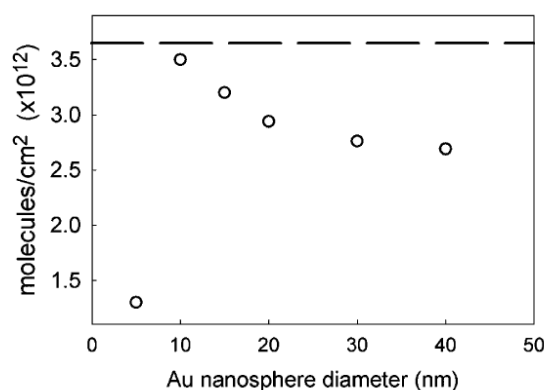


Fig. 2. Protein surface coverage for BSA on gold nanospheres. The dashed line is the maximum surface coverage found in reference [16] for citrate-coated gold substrates.

It is worthwhile to highlight some advantages of using this technique as compared to standard calorimetric techniques typically used to study denaturing in bulk protein solution [17]. If DSC were used to study our samples, the measured signal would be almost entirely from the free protein in solution and *not* the adsorbed protein. It is possible to remove the free protein in the solution by successive centrifuging and resuspension, but the protein coating adsorbed onto a nanoparticle can change significantly between the minimum possible amount required for stabilization and the more physiologically relevant concentrations [18]. This in itself rules out using any technique that cannot on its own differentiate between adsorbed and free protein. Finally, the technique in reference [17] does not really provide an advantage even if it could be used. The calorimetric technique also assumes first-order rate kinetics, but suffers from the additional complication that it convolutes the time and temperature dependence (hence the need to use different heating rates) whereas the technique we use effectively isolates the time and temperature dependence.

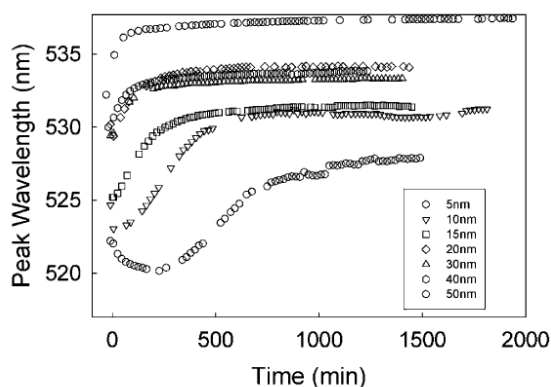


Fig. 3. Isothermal changes in the peak wavelength of the optical extinction spectrum at a temperature of 70 °C for all nanosphere sizes.

Figure 3 shows the time evolution of the values of the wavelength where the extinction is a maximum for a sample temperature of 70 °C. The data in Figure 3 correlates well with experiments taken in the mode where the spectrum is acquired and analyzed in the same way while the sample is heated at a constant rate [14]. Comparison to bulk studies suggests the change in λ_{\max} value is predominantly due to denaturing of the protein (temperature ramps on bare spheres show negligible changes), and so we can use the shift in the position of the extinction peak as a measure of what fraction of the sample denaturing process is complete at any particular time. In many cases, especially for the higher temperatures and larger spheres, the spectrum had already shown a significant shift (and hence a significant fraction of the protein had denatured) by the time the sample had reached the desired temperature. For the temperature of 70 °C shown in Figure 3, the denaturing on larger spheres was essentially complete before the desired temperature was reached, and so the data for the 60 nm and 100 nm spheres could not be obtained for the highest temperatures. It is worth noting that this type of measurement is not necessarily applicable to any protein/nanosphere combination. For example, if we used silver nanoparticles instead of gold, only a continuous redshift with no long time asymptote is observed during the denaturing process. This is very likely due to nanosphere aggregation that accompanies denaturing for that system.

Converting the value of λ_{\max} to the fraction of protein denatured is fairly straightforward. We assume that the fraction of denaturing is simply proportional to the relative fractional shift in λ_{\max} . This is described in more detail below. For the large-sphere data the peak position appears to be a monotonic function of the fraction denatured. This is evident both in Figure 3 and in reference [14]. However, for sphere sizes of 5 nm and 10 nm, the peak position appears to be non-monotonic as the fraction of denatured protein increases. This makes a simple one-to-one correspondence between peak position and fraction of denatured protein impossible. As an alternate way to quantify the fraction of denatured protein

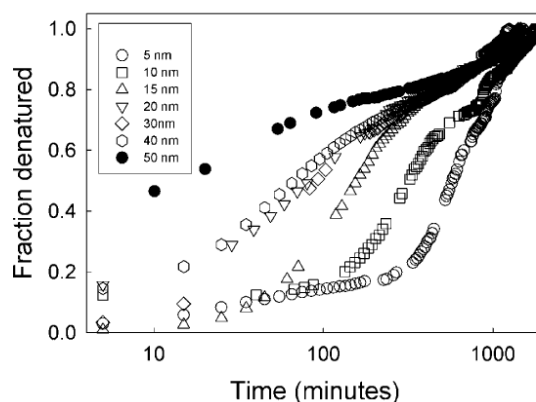


Fig. 4. Fraction of denaturing process that has occurred for 70 °C using the analysis procedure discussed in the text.

$N(t)$; $0 < N(t) < 1$ from the time dependence of the measured peak position, we calculate the line integral of the *shift* in peak position from its initial value. In order to ensure that scatter in the data is not mistaken for denaturing, the process is not deemed to have started until the variation from the starting position is > 0.4 nm. Similarly when the position of the maximum wavelength is within 0.4 nm of the asymptotic value, the denaturing process is deemed to have finished. More quantitatively we write the fraction of denaturing, $N(t)$, at time t as

$$N(t) = \frac{\int_a^t (1 + (\frac{d\lambda}{dt})^2)^{1/2}}{\int_a^b (1 + (\frac{d\lambda}{dt})^2)^{1/2}}, \quad (1)$$

where the point a is the time at which $\lambda_{\max} - \lambda_{\max}^{\text{start}} > 0.4$ nm is first satisfied and the point b is the time at which $\lambda_{\max}^{\text{end}} - \lambda_{\max} < 0.4$ nm is first satisfied (*i.e.*, $a < t < b$). We note that in some cases, a significant fraction of denaturing has already occurred by the time the sample is at the correct temperature. This results in $a < 0$ and $N(0) > 0$. The results of this process for the same 70 °C data are shown in Figure 4 for all sphere sizes where it was possible to obtain data. At this temperature the denaturing of the BSA on the 60 nm and 100 nm spheres was already complete by the time the sample had reached 70 °C. We note that while the derived values of $N(t)$ are now monotonic, there is still an anomalous shape in the curve where the original data was non-monotonic. This is unavoidable since there are times where the value of λ_{\max} is unchanging while denaturing is presumably still occurring. A possible reason for this is the fact that we are so far ignoring changes in the actual extinction value $\epsilon(\lambda_{\max})$. The way to eliminate this is to also consider the value of the extinction at the peak. Attempts to do this were not definitive as the value of the maximum extinction has an experimental uncertainty that is similar to the amount of change in that time period. It is interesting to note that the denaturing curves do show evidence for a two-step process (two distinct linear portions on the graph) especially for the 5, 10 and 15 nm spheres, but it is not possible to exclude this as be-

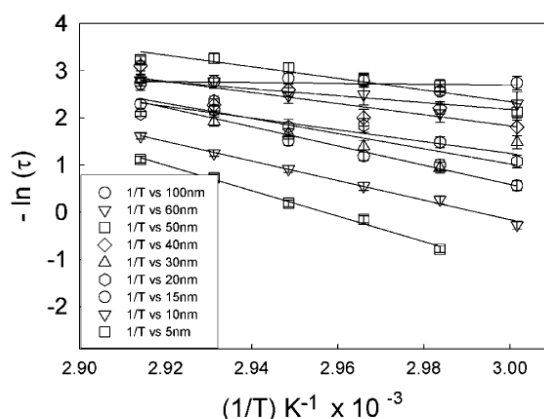


Fig. 5. Denaturing half-life as a function of $1/T$ shown for all sphere sizes. The slopes of these lines are the size-dependent activation barrier.

ing an artifact of the data reduction procedure. The result of having to use the procedure above is that we are forced to consider the curves shown in Figure 2 as approximate. This is really not a significant disadvantage at all as the only value we require is the lifetime of the denaturing process, and this can be determined to reasonable accuracy even with the uncertainties in the values of $N(t)$. Also the conformational states of the adsorbed proteins are also very likely heterogeneous, and so we are averaging over this distribution of conformations. In order to determine the activation barrier for thermal denaturing of proteins adsorbed to spheres of a particular size, we need to define a lifetime of the denaturing at each temperature. The actual choice (half-life, $1/e$ time, etc.) is not important as all choices will lead to the same activation barrier as long as they are related by a simple multiplicative factor. We use the time it takes for the denaturing to be halfway completed (*i.e.* $N(\tau) = 0.5$) as the lifetime. The activation energy for the denaturing process at that particular sphere size can be determined by plotting $-\log \tau$ versus $1/T$ (in kelvins) and determining the slope. The result of this for all sphere sizes is shown in Figure 5. The fact that the data plotted in this form is well described by linear fits for all sphere sizes suggests legitimacy of the procedure used.

The above process can be repeated for all sphere sizes to obtain the size dependence of the activation barrier for thermal denaturing. The result of this procedure is shown in Figure 6. It is clear from the figure that the activation barrier for the thermal denaturing of BSA adsorbed onto gold nanospheres is clearly dependent on the size of the nanoparticle. Also shown on this graph is the activation barrier for bulk BSA [19] of 314 ± 5 kJ/mol as determined using calorimetry. The fact that the activation barrier for denaturing the adsorbed particle is much less than that for bulk protein is not surprising as many proteins have a tendency to denature more easily on surfaces than in bulk solution. What is surprising is the extent of the dependence on the size of the nanoparticle, and the persistence

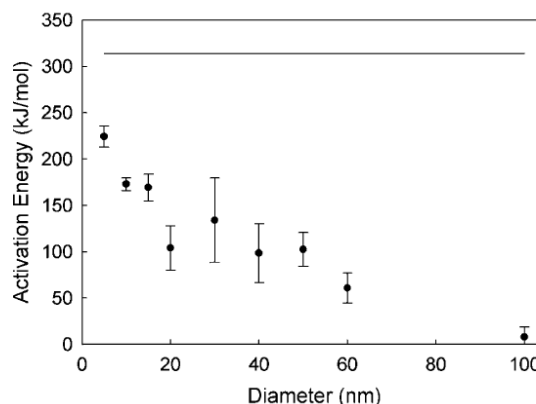


Fig. 6. Activation barrier for BSA denaturing as a function of sphere size. The solid line is the bulk value from reference [19].

of this effect to such large nanoparticle sizes. The difference between the 100 nm particle and the 5 nm particle is more than a factor of 25. Since the activation barrier provides information on the energetics of the actual structural changes during denaturing, it is interesting to consider the possibility of different denaturing pathways for the protein adsorbed onto small spheres and large spheres. Perhaps even more surprising than the differences between the activation energies for the different sphere sizes is the similarities. In particular we have shown in Figure 2 that the surface coverage on the 5 nm spheres is much lower than that on other spheres, and rough calculations suggest that only by losing its tertiary structure can the BSA have this value of coverage. Given this large difference between the molecular coverage on the 5 nm spheres *versus* larger spheres, it is surprising that the activation barrier appears to be a smoothly varying function of sphere size. This would seem to indicate that the denaturing signal has only a small contribution from the structural/conformational changes associated with changing from the native structure to that of the adsorbed molecules on the 5 nm spheres. We are currently developing an experiment to try to probe the secondary structure of the protein adsorbed on the nanoparticles.

The results of Figure 6 can be compared with our previous studies on the temperature-dependent thermal denaturing of BSA on gold nanospheres [14]. In that work we used a detailed mathematical model to probe structural changes of the adsorbed protein layer during thermal denaturing. That work indicated significant differences between the structural changes in the protein (in terms of the thickness and density of the adsorbed protein layer) adsorbed onto small (5 nm) and large (60 nm) spheres. The current work shows that in a *model-independent way* isothermal denaturing kinetics also show significant quantitative differences in the denaturing on large *versus* small spheres. These results are compelling, and indicate that certainly for the case of BSA on gold, there is a strong size dependence for the structural changes that take place

during denaturing. The differences between small spheres and large spheres on both initial adsorption and the denaturing process suggest that both the tertiary structure and secondary structure may exhibit such a size dependence. Given these results, it is worth pursuing the general idea that some structural changes in other proteins (especially those related to protein function) may be affected in a size-dependent way by their adsorption to different nanoparticles. This may have relevance in areas of health and exposure to nanoparticles as well as in areas where nanoparticles are used in therapy [20].

References

1. W. Norde, *Adv. Colloid Interface Sci.* **25**, 267 (1986).
2. J.J. Gray, *Curr. Opin. Struct. Biol.* **14**, 110 (2004).
3. V. Castells *et al.*, *Phys. Rev. E* **65**, 031912 (2002).
4. H. Larsericsdotter *et al.*, *J. Colloid Interface Sci.* **289**, 26 (2005).
5. M. Lundqvist *et al.*, *Langmuir* **20**, 10639 (2004).
6. C.A. Hayne, W. Norde, *J. Colloid Interface Sci.* **169**, 313 (1995).
7. P. Billsten *et al.*, *J. Colloid Interface Sci.* **175**, 77 (1995).
8. A. Vertegel *et al.*, *Langmuir* **20**, 6800 (2004).
9. A. Kondo *et al.*, *J. Colloid Interface Sci.* **143**, 214 (1991).
10. R. Kurrat *et al.*, *J. Colloid Interface Sci.* **185**, 1 (1997).
11. T.J. Su *et al.*, *J. Phys. Chem. B* **102**, 8100 (1998).
12. A.A. Kamvev *et al.*, *BioSci. Rep.* **22**, 541 (2002).
13. N.G. Khlebtsov *et al.*, *Colloid J.* **65**, 508517 (2003).
14. J.H. Teichroeb *et al.*, *Eur. Phys. J. E* **21**, 19 (2006).
15. M.A. Hyat (Editor), *Colloidal Gold: Principles, Methods, and Applications* (Academic Press, 1989).
16. S.H. Brewer *et al.*, *Langmuir* **21**, 9303 (2005).
17. J.M. Sanchez-Ruiz *et al.*, *Biochemistry* **27**, 1648 (1988).
18. P. Lea, D.K. Gross, *J. Histochem. Cytochem.* **40**, 751 (1992).
19. S. Baier, D.J. McClements, *J. Agric. Food Chem.* **49**, 2600 (2001).
20. X. Huang, I.H. El-Sayed, W. Qian, M.A. El-Sayed, *JACS* **128**, 2115 (2006).

Paper III

Influence of nanoparticle size on the pH dependent structure of adsorbed proteins studied with quantitative localized surface plasmon spectroscopy³

Heat is not the only way to perturb a protein in order to examine its stability and conformational changes. Changes in pH will also alter a protein's conformation through bond breaking, as well as shifting the charge. In this paper we seek to address the effect of curvature upon the conformation of conjugated BSA under subjection to acid perturbation. Transitions that occur in bulk protein may not occur once adsorbed. Additionally, transitions that are reversible under the relatively dilute conditions of a bulk solution, may become irreversible when confined to the high protein density situation of adsorption.

³Submitted to the European Physical Journal E – Soft Matter.

Influence of nanoparticle size on the pH dependent structure of adsorbed proteins studied with quantitative localized surface plasmon spectroscopy

J.H. Teichroeb, P.Z. McVeigh, J.A. Forrest

Department of Physics and Astronomy and Guelph-Waterloo Physics Institute,
Waterloo, ON, Canada, N2L 3G1

Abstract

We have studied pH dependent conformational transitions of Bovine Serum Albumin adsorbed onto different sizes of gold nanospheres. For larger spheres ($D > 10$ nm) there is evidence for a path dependent extended state near pH 4, over a very small pH range. For smaller nanospheres (5nm and 10 nm) the evidence for such a transition is either much weaker or completely suppressed. We suggest that the absence of the transition on small spheres is due to the fact that the protein adsorbed on such small spheres has already lost at least some of its tertiary structure. The results have important implications for the functionality of proteins adsorbed onto nanospheres or surfaces with nm scale roughness.

Introduction

Nanomaterials have received considerable attention in recent years, with applications in diverse fields including manufacturing, electronics, environmental remediation, cancer therapy and medical diagnostics¹. Since the length scales of such materials are close to that of the basic operating units in biological systems (proteins), a large number of techniques have been developed in terms of both medical therapy²⁻⁵ and imaging⁶. In such biological systems of interest colloidal gold displays properties which make it an appealing nanoparticle vector. The colloid is easily coated with proteins, allowing for immunolabelling and targeting to certain cell populations within the body – where the small particle size allows for excellent penetration into tissues⁶. By exploiting the surface plasmon resonance of such immunolabeled gold nanoparticles, laser induced hyperthermia-based therapies have been demonstrated in-vitro^{2, 7}.

The efficacy of any such molecular-targeting scheme is ultimately dependent on the specificity of binding between the molecule on the nanoparticle and the intended receptor. This mechanism is often presented diagrammatically using a simplistic 'lock-and-key' model, but such an approach tacitly assumes the tertiary structure of the protein remains unchanged upon adsorption to the nanoparticle. More generally, as nanoparticles continue to find new applications within our everyday environment, their exposure to biological systems will increase accordingly. Thus from either a therapy-optimization or health-regulation standpoint, we require a detailed understanding of how such systems interact on a molecular level. The interaction between an interface and protein has been discussed in several comprehensive reviews^{8, 9}, in particular, effects such as charge¹⁰, hydrophobicity^{11, 12}, and surface chemistry¹³ have been extensively investigated.

It has been demonstrated that the curvature of the surface can also be a significant factor in controlling adsorbed protein structure and functionality¹⁴⁻¹⁷. Roach *et al.*¹⁶ used infrared spectroscopy to show that Bovine Serum Albumin (BSA) underwent less conformational disordering on highly curved silica surfaces than on flat surfaces, but found this effect to be strongly dependent on surface chemistry. Curvature dependence can only reliably be studied by varying the local curvature (or size of sphere) while keep surface chemistry constant. For example, Teichroeb *et al.*¹⁷ employed localized surface plasmon resonance (LSPR) to find that thermal denaturing of BSA proceeded differently for proteins adsorbed to small (5nm) and large (60nm) gold nanospheres. Specifically, it was shown that BSA on 60nm spheres showed similarity to adsorption and denaturing in the bulk, while BSA on 5nm spheres acted as though some of the tertiary structure has been lost upon adsorption to the nanospheres – the 5nm

spheres exhibited an initial volume of adsorbed protein in reasonable agreement with the volume of a single BSA molecule.

To effectively study bound proteins at this scale, techniques must have the sensitivity to detect small concentrations of nanoparticles while rejecting the signal from free protein in solution which may be orders of magnitude larger. Circular dichroism (CD) is commonly used for the study of secondary structure in bulk solutions, but suffers from inconsistency in the determination of absolute secondary structure¹⁸. Applicability of CD to adsorbed protein layers implicitly assumes the optical properties of secondary units are unaffected by adsorption. The results obtained are only as good as this (untested) assumption. By employing a metallic nanosphere which admits surface plasmon resonance, visible light spectroscopy may be used to probe adsorbed protein properties. Such an approach may look qualitatively at shifts in the plasmon resonance^{19, 20} or employ a quantitative model to determine physical properties of the adsorbed layer^{17, 21, 22}. These visible light techniques are relatively cheap to perform, easy to assemble and carry out, and are insensitive to bulk solution protein – deriving signal only from the localized surface plasmon of the metallic nanoparticle (LSPR).

BSA has been shown to be a heart-shaped molecule having rough dimensions of a solid equilateral triangle with 8.0nm sides and a 3.0nm average depth, with three principle domains and a flexible conformation which can vary greatly with solution pH, as outlined by Carter²³. The isomers of interest are the Native (N) (pH 5-8), Basic (B) (pH 9-9.5), Fast (F) (pH 3-4), and Expanded (E) (pH <3). Transition from the N to the F form appears to involve an unfolding of alpha helices in domain III and its separation from the other domains in BSA²⁴. This results in domain III having a loose structure, causing reduced solubility due to exposure of hydrophobic groups. The transition to the E form involves further loss of alpha helices, and in particular intra-domain alpha helices, opening the molecule into an expanded form. Hydrodynamic studies²⁵ indicate a change in “axial ratio” from 4 to 9. The B form near pH 9 involves an unfolding of domain III once again, as well as more minor changes to domain II, and a separation of the domains²⁶. It is considered to be somewhat analogous to the N-F transition. Englebienne et al.²⁰ have studied the state of human serum albumin (HSA) on 50nm gold nanospheres from pH 7 to pH 12, observing a possible N-B and the higher pH Basic-Alkaline transition. Shang et al.¹⁹ examined the differences in spectra of BSA adsorbed to 15nm gold spheres at pH 3.8, 7.0, and 9.0, observing differences attributed to the F,N, and B forms respectively. Both of these studies involve a limited number of pH values in the region of physiological interest, and a single nanoparticle size.

Since these pH-dependant transitions arise from reversible alterations to the tertiary and secondary structure of BSA, they should provide a useful indicator of the sensitivity of a technique to changes in the protein structure on the surface of a nanoparticle. In addition the studies will reveal how adsorption to nanoparticles affects these conformational transitions that are well studied in bulk BSA. We have studied the properties (refractive index and layer thickness) of adsorbed BSA as a function of gold nanoparticle size from 5 nm to 40 nm and pH values between 1-7 using quantitative LSPR-based spectroscopy to determine the sensitivity of our quantitative approach and to examine the substrate curvature effect in this system.

Materials and Methods

Spectrophotometer Design

The spectrophotometer design employed a standard optical extinction arrangement. The light source was a tungsten-filament lamp with fiber coupling (Ocean Optics HL-2000, Dunedin, FL, USA), with the light being collimated before passing through the cuvette containing the sample solution. The light exiting the sample was collected into another fiber and directed to the spectrometer (Ocean Optics USB4000, Dunedin, FL, USA). The samples were contained in micro-volume disposable polystyrene cuvettes. The cuvettes were secured in a solid brass

mount with set screws which was attached to an optical translation stage. The stage was adjusted to ensure the collimated beam fell only into the middle of the sample area.

To enhance the thermal stability of the optical system, the spectrometer and optical fibers were contained in a temperature-controlled enclosure which contained a PID-based (OMEGA, Stamford, CT, USA) temperature controller with resistive heater. This kept the spectrometer at constant temperature within ± 0.25 K and provided for sufficient stability to carry out the desired experiments. The entire experimental apparatus was enclosed in a container to exclude all external light sources and particulate matter.

Sample Preparation and Data Acquisition

Charge stabilized gold nanospheres of various sizes (5, 10, 20, 30, 40nm) in aqueous solution at concentrations of (5.0×10^{13} , 5.7×10^{12} , 7.0×10^{11} , 2.0×10^{11} , 9.0×10^{10}) respectively, were purchased from Ted Pella Inc (Redding, CA, USA). BSA (>99%) in crystal form was obtained from Sigma (Oakville, ON, Canada). 100 μ L of 1mg/mL BSA in MilliQ H₂O was added to 400 μ L of the colloid and allowed to conjugate for 1 hour. An additional 500 μ L of 0.2% (by mass) BSA in MilliQ H₂O was then added to dilute the solution. Stock solutions to adjust the pH of the colloid samples from pH 1-7 were created using HCl (Sigma). We chose this range for its physiological relevance and similarity to other studies. It is important to note that these samples had the pH value changed from 7 (the pH at which the protein was initially adsorbed) to the final value in a single step.

Spectra were acquired using Spectra Suite (Ocean Optics, Dunedin, FL, USA) with an integration time of 90 msec, averaging 2000 measurements. The pH adjusting solution was placed in the cuvette, aligned, and a reference spectrum collected. The gold colloid-protein sample was then added to the cuvette and spectra acquired every 5min for 3 hours. The gold-protein-pH sample is not stirred, and requires some time for mixing to occur, as well as some time for the protein to adopt its new conformation. Spectral changes were monitored for up to 13 hours to determine the point at which they stabilized (3 hours). This procedure was repeated for all sphere size (5, 10, 20, 30, 40nm) and pH (1 - 7) combinations. For values below pH 1 the solutions for larger sphere sizes were not stable and the extinction spectra exhibited continual shifts to longer wavelengths attributed to particle aggregation.

In addition to samples where the final pH was arrived at in a single step, spectra were collected from individual samples, taken through a continuous series of pH changes. After conjugating the protein to the nanospheres as previously described, HCl was then added to the cuvette in order to bring the sample through a consecutive series of pH values. Samples were stirred and allowed approximately 20 minutes for equilibration at each step. Three schemes were employed for the continuously changing pH studies: 1) start at pH 7 and step through consecutively more acid pH's, 2) take a single step down to pH 3 and consecutively step back to pH 7, 3) start at pH 7 and move stepwise down to pH 3.3 followed by stepwise adjustment back to pH 7. Example LSPR spectra for the bare spheres are shown in Figure 1.

Data Analysis

Experimental spectra were automatically smoothed using a local smoothing technique with second degree polynomial regression and Gaussian density weighting of points with a sampling proportion of 0.1. Spectra were then normalized, and the peak location determined by fitting a linear function to the numerically-calculated derivative near to the zero crossing. Peak extinction values were taken as the maximum of the smoothed spectrum. This procedure allows us to determine the position of the extinction maximum to within 0.2nm.

Theoretical extinction spectra were generated for each of the sphere sizes used based on the routines provided by Bohren²⁷ for a sphere uniformly coated by an isotropic material, using MatLab routines from Matzler²⁸ as extended and previously documented¹⁷. Contour plots were produced containing peak wavelength and extinction as a function of protein coating thickness (h) and index of refraction (n), as shown in Figure 2. Comparison of the measured quantities with

calculated ones allow a manual “best fit” between theoretical h and n and experimental peak wavelength and extinction observations. Due to the previously noted mismatch between calculated and experimental extinction values²⁷, a corrective scaling factor was introduced. The scaling factor was derived from pH 7 to allow comparison to other studies²⁹. The extinction corresponding to an index of refraction of 1.57 at the experimental peak wavelength was determined from the contour plots. This was then taken as a ratio of the experimental extinction value, producing a scaling factor for all other pH's, for that sphere size. It is important to note that within reason, a poor choice of scaling factor does not change the qualitative shape of the h vs. n curve since, for a given sphere size, the same factor is used.

Results

Figure 3 displays peak wavelength values for all sphere sizes as a function of solution pH. The corresponding peak extinction values are not displayed as they do not exhibit any significant features within the uncertainty of the measurements. The difference between BSA on larger sphere sizes (20nm-40nm) and smaller sphere sizes 5nm-10nm is simply the sphere-size dependence of the extinction spectrum of the nanospheres themselves, and is not of interest for the current study. The more important feature to notice is the small but reproducible and significant increase in wavelength around pH 4 for the larger spheres (20nm-40nm), which does not appear for the smaller spheres (5nm,10nm). In order to gain a clearer understanding of this feature, spectra were acquired for samples with finer pH spacing in the region near pH 4, for representative larger (30nm) spheres (Figure 4) and smaller (5nm) spheres (Figures 5). The data in Figure 4 for the BSA on 30 nm spheres demonstrates a shift in the position of the extinction maximum, beginning near pH 4.6 on the basic side, and pH 3.4 on the acid side. These approached a sharp peak at pH 3.8. The sharpness of the peak in wavelength was unusual, and multiple trials at this pH revealed multiple values (though *all* showed the peak in this pH range). This suggests that the conformation at the transition pH is so sensitive to pH that we are not able to control our solution finely enough to reproduce the exact value of the position of the transition peak. It is evident in the coarse run (Figure 3) that much of the wavelength rise around pH 4 has returned to a lower value towards lower pH. This is also more evident in the more localized trials, and is also seen in the data of Englebienne²⁰. BSA molecules causing the same wavelength and extinction values on gold nanoparticles suggest that they are in the same state (or at least can be characterized by the same protein coating thickness and refractive index) at pH ~ 3 as they are for pH ~ 5 . This is similar to the observations of Su et al.³⁰ using neutron reflectivity of BSA adsorbed onto flat silicon substrates. Such an effect is also seen in the dual polarization interferometry (DPI) studies of Freeman et al.³¹ In bulk, it is expected that continuing toward lower pH will at the very least preserve the F structure, and at some point change even more drastically into the E structure. It is clear from this data that this is not necessarily the case for proteins adsorbed onto solid surfaces.

Figure 5 shows a higher pH resolution study with BSA on 5 nm spheres and highlights a key result of this study - the small (5nm and 10 nm) spheres show little evidence for the sharp transition at pH 3.8. In fact for the small spheres, the wavelength of the maximum extinction exhibits very little pH dependence at all. This result indicates that the process necessary to form this particular protein conformation at pH 3.8 does not occur for BSA adsorbed onto 5 nm and 10 nm spheres. It is possible that this represents an essentially native, but much more stable state of BSA as has been seen on silica particles³². However, given that the transition to the more acidic forms of the molecule involve loss of alpha helix and the breaking of interdomain bonds leading to more extended states of the molecules, it is reasonable that the protein on the 5nm and 10 nm spheres has already lost much of its tertiary structure upon adsorption. This is the same conclusion reached in ref¹⁶ when thermal denaturing was studied on similar gold nanospheres. The small residual effect seen in the actual peak extinction values may be an indication of changes in the secondary structure, that are not accompanied by any discernible change in tertiary structure. This is further reflected in the small changes in thickness and refractive index of the protein layer coating on the 5 nm nanospheres shown in Figure 7. While it

is hardly surprising that protein adsorption and conformational changes could be different on nanospheres than on flat substrates, it is less obvious that one would expect such qualitative changes as the sphere size changes from 5-10 nm to 20-40 nm. Future study in the sharpness of this transition from "large sphere" to "small sphere" behavior may be of interest. Results after modeling the data (including fine pH data) converted to thickness and indices of refraction are depicted in Figure 6 for 30nm, and Figure 7 for 5nm. Taking into account the density of BSA at pH 7, the number of protein molecules per Au nanosphere is estimated to be approximately 1, 11, 22, 37, 78, and 135 respectively for 5, 10, 15, 20, 30 and 40nm spheres. We found a BSA coating thickness of approximately 1nm for 5nm spheres which appears largely pH independent (Figure 7). This thickness is essentially the same as that obtained in our previous work¹⁷ and is very similar to the size of an alpha helix, again suggesting that the lack of transition on this sphere size is due to loss of the tertiary structure, as opposed to stabilization of a native like structure. The 30 nm spheres have a larger coating thickness of about 2 nm, which increases slightly towards lower pH, with an anomalous increase around pH 4. This is similar to the 2.4 nm thickness obtained by analysis of ellipsometric data²⁹. The protein coating refractive index displays increases at pH 4, and it is tempting to think that the feature may correspond to the N-F or F-E transitions, considering the increasing direction of the shift.

While the N-F and F-E transitions in the bulk are reversible, the differences between typical bulk behavior and that shown in the previous figures suggest this may not be the case for the adsorbed protein. For this reason we also performed a series of experiments aimed at quantifying the path dependence and reversibility of the protein conformation near pH 3.8. Figure 8 depicts the wavelength shift of samples which are individually taken through a series of pH changes. In Figure 8a the sample is taken down from pH 7 to pH 3 and back to pH 7, and exhibits a clear hysteresis in the wavelength. This indicates that the structure of the adsorbed protein layer at pH 7 depends on whether it has passed through the peak at pH 3.8. Figure 8b is taken in one rapid step down to pH 3, and back stepwise to pH 7. The wavelength passes through pH 3.8 about which it undergoes a rapid increase, and upon increase to more alkaline values subsequently recovers only about one half of the initial wavelength shift. Figure 8c similarly depicts two different samples taken stepwise down in pH, again with recovery of approximately one half of the initial shift at increasingly acidic values. All of these results indicate a degree of irreversibility of the protein conformation after passing through the transition at pH 3.8. Since the bulk transitions, including the changes in secondary structure, are reversible, it is likely that the irreversibility of the protein adsorbed on the nanospheres is an inter-molecular kinetic effect. Unlike in reasonably dilute protein solutions, the molecules adsorbed onto spheres are all forced to be in very near proximity to other protein molecules. The result of this is that upon losing tertiary structure, there will be a much greater tendency for intermolecular association or aggregation to occur. The disappearance of the transition effects to lower pH in Figures 4 and 6 thus is a result of using a separate sample for each point, each of which is brought to the desired pH quickly. It would be assumed that at pH 2.5 or 3, the same bonds (if not more) are likely to be broken as at pH 3.8. At lower pH however, the protein is also much more positively charged. This could suggest that a quick transition to pH 3 generates a large positive charge on BSA which pins it to the negatively charged sphere, preventing reorientation of the protein molecules, even if intra-protein bonds are broken. At pH 3.8, the intra-protein bonds are broken, but the protein is able to rearrange itself, possibly unfolding, and/or making room for new protein to adsorb.

Examining the modeled 30nm data (Figure 6), there is an obvious feature at pH 3.8, with both the index and thickness increasing about this point. The multiple 3.8 values (triangles) indicate that the transition is extremely sharp in thickness, and that the measurement becomes sensitive to variations in pH that are beyond experimental control. While it is clear that some form of transition is taking place around pH 3.8, it is not obvious as to whether this proceeds similarly to N-F or F-E expansions, as we do not observe two clear transitions as in studies of bulk protein. Bovine serum albumin is typically quoted as being a heart shaped molecule having rough dimensions of a solid equilateral triangle with 8.0nm sides and a 3.0nm average depth. Hydrodynamic studies²⁵

indicate a change in “axial ratio” from 4 to 9 during the F-E transition. Hence, even in the absence of excess protein, a conformational or orientation change could easily justify the change in thickness. Another striking feature of Figure 6 is the large difference in scale between the pH 3.8 transition forms and those at neighboring (both higher and lower) pH. If BSA was undergoing a simple expansion it would be expected to remain in this form post-transition, producing a step for each parameter towards lower pH. While there is evidence for such trends in both the index of refraction and coating thickness data, the effect is dwarfed by the magnitude of the transitional form. This effect is also present in the data of Su *et al.*³⁰. Since the changes in measured extinction values at the peak are within typical experimental scatter, we have modeled the data by using the average extinction value for all pH values. The results of this procedure are shown in Figure 6. In this case the thickness increases continuously from either side of the transition at pH 3.8..

Shang *et al.*³⁰⁸ perform a study which involves looking at pH effects on BSA conjugated to 15nm Au nanoparticles. Their method differs in that they do not conjugate the protein to the Au before changing pH, or placing in buffer, and instead use the same technique described below for studies employing flat substrates. Because of this, even at pH 2.7 aggregation takes place, presumably due to charge screening, forcing them to concentrate on pH's 3.8, 7.0, and 9.0. Comparing their plasmon resonances of conjugates reveals a similar pattern to us, with the peak wavelength of 3.8 being much more red shifted than either pH 7.0, or pH 9.0. BSA at pH 3.8 is positively charged, as opposed to pH 7, and 9 at which it is negative. While there is no indication of their degree of error, an increasing blue shift may well demonstrate that the surface Trp residue is in a more hydrophobic environment. Exactly what this means for BSA, however, is not clear. The fact that a surface Trp residue is placed in a more hydrophobic environment does not necessitate a change, but can be accommodated by an orientation or packing change. If at pH 3.8 the positive charge in conjunction with other surface forces favours the Trp residue facing away from the sphere, or other adsorbed BSA molecules, it may not blue shift, even if the protein is more denatured at pH 3.8. If on average BSA orients itself to face Trp away from the sphere, and other BSA at positive charge, one would also expect in this interpretation for the strength order of the blue shift to be pH 3.8 < pH 7 < pH 9. A similar interpretation may be applied to the red edge excitation study. Thus, in lieu of more evidence, the study is not at odds with our interpretation of the pH 3.8 transition. Circular dichroism (CD) studies performed by Shang *et al.* are analyzed by calculating helicity from a single point on the CD curve vs. Au particle concentration. Given the large number of basis fitting programs available, this is likely done because normal basis function do not fit the spectra. This indicates that either the spectra for protein associated with a surface contain too much error, or more likely cannot be interpreted in terms of basis sets that have been determined for free protein in solution. Despite this, if we examine the helicity values they find, two things are apparent. Firstly, the amount of error as quoted by Shang *et al.* precludes any conclusions about the slope of the helicity vs. concentration graph. Secondly, in terms of absolute helicity, the pH 3.8 spheres are the most denatured for *all* concentrations used in the study, which would tend to support our argument of a transition close to 3.8. Further FTIR studies by Shang *et al.* indicate at best a decrease in unordered structures at pH 3.8 and 9.0 as compared to 7.0. The net result of Shang *et al.*'s multi-technique study is that it can be interpreted in a complementary manner to our own.

It is useful to put the current results into the context of similar results on adsorbed films. With the exception of Englebienne²⁰ and Shang *et al.*³⁰⁸, most such studies have employed flat substrates. Comparison of these studies²⁹⁻³¹ reveals some general trends. As pH is changed from 7 – 5 – 3 the surface coverage changes from about 0.5-2.5-0.5 ng/mm². None of these studies use fine pH spacing so it is not possible to compare the results to the peak in Figure 4. The layer thickness of BSA can also be compared. Neutron reflectivity studies indicate a thickness (at pH 5.1) of 3.6 nm, while DPI suggests a thickness of ~4.5 nm at pH 5. At pH 3 and 7, the neutron reflectivity gives rise to a thickness of 3 nm, while DPI suggest a thickness < 1nm. In both cases, the surface coverage density is ~0.5 ng/mm² at pH 3 and 7, and roughly 2-2.5 at pH 5. While there are some notable differences, the qualitative description is similar using the two different experimental techniques.

Ellipsometric studies show a BSA layer thickness of 2.4 nm at pH 8. Since this region of pH is coincident with the N-B transition in BSA, this value is not in disagreement with those of neutron reflectivity and DPI. Given this consistency between the results on flat surface it makes sense to compare to the observation of protein on nanospheres. In the nanoparticle studies, the peak in thickness and refractive index (and hence material density) occurs at a pH value of 3.8. This is significantly different from the studies on flat substrates, and in fact if we were to use only pH values of 7, 5 and 3 it can be seen in Figure 3 that we would see no change in measured quantities. While the reason for the difference is not clear it is worth noting a potentially important difference in the way the protein samples are prepared. For the flat substrate studies, the protein is simply mixed with a pH adjusted buffer and allowed to adsorb onto the substrate. For the nanospheres, such a procedure would lead to nanoparticle aggregation and a variation on the technique is employed. In our studies, the BSA is adsorbed onto the nanoparticles at pH 7 and then after the adsorption, the protein coated nanospheres are mixed with a buffer solution to achieve the final pH value. The difference between these two cases is that the adsorption process takes place at different pH, and thus the state of the proteins that are being adsorbed are different in the flat substrate versus the nanoparticle experiment even when the final pH is the same. It is not clear what, if any, effect this will have or if this is responsible for the difference in pH value where a peak in thickness is observed. The lack of a high pH resolution study for flat substrates makes a direct comparison to our results impossible, but certainly we note that pH values of 5 and 5.1 seem to show similar results in DPI and neutron reflectivity, indicating that the peak is at least 0.1 pH units wide for flat substrates. This is wider than our observations in terms of the thickness peak of the protein coating. Finally, another key difference is the absence of *any* discernible transition for the 5 nm and 10 nm spheres. In such cases a reasonable explanation is that upon adsorption to the smallest nanospheres, the protein has already lost much (perhaps all) of its tertiary structure.

The differences between the structural transitions of BSA adsorbed onto flat surfaces versus nanospheres are significant. Protein function is almost always linked to structure and changes in tertiary structure (especially loss of such) when the protein is adsorbed onto nanoparticles has far-reaching implications. In particular, the results indicate that even when some nanoparticles (such as the ones here with diameter greater than or equal to 20 nm) allow the protein to adsorb and maintain some degree of the bulk structure, the same may not be true for smaller spheres. The extent and nanoparticle size where such effects occur may be strongly dependent on the type of protein, as well as nanoparticle composition. Detailed studies of the size dependence of protein function are clearly warranted.

Conclusions

We have measured the optical extinction spectrum of BSA coated nanospheres over a range of pH (1-7) and nanospheres size (5-40 nm). We observe an indication of a structural transition over a very limited range of pH near a value of pH 3.8. This transition is observed for sphere sizes from 20 nm to 40 nm), and unlike pH dependent conformational transitions in bulk BSA solutions, is not completely reversible. Protein adsorbed to spheres of diameter 5 nm or 10 nm show no evidence for a transition at any pH in the range studied. The results indicate that the effect of adsorption onto nanoparticles on tertiary structure can be strongly dependent on nanoparticle size.

Acknowledgements

This work was supported by the Natural Sciences and Engineering Research Council of Canada (NSERC). We are grateful for technical assistance by James Chan.

Figure Captions:

Figure 1. Example LSPR extinction spectra for uncoated 30nm Au nanospheres.

Figure 2. Contour plot displaying peak extinction (dotted lines), and wavelength (solid lines) for 5nm Au spheres calculated from Mie theory.

Figure 3. Plasmon peak wavelength vs. pH for BSA on Au sphere sizes (●) 5nm, (○) 10nm, (▼) 20nm, (△) 30nm, (■) 40nm.

Figure 4. Peak wavelength vs. pH for BSA on 30nm Au spheres. *Inset:* Peak extinction vs. pH for BSA on 30nm Au spheres.

Figure 5. Peak wavelength vs. pH for BSA on 5nm Au spheres. *Inset:* Peak extinction vs. pH for BSA on 5nm Au spheres.

Figure 6. (Triangles (▲) are multiple points at pH 3.8) Thickness vs. pH for BSA on 30nm Au from modeling, including finer pH spacing near pH 4.0. *Insets:* Index vs. pH for BSA on 30nm Au.

Figure 7. (●) Thickness vs. pH for BSA on 5nm Au from modeling, including finer pH spacing near pH 4.0. (▼) Index vs. pH for BSA on 5nm Au from modeling, including finer pH spacing near pH 4.0

Figure 8. Wavelength shift of samples which are individually taken through a series of pH changes. A) sample taken down from pH 7 to pH 3 and back to pH 7, B) sample taken in one rapid step down to pH 3, and back stepwise to pH 7, C) two different samples taken stepwise to lower pH.

References

1. Liu, W. T., Nanoparticles and their biological and environmental applications. *J Biosci Bioeng* **2006**, 102, (1), 1-7.
2. Huang, X.; El-Sayed, I. H.; Qian, W.; El-Sayed, M. A., Cancer cell imaging and photothermal therapy in the near-infrared region by using gold nanorods. *J Am Chem Soc* **2006**, 128, (6), 2115-20.
3. Huang, X.; Jain, P. K.; El-Sayed, I. H.; El-Sayed, M. A., Determination of the minimum temperature required for selective photothermal destruction of cancer cells with the use of immunotargeted gold nanoparticles. *Photochem Photobiol* **2006**, 82, (2), 412-7.
4. Lapotko, D. O.; Lukianova, E.; Oraevsky, A. A., Selective laser nano-thermolysis of human leukemia cells with microbubbles generated around clusters of gold nanoparticles. *Lasers Surg Med* **2006**, 38, (6), 631-42.
5. Hilger, I.; Hergt, R.; Kaiser, W. A., Use of magnetic nanoparticle heating in the treatment of breast cancer. *IEE Proc Nanobiotechnol* **2005**, 152, (1), 33-9.
6. Hayat, M. A., *Colloidal gold : principles, methods, and applications*. Academic Press: San Diego ; Toronto, 1989.
7. Zharov, V. P.; Mercer, K. E.; Galitovskaya, E. N.; Smeltzer, M. S., Photothermal nanotherapeutics and nanodiagnostics for selective killing of bacteria targeted with gold nanoparticles. *Biophys J* **2006**, 90, (2), 619-27.
8. Haynes, C.; Norde, W., *Colloids and Surfaces B: Biointerfaces* **1994**, 2, 517-566.
9. Malmsten, M., *Biopolymers at interfaces*. 2nd ed.; M. Dekker: New York ; Basel, 2003; p xii, 908.
10. Garrett, Q.; Laycock, B.; Garrett, R. W., Hydrogel Lens Monomer Constituents Modulate Protein Sorption. *Invest. Ophthalm. Vis. Sci.* **2000**, 2000, (41), 1687-1695.
11. Green, R. J.; Hopkinson, I.; Jones, R. A. L., Unfolding and intermolecular association in globular proteins adsorbed at interfaces. *Langmuir* **1999**, 15, 5102-5110.
12. Ostuni, E.; Grzybowski, B. A.; Mirksich, M.; Roberts, C. S.; Whitesides, G. M., Adsorption of proteins to hydrophobic sites on mixed self-assembled monolayers. *Langmuir* **2003**, 19, 1861-1872.
13. Xia, N.; Hu, Y.; Grainger, D. W.; Castner, D. G., Functionalized Poly(ethylene glycol)-Grafted Polysiloxane Monolayers for Control of Protein Building. *Langmuir* **2002**, 18, 3255-3262.
14. Vertegel, A. A.; Siegel, R. W.; Dordick, J. S., Silica nanoparticle size influences the structure and enzymatic activity of adsorbed lysozyme. *Langmuir* **2004**, 20, 6800-6807.
15. Lundqvist, M.; Sethson, I.; Jonsson, B.-H., Protein adsorption onto silica nanoparticles: conformational changes depend on the particles' curvature and the protein stability. *Langmuir* **2004**, 20, 10639-10647.
16. Roach, P.; Farrar, D.; Perry, C. C., Surface tailoring for controlled protein adsorption: effect of topography at the nanometer scale and chemistry. *J. Am. Chem. Soc.* **2006**, 128, 3939-3945.
17. Teichroeb, J. H.; Forrest, J. A.; Ngai, V.; Jones, L. W., Anomalous thermal denaturing of proteins adsorbed to nanoparticles. *Eur Phys J E Soft Matter* **2006**, 21, (1), 19-24.

18. Dalmas, B.; Bannister, W. H., Prediction of protein secondary structure from circular dichroism spectra: an attempt to solve the problem of the best-fitting reference protein subsets. *Anal Biochem* **1995**, 225, (1), 39-48.
19. Shang, L.; Wang, Y.; Jiang, J.; Dong, S., pH-Dependent protein conformational changes in albumin:gold nanoparticle bioconjugates: A spectroscopic study. *Langmuir* **2007**, 23, 2714-2721.
20. Englebienne, P.; Van Hoonacker, A.; Verhas, M., Surface plasmon resonance: principles, methods and applications in biomedical sciences. *Spectroscopy* **2003**, 17, 255-273.
21. Khlebtsov, N. G.; Bogatyrev, V. A.; Dykman, L. A.; Melnikov, A. G., Spectral Extinction of Colloidal Gold and Its Biospecific Conjugates. *J. Colloid Interface Sci* **1996**, 180, 436-445.
22. Chah, S.; Hammond, M. R.; Zare, R. N., Gold nanoparticles as a colorimetric sensor for protein conformational changes. *Chem. & Biol.* **2005**, 12, 323-328.
23. Carter, D. C.; Ho, J. X., Structure of serum albumin. *Adv Protein Chem* **1994**, 45, 153-203.
24. Khan, M. Y., Direct evidence for the involvement of domain III in the N-F transition of bovine serum albumin. *Biochem J* **1986**, 236, (1), 307-10.
25. Harrington, W. F.; Johnson, P.; Ottewill, R. H., Bovine serum albumin and its behaviour in acid solution. *Biochem J* **1956**, 62, (4), 569-82.
26. Khan, M. Y.; Agarwal, S. K.; Hangloo, S., Urea-induced structural transformations in bovine serum albumin. *J Biochem* **1987**, 102, (2), 313-7.
27. Bohren, C. F.; Huffman, D. R., *Absorption and Scattering of Light by Small Particles*. New York ; Toronto Wiley, 1983, 1983; p Xiv, 530 P.
28. Matzler, C., Research Report No. 2002-08. *Institute of Applied Physics, University of Bern, Switzerland* **2002**.
29. Arwin, H., Optical Properties of Thin Layers of Bovine Serum Albumin, γ -Globulin, and Hemoglobin. *Appl. Spectrosc.* **1986**, 40, 313-318.
30. Su, T. J.; Lu, J. R.; Thomas, R. K.; Cui, Z. F.; Penfold, J., The Conformational Structure of Bovine Serum Albumin Layers Adsorbed at the Silica-Water Interface. *J. Phys. Chem. B* **1998**, 102, 8100-8108.
31. Freeman, N. J.; Peel, L. L.; Swann, M. J.; Cross, G. H.; Reeves, A.; Brand, S.; Lu, J. R., Real time, high resolution studies of protein adsorption and structure at the solid-liquid interface using dual polarization interferometry. *J. Phys.:Condens. Matter* **2004**, 16, 2493-2496.
32. Giacomelli, C. E.; Norde, W., The Adsorption-Desorption Cycle. Reversibility of the BSA-Silica System *Journal of Colloid and Interface Science* **2001**, 233, (2), 234-240.

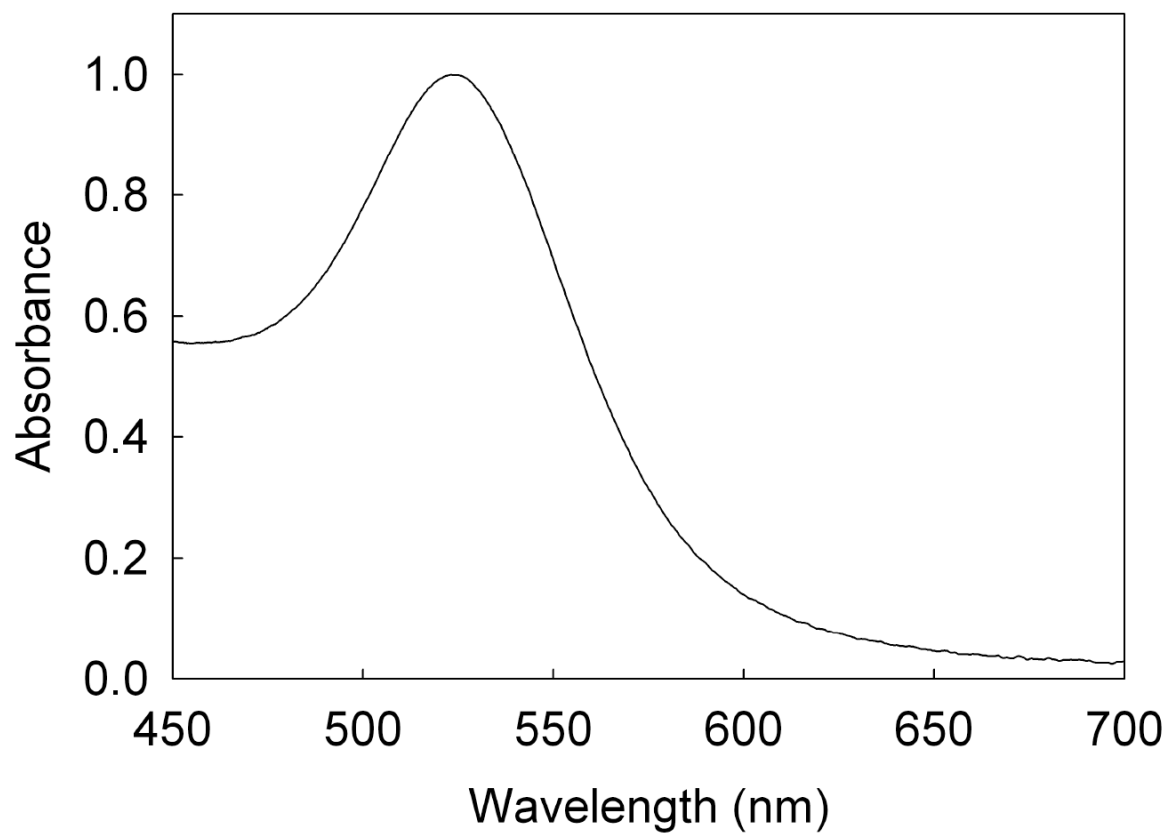


Figure 1

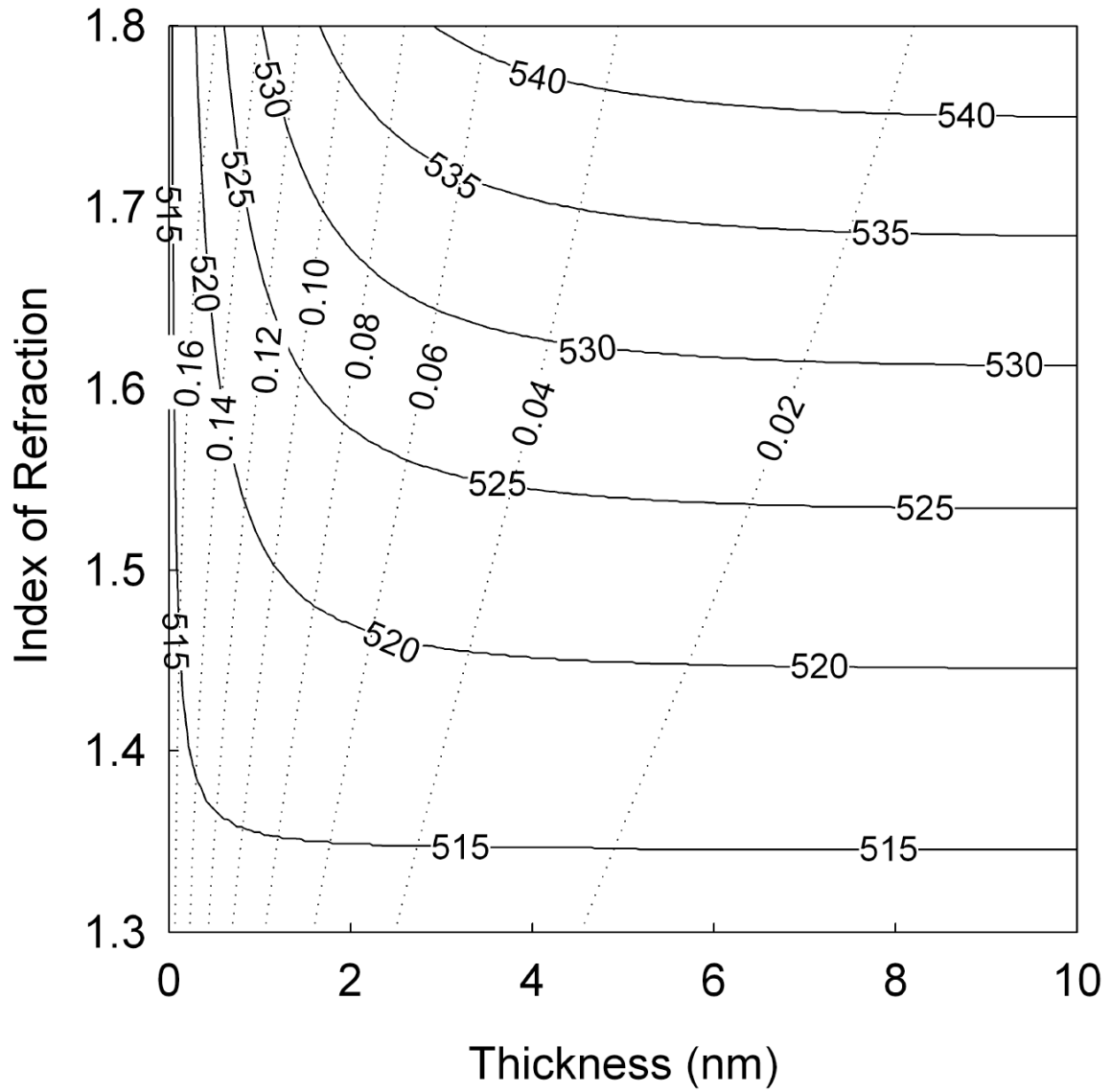


Figure 2

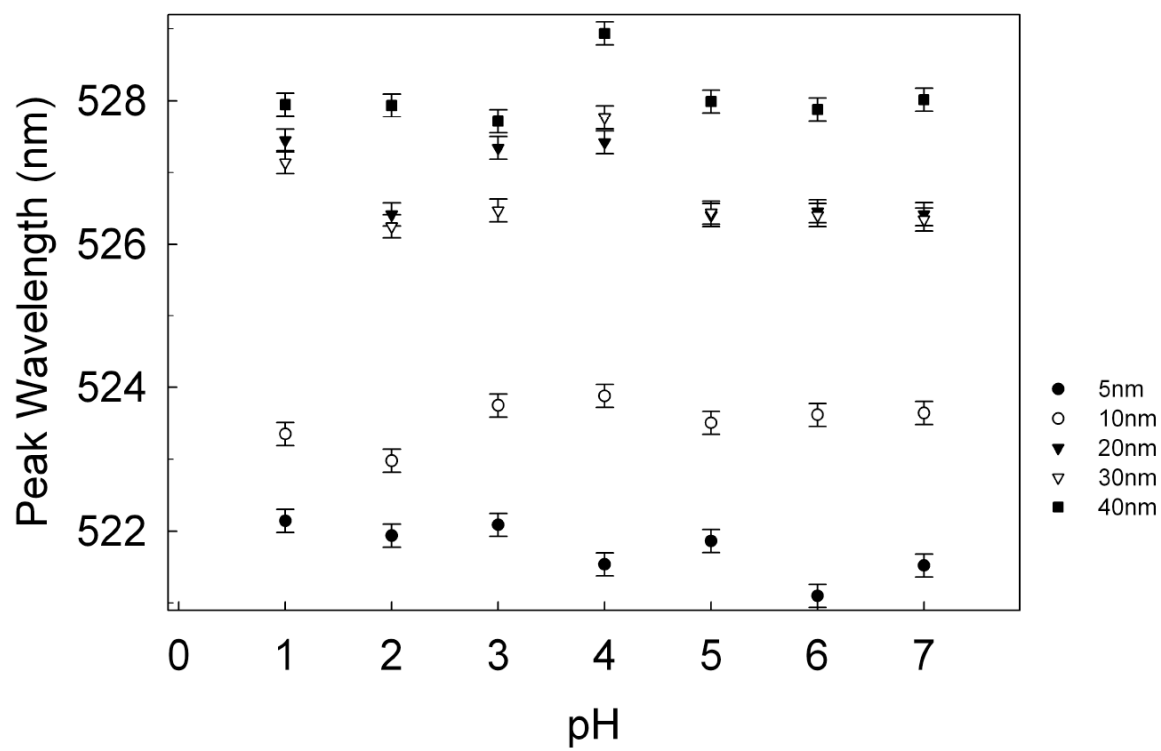


Figure 3

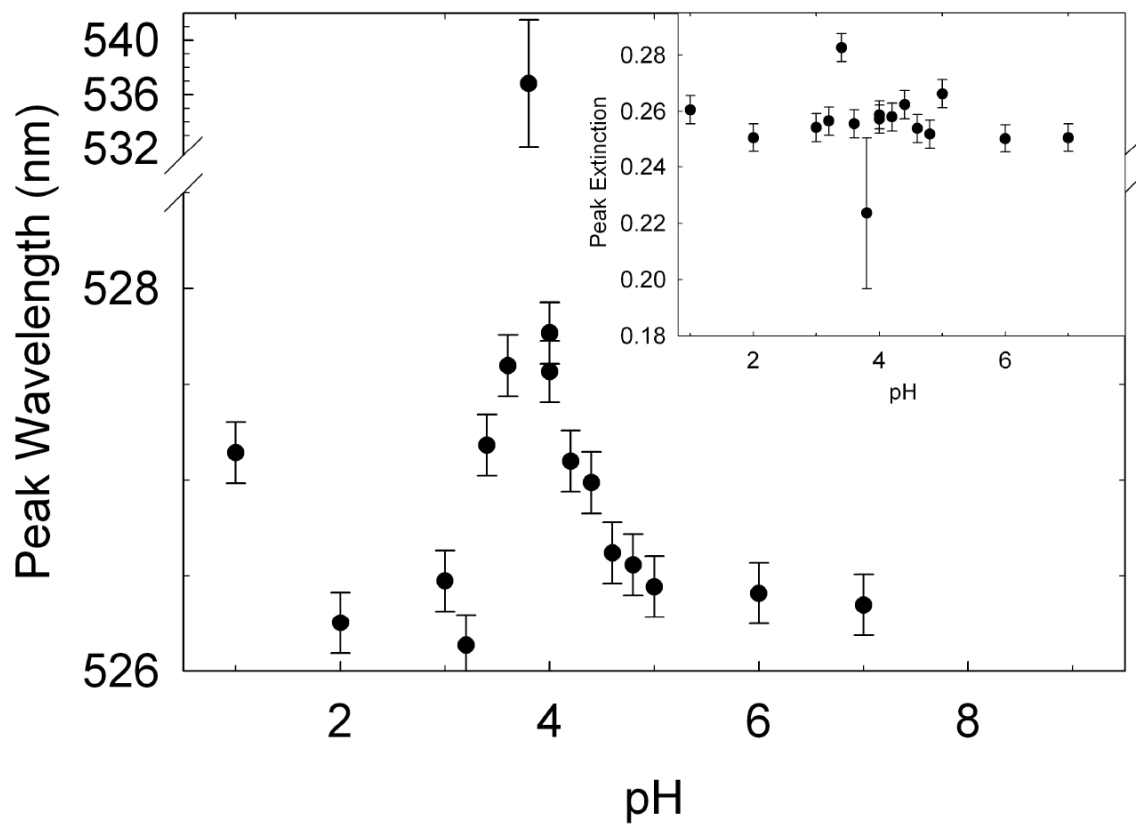


Figure 4

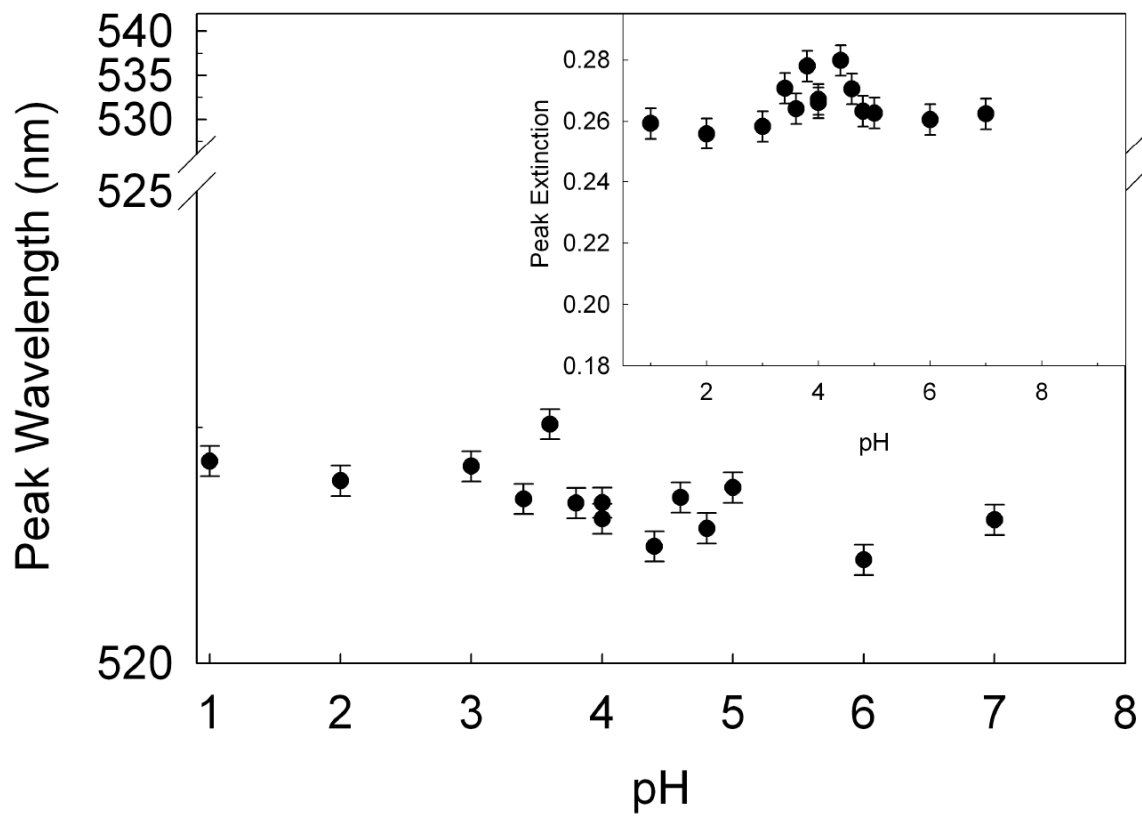


Figure 5

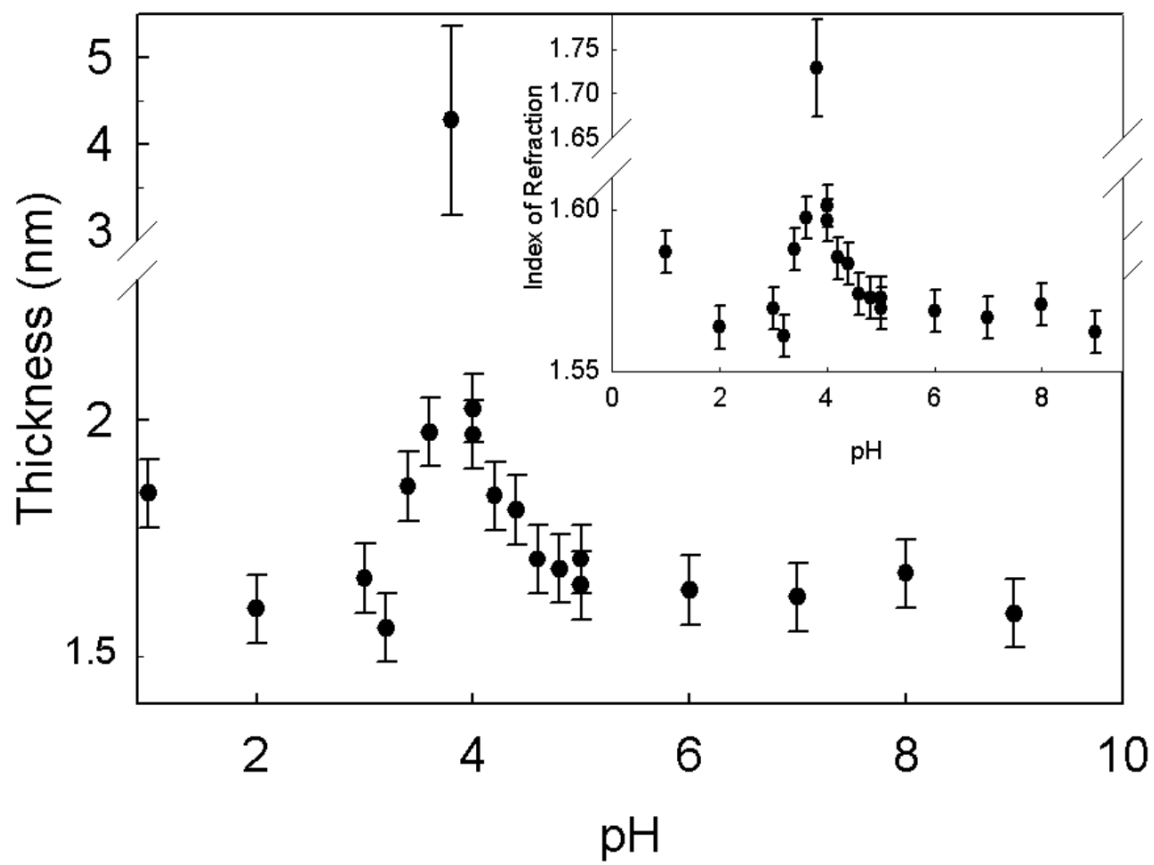


Figure 6

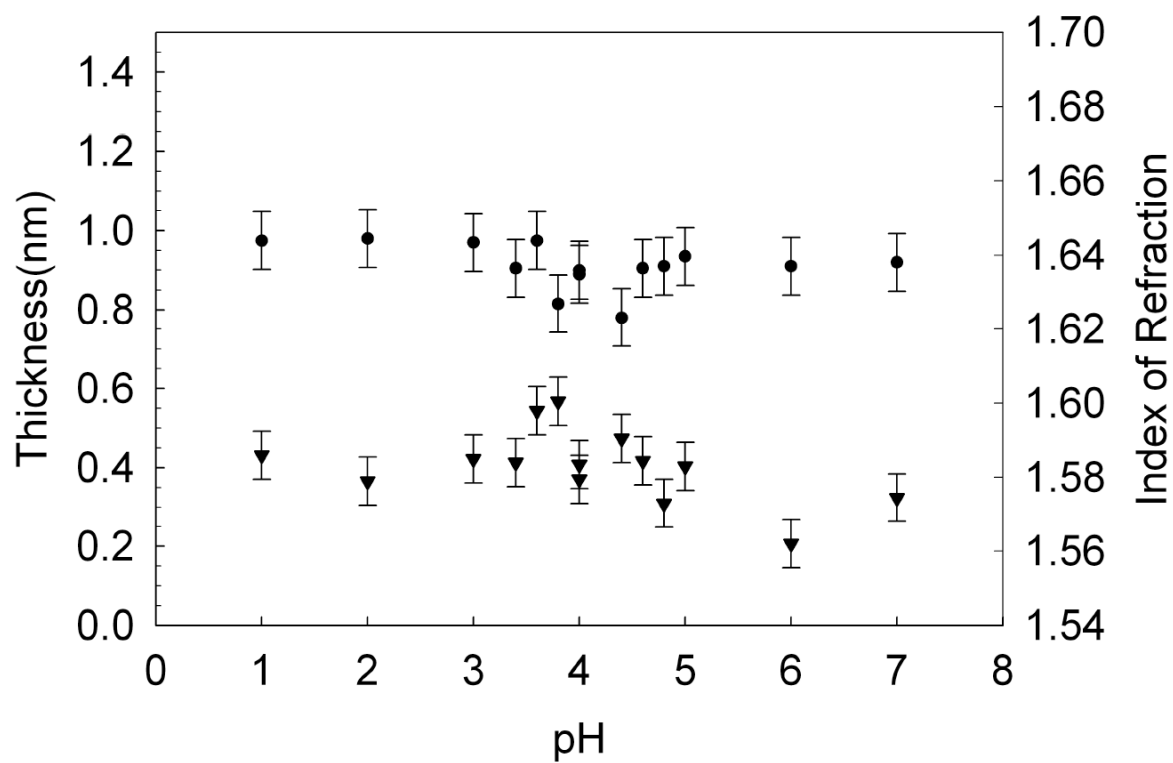
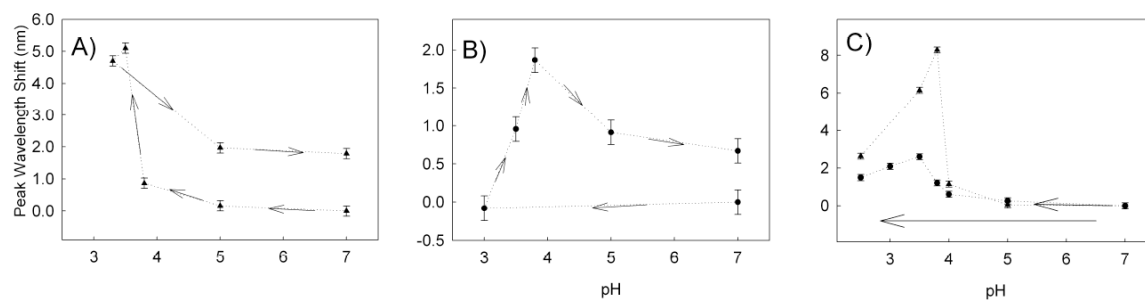


Figure 7

**Figure 8**

Paper IV

Quartz Crystal Microbalance Study of Protein Adsorption Kinetics on Poly(2-hydroxyethyl methacrylate)⁴

The previous three papers concentrated on curvature effects, and how they influence adsorbed protein. One feature of all the previous papers was that adsorption had already occurred. In the field of biomaterials, however, it is also of great concern as to the mechanisms by which proteins become adsorbed. This paper examines the kinetics of adsorption taking place on crosslinked polyHEMA surfaces. PolyHEMA is chosen as a model biomaterial for its wide application in various prostheses, in particular contact lenses. The quartz crystal microbalance (QCM) provides a unique opportunity to study protein adsorption. QCM has both extreme mass sensitivity (ng/cm^2) as well as a fast response time. Viscoelastic measurements provided by the QCM are shown to be informative with respect to dehydration of the swelled polyHEMA film. Lastly, because protein adsorption can depend strongly on protein-protein interactions in the bulk solution and on the surface, single protein adsorption results do not translate easily into multicomponent adsorption experiments. This is shown explicitly in measurements involving combinations of the studied proteins and comparison to their individual adsorption behaviour.

⁴Reprinted from Journal of Colloid and Interface Science, J.H. Teichroeb, J.A. Forrest, L.W. Jones, J. Chan and K. Dalton, Quartz crystal microbalance study of protein adsorption kinetics on poly(2-hydroxyethyl methacrylate), Pages 1-8, 2008, with permission from Elsevier.

License Number	1994271461393
License date	Jul 22, 2008
Licensed content publisher	Elsevier Limited
Licensed content publication	Journal of Colloid and Interface Science
Licensed content title	Quartz crystal microbalance study of protein adsorption kinetics on poly(2-hydroxyethyl methacrylate)
Licensed content author	J.H. Teichroeb, J.A. Forrest, L.W. Jones, J. Chan and K. Dalton
Licensed content date	4 June 2008
Volume number	n/a
Issue number	n/a
Pages	1-8
Type of Use	Thesis / Dissertation
Portion	Full article
Format	Print
You are the author of this Elsevier article	Yes
Are you translating?	No
Purchase order number	
Expected publication date	Sep 2008
Elsevier VAT number	GB 494 6272 12
Permissions price	0.00 USD
Value added tax 0.0%	0.00 USD
Total	0.00 USD



Contents lists available at ScienceDirect

Journal of Colloid and Interface Science

www.elsevier.com/locate/jcis



Quartz crystal microbalance study of protein adsorption kinetics on poly(2-hydroxyethyl methacrylate)

J.H. Teichroeb^{a,b,c}, J.A. Forrest^{a,b,*}, L.W. Jones^{a,c}, J. Chan^{a,b}, K. Dalton^c

^a Department of Physics and Astronomy, University of Waterloo, Waterloo, N2L 3G1, Canada

^b Guelph Waterloo Physics Institute, University of Waterloo, Waterloo, N2L 3G1, Canada

^c School of Optometry, University of Waterloo, Waterloo, N2L 3G1, Canada

ARTICLE INFO

Article history:

Received 14 February 2008

Accepted 28 May 2008

Keywords:

Protein adsorption

PolyHEMA

Hydrogel

Ocular biomaterials

ABSTRACT

The interaction of macromolecules with artificial biomaterials may lead to potentially serious complications upon implantation into a biological environment. The interaction of one of the most widely used biomaterials, polyHEMA, with lysozyme, bovine serum albumin (BSA), and lactoferrin was investigated using quartz crystal microbalance (QCM). The concentration dependence of adsorption was measured for the aforementioned proteins individually as well as for lysozyme-BSA, and lysozyme-lactoferrin combinations. An extension of Voinova's viscoelastic model to n layers was used to create thickness-time graphs for adsorption. For each of lactoferrin and lysozyme, two distinctly different timescales of adsorption could be differentiated. However, the mechanisms of adsorption appeared to differ between the two. Negative dissipation shifts were measured for low concentrations of lysozyme, trending to positive dissipation at higher concentrations. This suggested that lysozyme was adsorbed initially into the matrix, stiffening the hydrogel, and later onto the surface of polyHEMA. Additionally, trials with commercial no-rub cleaning solutions indicated little added effectiveness over buffer solutions. Mixtures of proteins showed behaviour which differed in some cases from the simple combination of single protein adsorption experiments.

Crown Copyright © 2008 Published by Elsevier Inc. All rights reserved.

1. Introduction

Artificial materials to repair damaged or absent biological tissue have been used for over two thousand years in dentistry. Recently, there has been an explosion in the use of, and search for, biomaterials in diverse medical fields [1]. Used in orthopedic and cardiovascular surgery, engineered body parts include joints, ligaments, stents, and artificial hearts. They are pervasive in dentistry, and are being used extensively in ophthalmology for contact lenses, drug delivery systems [2], artificial corneas, retinal tamponades, scleral buckles following retinal detachment and intraocular lenses. The ability to develop implantable biomaterials which are cheap, non-toxic, durable, and do not elicit an immune response is the ultimate goal of this field. However, the drive to find new, safer, and longer lasting options is inhibited by the deposition of unwanted macromolecules, in particular lipids, proteins and bacteria, leading to infections, wear, and clotting. For example, thrombus formation poses a life threatening condition for cardiovascular implants [3,4]. Catheter fouling [5] can lead to encrustation, and infection.

Poly(2-hydroxyethyl methacrylate) (polyHEMA) is a common synthetic, hydrogel material that is frequently used as a biomaterial. It has been used for breast augmentation surgery [6], synthetic skin [7], and has been incorporated into paranasal, chin, and malar facial implants [8]. First suggested by Wichterle [9] for use in contact lenses, polyHEMA has gained widespread use in ophthalmology. In addition to widespread use for contact lenses, it is also used for intraocular lenses following cataract surgery [10]. While new silicone hydrogel materials are becoming popular for contact lens use due to their high oxygen transmissibility [11], HEMA based lenses are still extensively used. Macromolecular buildup of components from the tear film onto contact lenses reduces visual clarity [12], increases inflammatory complications [13] and may increase the possibility of infection due to increased binding of bacteria and amoeba to the deposits [14,15]. PolyHEMA lenses can belong to any of groups I-IV depending on their water content and ionicity as determined by co-monomers such as vinylpyrrolidone, methacrylic acid, diacetone acrylamide and polyvinylpyrrolidone [16,17]. In terms of conventional contact lenses, group I lenses (low water content, non-ionic) such as pure polyHEMA typically adsorb the least amount of protein [16]. An important consideration is that for certain lenses (particularly group IV) proteins such as lysozyme, major basic protein, and lactoferrin have been known

* Corresponding author. Fax: +1 519 746 8115.

E-mail address: jforrest@sciborg.uwaterloo.ca (J.A. Forrest).

to penetrate into the matrix of the hydrogel [17–20]. While some macromolecular buildup can be removed, it is questionable as to the efficacy of commercial cleaning solutions for multi-use contact lenses. Studies indicate that only 1/3 to 1/2 of protein is removed [21], with lysozyme being the main contributor. In fact Senchyna et al. [22] find an increase in lysozyme adsorption to etafilcon (group IV) after PHMB (ReNu Multiplus) cleaning. Thus, it is productive to study pure polyHEMA as a model biomaterial, and investigate protein adsorption onto it. To do so, we have chosen to use the quartz crystal microbalance (QCM).

The conceptual basis for the QCM has been around for some time, and in 1959 Sauerbrey [23] showed that small rigid mass additions to the crystal would cause a decrease in frequency that is linearly proportional to mass. This was only generally applicable to operation in a gaseous environment. Nomura et al. extended this in 1980 to include operation in a fluid [24], where it was originally thought the crystal would experience too much energy dissipation to allow oscillation. Operation within fluid allowed studies of protein deposition to be performed. Fluid operation gives the opportunity to utilize QCM as an analysis tool to protein deposition onto biomaterials. In particular, the effects of adding charged moieties such as methacrylic acid (MAA), or hydrophobic moieties such as *n*-vinyl pyrrolidone (NVP) to polyHEMA have been examined with QCM [25]. Various works have developed continuum mechanics models for liquid operation of the QCM [26,27]. In particular, a model treating multilayer films as serial Voigt elements was developed by Voinova et al. [27]. A limiting factor for QCM use to study protein adsorption onto HEMA films is that the high water uptake of HEMA results in a material with a large dissipation for the shear waves used for QCM studies. This necessitates the constraint that HEMA films used should be at sub-micron thickness, in order to have the sensitivity to measure adsorbed protein. At the same time, there is likely a minimum thickness required for the film to exhibit bulk properties (for example the entanglement length). Part of the current work involves developing a way to make a cross linked poly(HEMA) film that is a few hundred nm in thickness and has long term stability, even when swelled with water. QCM allows real-time monitoring of label-free protein adsorption with high sensitivity (submonolayer). We are also able to monitor dissipation which can provide an indication as to how adsorption affects the hydrogel.

We have used the QCM to study adsorption of several protein components of the tear film onto polyHEMA films. Lysozyme, serum albumin, and lactoferrin are investigated at several concentrations, and the long-time behaviour of adsorption examined. Data were also collected using mixtures of two proteins, to look for competitive effects. Two commercially available contact lens disinfecting and rinsing solutions were measured for their efficacy at removing adsorbed protein. Additionally, we have produced polyHEMA films small enough to be operable on the QCM, while allowing a thickness that provides confidence the properties are the same as that shown by the bulk.

2. Materials and methods

Lysozyme from chicken egg white—95% protein (58100 units/mg) 3 times crystallized, dialyzed, and lyophilized was purchased from Sigma–Aldrich. Essentially fatty acid, and globulin free bovine serum albumin (BSA)—min. purity 99%, and lactoferrin from bovine colostrum—90% SDS–PAGE were purchased from Sigma–Aldrich, and used without further purification. Complete Moisture Plus No Rub Solution (Advanced Medical Optics, Santa Ana, California) and ReNu MultiPlus No Rub Solution (Bausch & Lomb, Rochester, NY, USA) were obtained commercially.

2.1. Preparation of submicron crosslinked polyHEMA films

The following procedure was adopted to produce stable, thin, uniform, crosslinked polyHEMA films from linear polyHEMA on QCM crystals. Linear PolyHEMA $M_v \sim 300,000$ was purchased from Sigma–Aldrich. PolyHEMA crystals were dissolved at 5% by weight into a solution with 5% water by weight in ethanol. The supernatant containing only dissolved polyHEMA was extracted and mixed with 7% ethylene glycol dimethacrylate (EGDMA) 98% purity from Sigma–Aldrich, inhibited with monomethyl ether of hydroquinone (MEHQ). 2-Hydroxy-2-methyl-propio-phenone a.k.a. Darocur 1173 (97% purity from Sigma–Aldrich) was dissolved 17% by weight into the PolyHEMA/EGDMA solution to act as an ultraviolet initiator [28]. A thin 2% by weight polystyrene film was spincoated at 3000 rpm onto the bare gold crystal to facilitate removal of the polyHEMA film, since once it was crosslinked it could no longer be dissolved.

Formation of crosslinked polyHEMA films required a nitrogen environment to prevent oxygen from scavenging the free radicals formed by the initiator and preventing initiation and crosslinking. To this end a chamber was built around the spincoater, which allowed dry nitrogen to be leaked in continuously, ensuring low oxygen levels. A Spectroline 11sc-1 shortwave UV (254 nm) pen light was fixed in the chamber approximately 1.5 inches above the surface of the spincoater. This light source was required by the ultraviolet initiator in order to break the 2-hydroxy-2-methyl-propio-phenone into free radicals and start the crosslinking reaction. While less common, it is not unusual to crosslink linear polymers as opposed to monomers. Free radicals are able to react with intra-chain points, forming crosslinking points even in the middle of the chain. This has been done for a number of systems such as: PEO [29,30], PVP [31], hydroxyethylcellulose [32], and between polymer mixtures such as PVP and PAA [33].

Several drops of polyHEMA/crosslinker/initiator solution were placed on the QCM crystal, which was on the spincoater. Nitrogen flow was started, and the chamber was then sealed. The crystal was spun at 5000 rpm for 30 s. Spinning was then stopped and the UV lamp was switched on for 2 min. The crystal was then removed from the chamber and soaked in ethanol with 5% water for half an hour to remove residual chemicals from the films. Crosslinking prevented the films from dissolving. Films were then washed and soaked in Milli-Q water for 20 min, before being dried at 80 °C for 30 min.

2.2. QCM measurement

Measurements were made with a Q-Sense D300 microbalance system (Q-Sense AB, Sweden). Solutions were gravity fed into the QCM. Because the QCM is sensitive to pressure changes the solutions were fed from a constant height, which minimized pressure effects. By first feeding solutions into a warming loop, which did not contact the crystal, any new solution coming into contact with the quartz crystal was within approximately 1 °C of the QCM-cell temperature of 34.5 °C. This temperature was chosen as it was close to physiological eye temperature of 33–36 °C [34]. Phosphate buffer solution (PBS) was made to a normal eye pH of 7.45 [35] according to the recipe: 0.110 M NaCl, 0.0190 M Na₂HPO₄, 0.00460 M NaH₂PO₄. Uncertainties were determined from the measurement of several samples.

Crystals were reused several times, and were first soaked in ethanol with 5% water to swell the polyHEMA, before dragging lens tissue across the surface. This tended to physically remove most of the polyHEMA, leaving behind the polystyrene, which was then removed by dropping toluene onto the crystal while it was spinning in the spincoater. Crystals were then ozone etched, and rinsed. An optical microscope was used to examine and rule out evidence of

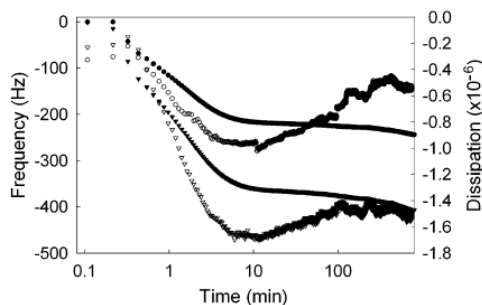


Fig. 1. Example of semi-raw QCM data for 1 mg/ml lysozyme adsorption. Both the third (15 MHz—circles) and fifth (25 MHz—triangles) overtones are shown for frequency (solid symbols) and dissipation (hollow symbols).

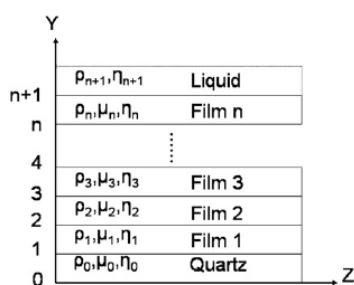


Fig. 2. Diagram of n -layer Voinova model. Top layer ($(n+1)$ th layer) is a purely viscous liquid solution. The n films are assumed not to undergo interfacial slip.

film residue before a crystal was reused. The frequency of the uncoated crystal was also compared to previous values to ensure that cleaning was thorough.

A Watson Marlow 205U/CA peristaltic pump was used to clean the QCM. Typically, a 2% solution of Hellmanex II (Hellma) in Milli-Q water at 35 °C was pumped through the QCM for a period of 4 h, before pumping through a rinsing solution of pure Milli-Q water for an hour twice. Scrupulous cleaning was needed to guarantee all protein was removed from components of the QCM to ensure repeatability. Cleaning was deemed complete when upon reintroducing buffer no protein or cleaning solution could be measured adsorbing to the clean crystal.

3. Extended viscoelastic model for n layered system

In order to interpret the results, raw frequency and dissipation data (e.g., in Fig. 1) were converted to the approximate thickness of the protein film. To do this we have extended the viscoelastic model of Voinova et al. [27] to n layers. The model assumes uniform homogeneous layers stacked on top of each other, with some film density (ρ), viscosity (η) and elastic shear modulus (μ) (Fig. 2). In addition, the quartz crystal parameters, density (ρ_0), elastic shear modulus (μ_0) and thickness (t_0), as well as the viscosity and density of solution (η_{n+1} , ρ_{n+1}) must be known. Here we assume that the top film is covered in a purely viscous liquid, and that the quartz is non-dissipative. Films are treated as serial Voigt elements, and the quartz as a harmonic oscillator.

Using the same notation as Voinova et al. the bulk wave equation is

$$\mu^* \frac{\partial^2 u_x(y, t)}{\partial y^2} = -\rho \omega^2 u_x(y, t),$$

where μ^* is the complex shear modulus, u_x is the displacement in the x -direction, and ω is the frequency.

The solution to this is

$$u_x(y, t) = (c_1 e^{-\xi y} + c_2 e^{\xi y}) e^{i\omega t}$$

with $\xi = \alpha + ik$ and

$$\alpha = \frac{1}{\delta} \sqrt{\frac{\sqrt{1+\chi^2} - \chi}{1+\chi^2}}, \quad k = \frac{1}{\delta} \sqrt{\frac{\sqrt{1+\chi^2} + \chi}{1+\chi^2}},$$

$$\chi = \frac{\mu}{\eta \omega}, \quad \delta = \sqrt{\frac{2\eta}{\rho \omega}}.$$

where α is the decay constant, κ is the wave vector. χ and δ are the viscoelastic ratio and viscous penetration depth, respectively. And we must satisfy no slip boundary conditions, such that there is a continuity of displacement u_x (and velocity v_x) and shear stress σ_{xy} at the interfaces of each layer.

$\sigma_{xy} = \mu \partial u_x(y, t) / \partial y + \eta \partial v_x(y, t) / \partial y$ is the shear stress/strain relation for a Voigt element in which σ_{xy} is the stress defined by the force in the x -direction per unit area defined by a normal vector in the direction y (i.e., x - z surface). We have chosen this direction arbitrarily.

Thus we are subject to the conditions:

$$u_x^0(h_1, t) = u_x^1(h_1, t),$$

$$u_x^1(h_2, t) = u_x^2(h_2, t),$$

...

$$u_x^i(h_{i+1}, t) = u_x^{i+1}(h_{i+1}, t),$$

...

$$u_x^n(h_{n+1}, t) = u_x^{n+1}(h_{n+1}, t)$$

where $u_x^i(h_j, t)$ represents displacement in the x -direction of the i th film at the j th boundary (distance h_j) between the $(j-1)$ th and j th films. The quartz crystal is the 0th film, while the liquid is the $(n+1)$ th film.

$$\sigma_{xy}^0(h_1, t) = \sigma_{xy}^1(h_1, t),$$

$$\sigma_{xy}^1(h_2, t) = \sigma_{xy}^2(h_2, t),$$

...

$$\sigma_{xy}^i(h_{i+1}, t) = \sigma_{xy}^{i+1}(h_{i+1}, t),$$

...

$$\sigma_{xy}^n(h_{n+1}, t) = \sigma_{xy}^{n+1}(h_{n+1}, t).$$

At the liquid/free surface we have the boundary condition:

$$\sigma_{xy}^{n+1}(h_{n+2}, t) = \sigma_{xy}^a(h_{n+2}, t),$$

where the superscript a denotes air. Since air cannot support stress, and we take the liquid to be purely viscous we have: $\eta_{n+1} \partial v_x^{n+1} / \partial y = 0$.

Substituting these into the general equation leads to the solution for β , which can be substituted into the frequency and dissipation relations to give the full solution:

$$\Delta f = \text{Im} \left(\frac{\beta}{2\pi \rho_0 h_0} \right), \quad \Delta D = -\text{Re} \left(\frac{\beta}{\pi f \rho_0 h_0} \right),$$

where

$$\beta = \kappa_1 \xi_1 \frac{1 - A_1 e^{2\xi_1 h_1}}{1 + A_1 e^{2\xi_1 h_1}},$$

$$A_j = \frac{\kappa_j \xi_j (1 + A_{j+1} e^{2\xi_{j+1} \Delta h_j}) - \kappa_{j+1} \xi_{j+1} (1 - A_{j+1} e^{2\xi_{j+1} \Delta h_j})}{\kappa_j \xi_j (1 + A_{j+1} e^{2\xi_{j+1} \Delta h_j}) + \kappa_{j+1} \xi_{j+1} (1 - A_{j+1} e^{2\xi_{j+1} \Delta h_j})},$$

$$j = 1, \dots, n$$

4

J.H. Teichroeb et al. / Journal of Colloid and Interface Science ••• (••••) ••••••••

and

$$A_j = 1, \quad j = n + 1,$$

where

$$\Delta h_i = h_{i+1} - h_i,$$

$$\xi_{1,2,\dots,n+1} = \alpha_{1,2,\dots,n+1} + i k_{1,2,\dots,n+1},$$

$$\kappa_{1,2,\dots,n+1} = \eta_{1,2,\dots,n+1} - \frac{i \mu_{1,2,\dots,n+1}}{\omega}, \quad \omega = 2\pi f,$$

where f is the frequency in question (1st, 3rd, 5th overtones).

The A_j 's are most easily determined using a recursive algorithm and a Matlab program was developed to solve the general system. In our specific case we have a three film system. Polystyrene forms the first layer, polyHEMA the second, and the adsorbing protein the third layer. Values for the viscosity and shear modulus of polystyrene were taken to be 0, and 1.208×10^9 Pa respectively, with a density of 1050 kg/m^3 [36]. The thickness was determined by holding μ and η constant in the Matlab program and varying the thickness until the experimental frequency and dissipation were reproduced. This led to a typical thickness of 95 nm for the polystyrene films that is consistent with ellipsometric measurements of similar films. To determine μ , η , and h for the polyHEMA film, μ , η , and h were varied until both the third and fifth overtone frequency and dissipation values were matched in a similar method to [37] using an automatic searching Matlab program. This matched the shift of taking polyHEMA from air to water, and extracted the desired parameters. This calculation was slightly complicated by the fact that polyHEMA swells in water. Assuming all change in polyHEMA was due to water uptake it was possible to define a simple relationship between thickness and density, thus reducing the number of variables required. The shear modulus was determined to be $4 \times 10^6 \pm 3 \times 10^6$ Pa, the viscosity 0.5 ± 0.1 Pa s, and the thickness 388 nm (swelled), with a density of 1076 kg/m^3 . The hydrated density of polyHEMA was determined by assuming a dry density of approximately 1150 kg/m^3 and shear modulus of 2.0×10^9 Pa which gave a semi-dry thickness of approximately 197 nm initially. However, using this assumption the water content of the hydrogel would be around 85% to give a thickness of 388 nm swelled. While this is not impossible, it is unlikely that the water content is over 60%. Garrett et al. [38] find pure polyHEMA has EWC of 40%, but up to 86% water for charged carboxymethylated polyHEMA.

A film whose surface is rough would experience higher dissipative forces from the water than would a smooth film operating in pure a pure shear mode. This would raise the effective water content of the film. Roughness effects were not included in the model. Since we simulate a smooth film that has the same frequency/dissipation response to its environment as the rough film, a higher roughness may account for the apparently high EWC. The aforementioned values, including thickness, for both films 1 and 2 were used for all simulations. Water was taken to have a shear modulus of zero, viscosity of 0.0072 Pa s (at 34 °C) and a density of 1000 kg/m^3 [39]. All protein was assumed to have a density of 1330 kg/m^3 [34]. Under shear, a certain amount of water moves with protein, increasing the effective weight [37,40]. While it is recognized that there will be differences between differing proteins [41], it is not possible to predict how they affect density, or the amount of dragged water without a priori knowledge. As such, comparisons between different proteins, which may have differences in bound water, are less exact than comparisons looking at the same protein. Bound water will increase the effective mass measured, and is expected to have more of an effect on thinner layers (monolayers) being more prominently a surface effect. When converting frequency and dissipation to thickness for protein, only

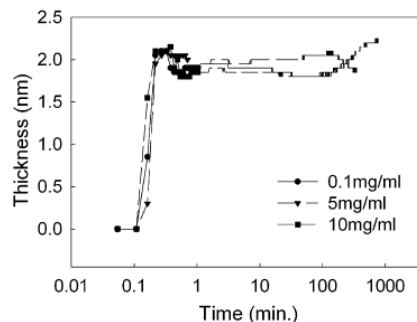


Fig. 3. Thickness vs time graph of adsorption of varying concentrations of BSA. Error in measurement $\approx \pm 0.15$ nm. Lines represent actual data, and are added to avoid ambiguity with symbol overlap.

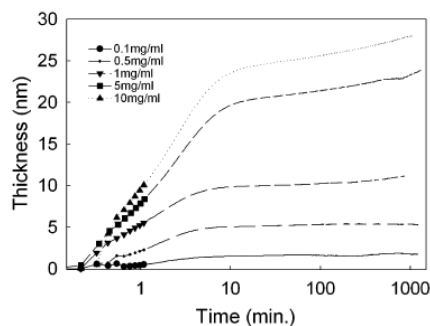


Fig. 4. Thickness vs time graph of adsorption of varying concentrations of lysozyme. Error $\approx \pm 0.4$ nm. Lines represent actual data, and are added to avoid ambiguity with symbol overlap.

frequency was considered. This was due to the fact that dissipation decreased upon initial adsorption, a phenomenon likely due to displaced water [25,42]. This does not amount to a Sauerbrey treatment, however, as a full viscoelastic model is used, which for the viscoelastic hydrogel film will affect results.

4. Results

Fig. 3 shows the derived layer thickness of bovine serum albumin adsorbing onto the polyHEMA substrate. The initial adsorption is fast, and reaches a "quasi-steady-state" value in less than 1 min. The protein layer thickness at this plateau is around 1.9 ± 0.15 nm or ($253 \pm 20 \text{ ng/cm}^2$). It is noteworthy that this plateau value remains concentration independent from 0.1 to 10 mg/ml.

In stark contrast to the behaviour of BSA, lysozyme (Fig. 4) initially adsorbs in a concentration dependent manner. There is no plateau as in the previous case; instead there is a second adsorption stage at a much slower rate. 1 mg/ml corresponds to a plateau value of $1330 \pm 50 \text{ ng/cm}^2$. Several attempts to describe this adsorption with a physical model were not successful, and an empirical double exponential fit $h(t) = a_1(1 - e^{-t/\tau_1}) + a_2(1 - e^{-t/\tau_2})$ was used instead. This generally fit quite well with a correlation coefficient (R value) of 0.99. Values for fitting parameters are given in Table 1. Fig. 5 displays rinsing data as a proportion of lysozyme removed for various adsorbing concentrations, including all rinsing stages. This involved rinsing twice with buffer, followed by rinsing with no rub solution, and finally again with buffer to remove any no rub solution. The amount of protein removed in general increases with the number of rinsings. Overall, an average of over 91% of protein was removed for the en-

Table 1
Fitting parameters for lysozyme adsorption

Concentration (mg/ml)	c_1 (nm)	τ_1 (min)	c_2 (nm)	τ_2 (min)
0.1	1.4963	2.1432	0.3074	377.6150
0.5	4.9876	1.6920	0.3535	42.3729
1.0	9.9851	1.5413	1.7775	866.3259
5.0	20.8726	2.7632	3.0331	587.5095
10.0	24.6720	2.5813	3.4410	386.5930

Note. Lysozyme adsorption fitting parameters based on the equation $h(t) = c_1(1 - e^{-t/\tau_1}) + c_2(1 - e^{-t/\tau_2})$. τ_1 and τ_2 means of 2.1 and 452.1 min, respectively.

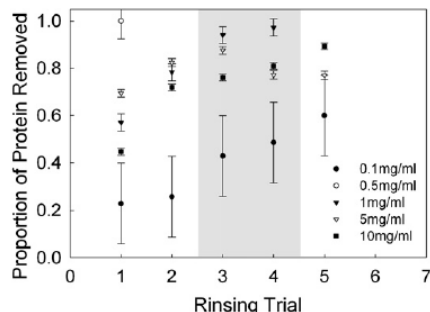


Fig. 5. Proportion of total protein removed during rinsing for various lysozyme concentrations after adsorption. Protocol included rinsing twice with buffer, followed by rinsing with no rub solution, and finally again with buffer to remove any no rub solution. Rinsing trials three and four in which no rub solution was used are in the shaded region.

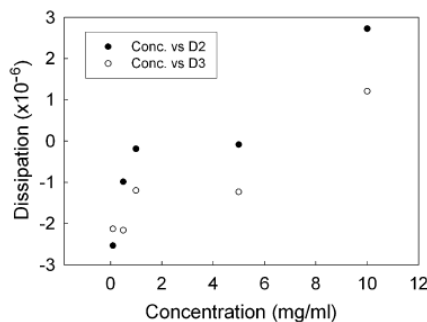


Fig. 6. Dissipation change due to lysozyme adsorption (at around 400 min). Values are presented for both the third (D2: 15 MHz) and fifth (D3: 25 MHz) overtones.

tire procedure (no rub and buffer rinsing) for concentration 0.5–10 mg/ml. Rinsing of the adsorbed protein for the concentration of 0.1 mg/ml removed less than other concentrations. The dissipation change as a function of concentration for lysozyme adsorption is shown in Fig. 6. Curiously, for concentrations up to 1 mg/ml a decrease in dissipation is measured. As we approach higher concentrations the decrease becomes less, and eventually positive.

Lactoferrin, unlike lysozyme, cannot be fit well to a double exponential. There appear to be two different timescales (Fig. 7). However, the first event occurs so rapidly (around 0.1 min) that only a few data points can be measured, and it makes up a smaller relative amount of the overall adsorption. This initial adsorption appears to be only moderately concentration dependent. The second main mechanism accounts for an increasing amount of the total adsorption with concentration. It is faster than for lysozyme, but the thickness is less. For 1 mg/ml, adsorption gives 558 ± 50 ng/cm² for short times to 744 ± 50 ng/cm² for longer times.

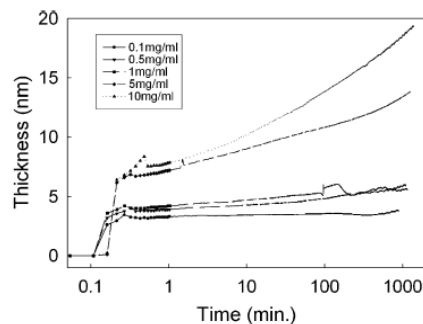


Fig. 7. Thickness vs time graph of adsorption of varying concentrations of lactoferrin. Error $\approx \pm 0.4$ nm. Lines represent actual data, and are added to avoid ambiguity with symbol overlap.

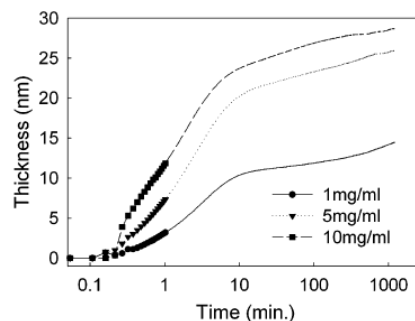


Fig. 8. Thickness vs time graph of adsorption of varying concentrations of lysozyme and BSA mixed 1:1 by mass-volume. Error $\approx \pm 0.4$ nm. Lines represent actual data, and are added to avoid ambiguity with symbol overlap.

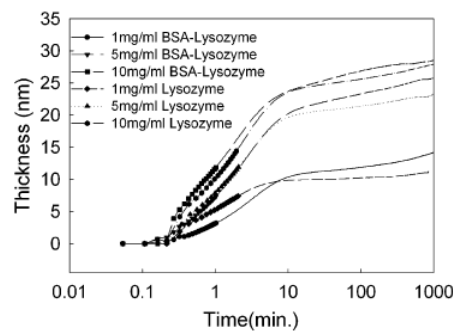


Fig. 9. Thickness vs time graph of adsorption of varying concentrations of lysozyme and BSA mixed 1:1 by mass-volume. Pure lysozyme adsorption plotted for comparison purposes. Error $\approx \pm 0.4$ nm. Lines represent actual data, and are added to avoid ambiguity with symbol overlap.

Fig. 8 shows the adsorption behaviour of a combination of BSA and lysozyme for concentrations of 1, 5, and 10 mg/ml, while Fig. 9 displays these against the equivalent adsorption for lysozyme alone. When lactoferrin and lysozyme are mixed in equal concentration (Fig. 10), the adsorption is greater than either single adsorption (Fig. 10). In fact, for the 1 mg/ml concentration the adsorption is greater than the sum of the two.

5. Discussion

Given the lack of dependence on concentration, it seems likely that the value of 1.9 ± 0.15 nm or (253 ± 20 ng/cm²) represents

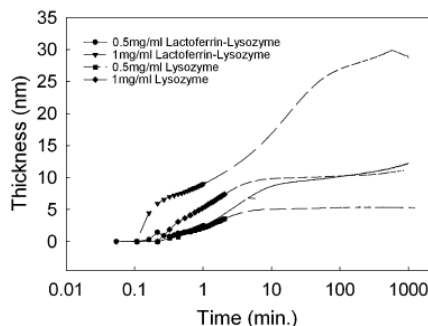


Fig. 10. Thickness vs time graph of adsorption of varying concentrations of lactoferrin and lysozyme mixed 1:1 by mass-volume. Error $\approx \pm 0.4$ nm. Lines represent actual data, and are added to avoid ambiguity with symbol overlap.

a protein monolayer, and that BSA (Fig. 3) does not form any significant multilayer for this system. This is consistent with studies done on conventional lenses, in which BSA is seen to adsorb minimally, with at best very weak concentration dependence [43]. The value of 1.9 nm also indicates that BSA, which is typically quoted as being a heart shaped molecule having rough dimensions of a solid equilateral triangle with 8.0 nm sides and a 3.0 nm average depth [44], has a tertiary structure upon adsorption that is different than that in bulk solution. This value is in good agreement with that of a BSA thickness of 2.3 nm seen on platinum substrates using ellipsometry [45], and with values of 274 nm/cm² of human serum albumin (HSA) on non-crosslinked polyHEMA for a concentration of 0.2 mg/ml using QCM [25]. ATR-FTIR measurements indicate around [46] 170 ng/cm² for HSA on polyHEMA with 38% water content, which is significantly lower than our value of coverage. They also find that the HSA undergoes significant denaturing at long times, especially on crosslinked spincoated polyHEMA, as compared to lathe cut polyHEMA. Denaturing typically renders a protein irreversibly adsorbed, which was evident to us and others [25] for albumin. Denaturation is normally not as favourable on hydrophilic substrates [47]. However, for proteins with low native stability such as BSA, conformational changes can act as a major driving force for adsorption [48] even under electrostatically, and hydrophilically unfavourable conditions such as on polyHEMA. The fact that adsorption seems mostly concentration independent, in our case, suggests that upon binding BSA spreads much faster than the supply rate of protein [49]. This is corroborated by the adsorption of HSA onto teflon (polyHEMA) [50] which is immediately irreversible, and conformationally changed, as compared to etafilcon A, and vifilcon A where conformational changes are much slower.

Lysozyme has dimensions of about $4.5 \times 3 \times 3$ nm [51]. This would mean monolayer coverage occurs somewhere between concentrations of 0.1 and 0.5 mg/ml (Fig. 4). Slightly lower values have been reported using QCM [25] of around 1072 ng/cm² total lysozyme for 1.9 mg/ml as compared to our value of 1330 ± 50 ng/cm² for 1 mg/ml. The increased adsorption we see may relate to the fact that our films have been crosslinked, or possibly due to our higher water content hydrogel. A concentration dependent plateau is not surprising [43], and a two stage process of adsorption onto hydrophilic substrates has been seen previously [52], with the initial stage being attributed to formation of a monolayer, and the second stage to multilayer formation. Fitting parameters from Table 1 indicate that upon normalizing them there would be two distinct mechanisms having different time constants. We do not ascribe any meaning to the differences in individual τ values since the time constants show only scatter about a means of 2.1 and 452.1 min. Interestingly, these values are of the same order

as those found on hydrophobic polytris(trimethylsilyloxy)silylstyrene of 6 min and greater than 240 min [53]. This demonstrates the strong dependence upon surface chemistry, in which an overall hydrophilic substrate such as polyHEMA can display similar time constants to a hydrophobic substrate. Coefficients show that both the total amount of protein, as well as the rate at which the protein is deposited, is increasing with concentration. This increase is not linear, but appears to slow down significantly towards higher concentrations. Thus, the coefficients must contain the concentration dependence, and they appear to plateau at higher concentrations. Despite representing multiple layers, the coefficients a_1 fit a Langmuir equation $\Gamma = \Gamma_{\max} Kc / (1 + Kc)$, with parameters $K = 0.46$, $\Gamma_{\max} = 29.98$ nm, R value of 0.999, and a_2 with parameters $K = 0.52$, 4.16 nm, R value of 0.976. This equation is typically used to describe a system where there are a finite number of "sites" for protein, or in our case a maximum thickness that can be reached even if our concentration becomes very large, and that concentration is the driving force for adsorption. In our case, the first mechanism attributed to the first time constant τ_1 appears to contribute to more than one layer. Other studies typically find two differing kinetics, with the first corresponding to formation of the monolayer, in which lysozyme binds to free surface, and may attract further bulk protein through complimentary dipole alignment [52,54]. It has been suggested that for adsorption to take place an event similar to nucleation often occurs, in which a nucleus of several lysozyme molecules adsorbs first, making further adsorption more favourable [49,55]. Cooperativity is also frequently seen, especially at monolayer levels [49], especially on hydrophobic substrates. However, given that we are using a hydrophilic substrate, with relatively high concentrations, and the first couple data points may be affected by the protein solution being injected, we see no evidence for either of these effects. The second constant τ_2 corresponds to a slower increase in effective mass, the size of which suggests that this is simply continued adsorption of multilayers as Subbaraman et al. [56] see increases in adsorption up to at least 28 days. However, the continued adsorption may still depend on a slow denaturing, or rearrangement of already adsorbed lysozyme to allow more to adsorb. Ball et al. suggest that multilayer growth may proceed by the same dipole mechanism as monolayer, but appear different, as further proteins must search longer for complementary spots, and are unable to satisfy their bonding requirements as rigorously [52]. Much of the multilayer absorption may be through dimers and trimers, which are formed during the longer period while the protein searches for a complementary adsorption spot [52]. Slowing adsorption could be explained in our case if, for instance, monomers were capable of binding even in the multilayer regime in our case due to attractive electrostatics between the weakly negatively charged polyHEMA, and the very positively charged lysozyme. The buildup of positively charged lysozyme, making further adsorption less and less favourable, as lysozyme does not typically adsorb to repulsive hydrophilic substrates [57], may eventually require dimer and trimer formation to adsorb. Finding charge equilibrium between bulk and adsorbed lysozyme would account for our concentration dependence. In terms of reversibility of adsorption, the lysozyme adsorbed during the fast process is often seen to be irreversibly bound, and conformationally altered [52,53]. By examining our rinsing data it is likely that this is the case.

While 91% of protein was removed on average during rinsing (Fig. 5), it is to be expected that for 0.1 mg/ml less was removed, since for 0.1 mg/ml it appears in Fig. 4 that a sub-monolayer is adsorbed. It is not surprising that this protein, which is in direct contact with the surface, is more tightly bound, and that it is harder to remove an equivalent percentage of it as compared to the 10 mg/ml concentration which has many loosely bound multilayers [52]. This does not need to be caused by spreading on the

surface, but could be due to surface aggregation [49], as lysozyme is known to sometimes form a gel-like structure upon adsorption [58]. Van der Veen et al. for example find that only 20% maximum of protein can be removed, and that the amount depends on the adsorption time up to 20 min (much longer than their observed spreading time of 100 s). Closer inspection of Fig. 5 shows that initial rinsing with buffer alone removed on average 80% of the protein (excluding 0.1 mg/ml). The final rinsing with buffer again removed as much as the no-rub. This suggests that equally successful results could be obtained using only buffer, but repeating the rinsing several more times. Another QCM study of adsorption onto polyHEMA [25] find 622 ng/cm² of reversible lysozyme and around 450 ng/cm² of irreversible lysozyme, which amounts to around 60% reversible. Crosslinking our films may be a factor in our higher reversibility. Also, hydrophilic surfaces are typically associated with more reversible protein [59], albeit our higher apparent water content does not necessarily represent greater surface hydrophilicity. Reversible systems also exhibit equilibrium conditions, such as the concentration dependence in our case.

We interpret lysozymes dissipation change in Fig. 6 similar to other studies [42] in that a decrease in D corresponds to the hydrogel layer becoming stiffer, probably due to dehydration. Dehydration of a surface can be a significant driving force for protein adsorption [48]. Hydrogel dehydration due to lysozyme has been previously demonstrated using dual polarization interferometry (DPI) [42], however, the film was only 3 nm thick and may not have been representative of bulk polyHEMA, especially when considering lysozyme is a 3 × 3 × 4 nm ellipsoid. Interestingly, while those films were polyHEMA-MAA, and are not crosslinked like our films, our dissipation value of 1.2 × 10⁻⁶ for the fifth overtone (D3) matches well with theirs [42] of 1.3 × 10⁻⁶. It is also noteworthy that this effect was not seen on pure uncrosslinked polyHEMA [25], suggesting that crosslinking may be responsible for dissipation decreases happening with our pure polyHEMA. The fact that the dissipation shift is the same, despite our film being an order of magnitude larger (388 vs 40 nm [42]) implies that if this is in fact due to penetration of lysozyme into the matrix, that it does not penetrate further than 40 nm and is mostly a surface phenomenon. D eventually becomes positive for high enough concentrations. This leads to the conclusion that while initial lysozyme may slightly penetrate the gel, later lysozyme must deposit on the surface, eventually leading to increased dissipation. Normally on pure polyHEMA, matrix penetration is not seen [28,60], so it is most probable that dehydration is brought about purely by surface adsorption.

Lysozyme's adsorption (Fig. 4) is contrasted with that of lactoferrin (Fig. 7). It is likely that lactoferrin is rapidly forming somewhere close to a monolayer during the initial rapid stage (around 0.1 min), and that further adsorption occurs similarly to lysozyme, as molecules undergo some sort of further alteration, allowing a multilayer to form. This alteration occurs at a much slower rate than adsorption. Similar studies on polyHEMA [25] for 1.8 mg/ml lactoferrin see around 1100 ng/cm², as compared to our 558 ± 50 ng/cm² for short times to 744 ± 50 ng/cm² for longer times with 1 mg/ml. Our concentration difference is likely enough to account for this difference. The second mechanism being faster.

When a solution with equal concentrations of BSA and lysozyme is used, the resulting thickness/time graph appears very similar to lysozyme (Fig. 8). The final amounts show a slight increase above lysozyme alone. For the 1 and 5 mg/ml the final slope is greater than that of lysozyme, suggesting there may be some weak interaction with BSA, making the second mechanism of adsorption more favourable (Fig. 9). Fig. 10 exhibits clear interaction phenomenon between lactoferrin and lysozyme, with the sum of the single protein adsorption experiments not able to account for the combined effect. Fig. 11, on the other hand, indicates that a combi-

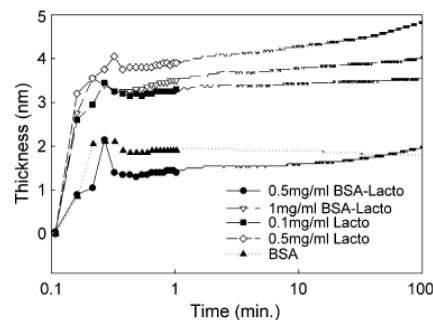


Fig. 11. Thickness vs time graph of adsorption of varying concentrations of lactoferrin and BSA mixed 1:1 by mass-volume. Error $\approx \pm 0.4$ nm. Lines represent actual data, and are added to avoid ambiguity with symbol overlap.

nation of lactoferrin and BSA do not adsorb as much as lactoferrin alone. In fact for the 0.5 mg/ml case, the amount of adsorption is equivalent to BSA alone. This does not imply, however, that the layer is only BSA as the layer may still be mixed. It may be the case that lysozyme which is strongly positively charged at pH 7 does not feel the effects of BSA as strongly, while lactoferrin, having a lesser positive charge is more affected by BSA. If our surface is slightly charged it is conceivable that the BSA, being slightly negative at pH 7 associates with lactoferrin, forming a less efficient packing layer. Lysozyme, being much more positively charged may still present a highly charged solute in the presence of BSA. These results highlight the problem with studying individual proteins. Frequently their behaviour is significantly different when competing, or cooperating with other macromolecules [61,62]. It also underscores the complexity of study multi-component solutions, in that it is not normally possible to measure individual contributions, nor is it possible to deconvolve them from a combined measurement.

6. Conclusion

An investigation of the adsorption behaviour of lysozyme, bovine serum albumin and lactoferrin to polyHEMA was performed using a quartz crystal microbalance. The adsorption data was converted to protein film thickness using a viscoelastic model. Adsorption showed several timescales depending on the protein. While bovine serum albumin adsorbed in a concentration independent way with a single timescale, lysozyme and lactoferrin exhibited concentration dependent adsorption with multiple timescales. This indicated two distinct mechanisms of adsorption. In the case of lactoferrin, however, the first mode of adsorption appeared to contribute mainly to a monolayer, while in the case of lysozyme the first mode contributed to multiple layers. Concentration dependence of the previously seen [42] negative dissipation shift for lysozyme adsorption showed a positive trend towards higher concentrations. This suggested that lysozyme was adsorbed initially into the matrix, and later onto the surface of polyHEMA. Rinsing trials showed commercial no-rub cleaning solutions had little advantage over rinsing with simple buffer solution. Adsorption of mixtures of proteins indicated that, while informative, single protein type adsorption experiments may behave very differently from real biomaterial environments containing multiple protein and lipid components.

References

- [1] B.D. Ratner, A.S. Hoffman, F.J. Schoen, J.E. Lemons (Eds.), *Biomaterials Science*, Academic Press, San Diego, 1996.


- [2] A. Yamanaka, Y. Yokoyama, H. Iwamoto, J. Artif. Organs 9 (2006) 67–70.
- [3] M.B. Gorbet, M.V. Sefton, Biomaterials 25 (2004) 5681–5703.
- [4] B.D.J. Ratner, Biomed. Mater. Res. 27 (1993) 283–287.
- [5] J.M. Schierholz, N. Yucel, A.F.E. Rump, J. Beuth, G. Pulverer, J. Antimicrob. Agents 19 (2002) 511–516.
- [6] K. Kliment, M. Stol, K. Fahoun, B. Stockar, J. Biomed. Mater. Res. 2 (1968) 237.
- [7] P. Nathan, B.G. Macmillan, I.A. Holder, Appl. Microbiol. 28 (1974) 465.
- [8] B.L. Eppley, A.M. Sadove, H. Holmstrom, K. Kahnberg, Aesth. Plast. Surg. 19 (1995) 445–450.
- [9] O. Wichterle, D. Lim, Nature 185 (1960) 117–118.
- [10] L. Allarakhia, R.L. Lindstrom, Int. Ophthalmol. 12 (1988) 185–191.
- [11] P.C. Nicolson, J. Vogt, Biomaterials 22 (2001) 3273–3283.
- [12] K.W. Gellatly, N.A. Brennan, N. Efron, Am. J. Optom. Physiol. Opt. 65 (1988) 937–941.
- [13] S.A. Fowler, M.R. Allansmith, Arch. Ophthalmol. 98 (1980) 95–99.
- [14] R.L. Taylor, M.D. Willcox, T.J. Williams, J. Verran, Optom. Vis. Sci. 75 (1998) 23–29.
- [15] P.A. Simmons, A. Tomlinson, R. Connor, J. Hay, D.V. Seal, Optom. Vis. Sci. 73 (1996) 362–368.
- [16] L. Minarik, J. Rapp, CLAO J. 15–16 (1989–1990) 185–188.
- [17] R. Sariri, B. Tighe, Iran. Polym. J. 5 (1996) 259–266.
- [18] L. Jones, et al., Optom. Vis. Sci. 77 (2000) 503–510.
- [19] M. Prager, R. Quintana, J. Biomed. Mater. Res. 36 (1997) 119–124.
- [20] D. Meadows, J. Paugh, CLAO J. 20 (1994) 237–241.
- [21] J. Jung, J. Rapp, CLAO J. 19 (1993) 47–49.
- [22] M. Senchyyna, et al., Curr. Eye Res. 28 (2004) 25–35.
- [23] G. Sauerbrey, Z. Phys. 155 (1959) 206–222.
- [24] T. Nomura, O. Hattori, Anal. Chim. Acta 115 (1980) 323–326.
- [25] M.S. Lord, M.H. Stenzel, A. Simmons, B.K. Milthorpe, Biomaterials 27 (2006) 567–575.
- [26] M. Rodahl, B. Kasemo, Sens. Actuators B 2 (1995) 743–746.
- [27] M.V. Voinova, M. Rodahl, M. Jonson, B. Kasemo, Phys. Scripta 59 (1999) 391–396.
- [28] Q. Garrett, B. Laycock, R.W. Garrett, Invest. Ophthalmol. Vis. Sci. 41 (2000) 1687–1695.
- [29] M. Doytcheva, D. Dotcheva, R. Stamenova, R. Orahovats, C. Tsvetanov, J. Leder, J. Appl. Polym. Sci. 64 (1997) 2299–2307.
- [30] S.H. Emami, R. Salovey, J. Appl. Polym. Sci. 88 (2003) 1451–1455.
- [31] L.C. Lopergolo, A.B. Lugao, L.H. Catalani, Polymer 44 (2003) 6217.
- [32] P. Petrov, E. Petrova, B. Tchorbanov, C.B. Tsvetanov, Polymer 48 (2007) 4943–4949.
- [33] S. Kadlubowski, A. Henke, P. Ulanski, J.M. Rosiak, L. Bromberg, T.A. Hatton, Polymer 48 (2007) 4974–4981.
- [34] R. Mapstone, Br. J. Ophthalmol. 52 (1968) 729–741.
- [35] L.G. Carney, R.M. Hill, Arch. Ophthalmol. 94 (1976) 821–824.
- [36] J. Brandrup, E.H. Immergut, E.A. Grulke (Eds.), Polymer Handbook, fourth ed., Wiley, New York, 1999.
- [37] F. Hook, B. Kasemo, T. Nylander, C. Fant, K. Sott, H. Elwing, Anal. Chem. 73 (2001) 5796–5804.
- [38] Q. Garrett, R.C. Chatelier, H.J. Griesser, B.K. Milthorpe, Biomaterials 19 (1998) 2175–2186.
- [39] L. Korson, W. Drost-Hansen, F.J. Miller, J. Phys. Chem. 73 (1969) 34–39.
- [40] F. Hook, J. Voros, M. Rodahl, R. Kurrat, P. Boni, J.J. Ramsden, M. Textor, N.D. Spencer, P. Tengvall, J. Gold, B. Kasemo, Colloids Surf. B Biointerfaces 24 (2002) 155–170.
- [41] J. Voros, Biophys. J. 87 (2004) 553–561.
- [42] M.S. Lord, M.H. Stenzel, A. Simmons, B.K. Milthorpe, Biomaterials 27 (2006) 1341–1345.
- [43] O. Moradi, H. Modarress, M. Noroozi, J. Colloid Interface Sci. 271 (2004) 16–19.
- [44] X.M. He, D.C. Carter, Nature 358 (1992) 209–215.
- [45] H. Arwin, Appl. Spectrosc. 40 (1986) 313–318.
- [46] E.J. Castillo, J.L. Koenig, J.M. Anderson, J. Lo, Biomaterials 5 (1984) 319–325.
- [47] W. Norde, C.E. Giacomelli, J. Biotechnol. 79 (2000) 259–268.
- [48] C.A. Haynes, W. Norde, Colloids Surf. B Biointerfaces 2 (1994) 517–566.
- [49] M. van der Veen, M.C. Stuart, W. Norde, Colloids Surf. B 54 (2007) 136–142.
- [50] Q. Garrett, H.J. Griesser, B.K. Milthorpe, R.W. Garrett, Biomaterials 20 (1999) 1345–1356.
- [51] C.C.F. Blake, D.F. Koenig, G.A. Mair, A.C.T. North, D.C. Phillips, V.R. Sarma, Nature 206 (1965) 757–761.
- [52] V. Ball, J.J. Ramsden, Colloids Surf. B Biointerfaces 17 (2000) 81–94.
- [53] Y. Yokoyama, R. Ishiguro, H. Maeda, M. Mukaiyama, K. Hiramoto, J. Colloid Interface Sci. 268 (2003) 23–32.
- [54] V. Ball, J.J. Ramsden, J. Phys. Chem. B 101 (1997) 5465.
- [55] V. Ball, A. Lustig, J.J. Ramsden, Phys. Chem. Chem. Phys. 1 (1999) 3667–3671.
- [56] L.N. Subbaraman, M.A. Glasier, M. Senchyyna, H. Sheardown, L. Jones, Curr. Eye Res. 31 (2006) 787–796.
- [57] M. van der Veen, W. Norde, M.C. Stuart, Colloids Surf. B Biointerfaces 35 (2004) 33–40.
- [58] V. Ball, R.A.L. Jones, Langmuir 11 (1995) 3542.
- [59] D.L. Elbert, J.A. Hubbell, Annu. Rev. Mater. Sci. 26 (1996) 265–394.
- [60] Q. Garrett, R.W. Garrett, B.K. Milthorpe, Invest. Ophthalmol. Vis. Sci. 40 (1999) 897–903.
- [61] A. Botempo, J. Rapp, Curr. Eye Res. 16 (1997) 776–781.
- [62] A. Botempo, J. Rapp, Curr. Eye Res. 16 (1997) 1258–1262.

Paper V

Imaging Protein Deposits on Contact Lens Materials⁵

This final paper looks at protein adsorption in a real world system – the contact lens. In particular, silicone hydrogels, which offer higher oxygen transmissibility, are examined. Controlling the kinetics, and amount of adsorption may be desirable, however, the state of protein is perhaps more important in terms of pathogenicity. Generally, amounts of protein adsorption are measured on contact lenses. A large amount of protein does not necessarily represent a problem if that protein maintains its native state and function, and remains exchangeable with the bulk. We have opted to look at the morphology of the protein deposits in this paper. This is something that is rarely examined, but may offer clues as to why these deposits form. Additionally, measurements of roughness, surface composition, and bare lens morphology were made, all of which may correlate with protein adsorption.

⁴Reprinted from Optometry and Vision Science, J.H. Teichroeb, J.A. Forrest, V. Ngai, J.W. Martin, L. Jones, J. Medley and K. Dalton, Imaging Protein Deposits on Contact Lens Materials.

Date: Thu, 14 Aug 2008 12:06:55 -0400 [14/08/2008 12:06:55 EDT]
From: "Zadnik, Kurt" <ovs@optometry.osu.edu> 
To: jhteichr@sciborg.uwaterloo.ca
Subject: RE: Copyright request
Headers: [Show All Headers](#)

Hi Jonathan,

Permission to reproduce the article is granted. Please use the following credit line with the article:

Initials, last name of author(s)
 Title of article
 Optometry and Vision Science (or American Journal of Optometry and
 Physiological Optics) Volume #, Issue #, Page(s) #
 (c)The American Academy of Optometry 2008

Please note that it is currently "in press" and scheduled for Optometry and
 Vision Science Vol. 85 Number 12 , December 2008.

Let me know if you have any other questions.

Best regards,
 Kurt

 Optometry and Vision Science
 Kurt A. Zadnik, Managing Editor
 The Ohio State University, College of Optometry
 338 West 10th Avenue
 Columbus, OH 43210
 Tel: (614) 292-4942; Fax: (614) 292-4949;
 E-mail: ovs@osu.edu
<http://ovs.edmgr.com>

ORIGINAL ARTICLE

Imaging Protein Deposits on Contact Lens Materials

Jonathan H. Teichroeb*, James A. Forrest†, Valentina Ngai‡, James W. Martin, Lyndon Jones§, and John Medley†

ABSTRACT

Purpose. The majority of studies investigating protein deposition on contact lens materials require that the deposit of interest be removed, potentially resulting in erroneous results if some proteins are not removed adequately. The purpose of this study was to investigate the use of *in situ* imaging methods to examine protein deposition on conventional poly(2-hydroxyethyl methacrylate) (polyHEMA)-based and silicone hydrogel contact lens materials.

Methods. Six silicone hydrogel and five polyHEMA-based hydrogel contact lens materials were examined by Atomic Force Microscopy (AFM) and/or Scanning Electron Microscopy (SEM) techniques, after being deposited with proteins in an *in vitro* model. AFM studies examined lenses deposited solely with lysozyme at approximate physiological concentrations and SEM studies were conducted on lenses exposed to a dilute mixture of lysozyme and albumin-conjugated gold spheres.

Results. AFM studies demonstrated that the lens materials had markedly differing surface topographies. SEM results showed that galyfilcon A and balafilcon A lenses deposited both lysozyme and albumin in relatively large aggregates, as compared with lotrafilcon A and B, in which the proteins were deposited in a more evenly spread, monolayer formation. Polymacon lenses deposited more protein than any of the silicone hydrogel materials and much of the protein was aggregated together. AFM data indicated that balafilcon A, lotrafilcon A and polymacon deposited lysozyme in a similar manner, with very little lysozyme being deposited in discrete areas. Galyfilcon A behaved very differently, with the lysozyme exhibiting both aggregates as well as string-like formations over the lens surface.

Conclusions. Imaging techniques that allow proteins to be examined *in situ* show much promise for determining the extent and physical characterization of protein on contact lens materials. These techniques indicate that the pattern of deposition of proteins onto silicone hydrogel contact lens materials differs between materials, depending upon their bulk and surface composition.

(Optom Vis Sci 2008;85:1-...)

Key Words: contact lens, silicone hydrogel, protein deposition, atomic force microscopy, scanning electron microscopy

The interaction of proteins with surfaces has important implications for any situation in which artificial materials interact with body fluids, and has received considerable attention.¹⁻⁶ A contact lens represents a fairly unique biomaterial, in that the device is external to the body and can therefore be removed with relative ease. This places different constraints on the material,

as well as allowing for avenues of study not available with permanently implanted biomaterials. The most commercially successful contact lens materials to-date are those based on poly(2-hydroxyethyl methacrylate) or, as they are more commonly termed, polyHEMA. Although these “conventional” hydrogel materials are easily adapted to, due to their low mechanical modulus and acceptable degree of in-eye wettability, a significant problem with contact lenses manufactured from these materials relates to their low levels of oxygen transmission, which results in significant hypoxic problems, particularly during overnight wear.⁷⁻¹¹ The newest generation contact lens materials are based upon those which incorporate various siloxane moieties¹² and have significantly increased levels of oxygen permeability compared with those based on poly-

*BSc

†PhD

‡MAsc

§PhD, FAAO

Department of Physics and Astronomy (JHT, JAF, JWM), Guelph Waterloo Physics Institute (JHT, JAF), School of Optometry (JHT, LJ), and Department of Mechanical Engineering (VN, JM), University of Waterloo, Waterloo, Ontario, Canada.

2 Imaging Protein on Contact Lenses—Teichroeb et al.

HEMA.^{13–15} As the oxygen transport is largely conducted through the polymer-phase of the material, the resulting materials have relatively low water contents, but high levels of oxygen permeability, as compared with conventional hydrogels, in which the oxygen permeability is directly proportional to the water content.^{12,15–18} In clinical use, these materials result in significantly reduced hypoxic complications, with no visible signs of oxygen deprivation following even closed-eye wear, in either short or long-term studies.^{19–27}

Previously developed silicone-based flexible materials (silicone elastomers) failed clinically due to their hydrophobic surfaces producing poor in-eye wetting and rapid deposition with components from the tears,²⁸ in addition to unacceptable lens movement and binding to the cornea.²⁹ To overcome these problems with modern silicone hydrogel materials, manufacturers have developed a variety of strategies to effectively “hide” the siloxane from the tear film components, preventing these hydrophobic domains from producing poorly wettable surfaces.^{15,30–36} The surface of lotrafilcon A and B lenses (CIBA Vision; Duluth, GA) are permanently modified in a gas plasma reactive chamber using a mixture of trimethylsilane oxygen and methane to create a permanent, ultrathin (25 nm), high refractive index, continuous hydrophilic surface.^{31,37,38} Balafilcon A lenses (Bausch & Lomb, Rochester, NY) are surface treated in a reactive gas plasma chamber, which transforms the siloxane components on the surface of the lenses into hydrophilic silicate compounds.^{15,30,39,40} Glassy, discontinuous silicate “islands” result,^{33,40} and the hydrophilicity of the transformed surface areas “bridges” over the underlying balafilcon A material. The galyfilcon A material (Johnson & Johnson, Jacksonville, FL) was the first non-surface-treated silicone hydrogel to become commercially available, closely followed by senofilcon A (Johnson & Johnson, Jacksonville, FL). Both of these materials incorporate a long chain, high molecular weight internal wetting agent based on poly(vinylpyrrolidone) (PVP), which is designed to provide a hydrophilic layer at the surface of the material that “shields” the silicone at the material interface, thereby reducing the degree of hydrophobicity seen at the surface of siloxane-based hydrogels.^{41,42} The galyfilcon A wetting agent is termed HydraClear and that used for the senofilcon A-based lens is “HydraClear Plus,” implying that more PVP is probably incorporated. The latest silicone hydrogel material, comfilcon A (CooperVision, Pleasanton, CA) has very little published information to-date, but appears to use proprietary chemistry that results in a highly wettable surface without any specific surface modification being required.⁴³ Despite these innovative approaches to produce silicone-based hydrogel materials, it appears that the incorporation of siloxane moieties into the bulk polymer provides a surface that expresses a relatively high proportion of silicon at the material surface.^{44,45} Thus, the surfaces are more hydrophobic than that typically seen with conventional hydrogels, as evidenced by the presence of relatively high advancing contact angles compared with conventional polyHEMA-based materials.^{46–50}

Although dozens of studies over the past 20 years or so have been conducted investigating the deposition of proteins onto conventional polyHEMA-based hydrogels,^{51–57} to-date, relatively few studies have been published on the amount of protein deposited on silicone hydrogel materials.^{41,50,58–64} The in-eye deposition of proteins from the tear film is an extremely important factor to consider with silicone hydrogels, particularly those that are worn

overnight for up to 30 nights without removal. The majority of published studies investigating protein deposition on silicone hydrogels thus far suffer from the fact that they have commonly used techniques in which the proteins must be removed from the contact lens materials, typically using strong surfactants, before the elute can be quantified. This may be problematic, as no technique is capable of eluting all the proteins of interest.^{62,65}

The purpose of this study was to use a variety of *in situ* imaging techniques to investigate the protein present on various contact lens materials without the need to remove it, and to identify the surface patterning or morphology of the protein adsorbed onto both silicone hydrogel and various polyHEMA-based hydrogel lens materials. The methods used were based on atomic force microscopy (AFM) and a modified form of colloidal gold immunocytochemistry, using scanning electron microscopy (SEM).

MATERIALS AND METHODS

Bare Lens Characterization

Atomic Force Microscopy

The characteristic properties of the contact lens materials studied are listed in Tables 1 and 2.

Six silicone hydrogel materials (senofilcon A, comfilcon A, lotrafilcon A, lotrafilcon B, galyfilcon A, balafilcon A) and two conventional polyHEMA-based materials (polymacon, omafilcon A) were imaged using an Explorer AFM (Veeco Instruments, Santa Barbara, CA) in tapping mode with MikroMasch NSC15/AIBS tips ($r < 10$ nm) from SPMTIPS.COM, at typical image sizes of 5 μ m and 50 μ m. Typically, contact lenses are imaged by AFM by first cutting and then flattening the lenses, leading to large stresses, and possible surface damage. Imaging of contact lenses by AFM was undertaken on spherical glass “holders” which mimic the curvature of the cornea (Fig. 1). These glass spheres had a radius of curvature of approximately 8 mm. Before imaging, the lenses were mounted on the sphere, and rinsed well with Millipore deionized water using a glass pipette to remove surfactants and salts from the packaging solutions, which would impede imaging. Lenses were then dried in ambient conditions for approximately 15 min, at which time the image was seen to cease changing, indicating surface moisture was in a steady state. After imaging, in ambient conditions, images were automatically leveled using algorithms provided with the AFM tools software.

X-Ray Photoelectron Spectroscopy

X-ray photoelectron spectroscopy (XPS) was performed on four silicone hydrogels (galyfilcon A, balafilcon A, lotrafilcon A, lotrafilcon B), and four conventional hydrogels (alphafilcon A, omafilcon A, ocufilcon D, etafilcon A). Lenses were prepared for XPS as previously described.⁴⁴ The lenses were prepared by soaking for 20 min in 0.9% saline, before drying them at a temperature of 30°C in a dry nitrogen atmosphere. Once dry, the lenses were broken into pieces small enough to place on double sided conductive carbon tape on XPS sample holders. An ultra-high vacuum Imaging XPS Microprobe system (Thermo VG Scientific ESCALab 250, Waltham, MA) equipped with a hemispherical analyzer (of 150 mm mean radius) and monochromatic AlK α (1486.60 eV) X-ray source XPS machine was used with resolution of 0.5 eV FWHM at 20 eV pass energy, and a spot size of approx-

T1-2,
AQ: 4

TABLE 1.
Properties of the silicone hydrogel lens materials evaluated in this study

Proprietary name	Night & Day	O ₂ OPTIX	PureVision	Acuvue OASYS	Acuvue advance	Biofinity
United States	Lotrafilcon A	Lotrafilcon B	Balafilcon A	Senofilcon A	Galyfilcon A	Comfilcon A
Adopted Name (USAN)						
Manufacturer	CIBA Vision	CIBA Vision	Bausch & Lomb	Vistakon	Vistakon	CooperVision
Center thickness (@ -3.00 D)	0.08	0.08	0.09	0.07	0.07	0.08
mm						
Water content (%)	24	33	36	38	47	48
Oxygen permeability ($\times 10^{-11}$)	140	110	91	103	60	128
Oxygen transmissibility ($\times 10^{-9}$)	175	138	101	147	86	160
Surface treatment	25 nm plasma coating with high refractive index	25 nm plasma coating with high refractive index	Plasma oxidation process	No surface treatment. Internal wetting agent (PVP)	No surface treatment. Internal wetting agent (PVP)	None
FDA group	I	I	III	I	I	I
Principal monomers	DMA + TRIS + siloxane macromer	DMA + TRIS + siloxane macromer	NVP + TPVC + NVA + PBVC	mPDMS + DMA + HEMA + siloxane macromer + PVP	mPDMS + DMA + EGDMA + HEMA + siloxane macromer + PVP	FM0411M; HOB; IBM; M3U; NVP; TAIC; VMA

DMA, N,N-dimethylacrylamide; EGDMA, ethyleneglycol dimethacrylate; FM0411M, α -methacryloyloxyethyl iminocarbonyloxypropyl-poly(dimethylsiloxy)-butyldimethylsilane; HOB, 2-hydroxybutyl methacrylate; IBM, isobornyl methacrylate; M3U, α - ω -bis(methacryloyloxyethyl iminocarbonyloxypropyl)-poly(dimethylsiloxy)-poly(trifluoropropylmethacrylate)-poly(ω -methoxy-poly(ethyleneglycol)propylmethacrylate); MA, methacrylic acid; mPDMS, monofunctional polydimethylsiloxane; NVA, N-vinyl amino acid; NVP, N-vinyl pyrrolidone; PBVC, poly[(dimethylsiloxy) di [silybutanol] bis(vinyl carbamate)]; PC, phosphorylcholine; TAIC, 1,3,5-triallyl-1,3,5-triazine-2,4,6-(1H,3H,5H)-trione; TEGDMA, tetraethyleneglycol dimethacrylate; TPVC, tris-(trimethylsiloxy) propylvinyl carbamate; TRIS, trimethylsiloxy silane; VMA, N-Vinyl-N-methylacetamide.

h15/zov-opx/zov-opx/zov01208/zov5373-08a | angn | S=4 | 10/22/08 | 0:54 | Art: OPX200758 | Input-go

4 Imaging Protein on Contact Lenses—Teichroeb et al.

TABLE 2.

Properties of the polyHEMA-based lens materials evaluated in this study

Proprietary name	SofLens 38	Biomedics 55	Acuvue 2	Proclear compatibles	SofLens 66
United States adopted name	Polymacon	Ocufilcon D	Etafilcon A	Omafilcon A	Alphafilcon A
Manufacturer	Bausch & Lomb	CooperVision	Vistakon	CooperVision	Bausch & Lomb
Center thickness (@ -3.00 D) mm	0.035	0.07	0.08	0.07	0.10
Water content (%)	38	55	58	62	66
Oxygen permeability ($\times 10^{-11}$)	8	15	17	20	23
Oxygen transmissibility ($\times 10^{-9}$)	23	21	21	28	23
Surface treatment	None	None	None	None	None
FDA group	I	IV	IV	II	II
Principal monomers	HEMA	HEMA + MA	HEMA + MA	HEMA + PC	HEMA + NVP

MA, methacrylic acid; NVP, N-vinyl pyrrolidone; PC, phosphorylcholine.

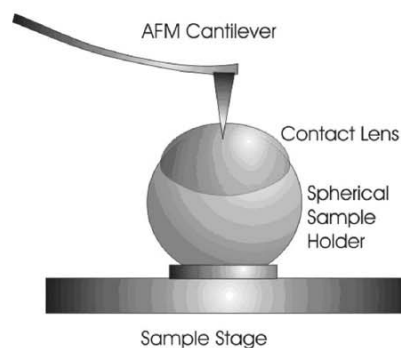


FIGURE 1.

Schematic of contact lens sample holder used in AFM studies. The curvature of the glass sphere allows the lens to be unperturbed while imaging.

imately 0.5 mm. CasaXPS 22,102 VAMAS processing software was used to analyze the data.

Characterizing Protein Coated Lens

Atomic Force Microscopy

The procedure for studying protein adsorbed to lenses using AFM was similar to that described for imaging unworn lenses from the blister package. Three times crystallized, dialyzed, and lyophilized Hen Egg Lysozyme (95% protein), and fatty acid and globulin free Bovine Serum Albumin (BSA; minimum 99%) were purchased from Sigma (St. Louis, MO) and used without further purification. As two very different, but major components of the tear film, lysozyme and BSA were chosen primarily due to their availability and low cost and the large body of literature published on their interaction with hydrogel contact lenses. The lenses, mounted on the spherical lens holder, were rinsed with Millipore deionized water. They were subsequently covered with a solution of 3 mg/ml lysozyme solution in phosphate buffer at a pH of 7, using a Poly-(tetrafluoroethylene) containment vessel. The lenses were exposed to the protein solution for 8 to 12 h at room temperature and then carefully rinsed again with Millipore deionized water. Imaging was started within 15 min of removing the lenses from the lysozyme solution, using tapping mode with MikroMasch tips, at image sizes of 2 to 80 μm . Several lenses (at least four) of each type were

imaged. Preliminary results showed structures which appeared to resemble lysozyme amyloid fibrils on the surface of galyfilcon A. In order to examine if the topography of the structures was indeed consistent with this fibril interpretation, lysozyme amyloid fibrils were formed according to the method of Stathopoulos et al.⁶⁶ This involved ultrasonicated the lysozyme in solution in order to denature it and form large aggregates. These were subsequently imaged with AFM for comparison purposes. Approximately fifteen additional galyfilcon lenses were imaged in an attempt to determine the repeatability and conditions under which any anomalous adsorption occurs (discussed later).

Scanning Electron Microscopy

Three silicone hydrogel materials (balafilcon A, lotrafilcon A and galyfilcon A), and one conventional hydrogel lens material (polymacon), were analyzed by SEM to examine the deposition patterns of lysozyme and/or albumin on their anterior surface. For the SEM studies, colloidal-gold biosensors were produced from 10 to 100 nm protein-conjugated gold spheres, which were prepared in-house and used to examine low levels of protein deposition in a way that would not be possible with more conventional techniques.⁶⁷⁻⁶⁹ Unconjugated gold colloid (Ted Pella, Redding, CA) at a concentration of 5.7×10^{12} particles/ml for the 10 nm gold spheres and 5.6×10^9 particles/ml for the 100 nm gold spheres was used to prepare two protein-sphere combinations. BSA was prepared with 100 nm gold spheres and lysozyme with 10 nm gold spheres, in the following manner. For the BSA coated spheres, six cuvettes were filled with two drops of 0.63 mg/ml BSA solution in Millipore deionized water at pH 7. Each cuvette was then diluted with 50 drops of pH 5.7 (lowered by HCl) Millipore deionized water and 40 drops of 100 nm gold solution. The resulting mixture was left unperturbed for 1 h to allow conjugation to take place. After this the solutions were centrifuged at 14,000 g for 30 min and resuspended four times with buffer solution to remove free protein. The spheres were centrifuged a fifth time and resuspended in water at pH 7. The lysozyme-conjugation followed the same method, with three drops of 1 mg/ml solution to 30 drops of protein. The initial pH was 9.45 and the final dilutions were made up with pH 7 water. The final solutions obtained had protein-conjugated sphere concentrations of approximately 1 $\mu\text{g}/\text{ml}$, which ensured that the solution contained more protein molecules conjugated to spheres than free protein in solution. Lenses were removed from their original packaging solution, rinsed for 10 s in Millipore deionized water and prepared for examination in a

AQ: 1

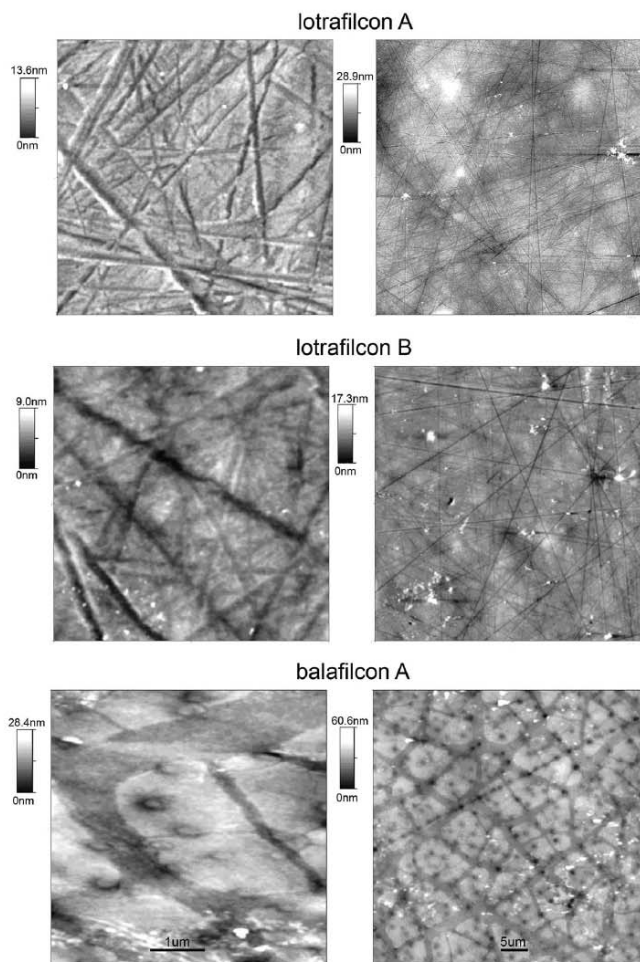


FIGURE 2.

Five micrometres (left) and 50 μm (right) AFM images of rinsed, unworn, lotrafilcon A, lotrafilcon B and balafilcon A lenses. Size bars are given in the lower images.

secluded fume hood to minimize air particle contamination. After rinsing, the lenses were placed posterior side down on a silicone rubber “eyeform,” which has approximately the same dimensions and geometry as a human eye. Two stacked rubber o-rings were placed over the lens, encasing the “corneal area” of the eye form. These o-rings delineated and “fenced in” the ten 25 μL drops of each albumin and lysozyme solution that were then added to each lens. The solution was left on the lenses for 12 h, with replenishing drops of equal amounts of both proteins to avoid evaporation at the 4- and 6-h marks. After the 12-h doping time, the o-rings were removed, any remaining solution was allowed to drain off the lenses and three drops of water were applied to the lenses to remove any free proteins. The lenses were finally placed in a plastic, covered container with a small opening and left to dry in ambient conditions for approximately 12 h at room temperature. After 12 h, the dehydrated lenses

were sputter-coated with gold and examined using a JSM-6460LA SEM (JEOL, Mississauga, ON) at a 10 KV accelerating voltage and 50 μA filament strength.

RESULTS

Figs. 2 to 4 show AFM images of various unworn silicone hydrogel and polyHEMA-based lenses. Fig. 2 shows that the lotrafilcon A and B lenses are relatively featureless (aside from some minor debris), and exhibit what appear to be shallow lines on the lens surface, while balafilcon A lenses reveal an “island-like” structure. Fig. 3 demonstrates that galyfilcon A exhibits a complex morphology, while senofilcon A, possessing a similar chemical composition to galyfilcon A, displays a comparable, but finer structure. Comfilcon A (the only silicone hydrogel material to incorporate neither a surface treatment nor an internal wetting agent) appears as

6 Imaging Protein on Contact Lenses—Teichroeb et al.

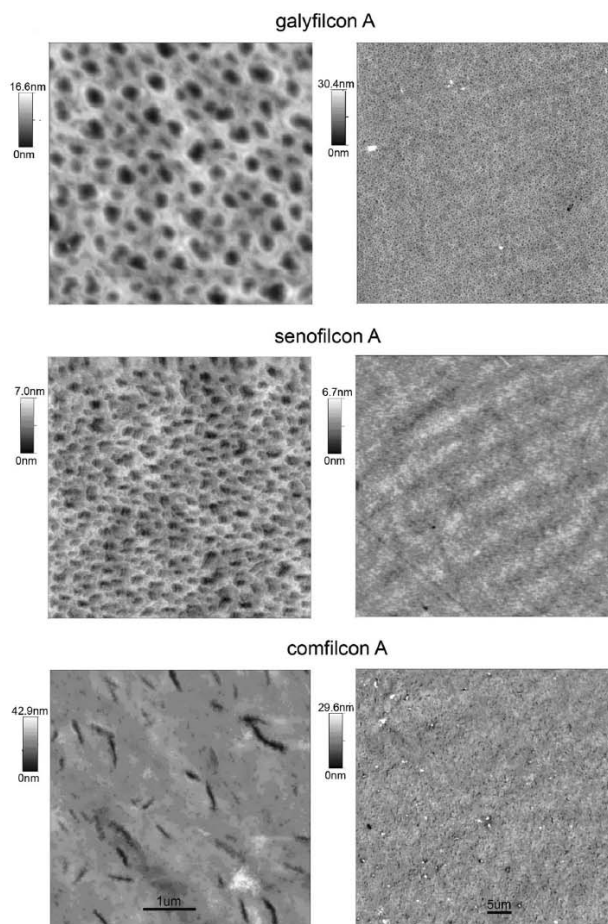


FIGURE 3. Five micrometres (left) and 50 μm (right) AFM images of rinsed, unworn, galyfilcon A, senofilcon A, comfilcon A lenses. Size bars are given in the lower images.

though there are oblong holes scattered across the surface. Fig. 4 shows that omafilcon A and polymacon lenses have relatively similar surface appearances, in which they exhibit multiple “dimples” which, when hydrated, are probably deeply extending pores into the material.

Roughness analysis performed on AFM images of lenses are given in Table 3. Since lenses may exhibit roughness on more than one length scale, average roughness $\left(R_a = \frac{1}{N} \sum_{i=1}^N |Z_i - \bar{Z}| \right)$ and root mean square roughness $\left(R_{RMS} = \sqrt{\frac{1}{N} \sum_{i=1}^N (Z_i - \bar{Z})^2} \right)$ is given for both 5 and 50 μm images. Balafilcon exhibited the greatest surface roughness, followed by polymacon, however, on the 5 μm scale comfilcon also displays a fairly rough surface. Senofilcon

has the least roughness of the lenses imaged, despite having a strong underlying structure.

The XPS data converted to relative amounts of selected surface elements (Fig. 5) shows that lotrafilcon A and lotrafilcon B are comparable in their silicon content, although lotrafilcon B exhibits some fluorine content that was missing in the lotrafilcon A scan. Of the silicone hydrogel materials, galyfilcon A and balafilcon A lenses appear to mask somewhat less of the siloxane moieties than the other materials. The trace silicon signals present in the conventional materials is most likely due to “contamination” during the manufacturing phase.

Protein-conjugated gold nanoparticles were used as biosensors to investigate trace small amounts of protein adsorbed onto the surface of the materials. Figs. 6 to 9 show typical SEM images of

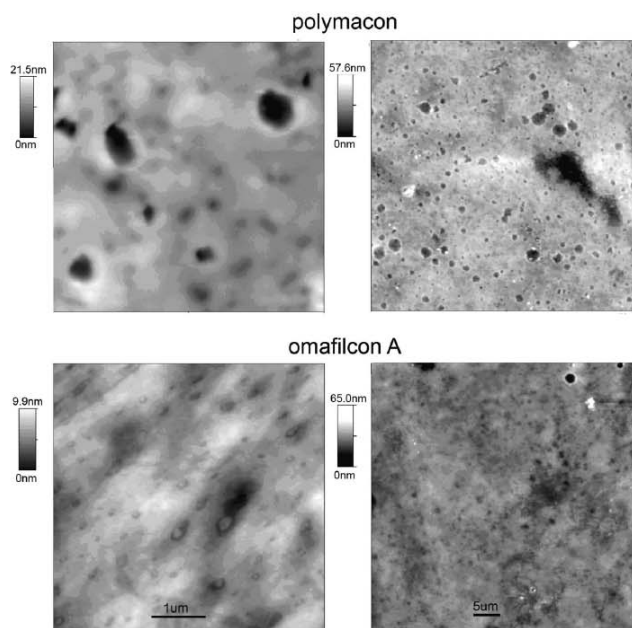


FIGURE 4.

Images of $5 \times 5 \mu\text{m}$ (left) and $50 \mu\text{m}$ (right) AFM rinsed, unworn, polymacon, omafilcon A lenses. Size bars are given in the lower images.

TABLE 3.

Roughness of bare lenses determined by atomic force microscopy

Material	Area roughness on $5 \mu\text{m}$ scale		Area roughness on $50 \mu\text{m}$ scale	
	R_a (nm) ± 0.2 nm	R_{rms} (nm) ± 0.2 nm	R_a (nm) ± 0.2 nm	R_{rms} (nm) ± 0.2 nm
Lotrafilcon A	1.12	1.45	1.56	2.06
Lotrafilcon B	0.77	1.03	1.60	2.30
Balafilcon A	2.21	3.01	4.17	5.24
Galyfilcon A	1.49	1.84	2.07	2.66
Senofilcon A	0.72	0.90	1.42	1.86
Comfilcon A	2.06	2.87	2.00	2.74
Polymacon	1.88	2.58	3.12	4.41
Omafilcon A	0.67	0.86	1.83	2.84

R_a , average roughness; R_{rms} , root mean square roughness.

the lens materials after exposure to the mixed solution of protein-conjugated gold nanospheres. The galyfilcon A material exhibited protein collected in large aggregates (Fig. 6), with very little non-aggregated protein, even at higher magnifications. This image was almost identical to that observed on the balafilcon A material. A very different pattern was observed with the lotrafilcon A material (Fig. 7). Although there were still large aggregates, the most notable feature is the obvious background of many single gold nanospheres. Each 100 nm sphere was conjugated to (and hence surrounded by) BSA, and so Fig. 7 provides a very strong indication of monolayer adsorption of albumin on the lotrafilcon material. There could not be much more than monolayer coverage as that would result in an inability to discern individual gold nanospheres. In order to see if the same behavior could be observed for

lysozyme it was necessary to use higher magnification, as the lysozyme was conjugated to 10 nm spheres. Fig. 8 shows the lotrafilcon material under magnifications of $10,000\times$ (a) and $30,000\times$ (b). Fig. 8b indicates that both sizes of spheres were present, with the bright spheres being the 100 nm BSA-labeled spheres and the dimmer, out-of-focus spheres being the 10 nm lysozyme-labeled ones, suggesting that the material surface is covered in a protein monolayer of a mixture of both lysozyme and albumin. The non-silicone hydrogel lens material, polymacon, revealed a greater degree of deposition of both proteins than that observed on any of the silicone-based lenses (Fig. 9a, b). Only small areas indicated some evidence for single layer coverage (Fig. 9b).

Figs. 10 to 14 show AFM tapping mode images after exposing the lens materials to lysozyme. Fig. 10 shows an image of balafilcon

8 Imaging Protein on Contact Lenses—Teichroeb et al.

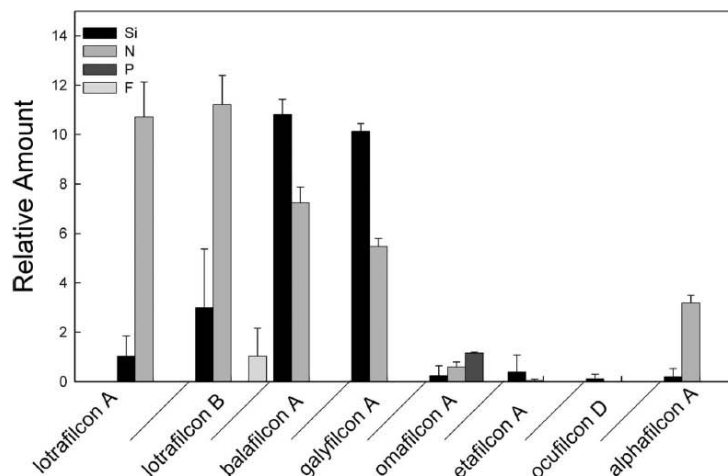


FIGURE 5.

Relative amounts of selected elements at the surface of various contact lenses by XPS. Si (silicon), N (Nitrogen), P (Phosphorus), F (Fluorine).

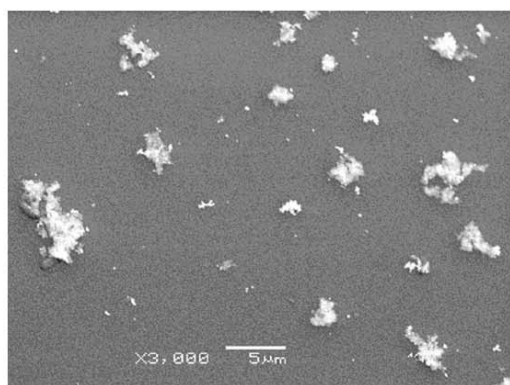


FIGURE 6.

Low magnification (3000 \times) SEM image of galyfilcon A exposed to a mixed solution of protein conjugated gold nanospheres. The protein deposition consisted of large, discrete aggregates of BSA and lysozyme.

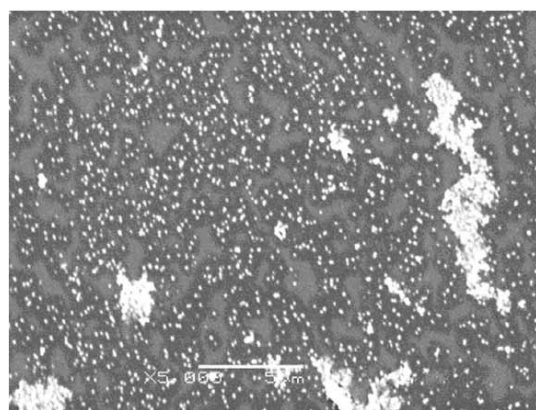


FIGURE 7.

Low magnification (5000 \times) SEM image of lotrafilcon A exposed to a mixed solution of protein conjugated gold nanospheres. The image demonstrates discrete aggregates of nanospheres, with a significant background of 100 nm albumin-conjugated spheres.

A at a $50 \times 50 \mu\text{m}$ scan size. The only difference between images of a lens taken directly from the packaging solution (Fig. 3) and that of the protein-coated lens (Fig. 10) are the accumulated protein deposits, which show up in the image as discrete white areas. Although the deposits in the image are large (micrometers in width and up to 100 nm high) compared with the surface of the unworn lens, they represent a very small amount of total protein. Very similar images were obtained for lotrafilcon A, senofilcon A (Fig. 11), comfilcon A (Fig. 12) and polymacon. In contrast, Figs. 13 and 14 demonstrates that galyfilcon A behaved quite differently. Fig. 13 shows a $50 \times 50 \mu\text{m}$ scan of the material, revealing similarly large aggregates to that seen in Fig. 11, with numerous much smaller, extended “string-like” structures in the background. Although these structures seem to be comprised of a much smaller amount of protein than the larger aggregates, their novel morphology makes them especially in-

teresting. Fig. 14 shows a higher resolution $20 \times 20 \mu\text{m}$ scan. Of all the materials studied, only the galyfilcon material demonstrated these unusual string-like deposits, with other areas of the galyfilcon material showing only the large aggregates typically seen on the other materials. The appearance of the anomalous aggregates was unique to galyfilcon A samples, and we were unable to determine conditions under which they would be completely repeatable. Fig. 15 shows an AFM image of lysozyme fibrils created using the ultrasonication technique previously described.⁶⁶ The lysozyme aggregates are fibrillar in nature, and exhibit characteristic amyloid traits, which appear morphologically similar to the lysozyme deposits seen on the galyfilcon A material in Figs. 13 and 14.

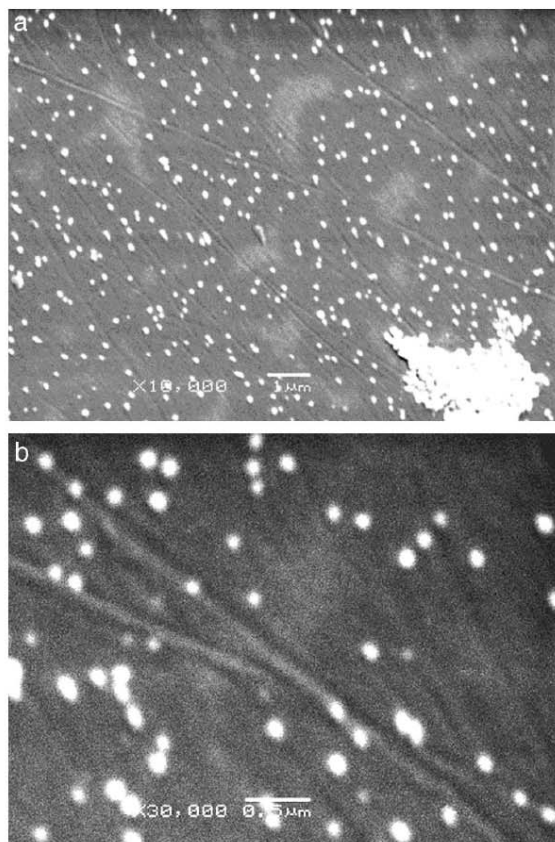


FIGURE 8. a, 10,000 \times . b, 30,000 \times magnification SEM images of lotrafilcon A material exposed to a mixed solution of protein conjugated gold nanospheres. Each image indicates two sphere sizes, indicating that both BSA and lysozyme were bound to the lens material.

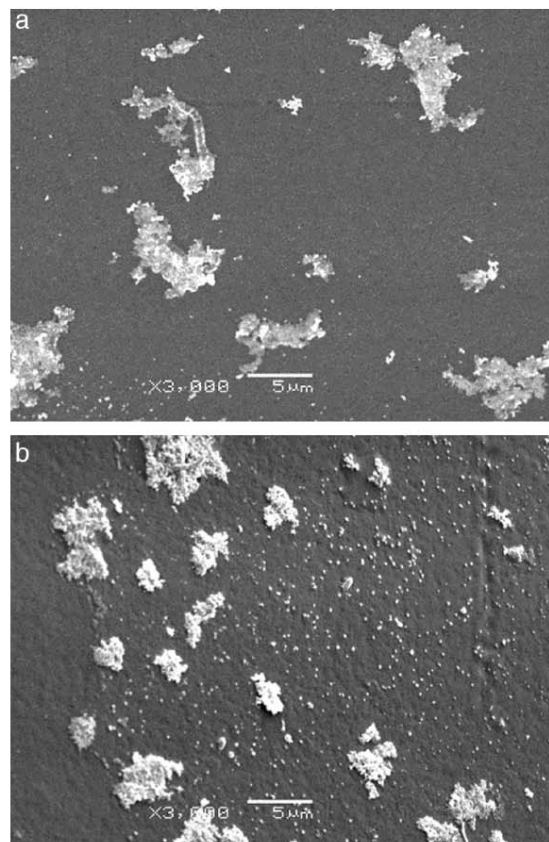


FIGURE 9. Low magnification (3000 \times) SEM images of the polyacon material exposed to a mixed solution of protein conjugated gold nanospheres. a, shows behavior similar to that seen with the galyfilcon A material, where most of the protein is concentrated in aggregates. b, provides evidence for some regions displaying a more uniform coverage, similar (but differing in magnitude) to that observed with lotrafilcon A.

DISCUSSION

In this study we sought to use two distinctly different imaging techniques (AFM and SEM) to determine the interaction between proteins and silicone hydrogels. To our knowledge, this is the first time these techniques have been used to visualize the deposition morphology of proteins on silicone hydrogel materials. The advantage of both techniques over those previously reported^{59–63} is that the protein can be examined *in situ* with minimal disturbance, once the lens materials have been doped. Despite this obvious advantage over destructive methodologies, interpretation of the results must be considered with some caution, in light of the fact that the studies were conducted with dehydrated lenses, which obviously differs from that encountered *in vivo*. Additionally, these techniques are limited to small regions and surface bound proteins. However, as all materials were treated in an identical manner before imaging, the results prove to be of interest in terms of comparisons between materials, and as a complement to traditional methods of analyzing protein deposition on contact lens materials.

AFM examination of unworn lenses (Figs. 2 to 4) show that the surface morphology of the lens materials under investigation differ markedly. The AFM images of polyacon, etafilcon A, galyfilcon A, lotrafilcon A and balafilcon A are similar to those previously described.^{33,70–72} The AFM images of omafilcon A, senofilcon A and comfilcon A have not previously been reported. The surfaces of the lotrafilcon A and lotrafilcon B materials (Fig. 2) appear to be identical, as they should, given that they both undergo the same surface treatment process after they have been molded. Their surface topography exhibits multiple “lines,” which have been previously described.^{33,73} This surface appearance is very similar to that seen in lathe-cut lenses,^{72,74} confirming that the appearance is almost certainly due to lathe-marks on the molds made to manufacture the lotrafilcon-based lenses and also suggesting that the plasma treatment has evenly and effectively covered the surface of the lens. The balafilcon A lens (Fig. 2) exhibited an “island-like” structure (which is a consequence of the conversion of part of the surface into silicates), with pores extending down into the bulk of

10 Imaging Protein on Contact Lenses—Teichroeb et al.

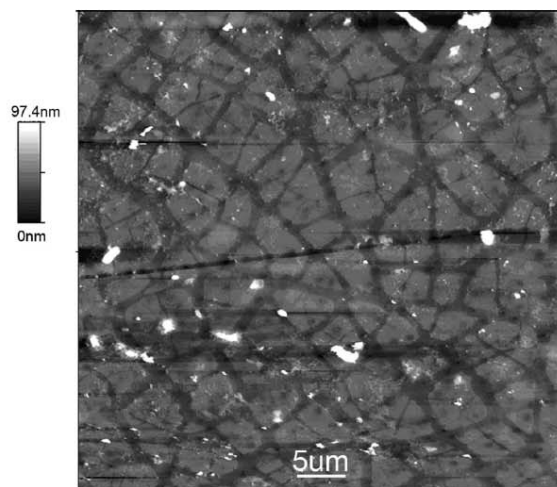


FIGURE 10.

AFM image of balafilcon A after exposure to 3 mg/ml lysozyme at pH 7 at room temperature for 8 to 12 h. The background plasma surface treatment is clearly visible beneath the areas of aggregated protein, which show up as discrete white areas.

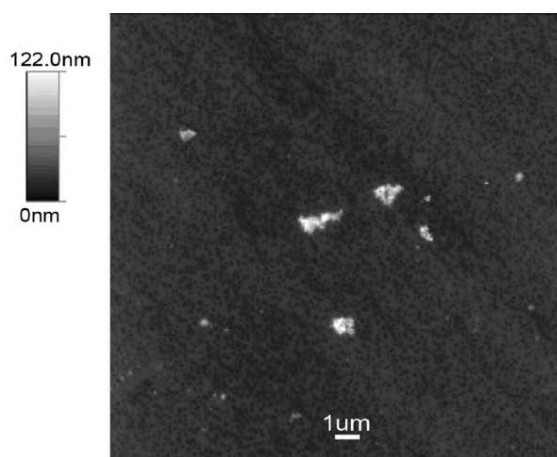


FIGURE 11.

AFM image ($20 \times 20 \mu\text{m}$) of senofilcon A after exposure to 3 mg/ml lysozyme at pH 7 at room temperature for 8 to 12 h.

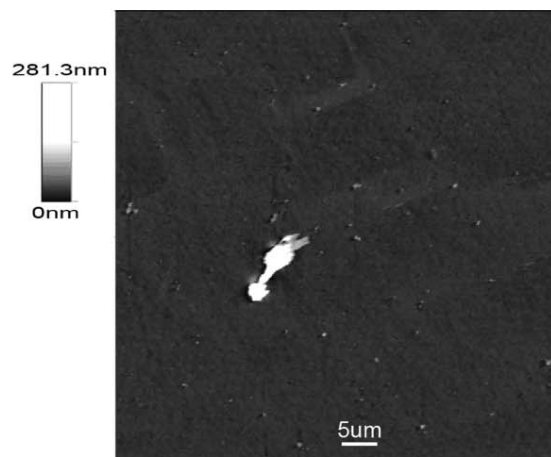


FIGURE 12.

AFM image ($60 \times 60 \mu\text{m}$) of comfilcon A after exposure to 3 mg/ml lysozyme at pH 7 at room temperature for 8 to 12 h.

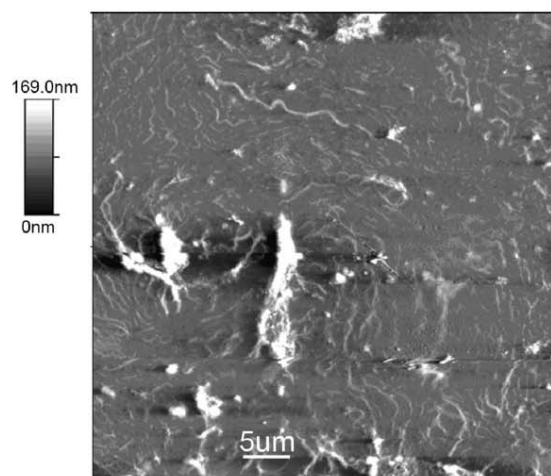


FIGURE 13.

AFM image ($50 \times 50 \mu\text{m}$) of galyfilcon A after exposure to 3 mg/ml lysozyme at pH 7 at room temperature for 8 to 12 h. The lack of surface treatment is apparent, along with the areas of accumulated protein and finer, fibrillar structures.

the lens material, similar to that previously reported.^{33,40,73} The galyfilcon A and senofilcon A lenses (Fig. 3) are similar in surface appearance and have a relatively “sponge-like” surface topography, which likely arises from their unique incorporation of PVP to enhance wettability. The omafilcon A and polymacon lenses (Fig. 4) exhibit multiple “dimples” which, when hydrated, are likely pores in the lens material. Interestingly, of all the silicone hydrogel materials, it was only the non-surface-treated comfilcon A material (Fig. 3) that exhibited some features comparable with the poly-HEMA-based lenses, potentially implying that its “inherent wettability” may cause it to act somewhat like a conventional lens.

The elemental data from XPS (Fig. 5) provides additional information about the surface treatment techniques and the ability of the lenses to “mask” the siloxane from the tear film. The data shows that within the silicone hydrogel lens materials tested, the lotrafilcon-based materials exhibit the lowest amount of silicon on their surface and the balafilcon A and galyfilcon A-based lenses exhibit the greatest amount of silicon. This is likely due to the fact that the surface treatment process of the lotrafilcon materials is more uniform in its coverage, thus masking more siloxane. In contrast, the inhomogeneous nature of the balafilcon surface treatment^{33,40,73} likely exposes parts of the underlying material bulk, where more siloxane could be present. It would also appear that the amount of

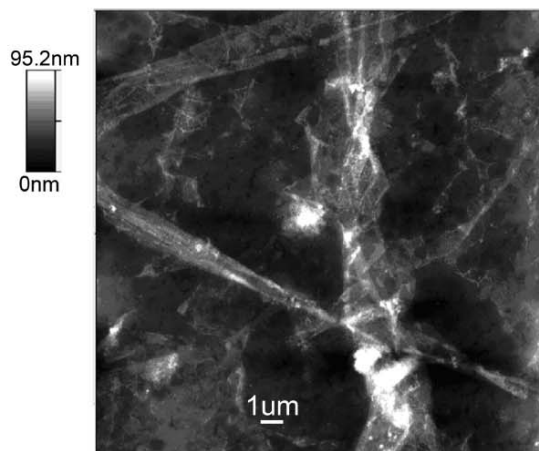


FIGURE 14.

AFM image ($20 \times 20 \mu\text{m}$) of galyfilcon A after exposure to 3 mg/ml lysozyme at pH 7 at room temperature for 8 to 12 h. The fibrillar structure of the deposited protein on the lens surface is clearly obvious.

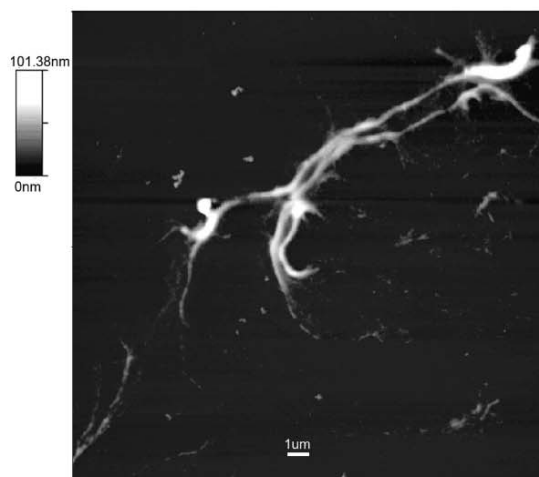


FIGURE 15.

AFM image of lysozyme fibrils created using an ultrasonication technique.

PVP incorporated into the galyfilcon A bulk material is insufficient to adequately mask the silicon signal at the galyfilcon A interface, and further work to compare the signal at the senofilcon A surface, which incorporates more PVP into the material, appears warranted. Interestingly, recent studies have shown that both balafilcon A and galyfilcon A collect more lipid and protein deposits than lotrafilcon^{63,64,75} and that they have higher contact angles,⁷⁶ as would be expected in materials that exhibit higher levels of hydrophobic siloxane groups at their surface. However, it must be borne in mind that the clinical impact of this enhanced silicon signal remains unknown.

Although the use of SEM in isolation does not allow for the quantification of the amount of protein adsorbed onto hydrogel

materials, the novel use of protein-conjugated gold nanoparticles does allow for semi-quantification and allows the derivation of data relating to competitive adsorption between the two proteins under investigation. Images indicate that the galyfilcon and balafilcon materials attract relatively little protein and that this protein does not form a distinct monolayer, but is instead aggregated in distinct clumps across the lens surface (Fig. 6). The lotrafilcon material also attracts only a small amount of protein, but the protein is distributed across the entire material surface (Figs. 7 and 8), with both lysozyme and albumin being readily seen. This is in contrast to the polyHEMA-based hydrogel (Fig. 9), which adsorbs greater quantities of protein than any of the silicone hydrogel materials and exhibits uneven aggregates, with only limited areas exhibiting full, monolayer coverage.

The AFM protein-deposition studies (Figs. 10 to 15) demonstrated that the silicone hydrogel materials deposit only small amounts of lysozyme onto their surfaces, confirming previous results using other methods.^{41,50,58–61,63,77} Using this technique it was clear that galyfilcon A collects lysozyme deposits in a unique filamentous pattern (Figs. 13 and 14). Based upon the appearance of lysozyme fibrils,⁷⁸ the formation of these characteristic string-like deposits suggests that the lysozyme on the surface has been denatured. One key difference between the features in Figs. 13 and 14 and these fibrillar structures (Fig. 15) is the lateral size of the features, with the deposits in Fig. 14 being at least an order of magnitude wider than lysozyme fibrils. However, it is known that amyloid fibrils may form supermolecular structures through oligomerization⁷⁹ and these “string-like” structures show striking resemblance to the AFM images of amyloid lysozyme fibrils in Fig. 15. Although positive identification of an amyloid nature has not yet been confirmed by congo red, this unusual morphology was not seen on any other lens types imaged. This suggests the unique surface structure of galyfilcon A may promote this particular organization. It is possible that the polyvinyl alcohol at the galyfilcon interface may have precipitated the lysozyme into these fibrillar structures, due to an incompatibility between the surrounding lysozyme solution and any polyvinyl alcohol that may be released from the material surface. However, the lysozyme appearance on senofilcon A (Fig. 11) was quite different, despite the fact that both materials include PVP as their method to enhance surface wettability. Anecdotally, clinicians report that these two materials behave differently in a clinical setting and it would appear that their performance when exposed to proteins is characteristically quite different. Of further interest is that recent data from our group using a different methodology based on a micrococcy assay.⁶³

Micrococcy assay demonstrates that galyfilcon and senofilcon have similar tendencies to denature lysozyme, and so this result obviously requires further investigation. It is tempting to believe that the affinity for lysozyme to assemble on galyfilcon A is related to the fact that it does not mask as much siloxane as some other silicone hydrogel materials, such as lotrafilcon A (Fig. 5); however, balafilcon A displays similar levels of siloxane exposure to galyfilcon, but with none of the same protein structures. The inclusion of an internal wetting agent in galyfilcon A may create a topology which is favorable for fibril-like formation, or the formation or supermolecular organizations of fibrils; however, we have also not, as of yet, seen this structure on senofilcon A, which might have been expected, since both are produced using PVP as an internal

12 Imaging Protein on Contact Lenses—Teichroeb et al.

wetting agent. In addition, the surface morphology of the unworn lenses as elucidated by AFM (Fig. 3) show remarkable resemblance, although the senofilcon A structure appears somewhat finer, with a lower roughness than that exhibited by galyfilcon A.

It is worth noting that in none of the SEM images do we see evidence of the string-like structures seen in the AFM images. One possible reason for this is the large difference in concentration, with the protein solutions for the AFM images being approximately 10^3 times more concentrated than those in the SEM studies. Alternatively, because the protein is physically bonded to the gold spheres, it may not be able to access all conformational and aggregate states that the free protein can.

In conclusion, using two *in vitro* model systems, we have demonstrated that siloxane-based hydrogel contact lens materials deposit low levels of proteins and that the morphology of the protein deposition differs between materials, depending upon the constituent monomers and surface composition of the materials in question. Longer term, *in vivo* studies will be required to investigate the clinical significance of these novel findings. The techniques presented provide a valuable addition to traditional methods that require elution or removal of the deposited species from the materials in question, and will assist researchers in the analysis of proteins deposited on many hydrogel biomaterials, including contact lenses.

ACKNOWLEDGMENTS

This study was supported by National Sciences and Engineering Research Council (NSERC) Canada and the Canada Foundation for Innovation (CFI).

The authors have no financial interest in any of the products mentioned in this article, but do receive research funds from companies who produce the lens materials described.

This paper was originally presented, in part, as a poster at the American Academy of Optometry Meeting, in Tampa, Florida in December 2004.

Received November 27, 2007; accepted May 27, 2008.

REFERENCES

- Norde W, Lyklema J. Why proteins prefer interfaces. *J Biomater Sci Polym Ed* 1991;2:183–202.
- Norde W, Anusiem AC. Adsorption, desorption and readsorption of proteins on solid surfaces. *Colloids Surf* 1992;66:73–80.
- Norde W. Adsorption of proteins at solid-liquid interfaces. *Cell Mater* 1995;5:97–112.
- Andrade JD, Hlady V. Vroman effects, techniques, and philosophies. *J Biomater Sci Polym Ed* 1991;2:161–72.
- Andrade JD. Needs, problems, and opportunities in biomaterials and biocompatibility. *Clin Mater* 1992;11:19–23.
- Dupres V, Verbelen C, Dufrene YF. Probing molecular recognition sites on biosurfaces using AFM. *Biomaterials* 2007;28:2393–402.
- Soni PS, Hathcoat G. Complications reported with hydrogel extended wear contact lenses. *Am J Optom Physiol Opt* 1988;65:545–51.
- Holden BA, Sweeney DF, Vannas A, Nilsson KT, Efron N. Effects of long-term extended contact lens wear on the human cornea. *Invest Ophthalmol Vis Sci* 1985;26:1489–501.
- Poggio EC, Glynn RJ, Schein OD, Seddon JM, Shannon MJ, Scardino VA, Kenyon KR. The incidence of ulcerative keratitis among users of daily-wear and extended-wear soft contact lenses. *N Engl J Med* 1989;321:779–83.
- Schein OD, Glynn RJ, Poggio EC, Seddon JM, Kenyon KR. The relative risk of ulcerative keratitis among users of daily-wear and extended-wear soft contact lenses. A case-control study. *Microbial Keratitis Study Group. N Engl J Med* 1989;321:773–8.
- Cheng KH, Leung SL, Hoekman HW, Beekhuis WH, Mulder PG, Geerards AJ, Kijlstra A. Incidence of contact-lens-associated microbial keratitis and its related morbidity. *Lancet* 1999;354:181–5.
- Tighe B. Contact lens materials. In: Phillips A, Speedwell L, eds. *Contact Lenses*, 5th ed. Edinburgh: Butterworth-Heinemann; 2007: 59–78.
- Alvord L, Court J, Davis T, Morgan CF, Schindhelm K, Vogt J, Winterton L. Oxygen permeability of a new type of high Dk soft contact lens material. *Optom Vis Sci* 1998;75:30–6.
- Compan V, Andrio A, Lopez-Alemay A, Riande E, Refojo MF. Oxygen permeability of hydrogel contact lenses with organosilicon moieties. *Biomaterials* 2002;23:2767–72.
- Tighe B. Silicone hydrogels: structure, properties and behaviour. In: Sweeney D, ed. *Silicone Hydrogels: Continuous Wear Contact Lenses*, 2nd ed. Oxford: Butterworth-Heinemann; 2004:1–27.
- Jones L, Dumbleton K. Soft lens extended wear and complications. In: Hom MM, Bruce AS, eds. *Manual of Contact Lens Prescribing and Fitting*, 3rd ed. St Louis, MO: Butterworth-Heinemann Elsevier; 2006:393–441.
- Morgan PB, Efron N. The oxygen performance of contemporary hydrogel contact lenses. *Cont Lens Anterior Eye* 1998;21:3–6.
- Efron N, Morgan PB, Cameron ID, Brennan NA, Goodwin M. Oxygen permeability and water content of silicone hydrogel contact lens materials. *Optom Vis Sci* 2007;84:328–37.
- Papas EB, Vajdic CM, Austen R, Holden BA. High-oxygen-transmissibility soft contact lenses do not induce limbal hyperaemia. *Curr Eye Res* 1997;16:942–8.
- Dumbleton KA, Chalmers RL, Richter DB, Fonn D. Changes in myopic refractive error with nine months' extended wear of hydrogel lenses with high and low oxygen permeability. *Optom Vis Sci* 1999; 76:845–9.
- Dumbleton KA, Chalmers RL, Richter DB, Fonn D. Vascular response to extended wear of hydrogel lenses with high and low oxygen permeability. *Optom Vis Sci* 2001;78:147–51.
- Dumbleton K. Adverse events with silicone hydrogel continuous wear. *Cont Lens Anterior Eye* 2002;25:137–46.
- du Toit R, Simpson TL, Fonn D, Chalmers RL. Recovery from hyperemia after overnight wear of low and high transmissibility hydrogel lenses. *Curr Eye Res* 2001;22:68–73.
- Keay L, Sweeney DF, Jalbert I, Skotnitsky C, Holden BA. Microcyst response to high Dk/t silicone hydrogel contact lenses. *Optom Vis Sci* 2000;77:582–5.
- Fonn D, du Toit R, Simpson TL, Vega JA, Situ P, Chalmers RL. Sympathetic swelling response of the control eye to soft lenses in the other eye. *Invest Ophthalmol Vis Sci* 1999;40:3116–21.
- Covey M, Sweeney DF, Terry R, Sankaridurg PR, Holden BA. Hypoxic effects on the anterior eye of high-Dk soft contact lens wearers are negligible. *Optom Vis Sci* 2001;78:95–9.
- Dumbleton K, Keir N, Moezzi A, Feng Y, Jones L, Fonn D. Objective and subjective responses in patients refitted to daily-wear silicone hydrogel contact lenses. *Optom Vis Sci* 2006;83:758–68.
- Huth S, Wagner H. Identification and removal of deposits on polydimethylsiloxane silicone elastomer lenses. *Int Contact Lens Clin* 1981;8:19–26.
- Rae ST, Huff JW. Studies on initiation of silicone elastomer lens adhesion in vitro: binding before the indentation ring. *CLAO J* 1991; 17:181–6.
- Grobe G, Kunzler J, Seelye D, Salamone J. Silicone hydrogels for contact lens applications. *Polym Mater Sci Eng* 1999;80:108–9.

31. Nicolson PC, Vogt J. Soft contact lens polymers: an evolution. *Biomaterials* 2001;22:3273–83.
32. Nicolson PC. Continuous wear contact lens surface chemistry and wearability. *Eye Contact Lens* 2003;29:S30–2.
33. Gonzalez-Mejome JM, Lopez-Aleman A, Almeida JB, Parafita MA, Refojo MF. Microscopic observation of unworn siloxane-hydrogel soft contact lenses by atomic force microscopy. *J Biomed Mater Res B Appl Biomater* 2006;76:412–8.
34. Gonzalez-Mejome JM, Lopez-Aleman A, Almeida JB, Parafita MA, Refojo MF. Microscopic observations of superficial ultrastructure of unworn siloxane-hydrogel contact lenses by cryo-scanning electron microscopy. *J Biomed Mater Res B Appl Biomater* 2006;76:419–23.
35. Jones L, Subbaraman LN, Rogers R, Dumbleton K. Surface treatment, wetting and modulus of silicone hydrogels. *Optician* 2006; 232:28–34. Available at: <http://www.opticianonline.net/assets/getAsset.aspx?ItemID=2113>. Accessed August 22, 2008.
36. Lira M, Santos L, Azeredo J, Yebra-Pimentel E, Oliveira ME. Comparative study of silicone-hydrogel contact lenses surfaces before and after wear using atomic force microscopy. *J Biomed Mater Res B Appl Biomater* 2008;85:361–7.
37. Nicolson PC, Baron RC, Chabreck P, Court J, Domschke A, Griesser HJ, Ho A, Hopken J, Laycock BG, Liu Q, Lohmann D, Meijs GF, Papas E, Riffle JS, Schindhelm K, Sweeney D, Terry WL Jr, Vogt J, Winterton LC. Extended wear ophthalmic lens. US Patent 5,760,100. June 2, 1998.
38. Weikart CM, Matsuzawa Y, Winterton L, Yasuda HK. Evaluation of plasma polymer-coated contact lenses by electrochemical impedance spectroscopy. *J Biomed Mater Res* 2001;54:597–607.
39. Valint PL Jr, Grobe GL III, Ammon DM Jr, Moorehead MJ. Plasma surface treatment of silicone hydrogel contact lenses. US Patent 6,193,369. February 27, 2001.
40. Lopez-Aleman A, Compan V, Refojo MF. Porous structure of Purevision versus Focus Night&Day and conventional hydrogel contact lenses. *J Biomed Mater Res* 2002;63:319–25.
41. Steffen R, Schneider C. A next generation silicone hydrogel lens for daily wear. Part 1: material properties. *Optician* 2004;227:23–5.
42. Steffen RB, McCabe KP. Finding the comfort zone. *Contact Lens Spectrum* 2004;13(Suppl.):1–4. Available at: <http://www.clspectrum.com/article.aspx?article=12543>. Accessed August 22, 2008.
43. Jones L. Comfilcon A: a new silicone hydrogel material. *Contact Lens Spectrum* 2007;22:21. Available at: <http://www.clspectrum.com/article.aspx?article=100764>. Accessed August 22, 2008.
44. Karlgard CC, Sarkar DK, Jones LJ, Moresoli C, Leung KT. Drying methods for XPS analysis of PureVision, Focus Night&Day and conventional hydrogel contact lenses. *Appl Surf Sci* 2004;230:106–14.
45. Maldonado-Codina C, Morgan PB, Efron N, Canry JC. Characterization of the surface of conventional hydrogel and silicone hydrogel contact lenses by time-of-flight secondary ion mass spectrometry. *Optom Vis Sci* 2004;81:455–60.
46. Court JL, Redman RP, Wang JH, Leppard SW, Obyrne VJ, Small SA, Lewis AL, Jones SA, Stratford PW. A novel phosphorylcholine-coated contact lens for extended wear use. *Biomaterials* 2001;22: 3261–72.
47. Bruinsma GM, van der Mei HC, Busscher HJ. Bacterial adhesion to surface hydrophilic and hydrophobic contact lenses. *Biomaterials* 2001;22:3217–24.
48. Henriques M, Sousa C, Lira M, Elisabete M, Oliveira R, Azeredo J. Adhesion of *Pseudomonas aeruginosa* and *Staphylococcus epidermidis* to silicone-hydrogel contact lenses. *Optom Vis Sci* 2005;82:446–50.
49. Maldonado-Codina C, Morgan PB. In vitro water wettability of silicone hydrogel contact lenses determined using the sessile drop and captive bubble techniques. *J Biomed Mater Res A* 2007;83:496–502.
50. Santos L, Rodrigues D, Lira M, Oliveira ME, Oliveira R, Vilar EY, Azeredo J. The influence of surface treatment on hydrophobicity, protein adsorption and microbial colonisation of silicone hydrogel contact lenses. *Cont Lens Anterior Eye* 2007;30:183–8.
51. Sack RA, Jones B, Antignani A, Libow R, Harvey H. Specificity and biological activity of the protein deposited on the hydrogel surface. Relationship of polymer structure to biofilm formation. *Invest Ophthalmol Vis Sci* 1987;28:842–9.
52. Leahy CD, Mandell RB, Lin ST. Initial in vivo tear protein deposition on individual hydrogel contact lenses. *Optom Vis Sci* 1990;67: 504–11.
53. Bohnert JL, Horbett TA, Ratner BD, Royce FH. Adsorption of proteins from artificial tear solutions to contact lens materials. *Invest Ophthalmol Vis Sci* 1988;29:362–73.
54. Jones L, Mann A, Evans K, Franklin V, Tighe B. An in vivo comparison of the kinetics of protein and lipid deposition on group II and group IV frequent-replacement contact lenses. *Optom Vis Sci* 2000; 77:503–10.
55. Garrett Q, Garrett RW, Milthorpe BK. Lysozyme sorption in hydrogel contact lenses. *Invest Ophthalmol Vis Sci* 1999;40:897–903.
56. Garrett Q, Griesser HJ, Milthorpe BK, Garrett RW. Irreversible adsorption of human serum albumin to hydrogel contact lenses: a study using electron spin resonance spectroscopy. *Biomaterials* 1999;20: 1345–56.
57. Garrett Q, Laycock B, Garrett RW. Hydrogel lens monomer constituents modulate protein sorption. *Invest Ophthalmol Vis Sci* 2000; 41:1687–95.
58. McNally J, McKenney CD. A clinical look at a silicone hydrogel extended wear lens. *Contact Lens Spectrum* 2002;17:38–41. Available at: <http://www.clspectrum.com/article.aspx?article=12085>. Accessed August 22, 2008.
59. Jones L, Senchyna M, Glasier MA, Schickler J, Forbes I, Louie D, May C. Lysozyme and lipid deposition on silicone hydrogel contact lens materials. *Eye Contact Lens* 2003;29:S75–9.
60. Senchyna M, Jones L, Louie D, May C, Forbes I, Glasier MA. Quantitative and conformational characterization of lysozyme deposited on balafilcon and etafilcon contact lens materials. *Curr Eye Res* 2004; 28:25–36.
61. Subbaraman LN, Bayer S, Gepr S, Glasier MA, Lorentz H, Senchyna M, Jones L. Rewetting drops containing surface active agents improve the clinical performance of silicone hydrogel contact lenses. *Optom Vis Sci* 2006;83:143–51.
62. Subbaraman LN, Glasier MA, Senchyna M, Sheardown H, Jones L. Extraction efficiency of an extraction buffer used to quantify lysozyme deposition on conventional and silicone hydrogel contact lens materials. *Eye Contact Lens* 2007;33:169–73.
63. Suwala M, Glasier MA, Subbaraman LN, Jones L. Quantity and conformation of lysozyme deposited on conventional and silicone hydrogel contact lens materials using an in vitro model. *Eye Contact Lens* 2007;33:138–43.
64. Subbaraman LN, Glasier MA, Senchyna M, Sheardown H, Jones L. Kinetics of in vitro lysozyme deposition on silicone hydrogel, PMMA, and FDA groups I, II, and IV contact lens materials. *Curr Eye Res* 2006;31:787–96.
65. Keith D, Hong B, Christensen M. A novel procedure for the extraction of protein deposits from soft hydrophilic contact lenses for analysis. *Curr Eye Res* 1997;16:503–10.
66. Stathopoulos PB, Scholz GA, Hwang YM, Rumfeldt JA, Lepock JR, Meiering EM. Sonication of proteins causes formation of aggregates that resemble amyloid. *Protein Sci* 2004;13:3017–27.
67. Gole A, Dash C, Soman C, Sainkar SR, Rao M, Sastry M. On the preparation, characterization, and enzymatic activity of fungal protease-gold colloid bioconjugates. *Bioconj Chem* 2001;12:684–90.
68. Jurgens L, Nichtl A, Werner U. Electron density imaging of protein

bal15/zov-opx/zov-opx/zov01208/zov5373-08a	angnes	S=4	10/22/08	0:54	Art: OPX200758	Input-go
--	--------	-----	----------	------	----------------	----------

- 14 Imaging Protein on Contact Lenses—Teichroeb et al.
- films on gold-particle surfaces with transmission electron microscopy. *Cytometry* 1999;37:87–92.
69. Hayat MA. *Colloidal Gold: Principles, Methods and Applications*, vol 1. San Diego: Academic Press; 1989.
70. Bhatia S, Goldberg EP, Enns JB. Examination of contact lens surfaces by Atomic Force Microscope (AFM). *CLAO J* 1997;23:264–9.
71. Grobe GL III, Valint PL Jr, Ammon DM Jr. Surface chemical structure for soft contact lenses as a function of polymer processing. *J Biomed Mater Res* 1996;32:45–54.
72. Maldonado-Codina C, Efron N. Impact of manufacturing technology and material composition on the surface characteristics of hydrogel contact lenses. *Clin Exp Optom* 2005;88:396–404.
73. Guryca V, Hobzova R, Pradny M, Sirc J, Michalek J. Surface morphology of contact lenses probed with microscopy techniques. *Cont Lens Anterior Eye* 2007;30:215–22.
74. Baguet J, Sommer F, Duc TM. Imaging surfaces of hydrophilic contact lenses with the atomic force microscope. *Biomaterials* 1993;14:279–84.
75. Carney FP, Nash WL, Sentell KB. The adsorption of major tear film lipids in vitro to various silicone hydrogels over time. *Invest Ophthalmol Vis Sci* 2008;49:120–4.
76. Lorentz H, Rogers R, Jones L. The impact of lipid on contact angle wettability. *Optom Vis Sci* 2007;84:946–53.
77. Zhang S, Borazjani RN, Salamone JC, Ahearn DG, Crow SA Jr, Pierce GE. In vitro deposition of lysozyme on etafilcon A and balafilcon A hydrogel contact lenses: effects on adhesion and survival of *Pseudomonas aeruginosa* and *Staphylococcus aureus*. *Cont Lens Anterior Eye* 2005;28:113–9.
78. Krebs MR, Wilkins DK, Chung EW, Pitkeathly MC, Chamberlain AK, Zurdo J, Robinson CV, Dobson CM. Formation and seeding of amyloid fibrils from wild-type hen lysozyme and a peptide fragment from the beta-domain. *J Mol Biol* 2000;300:541–9.
79. Chiti F, Webster P, Taddei N, Clark A, Stefani M, Ramponi G, Dobson CM. Designing conditions for in vitro formation of amyloid protofilaments and fibrils. *Proc Natl Acad Sci U S A* 1999;96:3590–4.

James Forrest

*Department of Physics and Astronomy
University of Waterloo
Waterloo, ON N2L 3G1
Canada
e-mail: jforrest@sciborg.uwaterloo.ca*